UNIVERSITY OF CALIFORNIA, SAN DIEGO

Advances and Applications of Mass Spectral Techniques for the Characterization of Atmospheric Aerosol Particles

A dissertation submitted in partial satisfaction of the requirements for the degree
Doctor of Philosophy

in

Chemistry

by

Lindsay Erighn Hatch

Committee in Charge:

Professor Kimberly Prather, Chair
Professor Nathan Gianneschi
Professor Judy Kim
Professor Lynn Russell
Professor Amitabha Sinha

2012

The dissertation of Lindsay Erighn Hatch is approved, and it is acceptable in quality and form for publication on microfilm and electronically:

_____

_____

_____

_____

_____

Chair

University of California, San Diego

2012

DEDICATION

To my mom, who was pushed out of science classes for being female, but always maintained a strong intellectual curiosity and analytical mind.

EPIGRAPH

The old man said to me,
"Long before these crowded streets
Here stood my dreaming tree."
Below it he would sit
For hours at a time
Now progress takes away
What forever took to find

Dave Matthews Band, "The Dreaming Tree"

Be the change you wish to see in the world.

Mahatma Ghandi

TABLE OF CONTENTS

LIST OF ABBREVIATIONS

Ac	Acetone
AMIGAS	August Mini-Intensive Gas and Aerosol Study
AMS	Aerosol Mass Spectrometry
ANARChE	Aerosol Nucleation and Real-Time Characterization Experiment
APA	Absolute Peak Area
ATOFMS	Aerosol Time of Flight Mass Spectrometry
BB	Biomass Burning
BEPOX	Butane Epoxydiol
CCN	Cloud Condensation Nucleus
CIMS	Chemical Ionization Mass Spectrometry
DC	Direct Current
E-AIM	Extended Aerosol Inorganics Model
EC	Elemental Carbon
ESI	Electrospray Ionization
FT-ICR	Fourier-Transform Ion Cyclotron Resonance
GC	Gas Chromatography
HR-MS	High Resolution Mass Spectrometry
IEPOX	Isoprene Epoxydiol
i.d.	Inner Diameter
IF	Ion Funnel
IN	Ice Nuclei
IP	Ionization Potential
IS	Internal Standard
JST	Jefferson St.
KE	Kinetic Energy
LDI	Laser Desorption/Ionization
MCP	Microchannel Plate
MOUDI	Micro-Orifice Uniform Deposit Impactor
NIST	National Institutes of Standards and Technology
OC	Organic Carbon
PA	Proton Affinity

PALMS	Particle Ablation by Laser Mass Spectrometry
PBL	Planetary Boundary Layer
PILS	Particle into Liquid Sampler
$PM_{2.5}$	Particulate Matter <2.5 μm
POA	Primary Organic Aerosol
PTRMS	Proton-Transfer-Reaction Mass Spectrometry
RF	Radiofrequency
RH	Relative Humidity
RPA	Relative Peak Area
SEARCH	Southeastern Aerosol Research and Characterization
SOA	Secondary Organic Aerosol
SOAR	Study of Organic Aerosols in Riverside
SPMS	Single Particle Mass Spectrometry
TAG	Thermal-Desorption Aerosol Gas Chromatography
TC	Tropical Cyclone
TD	Thermodenuder
TEA	Triethylamine
UPLC	Ultra Performance Liquid Chromatography
VOC	Volatile Organic Compound
WSOC	Water Soluble Organic Carbon

LIST OF FIGURES

LIST OF TABLES

ACKNOWLEDGEMENTS

Of course the work described in this thesis would not have been possible without my advisor, Prof. Kimberly Prather, and she deserves my first ode of gratitude. Over the last 6 years, I have had tremendous opportunities to work on state-of-the art research projects that have allowed me to grow as a scientist. She has provided me with the freedom to explore the various research projects described herein and the opportunities to present this work at conferences. I have also learned a great deal about focusing on the bigger picture implications and making sure to engage the community in our research. I thank her for all of these experiences.

In addition, I am much indebted to all Prather Group members who have come and gone over the last few years, including Joseph Mayer, Dr. Hiroshi Furutani, Dr. Ryan Moffet, Dr. Matt Spencer, Dr. Xueying Qin, Dr. Laura Shields, Dr. Steve Toner, Dr. Ryan Sullivan, Dr. Kerri Pratt, Dr. Robert Moision, Dr. Thomas Rebotier, Dr. Yongxuan Su, Dr. Andrew Ault, Dr. Meagan Moore, Dr. Cassandra Gaston, Dr. Ying Wang, Dr. Alberto Cazorla, Dr. Defeng Zhao, Dr. Luis Cuadra-Rodriguez, Dr. Timothy Guasco, Dr. Melanie Zauscher, Dr. Jessie Creamean, Dr. Jessica Axson, John Holecek, Liz Fitzgerald, Kaitlyn Suski, Jack Cahill, Doug Collins, Matt Ruppel, Camille Sultana, Chris Lee, Katherine Nadler, and Maggie Yandell. Whether I worked with them on a project, or they offered guidance, suggestions, moral support, or just a good laugh, they have all made my grad school experience much richer. The team spirit and camaraderie of this group are unparalleled.

Several group members deserve special recognition. Dr. Kerri Pratt was my first mentor in the group. She taught me much of what I have learned about ATOFMS and data analysis and I continue to admire her dedication. Dr. Andy Ault and Dr. Cassandra Gaston were always willing to talk through data or other ATOFMS conundrums and of course share some good stories and jokes along the way. Jessie Creamean was a great field study companion and lab mate. I will always remember our many stories from Atlanta and our subsequent adventures into veganism. Dr. Melanie Zauscher is one of the most generous people I have met; she always goes out of her way to help out whoever and whenever she can. Liz Fitzgerald has been great fun around lab and I admire her ability to make the most of any situation. Jack Cahill has always been one to really dig into a subject and I appreciate our scientific discussions over the last few years. As much as

the education I have received in graduate school, I am grateful for these friendships that have developed along this journey.

A wide range of skills are required to even attempt to develop a new instrument. I must credit Dr. Hiroshi Furutani and Dr. Robert Moision for teaching me the ins-and-outs (and, well, the dos-and-don'ts) of instrument development. Joseph Mayer is also thanked for training me in the technical design and machining process… and for injecting his dry sense of humor along the way ("The only dimension that be real portant is the holy bolt circle, therwise ± 0.01" is just fine for them all little bity numbers."). George Kassabian of the UCSD Physics Electronics Shop is also gratefully acknowledged for tremendously helpful discussions regarding the homebuilt electronics utilized in the instrument.

I appreciate the feedback provided along the way by my doctoral committee, Profs Amit Sinha, Judy Kim, Mike Sailor, Lynn Russell, and I thank Nathan Gianneschi for graciously stepping in for my defense. Individuals around the Chemistry department have also made my graduate experience smoother. Rick Thomas was quick and cheerful in responding to my (many) complaints regarding the office temperature. And Myra Kosak, Carmen Alfaro, and Sofia Clemente made sure reimbursements were processed quickly.

I have also learned extensively from a number of collaborators outside of UCSD. Prof. Jason Surratt was extremely willing to work with us and provide his expertise regarding organosulfate chemistry and arranged to send us synthesized standards. Additional help with the organosulfate work and AMIGAS field campaign came from ManNin Chan, Prof. John Seinfeld, Dr. Eric Edgerton, Dr. Stephanie Shaw, and Jerry Brown. Alex Huffman and Prof. Jose Jimenez are thanked for the use of the thermodenuder and sharing their data from the SOAR campaign. I am also very grateful to Prof. Kelley Barsanti for breaking me into the world of atmospheric modeling. It has been great working with her in graduate school and I look forward to continuing our collaboration as I move on to a post-doc position in her lab. I am also very thankful for the discussions with Dr. Jean Futrell regarding our ventures into chemical ionization mass spectrometry. It was great fun to hear the stories amassed over the illustrious career of such a pioneer in mass spectrometry. Dr. Lizabeth Alexander was also very generous in sharing her experience with hollow cathode ion sources.

I probably would not have applied to graduate school if not for the *amazing* faculty of the Chemistry Department at Smith College, in particular Prof. Maureen Fagan and Prof. Shizuka

Hsieh. Maureen, my undergraduate thesis advisor, took me under her wing to tackle a new project with local environmental implications. This project cemented my interests in both analytical and environmental chemistry. Shizuka was eager to help me learn atmospheric chemistry through an independent study program we created when classes were not available on the subject. She also refused to let me give up on several occasions, and that has undoubtedly carried through and contributed to my success as a graduate student.

I thank my parents, Donna and Peter, and my brother, Mike, for supporting me when my educational pursuits brought me out to the left coast. And while I regret that I've missed most of her childhood, my niece McKenna has never stopped smiling back at me from the pictures behind my computer, which always brightened up a gloomy day. I am also deeply grateful to Ronen Levy (טדי דוב שלי) for his unwavering love, support, and making sure life stayed interesting outside of the lab.

The work in this thesis was supported by a number of funding sources. The AMIGAS campaign was funded by the Electric Power Research Institute, which also supported, in part, the development of the chemical ionization mass spectrometer described in Chapter 6. The remaining funding was provided by the National Science Foundation. The SOAR campaign was supported by the California Air Resources Board. I am also grateful for a National Science Foundation Graduate Research Fellowship that supported me from 2008-2011 and allowed the freedom to work on a variety of projects.

Chapter 2 is reproduced with permission from the American Chemical Society: Hatch, L.E.; Creamean, J.M.; Ault, A.P.; Surratt, J.D.; Chan, M.N.; Seinfeld, J.H.; Edgerton, E.S.; Su, Y.; Prather, K.A., Measurements of isoprene-derived organosulfates in ambient aerosols by aerosol time-of-flight mass spectrometry, Part 1: Single particle observations. *Environ. Sci. Tech.,* **2011**, *45*(12), 5105-5111. The dissertation author was the primary researcher/author of this chapter.

Chapter 3 is reproduced with permission from the American Chemical Society: Hatch, L.E.; Creamean, J.M.; Ault, A.P.; Surratt, J.D.; Chan, M.N.; Seinfeld, J.H.; Edgerton, E.S.; Su, Y.; Prather, K.A., Measurements of isoprene-derived organosulfates in ambient aerosols by aerosol time-of-flight mass spectrometry, Part 2: Temporal variability & formation mechanisms**.** *Environ. Sci. Tech.,* **2011**, *45(20),* 8648-8655. The dissertation author was the primary researcher/author of this chapter.

Chapter 4 is in preparation for submission to Aerosol Science & Technology: Hatch, L.E.; Pratt, K. A.; Huffman, J. A.; Jimenez, J. L.; and Prather, K. A., Impacts of aerosol aging on laser desorption/ionization in single particle mass spectrometers. The dissertation author was the primary researcher/author of this chapter.

Chapter 5 is in preparation for submission to Environmental Science & Technology: Hatch, L.E.; Barsanti, K. C.; Pratt, K. A.; Huffman, J. A.; Jimenez, J. L.; and Prather, K. A., Mixing-state dependence of nitrate volatility from atmospheric aerosol particles. The dissertation author was the primary researcher/author of this chapter.

VITA

2006	Bachelor of Arts, Smith College
2006-2007	Teaching Assistant, Chemistry & Biochemistry, University of California, San Diego
2008	Master of Science, University of California, San Diego
2008-2012	Research Assistant, University of California, San Diego
2012	Doctor of Philosophy, University of California, San Diego

PUBLICATIONS

Hatch, L.E., Biodegradation of haloacetic acids in drinking water, B.A. Thesis, Smith College, Northampton, MA, 2006.

Pratt, K.A., Hatch, L.E., Prather, K.A., Seasonal volatility dependence of ambient particle phase amines, *Environ. Sci. Technol*. **2009**, *43*, 5276-5281.

Hatch, L.E.; Creamean, J.M.; Ault, A.P.; Surratt, J.D.; Chan, M.N.; Seinfeld, J.H.; Edgerton, E.S.; Su, Y.; Prather, K.A., Measurements of isoprene-derived organosulfates in ambient aerosols by aerosol time-of-flight mass spectrometry, Part 1: Single particle observations. *Environ. Sci. Tech.*, **2011**, *45*(12), 5105-5111.

Hatch, L.E.; Creamean, J.M.; Ault, A.P.; Surratt, J.D.; Chan, M.N.; Seinfeld, J.H.; Edgerton, E.S.; Su, Y.; Prather, K.A., Measurements of isoprene-derived organosulfates in ambient aerosols by aerosol time-of-flight mass spectrometry, Part 2: Temporal variability & formation mechanisms**.** *Environ. Sci. Tech.*, **2011**, *45(20)*, 8648-8655.

Hatch, L.E.; Pratt, K. A.; Huffman, J. A.; Jimenez, J. L.; Prather, K. A., Impacts of aerosol aging on laser desorption/ionization in single particle mass spectrometers. *In preparation.*

Hatch, L.E.; Barsanti, K.C.; Pratt, K. A.; Huffman, J. A.; Jimenez, J. L.; Prather, K. A., Prather, Mixing-state dependence of nitrate volatility from atmospheric aerosol particles. *In preparation.*

Zauscher, M.D., Cahill, J.F., Suski, K.J., Hatch, L.E., Sullivan, A.P., Collett, J.L., and Prather, K.A. Quantitative comparison and aerosol mixing state in the western California Sierra Nevada foothills during pollution transport events in winter 2010. *In preparation.*

FIELDS OF STUDY

Major Field: Chemistry & Biochemistry

Studies in Mass Spectrometry:
Professor Kimberly Prather

Studies in Atmospheric Chemistry:
Professor Kimberly Prather

ABSTRACT OF THE DISSERTATION

Advances and Applications of Mass Spectral Techniques for the Characterization of Atmospheric Aerosol Particles

by

Lindsay Erighn Hatch

Doctor of Philosophy in Chemistry

University of California, San Diego, 2012

Professor Kimberly Prather, Chair

Aerosol particles are ubiquitous in the atmosphere and induce significant impacts on human health and climate that depend on their physical and chemical properties, such as size, composition, and mixing state (chemical associations). Measurements of aerosol composition at the single-particle level are necessary to better understand these effects. Aerosol time-of-flight mass spectrometry (ATOFMS) is able to monitor the size and chemical composition of individual particles in real time. In this doctoral research, ATOFMS analysis was extended to identify new mass spectral markers and improve the potential for quantitative measurements. Development of novel instrumentation was also undertaken.

Ion markers indicative of organosulfate compounds were identified in ATOFMS mass spectra collected in Atlanta, GA. In this study, the mixing state and temporal behavior of particulate organosulfate compounds were observed for the first time. Organosulfates were

overwhelmingly detected in carbonaceous submicron particles and the temporal trends indicated that they likely formed by the daytime oxidation of isoprene followed by aqueous reaction with sulfate overnight. These results highlight the roles of mixing state and multi-phase reactivity on the formation of secondary organic aerosols.

ATOFMS measurements of thermally-conditioned aerosol residuals obtained during the 2005 Study of Organic Aerosols in Riverside, CA were analyzed to determine the impacts of atmospheric aging on the laser desorption/ionization process. Coatings of secondary species suppressed the ionization efficiency, thereby impacting the mass spectral peak areas; however, a novel analysis method was found to correct these artifacts and produced strong agreement with collocated quantitative instrumentation. This new analysis technique was then applied to investigate the mixing-state dependence of aerosol volatility observed in Riverside. It was observed that particulate nitrate evaporated at different temperatures from different particle types (e.g., organic vs. biomass burning), which may influence the regional transport of nitrate species.

ATOFMS provides important insights into size-resolved particle sources; however it heavily fragments most organic species, resulting in loss of the molecular information. Therefore, a novel chemical ionization mass spectrometer was developed to better characterize the molecular organic aerosol constituents. In particular, an ion funnel was incorporated into a home-built proton-transfer-reaction mass spectrometer. Initial characterization studies and ion simulations indicated that the ion funnel can provide high-efficiency ion transfer from the ionization region to the mass spectrometer. These results demonstrate the potential for this instrument to ultimately achieve highly sensitive analyses of organic aerosols.

1 Introduction

1.1 Atmospheric aerosol particles

Aerosol particles are ubiquitous in the atmosphere and exert a number of significant environmental impacts, including degrading visibility, affecting global climate, and deteriorating public health. While an aerosol is technically defined as a suspension of liquid or solid particles in a gas, 'aerosol' and 'particle' will be used interchangeably throughout this thesis. Particles are directly emitted into the atmosphere from a variety of primary sources, both natural and anthropogenic (man-made), that result in aerosols across a range of sizes and composition. Natural sources include sea spray and dust storms; whereas anthropogenic sources are largely combustion related, for example, vehicular exhaust, industrial processes, and biomass burning. New particles can also form in the atmosphere from gas-phase precursors in a process known as nucleation.

Due to different formation processes, particle size distributions can span several orders of magnitude. The smallest particles (<0.010 μm) form by nucleation and are known as the nuclei mode.[1] The ultrafine mode encompasses particles <0.10 μm and are largely emitted during combustion processes.[2,3] The small size of these particles results in fast coagulation timescales, thereby limiting their atmospheric lifetime.[1] Particles in the accumulation (submicron) mode (0.1 - ~1 μm) form by coagulation and condensational growth of existing atmospheric particles; these aerosols have the longest atmospheric lifetime due to inefficient loss processes.[1] Particles larger than the accumulation mode (supermicron) are produced from mechanical generation (e.g., wind-blown dust and wave breaking); large particles, however, readily settle out gravitationally.[4] Accumulation mode particles can remain in the atmosphere for days to weeks, whereas the residence time of larger and smaller particles is generally less than a few days.[4]

Particulate matter can exert significant adverse health effects (ref. 5 and references therein). Long-term exposure of high particle concentrations has been linked to increased mortality, with a ~10-15% increase in the mortality rate for every 10 $\mu g/m^3$ increase in the mass of particulate matter.[5] Increased incidences of cardiovascular disease and decreased lung function have also been attributed to high concentrations of particulate matter.[5,6] Particles in the accumulation mode are likely to be most significant regarding health effects because they persist longest in the atmosphere and can penetrate deep into the lungs.[7] However, ultrafine particles can

diffuse more readily into tissues and may also be more biologically active.[8] The exact biological mechanisms by which particulate matter induces these health effects remain uncertain;[5] however specific chemical components are known to be toxic.[9,10] Further, mixing of chemicals has been shown to exhibit synergistic effects that exacerbate health effects relative to the individual components;[11,12] therefore it is important to know, not only the chemical composition of atmospheric aerosols, but also how constituents are mixed throughout the particle population.

Aerosols can also influence the radiative balance of the Earth. Whereas the climate forcing induced by anthropogenic greenhouse gases is largely well understood, the forcing induced by aerosols remains significantly uncertain due to their high chemical, spatial, and temporal variability.[13] Particles can also impact climate in a number of direct and indirect ways, further complicating their climatic impacts. Aerosols can directly scatter or absorb incoming solar radiation, which can cool or warm the Earth; the magnitude and sign of the radiative forcing depends on the size and composition.[14] Aerosol absorption can be predominantly attributed to soot[15] and light-absorbing organic compounds.[16,17] However, the majority of aerosols have a cooling effect by scattering light back to space.[13] How components are distributed among aerosols can further impact the extent of the radiative forcing. For instance, sulfate aerosols efficiently scatter solar radiation;[18] however, sulfate coated on soot actually increases the absorption relative to uncoated soot.[19-21] Therefore, the mixing of components in an aerosol population can significantly affect the climate forcing induced by aerosols.

Particles can further impact climate by acting as cloud seeds, known as cloud condensation nuclei (CCN) and ice nuclei (IN). Cloud droplets form when supersaturated water vapor condenses onto existing particles. However, not all particles are able to act as CCN and IN; the activity is strongly dependent on size and composition. The high curvature of small particles (<0.1 μm) results in high vapor pressure above the droplet, which inhibits cloud droplet formation. However, this curvature effect can be balanced by the presence of soluble material that lowers the vapor pressure via Raoult's Law. The relative fractions of soluble and insoluble material in these particles will therefore have significant impacts on the CCN activity.[22] However, composition plays the largest role in particles <0.2 μm because nearly all particles at larger sizes will likely activate.[22] The number of CCN-active particles in a rising air parcel can influence the resulting cloud properties. A large influx of CCN-active particles into a forming cloud can increase the number of cloud seeds, thereby producing more numerous and smaller cloud droplets for a fixed atmospheric water content, which increases cloud albedo and thus

radiative forcing.[23] Further, because smaller droplets rain out less efficiently, this effect may also reduce or delay precipitation, which can significantly impact the hydrological cycle.[24] These indirect effects of aerosols remain one of least understood climate forcings.

1.1.1 Aerosol composition & atmospheric processing

The diverse particle sources described above loft widely different chemical constituents into the atmosphere; these primary particles further undergo extensive processing during their atmospheric lifetime as a result of coagulation, condensation, evaporation, and heterogeneous reactions. The physical and chemical properties of aerosols therefore vary greatly in time and location, due to variability in emission sources, atmospheric processing, and meteorology.

1.1.1.1 Inorganic aerosol components

Inorganic aerosols emitted from primary sources are typically in the supermicron mode (>1 μm) due to their formation mechanisms. Sea spray, dominated by sodium chloride, is formed by breaking waves. Mineral dust, which becomes suspended by wind erosion, is comprised of Al, Si, Mg, Ca, Fe, K, and Na in various minerologies.[25,26] A few combustion sources can also introduce inorganic components to accumulation mode particles. Biomass burning, for example, can emit potassium chloride salts.[27] The residual fuel used to power ships is also enriched in a number of metals, such as vanadium, iron, and nickel that have been detected in atmospheric particles.[28] Combustion sources also emit elemental carbon.[29] The majority of the inorganic species in submicron aerosols, however, forms by gas-to-particle conversion. Gas-phase SO_2 emitted by power plants can react with oxidants in the gas or aqueous phase, ultimately forming sulfuric acid.[30] The vapor pressure of sulfuric acid is sufficiently low that it can be considered non-volatile under typical atmospheric conditions and thus exists almost completely in the particle phase.[1] Nitric acid also forms in the atmosphere from nitrogen oxides emitted from combustion sources.[30] Ammonia is the predominant base in the atmosphere and can neutralize sulfuric and nitric acids in the particle phase.[31,32] Ammonium, sulfate, and nitrate are therefore significant components of submicron particles.[e.g.,33-35] These are considered secondary inorganic aerosol constituents because they form in the atmosphere, rather than by direct emission. Unlike ammonium sulfate, however, ammonium nitrate is semi-volatile and exists to a significant extent in both the particle phase and in the gas phase as NH_3 and HNO_3.[36,37]

1.1.1.2 Organic aerosol components

Globally, organic components comprise ~20-80% of aerosol mass and can arise from both primary and secondary sources.[38,39] Significant sources of primary organic aerosols (POA) include combustion sources, food cooking, and biomass burning. Combustion-related emissions are generally comprised of long-chain or cyclic alkanes and polycyclic aromatic hydrocarbons.[40] Food-cooking emissions are dominated by fatty acids and cholesterol.[41,42] Biomass burning emissions include similar components as combustion and food cooking, but also include more oxygenated organics, such as levoglucosan (derived from cellulose) and methoxyphenols.[43]

A large fraction of particulate organics arises from the oxidation and condensation of gas-phase precursors, known as secondary organic aerosol (SOA). Plant emissions represent the largest source of volatile organic compounds (VOCs), with isoprene and monoterpenes being the dominant biogenic VOCs.[44,45] These species, as well as anthropogenic VOCs, may become oxidized through photochemical processes induced by sunlight (UV radiation), as well as by reactions with gas-phase oxidants, such as ozone and hydroxyl radical (refs. 46,47 and references therein). These reactions add significant functionality to the parent molecule, including hydroxyl, ketone, aldehyde, carboxylic acid, organonitrate, and organosulfate groups.[48-50] The increased polarity of the product compounds results in reduced volatility, and thus they are more likely to condense onto existing particles.[51] Species can react further within the aqueous and organic phases to produce even lower volatility products.[44,52,53] Therefore, given the variety of organic components emitted from primary sources and the number of secondary reactions, many thousands of different organic compounds are possible in atmospheric aerosols.[54]

1.1.1.3 Atmospheric processing

During a particle's multiday residence time in the atmosphere, it undergoes significant processing, also known as aging. Reactions between gas-phase and particle-phase components (i.e., heterogeneous reactions) can displace primary components (e.g., nitrate can displace chloride in sea salt[55]), or gas-phase oxidants can oxidize organics present on the particle surface.[56] Many atmospheric components are semi-volatile and exist in significant concentrations in both gas and particle phases; the partitioning between these phases is highly dynamic and responds appropriately to maintain equilibrium.[57] Primary particles may acquire secondary species following their formation (e.g., ammonium sulfate/nitrate, SOA), or semi-volatile components may evaporate from the particle phase as an air parcel becomes diluted during transport. Particles can also undergo significant cloud processing as a result of the formation and evaporation of

cloud droplets. The high liquid water content in cloud droplets promotes uptake of gas-phase species, which can react in the condensed-phase to form lower volatility compounds that remain in the particle phase following evaporation of the cloud.[58,59]

Meteorology can also significantly impact regional and local aerosol chemistry in a number of ways. Shifting winds can introduce particles from different sources to a given area depending on the source locations relative to the wind direction. Winds can also carry pollutants significant distances.[60,61] Diurnal changes also occur due to the presence and absence of sunlight. In the nocturnal atmosphere, the lack of solar heating results in lower temperatures and higher relative humidity (RH), which initiate condensation of semi-volatile and water-soluble species. The stability of the atmosphere can further have a substantial impact on pollutant concentrations. The temperature of the atmosphere typically decreases with altitude; such temperature profiles promote vertical mixing and a well-mixed planetary boundary layer (PBL, the region of the atmosphere closest to Earth's surface).[62] Temperature inversions occur when atmospheric temperature increases with altitude; radiation inversions are an example and form due to overnight radiative cooling of the surface.[1] Temperature inversions result in a stable PBL that prohibits mixing and ventilation; atmospheric pollutants thus become trapped and accumulate near the surface resulting in very poor air quality.[63] The buildup of gases and particles under an inversion can further accelerate reactions and processing.[64]

As a result of diverse particle sources and aging processes, atmospheric particles are complex mixtures of inorganic and organic material that exist in varying degrees of internal (present within the same particle) or external (occur in distinct particles) mixing states. Condensation of secondary components onto primary aerosols can substantially change the chemical composition, size, and resulting atmospheric behavior of the aerosols (e.g., optical properties, CCN activity). Therefore, comprehensive analyses of atmospheric particles are essential in order to better understand the sources and processing of ambient aerosols and their impacts on human health and climate.

1.2 Aerosol analysis methods

A variety of tools are available to characterize different aerosol properties, including size, CCN activity, optical properties, etc. Herein, several common techniques available for measuring the composition of atmospheric particulate matter will be briefly outlined. The approaches can be generally classified into two main categories: off-line and on-line sampling. Off-line

measurements entail collecting particles onto a substrate followed by laboratory analyses; whereas analysis is performed in the field for on-line instruments with minimal sample pretreatment. Since there is no single instrument that can analyze all PM components in high time resolution, these various tools remain highly complementary.

1.2.1 Off-line measurement techniques

Aerosol sampling for off-line analysis generally occurs via filtration or impaction onto a substrate, with sampling times typically on the order of hours to days. These long sampling times result in very poor temporal resolution; however, a significant benefit of this type of sampling is the collection of sufficient material to perform comprehensive analyses. These approaches have been particularly advantageous for the organic fraction of atmospheric particulate matter, given the thousands of possible compounds present in the atmosphere.[54] Gas chromatography-mass spectrometry (GC/MS) is one of the traditional techniques applied to organic aerosols and provides separation of the multitude of different organic compounds to improve molecular identification.[65,66] This technique has identified molecular tracers indicative of distinct aerosol sources.[40,67] However, standard GC/MS approaches are unable to fully separate the complex mixture in ambient aerosols; for instance, in the GC/MS analysis of samples collected in a roadway tunnel, only ~10% of the compounds could be resolved.[68] The recent applications of two-dimensional GC has provided substantially improved separation capability,[69] while also highlighting the complexity of organic aerosol with ~15,000 chromatographic peaks in one ambient aerosol sample.[70] GC analysis is only amenable to compounds that will volatilize in the injection port, and therefore alternative chromatographic approaches have also been utilized. Liquid chromatography can be applied for analysis of low-volatility organic constituents of atmospheric aerosols, including high molecular weight species,[71] whereas ion chromatography can measure dissolved inorganic ions[72] and organic acids.[73] Liquid chromatography has increasingly been applied to characterize the polar organic compounds typical of SOA.[74,75] These chromatographic methods provide a means of separating the complex mixture and make the identification of individual components far more tractable.

Other off-line techniques have further advanced the state-of-knowledge regarding the composition of ambient aerosols. Ultra-high-resolution mass spectrometry analyses coupled with ionization methods that minimize fragmentation can identify thousands of compounds in aerosol samples based solely on ion *m/z* by providing the molecular formulas of aerosol constituents.[17,76] Spectroscopy methods, including Fourier-transform infrared spectroscopy and nuclear magnetic

resonance spectroscopy, provide quantitative estimates of the contributions from specific functional groups present in an organic aerosol population, without the need to identify individual compounds.[48,77-79] Microscopic imaging has also permitted assessment of the complex morphology of ambient aerosol particles.[e.g.,28,80,81] These off-line methods have provided in-depth chemical characterization of atmospheric particulate matter. However their poor temporal resolution and/or extensive sample preparation and analysis times have limited the scientific understanding regarding atmospheric transformations of aerosol composition.

1.2.2 On-line measurement techniques

To monitor rapid changes in aerosol composition that occur as a result of chemical processing or shifts in meteorology, sampling must be performed on much faster timescales than off-line techniques can provide. To this end, instruments have been developed that are capable of measuring aerosol composition in real time or near real time. A few recent advances are highlighted herein.

A number of instruments have been developed to couple the advantages of chromatographic separation and on-line analysis by utilizing *in-situ* particle collection schemes. Thermal-desorption aerosol gas chromatography (TAG) employs a particle collection-thermal desorption cell with direct injection onto the GC column.[82] The system is fully automated, with a full cycle taking approximately 1 hour.[82] TAG has provided highly time-resolved chemical speciation of the organic fraction of atmospheric particles,[83] however, a large portion of aerosol material could not be resolved with one-dimensional separation.[82] Recently, TAG has been upgraded to employ comprehensive two-dimensional GC, which substantially improves the separation and identification capabilities.[84] An alternative *in-situ* collection approach is the particle-into-liquid sampler (PILS), which passes aerosols through a region supersaturated with respect to water resulting in condensational particle growth.[85] The grown particles are collected by inertial impaction, yielding an aqueous solution of the soluble aerosol components.[85] PILS has been coupled to ion chromatography to measure ionic constituents (e.g., sulfate, nitrate, sodium, potassium)[85] and total organic carbon analyzers to measure the water-soluble organic carbon content of atmospheric particles.[86]

Two predominant real-time techniques have emerged in the last couple decades: single particle mass spectrometry (SPMS) and aerosol mass spectrometry (AMS). The aerosol time-of-flight mass spectrometer (ATOFMS) was the first SPMS instrument,[87] and measures the size and

chemical composition of individual particles. This measurement capability provides insight into the size-resolved chemical mixing state of aerosol components. ATOFMS was the predominant instrument used in this doctoral work and will be described in detail in the following section. AMS data from collaborators was also used in Chapters 4 & 5 of this thesis.

AMS has also become a widely used instrument in the atmospheric science community for the real-time, quantitative analysis of aerosol components.[88,89] In the AMS instrument, aerosols are introduced through vacuum stages into the mass spectrometer region, where they are flash vaporized on a heater maintained at 600 ºC; the desorbed constituents are subsequently ionized via electron impact ionization (70 eV).[90] The AMS measures only non-refractory organic and inorganic aerosol material, or constituents that volatilize at 600 ºC; on the other hand, it is "blind" to refractory material that does not volatilize at that temperature, for example, sea salt.[91] The AMS also largely provides the bulk aerosol composition, rather than mixing state.[92]

1.2.3 Aerosol time-of-flight mass spectrometry

The original ATOFMS prototype was developed by Prather *et al.* in 1994,[87] and has evolved substantially since then[93-95] into instruments that have been deployed around world and aboard ground, ship, and aircraft platforms. While there are several permutations, all ATOFMS instruments consist of a particle inlet, sizing region, and the ionization and mass spectrometer region (Figure 1.1); each region is described in the following sections.

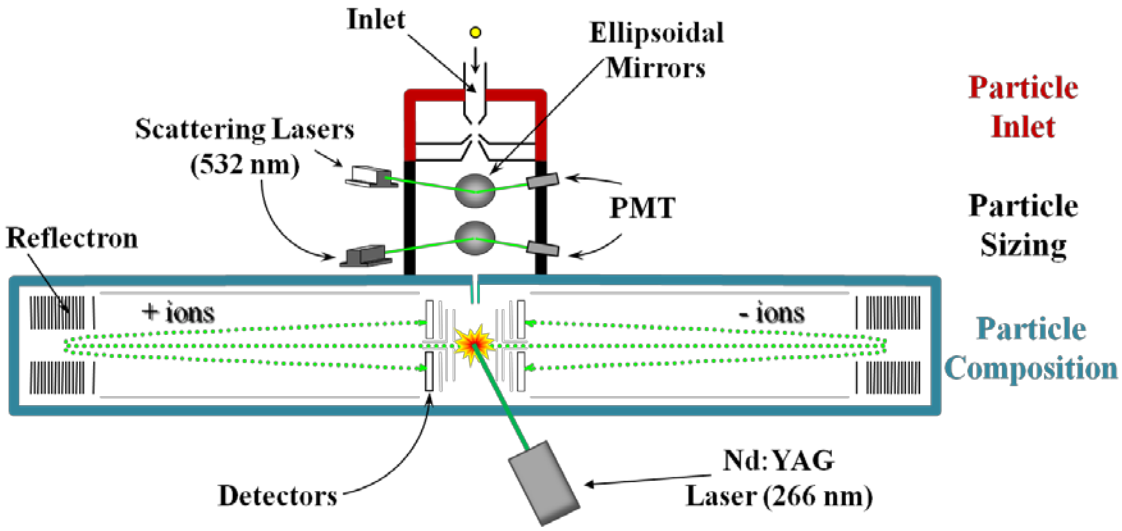

Figure 1.1 Schematic of the ATOFMS instrument based on Gard *et al.*[93] Figure courtesy of A. Ault.

1.2.3.1 Inlet configurations

Aerosols are introduced into ATOFMS via either a converging nozzle[93] or an aerodynamic lens,[94,95] each covering different size ranges. The nozzle inlet, shown in Figure 1.1, provides the broadest range, measuring particles from 0.2-3 μm. Aerosols are pulled through the nozzle from atmospheric pressure to 2 Torr, resulting in a supersonic expansion that accelerates particles to a size-dependent terminal velocity.[93] Particles subsequently traverse two differentially-pumped stages, which collimate the particle beam and eliminate background gas. Aerodynamic lenses focus particles into a tight beam by a series of expansions and contractions defined by a set of orifices.[96,97] The first ATOFMS to incorporate an aerodynamic lens reported significantly improved particle detection efficiencies compared to the standard nozzle-inlet ATOFMS.[94] These inlets are much more effective for introducing small particles; efficient detection of particles from 0.05-0.3 μm can be achieved with proper tuning and removal of larger particles prior to the inlet.[94] Both versions were used in the measurements described in Chapters 2 & 3. A new ATOFMS has recently been constructed for use on aircraft platforms and also utilizes an aerodynamic lens inlet that transmits particles over the range 0.1-1 μm.[95] The ground-based prototype of this aircraft-ATOFMS was applied in the measurements of Chapters 4 & 5.

1.2.3.2 Sizing region

The particle sizing region consists of two continuous-wave lasers (λ = 532 nm, 50 mW) positioned a fixed 6 cm apart. Particles scatter light as they cross the laser beam, which is focused via ellipsoidal mirrors onto a photomultiplier tube.[93] The signals from the two scattering lasers define the particle transit time across the fixed distance, and therefore the particle velocity. Particle velocity can be converted to vacuum aerodynamic diameter via calibrations with polystyrene latex spheres of known size. The scattered light signals also trigger a timing circuit to fire the desorption/ionization laser when the particle arrives in the mass spectrometer source region.

1.2.3.3 Ionization and detection

Particle ablation is accomplished via single-step laser desorption/ionization (LDI). A 266 nm, Q-switched Nd:YAG laser, generally operating at ~1 mJ, fires at the moment the particle arrives in the path of the laser beam, as triggered by the timing circuit. The laser pulse generates a plasma of ions and neutrals from the individual particle with ionization occurring via multi-photon ionization, electron capture, and charge transfer. Both positive and negative ions form

and are extracted into opposite sides of the mass spectrometer by high electrostatic fields applied to source plates on either side of the ionization region. ATOFMS can detect both refractory and non-refractory aerosol components; however, most organic species are heavily fragmented.

The mass analyzer of the original transportable ATOFMS instruments is a dual-polarity, collinear, reflectron time-of-flight mass spectrometer. Positive and negative ions travel in opposite directions down the flight tube (Figure 1.1). A reflectron is essentially an ion mirror that improves mass resolution by reducing the spread of kinetic energy (KE) among ions of the same *m/z*; ions of higher KE penetrate further into the reflectron than lower energy ions, thereby narrowing the difference in flight time from ionization to detection. Microchannel plate (MCP) detectors are used to detect the ion arrival time.

The TOFMS was significantly improved in the new aircraft-ATOFMS.[95] The flight path was redesigned to a *z*-configuration (Figure 1.2), which eliminated artifacts observed in the mass spectrometers of older ATOFMS instruments, such as cross-talk between the MCP detectors. The electrostatic ion optics were also enhanced, resulting in improved mass resolution, transmission efficiency, and higher *m/z* range.[95]

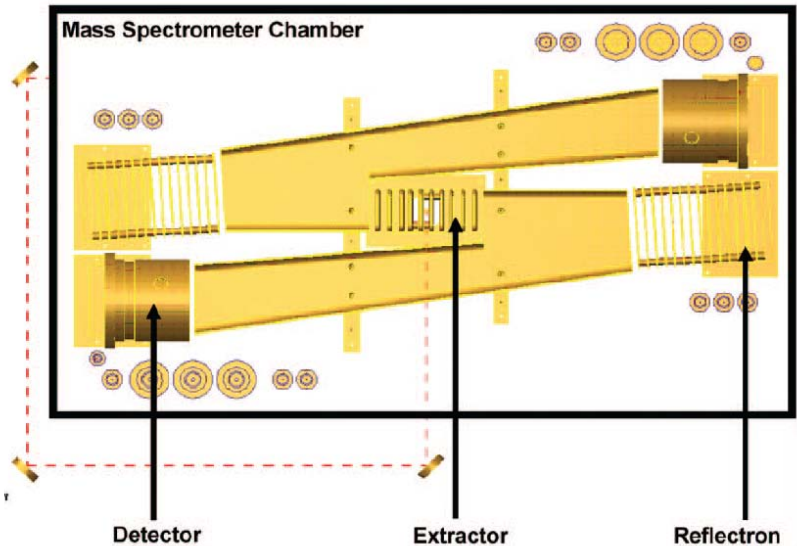

Figure 1.2 Mass spectrometer design used in the aircraft-ATOFMS. Reprinted with permission from ref 95. Copyright 2009, American Chemical Society.

1.3 Scope of this thesis

The research described herein aims to extend the analytical capability for characterizing aerosol composition and processing. The existing off-line and on-line aerosol analysis tools

described in Sections 1.2.1 and 1.2.2 provide invaluable information regarding molecular identification and/or quantitative measures of aerosol components; however, most cannot provide insight into the mixing state of the aerosol population and few provide real-time measurements. Knowledge of the chemical mixing state is essential for adequately assessing and ultimately predicting the environmental impacts of aerosols since chemical associations at the single particle level can influence optical and CCN properties, as well as human health. Ideally, a single-particle mass spectrometer would be able to speciate molecular components and provide quantitative estimates of particle composition. While these goals may never be fully achieved with single-step LDI, this thesis provides additional steps in that direction. Comparisons between ATOFMS and collocated measurements were used to better understand the ambient single particle data with regard to ion peak identification and the ability to relate ion peak areas to mass. The insight gained from these comparisons was then applied to learn more about the processing of ambient aerosols.

Chapter 2 describes the assignment of new ATOFMS marker ions indicative of organosulfate species. Recent laboratory and field studies have identified these compounds as potentially significant secondary products of the reaction between biogenic and anthropogenic emissions.[e.g.,50,75,98,99] However, their detection in ambient aerosols has been limited to filter sampling techniques, which lack the time and size resolution to provide further insight into the atmospheric formation of organosulfates.[50,100] During a 2008 field campaign in Atlanta, GA, both single-particle measurements and analyses of filter extracts by ultra-performance liquid chromatography coupled to electrospray ionization-high-resolution time-of-flight mass spectrometry (UPLC/ESI-HR-TOFMS) were performed. The UPLC/ESI-HR-TOFMS analyses unequivocally identified organosulfate components in the Atlanta aerosols and were used to identify high mass ions in the negative-ion spectra collected by ATOFMS. These comparisons established that ATOFMS is well suited to measure intact organosulfate species and provided the first determinations of the mixing-state (Chapter 2) and highly-time resolved diurnal trends (Chapter 3) of these species. Insights into the atmospheric formation mechanisms are discussed.

While single-particle mass spectrometers provide important observations of the size-resolved mixing state of ambient particles, their ability to quantify aerosol components has been extremely limited due to matrix effects[101,102] and inconsistent laser-particle interactions.[103] Characterization of these effects have largely been limited to laboratory studies with simple test particles.[104] Aerosols in the atmosphere are significantly more complex due to the chemical array

of particle sources and aging processes and therefore they may exhibit more complicated and variable interactions with the D/I laser. In Chapter 4, the impacts of particle aging on the LDI process are explored based on ATOFMS measurements of thermally-conditioned aerosols sampled in the highly polluted Riverside, CA area. Collocated AMS measurements were used as a quantitative assessment of the changes in the mass of particle constituents following heating. It will be demonstrated that secondary coatings suppress the extent of ionization from ambient particles during LDI, which impacted the raw ion intensities of individual components. A method is proposed to correct for these effects that produces strong agreement with the AMS measurements, demonstrating the potential to accurately relate ion peak areas to the mass of aerosol components. This work provides important steps toward the goal of single particle mass spectrometers being able to provide quantitative measurements of aerosol composition.

The results of Chapter 4 demonstrate that the change in ion peak area following heating of a given species can be used to assess its volatility from particles of different sources. This method is applied in Chapter 5 to characterize the influence of chemical associations on the volatility of nitrate from particles of different composition. In particular, nitrate persisted to much higher temperatures in particles that contain refractory metal ions, even though nitrate was predominantly ammonium nitrate. These findings imply that nitrate is more strongly bound to those particles, which may have implications for regional nutrient deposition given that the lifetime—and therefore transport distance—is significantly longer for particle-phase nitrate than gas-phase nitric acid.[105]

ATOFMS mass spectra contain markers for distinct organic compounds, including organosulfates (Chapter 2), organic acids,[106] amines,[107] and polycyclic aromatic hydrocarbons.[108,109] The majority of the organic aerosol components, however, are heavily fragmented under the harsh conditions of LDI, thus limiting the chemical information that can be attained. It is therefore advantageous to investigate softer ionization mechanisms that can achieve molecular ionization of the organic components in aerosols. Chapter 6 describes the first stages of development for a single-particle, chemical-ionization mass spectrometer. The extremely low mass present for individual compounds within a single particle necessitates ultra-high instrument sensitivity that has not yet been achieved in chemical ionization mass spectrometers targeting organic aerosols. To this end, an ion funnel was implemented, which has been shown in other mass-spectrometric based techniques to achieve nearly 100% ion transmission across interfaces of differentially-pumped chambers.[110] Proof-of-concept experiments were performed to

demonstrate the utility of ion funnels in PTRMS, which may ultimately provide the essential leap toward achieving real-time molecular speciation of organic aerosol constituents.

1.4 Acknowledgements

Kaitlyn Suski is thanked for reviewing this chapter.

1.5 References

1. Seinfeld, J. H.; Pandis, S. N., *Atmospheric Chemistry & Physics: From Air Pollution to Climate Change*. 2nd. ed.; John Wiley & Sons, Inc.: New Jersey, 2006.

2. Hildemann, L. M.; Markowski, G. R.; Jones, M. C.; Cass, G. R., Submicrometer Aerosol Mass Distributions of Emissions from Boilers, Fireplaces, Automobiles, Diesel Trucks, and Meat-Cooking Operations. *Aerosol Sci. Technol.* **1991,** *14*, (1), 138-152.

3. Hughes, L. S.; Cass, G. R.; Gone, J.; Ames, M.; Olmez, I., Physical and chemical characterization of atmospheric ultrafine particles in the Los Angeles area. *Environ. Sci. Technol.* **1998,** *32*, (9), 1153-1161.

4. Hobbs, P. V., *Introduction to Atmospheric Chemistry*. Cambridge University Press: New York, NY, 2000.

5. Pope, C. A.; Dockery, D. W., Health effects of fine particulate air pollution: Lines that connect. *J. Air Waste Manage. Assoc.* **2006,** *56*, (6), 709-742.

6. Dockery, D. W., Epidemiologic evidence of cardiovascular effects of particulate air pollution. *Environ. Health Perspect.* **2001,** *109*, 483-486.

7. Tjalve, H.; Henriksson, I., Uptake of metals in the brain via olfactory pathways. *Neurotoxicology* **1999,** *20*, (2-3), 181-195.

8. Oberdorster, G.; Oberdorster, E.; Oberdorster, J., Nanotoxicology: An emerging discipline evolving from studies of ultrafine particles. *Environ. Health Perspect.* **2005,** *113*, (7), 823-839.

9. Xia, T.; Korge, P.; Weiss, J. N.; Li, N.; Venkatesan, M. I.; Sioutas, C.; Nel, A., Quinones and aromatic chemical compounds in particulate matter induce mitochondrial dysfunction: Implications for ultrafine particle toxicity. *Environ. Health Perspect.* **2004,** *112*, (14), 1347-1358.

10. Nemmar, A.; Hoylaerts, M. F.; Hoet, P. H. M.; Dinsdale, D.; Smith, T.; Xu, H. Y.; Vermylen, J.; Nemery, B.; Nemery, B., Ultrafine particles affect experimental thrombosis in an in vivo hamster model. *Am. J. Respir. Crit. Care Med.* **2002,** *166*, (7), 998-1004.

11. Campen, M. J.; Nolan, J. P.; Schladweiler, M. C. J.; Kodavanti, U. P.; Evansky, P. A.; Costa, D. L.; Watkinson, W. P., Cardiovascular and thermoregulatory effects of inhaled PM-associated transition metals: A potential interaction between nickel and vanadium sulfate. *Toxicol. Sci.* **2001,** *64*, (2), 243-252.

12. Zhou, Y. M.; Zhong, C. Y.; Kennedy, I. M.; Leppert, V. J.; Pinkerton, K. E., Oxidative stress and NF kappa B activation in the lungs of rats: a synergistic interaction between soot and iron particles. *Toxicol. Appl. Pharmacol.* **2003,** *190*, (2), 157-169.

13. Hansen, J.; Sato, M.; Kharecha, P.; von Schuckmann, K., Earth's energy imbalance and implications. *Atmos. Chem. Phys.* **2011,** *11*, (24), 13421-13449.

14. Charlson, R. J.; Schwartz, S. E.; Hales, J. M.; Cess, R. D.; Coakley, J. A.; Hansen, J. E.; Hofmann, D. J., Climate Forcing by Anthropogenic Aerosols. *Science* **1992,** *255*, (5043), 423-430.

15. Ramanathan, V.; Carmichael, G., Global and regional climate changes due to black carbon. *Nature Geoscience* **2008,** *1*, (4), 221-227.

16. Andreae, M. O.; Gelencser, A., Black carbon or brown carbon? The nature of light-absorbing carbonaceous aerosols. *Atmos. Chem. Phys.* **2006,** *6*, 3131-3148.

17. Laskin, J.; Laskin, A.; Roach, P. J.; Slysz, G. W.; Anderson, G. A.; Nizkorodov, S. A.; Bones, D. L.; Nguyen, L. Q., High-Resolution Desorption Electrospray Ionization Mass Spectrometry for Chemical Characterization of Organic Aerosols. *Anal. Chem.* **2010,** *82*, (5), 2048-2058.

18. Kiehl, J. T.; Briegleb, B. P., The Relative Roles of Sulfate Aerosols and Greenhouse Gases in Climate Forcing. *Science* **1993,** *260*, (5106), 311-314.

19. Bond, T. C.; Habib, G.; Bergstrom, R. W., Limitations in the enhancement of visible light absorption due to mixing state. *J. Geophys. Res.* **2006,** *111*, (D20).

20. Jacobson, M. Z., Strong radiative heating due to the mixing state of black carbon in atmospheric aerosols. *Nature* **2001,** *409*, (6821), 695-697.

21. Moffet, R. C.; Prather, K. A., In-situ measurements of the mixing state and optical properties of soot with implications for radiative forcing estimates. *Proc. Nat. Acad. Sci.* **2009,** *106*, (29), 11872-11877.

22. McFiggans, G.; Artaxo, P.; Baltensperger, U.; Coe, H.; Facchini, M. C.; Feingold, G.; Fuzzi, S.; Gysel, M.; Laaksonen, A.; Lohmann, U.; Mentel, T. F.; Murphy, D. M.; O'Dowd, C. D.; Snider, J. R.; Weingartner, E., The effect of physical and chemical aerosol properties on warm cloud droplet activation. *Atmos. Chem. Phys.* **2006,** *6*, 2593-2649.

23. Crutzen, P. J.; Andreae, M. O., Biomass Burning in the Tropics - Impact on Atmospheric Chemistry and Biogeochemical Cycles. *Science* **1990,** *250*, (4988), 1669-1678.

24. Lohmann, U.; Feichter, J., Global indirect aerosol effects: a review. *Atmospheric Chemistry and Physics* **2005,** *5*, 715-737.

25. Reid, E. A.; Reid, J. S.; Meier, M. M.; Dunlap, M. R.; Cliff, S. S.; Broumas, A.; Perry, K.; Maring, H., Characterization of African dust transported to Puerto Rico by individual particle and size segregated bulk analysis. *J. Geophys. Res.* **2003,** *108*, (D19).

26. Gomes, L.; Gillette, D. A., A Comparison of Characteristics of Aerosol from Dust Storms in Central-Asia with Soil-Derived Dust from Other Regions. *Atmospheric Environment Part a-General Topics* **1993,** *27*, (16), 2539-2544.

27. Allen, A. G.; Miguel, A. H., Biomass Burning in the Amazon - Characterization of the Ionic Component of Aerosols Generated Tom Flaming and Smoldering Rain-Forest and Savanna. *Environ. Sci. Technol.* **1995,** *29*, (2), 486-493.

28. Moldanova, J.; Fridell, E.; Popovicheva, O.; Demirdjian, B.; Tishkova, V.; Faccinetto, A.; Focsa, C., Characterisation of particulate matter and gaseous emissions from a large ship diesel engine. *Atmos. Environ.* **2009,** *43*, (16), 2632-2641.

29. Bond, T. C.; Streets, D. G.; Yarber, K. F.; Nelson, S. M.; Woo, J. H.; Klimont, Z., A technology-based global inventory of black and organic carbon emissions from combustion. *Journal of Geophysical Research-Atmospheres* **2004,** *109*, (D14).

30. Hewitt, C. N., The atmospheric chemistry of sulphur and nitrogen in power station plumes. *Atmos. Environ.* **2001,** *35*, (7), 1155-1170.

31. Russell, A. G.; Cass, G. R., Verification of a Mathematical-Model for Aerosol Nitrate and Nitric-Acid Formation and Its Use for Control Measure Evaluation. *Atmos. Environ.* **1986,** *20*, (10), 2011-2025.

32. Bouwman, A. F.; Lee, D. S.; Asman, W. A. H.; Dentener, F. J.; VanderHoek, K. W.; Olivier, J. G. J., A global high-resolution emission inventory for ammonia. *Global Biogeochem. Cycles* **1997,** *11*, (4), 561-587.

33. Chow, J. C.; Watson, J. G.; Lowenthal, D. H.; Solomon, P. A.; Magliano, K. L.; Ziman, S. D.; Richards, L. W., PM(10) and PM(2.5) Compositions in California San Joaquin Valley. *Aerosol Sci. Technol.* **1993,** *18*, (2), 105-128.

34. Ho, K. F.; Lee, S. C.; Chan, C. K.; Yu, J. C.; Chow, J. C.; Yao, X. H., Characterization of chemical species in PM2.5 and PM10 aerosols in Hong kong. *Atmos. Environ.* **2003,** *37*, (1), 31-39.

35. Pakkanen, T. A.; Loukkola, K.; Korhonen, C. H.; Aurela, M.; Makela, T.; Hillamo, R. E.; Aarnio, P.; Koskentalo, T.; Kousa, A.; Maenhaut, W., Sources and chemical composition of atmospheric fine and coarse particles in the Helsinki area. *Atmos. Environ.* **2001,** *35*, (32), 5381-5391.

36. Stelson, A. W.; Seinfeld, J. H., Relative-Humidity and Temperature-Dependence of the Ammonium-Nitrate Dissociation-Constant. *Atmos. Environ.* **1982,** *16*, (5), 983-992.

37. Nowak, J. B.; Neuman, J. A.; Bahreini, R.; Middlebrook, A. M.; Holloway, J. S.; McKeen, S. A.; Parrish, D. D.; Ryerson, T. B.; Trainer, M., Ammonia sources in the California South Coast Air Basin and their impact on ammonium nitrate formation. *Geophysical Research Letters* **2012,** *39*.

38. Jacobson, M. C.; Hansson, H. C.; Noone, K. J.; Charlson, R. J., Organic atmospheric aerosols: Review and state of the science. *Rev. Geophys.* **2000,** *38*, (2), 267-294.

39. Kanakidou, M.; Seinfeld, J. H.; Pandis, S. N.; Barnes, I.; Dentener, F. J.; Facchini, M. C.; Van Dingenen, R.; Ervens, B.; Nenes, A.; Nielsen, C. J.; Swietlicki, E.; Putaud, J. P.; Balkanski, Y.; Fuzzi, S.; Horth, J.; Moortgat, G. K.; Winterhalter, R.; Myhre, C. E. L.; Tsigaridis, K.; Vignati, E.; Stephanou, E. G.; Wilson, J., Organic aerosol and global climate modelling: a review. *Atmos. Chem. Phys.* **2005,** *5*, 1053-1123.

40. Cass, G. R., Organic molecular tracers for particulate air pollution sources. *Trac-Trends in Analytical Chemistry* **1998,** *17*, (6), 356-366.

41. Rogge, W. F.; Hildemann, L. M.; Mazurek, M. A.; Cass, G. R.; Simonelt, B. R. T., Sources of Fine Organic Aerosol .1. Charbroilers and Meat Cooking Operations. *Environ. Sci. Technol.* **1991,** *25*, (6), 1112-1125.

42. Robinson, A. L.; Subramanian, R.; Donahue, N. M.; Bernardo-Bricker, A.; Rogge, W. F., Source apportionment of molecular markers and organic aerosol. 3. Food cooking emissions. *Environ. Sci. Technol.* **2006,** *40*, (24), 7820-7827.

43. Simoneit, B. R. T., Biomass burning - A review of organic tracers for smoke from incomplete combustion. *Appl. Geochem.* **2002,** *17*, (3), 129-162.

44. Carlton, A. G.; Wiedinmyer, C.; Kroll, J. H., A review of Secondary Organic Aerosol (SOA) formation from isoprene. *Atmos. Chem. Phys.* **2009,** *9*, (14), 4987-5005.

45. Kesselmeier, J.; Staudt, M., Biogenic volatile organic compounds (VOC): An overview on emission, physiology and ecology. *Journal of Atmospheric Chemistry* **1999,** *33*, (1), 23-88.

46. Hallquist, M.; Wenger, J. C.; Baltensperger, U.; Rudich, Y.; Simpson, D.; Claeys, M.; Dommen, J.; Donahue, N. M.; George, C.; Goldstein, A. H.; Hamilton, J. F.; Herrmann, H.; Hoffmann, T.; Iinuma, Y.; Jang, M.; Jenkin, M. E.; Jimenez, J. L.; Kiendler-Scharr, A.; Maenhaut, W.; McFiggans, G.; Mentel, T. F.; Monod, A.; Prevot, A. S. H.; Seinfeld, J. H.; Surratt, J. D.; Szmigielski, R.; Wildt, J., The formation, properties and impact of secondary organic aerosol: current and emerging issues. *Atmos. Chem. Phys.* **2009,** *9*, (14), 5155-5236.

47. Kroll, J. H.; Seinfeld, J. H., Chemistry of secondary organic aerosol: Formation and evolution of low-volatility organics in the atmosphere. *Atmos. Environ.* **2008,** *42*, (16), 3593-3624.

48. Russell, L. M.; Bahadur, R.; Ziemann, P. J., Identifying organic aerosol sources by comparing functional group composition in chamber and atmospheric particles. *Proceedings of the National Academy of Sciences of the United States of America* **2011,** *108*, (9), 3516-3521.

49. Yu, J. Z.; Cocker, D. R.; Griffin, R. J.; Flagan, R. C.; Seinfeld, J. H., Gas-phase ozone oxidation of monoterpenes: Gaseous and particulate products. *Journal of Atmospheric Chemistry* **1999,** *34*, (2), 207-258.

50. Surratt, J. D.; Gomez-Gonzalez, Y.; Chan, A. W. H.; Vermeylen, R.; Shahgholi, M.; Kleindienst, T. E.; Edney, E. O.; Offenberg, J. H.; Lewandowski, M.; Jaoui, M.; Maenhaut, W.; Claeys, M.; Flagan, R. C.; Seinfeld, J. H., Organosulfate formation in biogenic secondary organic aerosol. *J. Phys. Chem. A* **2008,** *112*, (36), 8345-8378.

51. Seinfeld, J. H.; Pankow, J. F., Organic atmospheric particulate material. *Annu. Rev. Phys. Chem.* **2003,** *54*, 121-140.

52. Barsanti, K. C.; Pankow, J. F., Thermodynamics of the formation of atmospheric organic particulate matter by accretion reactions - Part 1: aldehydes and ketones. *Atmos. Environ.* **2004,** *38*, (26), 4371-4382.

53. Lim, Y. B., Tan, Y., Perri, M. J., Seitzinger, S. P., Turpin, B. J., Aqueous chemistry and its role in secondary organic aerosol (SOA) formation. *Atmos. Chem. Phys.* **2010,** *10*, (11), 10521-10539.

54. Goldstein, A. H.; Galbally, I. E., Known and unexplored organic constituents in the earth's atmosphere. *Environ. Sci. Technol.* **2007,** *41*, (5), 1514-1521.

55. Gard, E. E.; Kleeman, M. J.; Gross, D. S.; Hughes, L. S.; Allen, J. O.; Morrical, B. D.; Fergenson, D. P.; Dienes, T.; Galli, M. E.; Johnson, R. J.; Cass, G. R.; Prather, K. A., Direct observation of heterogeneous chemistry in the atmosphere. *Science* **1998,** *279*, (5354), 1184-1187.

56. Bertram, A. K.; Ivanov, A. V.; Hunter, M.; Molina, L. T.; Molina, M. J., The reaction probability of OH on organic surfaces of tropospheric interest. *J. Phys. Chem. A* **2001,** *105*, (41), 9415-9421.

57. Pankow, J. F., Gas/particle partitioning of neutral and ionizing compounds to single and multi-phase aerosol particles. 1. Unified modeling framework. *Atmos. Environ.* **2003,** *37*, (24), 3323-3333.

58. Hoppel, W. A.; Frick, G. M.; Fitzgerald, J. W.; Wattle, B. J., A Cloud Chamber Study of the Effect That Nonprecipitating Water Clouds Have on the Aerosol-Size Distribution. *Aerosol Sci. Technol.* **1994,** *20*, (1), 1-30.

59. Blando, J. D.; Turpin, B. J., Secondary organic aerosol formation in cloud and fog droplets: a literature evaluation of plausibility. *Atmos. Environ.* **2000,** *34*, (10), 1623-1632.

60. Uematsu, M.; Duce, R. A.; Prospero, J. M.; Chen, L.; Merrill, J. T.; Mcdonald, R. L., Transport of Mineral Aerosol from Asia over the North Pacific-Ocean. *Journal of Geophysical Research-Oceans and Atmospheres* **1983,** *88*, (Nc9), 5343-5352.

61. Portin, H.; Mielonen, T.; Leskinen, A.; Arola, A.; Parjala, E.; Romakkaniemi, S.; Laaksonen, A.; Lehtinen, K. E. J.; Komppula, M., Biomass burning aerosols observed in Eastern Finland during the Russian wildfires in summer 2010-Part 1: In-situ aerosol characterization. *Atmospheric Environment* **2012,** *47*, 269-278.

62. Wallace, J. M.; Hobbs, P. V., *Atmospheric Science: An Introductory Survey*. 2nd ed.; Elsevier, Inc.: San Diego, CA, 2006.

63. Watson, J. G.; Chow, J. C., A wintertime PM2.5 episode at the fresno, CA, supersite. *Atmos. Environ.* **2002,** *36*, (3), 465-475.

64. Fu, Q. Y.; Zhuang, G. S.; Wang, J.; Xu, C.; Huang, K.; Li, J.; Hou, B.; Lu, T.; Streets, D. G., Mechanism of formation of the heaviest pollution episode ever recorded in the Yangtze River Delta, China. *Atmos. Environ.* **2008,** *42*, (9), 2023-2036.

65. Hildemann, L. M.; Mazurek, M. A.; Cass, G. R.; Simoneit, B. R. T., Quantitative Characterization of Urban Sources of Organic Aerosol by High-Resolution Gas-Chromatography. *Environ. Sci. Technol.* **1991,** *25*, (7), 1311-1325.

66. Hays, M. D.; Lavrich, R. J., Developments in direct thermal extraction gas chromatography-mass spectrometry of fine aerosols. *Trac-Trends in Analytical Chemistry* **2007,** *26*, (2), 88-102.

67. Rogge, W. F.; Hildemann, L. M.; Mazurek, M. A.; Cass, G. R.; Simoneit, B. R. T., Sources of Fine Organic Aerosol .2. Noncatalyst and Catalyst-Equipped Automobiles and Heavy-Duty Diesel Trucks. *Environ. Sci. Technol.* **1993,** *27*, (4), 636-651.

68. Fraser, M. P.; Cass, G. R.; Simoneit, B. R. T., Particulate organic compounds emitted from motor vehicle exhaust and in the urban atmosphere. *Atmos. Environ.* **1999,** *33*, (17), 2715-2724.

69. Ma, Y.; Hays, M. D.; Geron, C. D.; Walker, J. T.; Gichuru, M. J. G., Technical Note: Fast two-dimensional GC-MS with thermal extraction for anhydro-sugars in fine aerosols. *Atmospheric Chemistry and Physics* **2010,** *10*, (9), 4331-4341.

70. Welthagen, W.; Schnelle-Kreis, J.; Zimmermann, R., Search criteria and rules for comprehensive two-dimensional gas chromatography-time-of-flight mass spectrometry analysis of airborne particulate matter. *J. Chromatogr. A* **2003,** *1019*, (1-2), 233-249.

71. Stone, E. A.; Hedman, C. J.; Sheesley, R. J.; Shafer, M. M.; Schauer, J. J., Investigating the chemical nature of humic-like substances (HULIS) in North American atmospheric aerosols by liquid chromatography tandem mass spectrometry. *Atmos. Environ.* **2009,** *43*, (27), 4205-4213.

72. McInnes, L. M.; Quinn, P. K.; Covert, D. S.; Anderson, T. L., Gravimetric analysis, ionic composition, and associated water mass of the marine aerosol. *Atmos. Environ.* **1996,** *30*, (6), 869-884.

73. Souza, S. R.; Vasconcellos, P. C.; Carvalho, L. R. F., Low molecular weight carboxylic acids in an urban atmosphere: Winter measurements in Sao Paulo City, Brazil. *Atmos. Environ.* **1999,** *33*, (16), 2563-2574.

74. Anttila, P.; Hyotylainen, T.; Heikkila, A.; Jussila, M.; Finell, J.; Kulmala, M.; Riekkola, M. L., Determination of organic acids in aerosol particles from a coniferous forest by liquid chromatography-mass spectrometry. *J. Sep. Sci.* **2005,** *28*, (4), 337-346.

75. Iinuma, Y.; Muller, C.; Berndt, T.; Boge, O.; Claeys, M.; Herrmann, H., Evidence for the existence of organosulfates from beta-pinene ozonolysis in ambient secondary organic aerosol. *Environ. Sci. Technol.* **2007,** *41*, (19), 6678-6683.

76. Altieri, K. E.; Turpin, B. J.; Seitzinger, S. P., Oligomers, organosulfates, and nitrooxy organosulfates in rainwater identified by ultra-high resolution electrospray ionization FT-ICR mass spectrometry. *Atmos. Chem. Phys.* **2009,** *9*, (7), 2533-2542.

77. Schwartz, R. E.; Russell, L. M.; Sjostedt, S. J.; Vlasenko, A.; Slowik, J. G.; Abbatt, J. P. D.; Macdonald, A. M.; Li, S. M.; Liggio, J.; Toom-Sauntry, D.; Leaitch, W. R., Biogenic oxidized

organic functional groups in aerosol particles from a mountain forest site and their similarities to laboratory chamber products. *Atmos. Chem. Phys.* **2010,** *10*, (11), 5075-5088.

78. Finessi, E.; Decesari, S.; Paglione, M.; Giulianelli, L.; Carbone, C.; Gilardoni, S.; Fuzzi, S.; Saarikoski, S.; Raatikainen, T.; Hillamo, R.; Allan, J.; Mentel, T. F.; Tiitta, P.; Laaksonen, A.; Petaja, T.; Kulmala, M.; Worsnop, D. R.; Facchini, M. C., Determination of the biogenic secondary organic aerosol fraction in the boreal forest by NMR spectroscopy. *Atmos. Chem. Phys.* **2012,** *12*, (2), 941-959.

79. Decesari, S.; Mircea, M.; Cavalli, F.; Fuzzi, S.; Moretti, F.; Tagliavini, E.; Facchini, M. C., Source attribution of water-soluble organic aerosol by nuclear magnetic resonance spectroscopy. *Environ. Sci. Technol.* **2007,** *41*, (7), 2479-2484.

80. Moffet, R. C.; Henn, T. R.; Tivanski, A. V.; Hopkins, R. J.; Desyaterik, Y.; Kilcoyne, A. L. D.; Tyliszczak, T.; Fast, J.; Barnard, J.; Shutthanandan, V.; Cliff, S. S.; Perry, K. D.; Laskin, A.; Gilles, M. K., Microscopic characterization of carbonaceous aerosol particle aging in the outflow from Mexico City. *Atmos. Chem. Phys.* **2010,** *10*, (3), 961-976.

81. Posfai, M.; Simonics, R.; Li, J.; Hobbs, P. V.; Buseck, P. R., Individual aerosol particles from biomass burning in southern Africa: 1. Compositions and size distributions of carbonaceous particles. *J. Geophys. Res.* **2003,** *108*, (D13).

82. Williams, B. J.; Goldstein, A. H.; Kreisberg, N. M.; Hering, S. V., An in-situ instrument for speciated organic composition of atmospheric aerosols: Thermal Desorption Aerosol GC/MS-FID (TAG). *Aerosol Sci. Technol.* **2006,** *40*, (8), 627-638.

83. Williams, B. J.; Goldstein, A. H.; Kreisberg, N. M.; Hering, S. V.; Worsnop, D. R.; Ulbrich, I. M.; Docherty, K. S.; Jimenez, J. L., Major components of atmospheric organic aerosol in southern California as determined by hourly measurements of source marker compounds. *Atmos. Chem. Phys.* **2010,** *10*, (23), 11577-11603.

84. Worton, D. R.; Kreisberg, N. M.; Isaacman, G.; Teng, A. P.; McNeish, C.; Gorecki, T.; Hering, S. V.; Goldstein, A. H., Thermal Desorption Comprehensive Two-Dimensional Gas Chromatography: An Improved Instrument for In-Situ Speciated Measurements of Organic Aerosols. *Aerosol Sci. Technol.* **2012,** *46*, (4), 380-393.

85. Weber, R. J.; Orsini, D.; Daun, Y.; Lee, Y. N.; Klotz, P. J.; Brechtel, F., A particle-into-liquid collector for rapid measurement of aerosol bulk chemical composition. *Aerosol Sci. Technol.* **2001,** *35*, (3), 718-727.

86. Sullivan, A. P.; Peltier, R. E.; Brock, C. A.; de Gouw, J. A.; Holloway, J. S.; Warneke, C.; Wollny, A. G.; Weber, R. J., Airborne measurements of carbonaceous aerosol soluble in water over northeastern United States: Method development and an investigation into water-soluble organic carbon sources. *J. Geophys. Res.* **2006,** *111*, (D23).

87. Prather, K. A.; Nordmeyer, T.; Salt, K., Real-Time Characterization of Individual Aerosol-Particles Using Time-of-Flight Mass-Spectrometry. *Anal. Chem.* **1994,** *66*, (9), 1403-1407.

88. Canagaratna, M. R.; Jayne, J. T.; Jimenez, J. L.; Allan, J. D.; Alfarra, M. R.; Zhang, Q.; Onasch, T. B.; Drewnick, F.; Coe, H.; Middlebrook, A.; Delia, A.; Williams, L. R.; Trimborn, A. M.; Northway, M. J.; DeCarlo, P. F.; Kolb, C. E.; Davidovits, P.; Worsnop, D. R., Chemical and microphysical characterization of ambient aerosols with the aerodyne aerosol mass spectrometer. *Mass Spectrom. Rev.* **2007,** *26*, (2), 185-222.

89. Jimenez, J. L.; Jayne, J. T.; Shi, Q.; Kolb, C. E.; Worsnop, D. R.; Yourshaw, I.; Seinfeld, J. H.; Flagan, R. C.; Zhang, X. F.; Smith, K. A.; Morris, J. W.; Davidovits, P., Ambient aerosol sampling using the Aerodyne Aerosol Mass Spectrometer. *J. Geophys. Res.* **2003,** *108*, (D7).

90. Jayne, J. T.; Leard, D. C.; Zhang, X. F.; Davidovits, P.; Smith, K. A.; Kolb, C. E.; Worsnop, D. R., Development of an aerosol mass spectrometer for size and composition analysis of submicron particles. *Aerosol Sci. Technol.* **2000,** *33*, (1-2), 49-70.

91. DeCarlo, P. F.; Kimmel, J. R.; Trimborn, A.; Northway, M. J.; Jayne, J. T.; Aiken, A. C.; Gonin, M.; Fuhrer, K.; Horvath, T.; Docherty, K. S.; Worsnop, D. R.; Jimenez, J. L., Field-deployable, high-resolution, time-of-flight aerosol mass spectrometer. *Anal. Chem.* **2006,** *78*, (24), 8281-8289.

92. Docherty, K. S.; Aiken, A. C.; Huffman, J. A.; Ulbrich, I. M.; DeCarlo, P. F.; Sueper, D.; Worsnop, D. R.; Snyder, D. C.; Peltier, R. E.; Weber, R. J.; Grover, B. D.; Eatough, D. J.; Williams, B. J.; Goldstein, A. H.; Ziemann, P. J.; Jimenez, J. L., The 2005 Study of Organic Aerosols at Riverside (SOAR-1): instrumental intercomparisons and fine particle composition. *Atmos. Chem. Phys.* **2011,** *11*, (23), 12387-12420.

93. Gard, E.; Mayer, J. E.; Morrical, B. D.; Dienes, T.; Fergenson, D. P.; Prather, K. A., Real-time analysis of individual atmospheric aerosol particles: Design and performance of a portable ATOFMS. *Anal. Chem.* **1997,** *69*, (20), 4083-4091.

94. Su, Y. X.; Sipin, M. F.; Furutani, H.; Prather, K. A., Development and characterization of an aerosol time-of-flight mass spectrometer with increased detection efficiency. *Anal. Chem.* **2004,** *76*, (3), 712-719.

95. Pratt, K. A.; Mayer, J. E.; Holecek, J. C.; Moffet, R. C.; Sanchez, R. O.; Rebotier, T. P.; Furutani, H.; Gonin, M.; Fuhrer, K.; Su, Y. X.; Guazzotti, S.; Prather, K. A., Development and Characterization of an Aircraft Aerosol Time-of-Flight Mass Spectrometer. *Anal. Chem.* **2009,** *81*, (5), 1792-1800.

96. Liu, P.; Ziemann, P. J.; Kittelson, D. B.; Mcmurry, P. H., Generating Particle Beams of Controlled Dimensions and Divergence .1. Theory of Particle Motion in Aerodynamic Lenses and Nozzle Expansions. *Aerosol Sci. Technol.* **1995,** *22*, (3), 293-313.

97. Liu, P.; Ziemann, P. J.; Kittelson, D. B.; Mcmurry, P. H., Generating Particle Beams of Controlled Dimensions and Divergence .2. Experimental Evaluation of Particle Motion in Aerodynamic Lenses and Nozzle Expansions. *Aerosol Sci. Technol.* **1995,** *22*, (3), 314-324.

98. Liggio, J.; Li, S. M., Organosulfate formation during the uptake of pinonaldehyde on acidic sulfate aerosols. *Geophys. Res. Lett.* **2006,** *33*, (13).

99. Noziere, B.; Ekstrom, S.; Alsberg, T.; Holmstrom, S., Radical-initiated formation of organosulfates and surfactants in atmospheric aerosols. *Geophys. Res. Lett.* **2010,** *37*.

100. Surratt, J. D.; Kroll, J. H.; Kleindienst, T. E.; Edney, E. O.; Claeys, M.; Sorooshian, A.; Ng, N. L.; Offenberg, J. H.; Lewandowski, M.; Jaoui, M.; Flagan, R. C.; Seinfeld, J. H., Evidence for organosulfates in secondary organic aerosol. *Environ. Sci. Technol.* **2007,** *41*, (2), 517-527.

101. Reilly, P. T. A.; Lazar, A. C.; Gieray, R. A.; Whitten, W. B.; Ramsey, J. M., The elucidation of charge-transfer-induced matrix effects in environmental aerosols via real-time aerosol mass spectral analysis of individual airborne particles. *Aerosol Sci. Technol.* **2000,** *33*, (1-2), 135-152.

102. Reinard, M. S.; Johnston, M. V., Ion formation mechanism in laser desorption ionization of individual nanoparticles. *J. Am. Soc. Mass. Spectrom.* **2008,** *19*, (3), 389-399.

103. Zelenyuk, A.; Yang, J.; Imre, D., Comparison between mass spectra of individual organic particles generated by UV laser ablation and in the IR/UV two-step mode. *Int. J. Mass spectrom.* **2009,** *282*, (1-2), 6-12.

104. Gross, D. S.; Galli, M. E.; Silva, P. J.; Prather, K. A., Relative sensitivity factors for alkali metal and ammonium cations in single particle aerosol time-of-flight mass spectra. *Anal. Chem.* **2000,** *72*, (2), 416-422.

105. Kajino, M.; Ueda, H.; Nakayama, S., Secondary acidification: Changes in gas-aerosol partitioning of semivolatile nitric acid and enhancement of its deposition due to increased emission and concentration of SO(x). *J. Geophys. Res.* **2008,** *113*, (D3).

106. Sullivan, R. C.; Prather, K. A., Investigations of the diurnal cycle and mixing state of oxalic acid in individual particles in Asian aerosol outflow. *Environ. Sci. Tech.* **2007,** *41*, (23), 8062-8069.

107. Angelino, S.; Suess, D. T.; Prather, K. A., Formation of aerosol particles from reactions of secondary and tertiary alkylamines: Characterization by aerosol time-of-flight mass spectrometry. *Environ. Sci. Tech.* **2001,** *35*, (15), 3130-3138.

108. Silva, P. J.; Prather, K. A., Interpretation of mass spectra from organic compounds in aerosol time-of-flight mass spectrometry. *Anal. Chem.* **2000,** *72*, (15), 3553-3562.

109. Sodeman, D. A.; Toner, S. M.; Prather, K. A., Determination of single particle mass spectral signatures from light-duty vehicle emissions. *Environ. Sci. Tech.* **2005,** *39*, (12), 4569-4580.

110. Kelly, R. T.; Tolmachev, A. V.; Page, J. S.; Tang, K. Q.; Smith, R. D., The Ion Funnel: Theory, Implementations, and Applications. *Mass Spectrom. Rev.* **2010,** *29*, (2), 294-312.

2 Measurements of isoprene-derived organosulfates in ambient aerosols by aerosol time-of-flight mass spectrometry- Part 1: Single particle atmospheric observations in Atlanta

2.1 Abstract

Organosulfate species have recently been identified as a potentially significant class of secondary organic aerosol (SOA) species, yet little is known about their behavior in the atmosphere. In this work, organosulfates were observed in individual ambient aerosols using single particle mass spectrometry in Atlanta, GA during the 2002 Aerosol Nucleation and Real-time Characterization Experiment (ANARChE) and the 2008 August Mini-Intensive Gas and Aerosol Study (AMIGAS). Organosulfates derived from biogenically-produced isoprene were detected as deprotonated molecular ions in negative-ion spectra measured by aerosol time-of-flight mass spectrometry; comparison to high-resolution mass spectrometry data obtained from filter samples corroborated the peak assignments. The size-resolved chemical composition measurements revealed that organosulfate species were mostly detected in submicron aerosols and across a range of aerosols from different sources, consistent with secondary reaction products. Detection of organosulfates in a large fraction of negative-ion ambient spectra—*ca.* 90-95% during ANARChE and ~65% of submicron particles in AMIGAS—highlights the ubiquity of organosulfate species in the ambient aerosols of biogenically-influenced urban environments.

2.2 Introduction

Secondary organic aerosol (SOA) can contribute substantially to atmospheric aerosol mass and arises from both biogenic and anthropogenic emissions of volatile organic compounds (VOCs). In heavily forested regions, the biogenic contribution to SOA can be substantial due to high emissions of VOCs from vegetation.[1] Isoprene (2-methyl-1,3-butadiene, C_5H_8) is an abundant biogenic VOC and has recently emerged as a potentially significant source of SOA.[2,3] The two double bonds of isoprene are highly reactive toward atmospheric oxidants and are therefore susceptible to oxidation, ultimately forming semi-volatile compounds such as 2-methyltetrols and 2-methylglyceric acid (ref 2 and references therein). Subsequent gas-to-particle partitioning can result in further particle-phase reactions yielding high-mass oligomers and organosulfate compounds ($ROSO_3H$).[2] In this manuscript, we investigate the isoprene-derived organosulfate species, a class of low-volatility oxidation products that could potentially contribute

significantly to organic aerosol mass, and further, due to their high polarity and water solubility, could enhance the cloud condensation nuclei (CCN) activity of organic aerosols.[4]

Particulate organosulfate species have been previously measured in filter samples of ambient aerosols using a variety of off-line analytical methods. Surratt *et al.*[5] detected both isoprene- and monoterpene-derived organosulfates in the southeastern United States utilizing high performance liquid chromatography coupled to electrospray ionization mass spectrometry (ESI-MS); a similar method was used to characterize organosulfates in aerosols collected from K-puszta, Hungary[6] and Bavaria, Germany.[7] Altieri *et al.*[8] measured similar organosulfate species in New Jersey rainwater samples using Fourier-transform ion-cyclotron resonance mass spectrometry (FT-ICRMS). Additionally, organosulfates were detected by ESI-FT-ICRMS in atmospheric fog samples.[9] Organosulfate functional groups have also been detected in a marine environment with continental influence by Fourier-transform infrared spectroscopy,[10] and in a remote marine environment impacted only by oceanic biological sources (e.g., algal blooms) using ESI-MS.[11] These studies have provided valuable insight into the important contribution of organosulfate species to ambient aerosols in diverse environments. However, nearly all previous studies relied on off-line sample collection and analysis, which provides limited information on the average bulk aerosol composition.

On-line mass spectrometric-based measurements are capable of providing real-time information on the evolving aerosol population. Currently there are two widely-used methods of on-line aerosol mass spectrometry: single-particle mass spectrometry (SPMS- e.g. aerosol time-of-flight mass spectrometry; ATOFMS[12]), which uses laser desorption/ionization (LDI) for aerosol analysis, and the aerosol mass spectrometer (AMS)[13] that uses thermal desorption with subsequent electron-impact ionization. Recently Farmer *et al.*[14] demonstrated a high degree of fragmentation during the measurement of organosulfate compounds by the AMS; organosulfates were shown to decompose almost completely into inorganic sulfate and organic fragments. Since ambient aerosols are often internal mixtures of organic carbon and inorganic sulfate,[15] extensive fragmentation makes it nearly impossible for the AMS to detect organosulfate species within the complex ambient aerosol matrix.

Recently, an SPMS technique was utilized for aircraft observations of isoprene-derived organosulfates. Measurements by the Particle Ablation by Laser Mass Spectrometry (PALMS) instrument displayed high levels of organosulfate species in the tropical free troposphere and

southeastern United States.[16] While this study provided unique quantitative characterization of organosulfates from SPMS, several features of ATOFMS provide additional information. PALMS uses a higher energy laser for particle ablation than ATOFMS (λ = 193 vs. 266 nm), which can induce greater fragmentation of organic species and thereby limits the detection of organosulfates unless the instrument is operated in a lower laser power mode, as described in ref 16. Further, whereas the TOF mass analyzer of PALMS is restricted to single-polarity measurements, ATOFMS measures both positive and negative spectra for single particles which yield more detailed information on the mixing state (i.e. sources and aging) of ambient aerosols.

In this study, single-particle ATOFMS measurements were made during the 2002 Aerosol Nucleation and Real-time Characterization Experiment (ANARChE) and the 2008 August Mini-Intensive Gas and Aerosol Study (AMIGAS) in Atlanta, GA. The southeastern United States is characterized by high concentrations of both isoprene[17] and anthropogenic SO_2 from coal-burning power plants and industrial emissions.[18] The atmospheric oxidation of both isoprene and SO_2 via reaction with hydroxyl radical forms the organic and sulfate precursors necessary for organosulfate formation, and therefore the Atlanta region provides an ideal location to characterize these compounds in ambient aerosols. Initial observations of organosulfates in individual ambient aerosols obtained through on-line measurements are discussed herein. Detailed discussions of the temporal variability and possible formation mechanisms of organosulfate compounds are included in Chapter 3.

2.3 Experimental

2.3.1 Field measurements

Aerosol sampling was performed during two field studies at the Jefferson Street (JST) Southeastern Aerosol Research and Characterization (SEARCH) Network site (33.8º N, 84.4º W), a mixed residential-industrial location about 4 km northwest of metro Atlanta.[19] Real-time ATOFMS measurements were made of single particles during ANARChE from August 4-11, 2002 and AMIGAS from August 22-September 11, 2008. Because these studies were conducted during the same time of year, they provide a good opportunity to compare and verify the observed trends. Time is given in local time.

ATOFMS has been described in detail previously;[12] a brief summary is provided here. Aerosols enter the instrument via an inlet and are accelerated to a size-dependent terminal

velocity. Two different ATOFMS instruments were utilized during these studies, differing mainly in the aerosol inlet and detectable particle size range. During ANARChE, an aerodynamic lens inlet was used[20] with a size-cut upstream provided by stages of a micro orifice uniform deposit impactor (MOUDI);[21] aerosols with aerodynamic diameters of 50-350 nm were analyzed. During AMIGAS, a converging nozzle inlet was used to detect aerosols in the 200–3000 nm range. Following the inlet, the ATOFMS instruments are nominally the same. In the particle sizing region, aerosols traverse two 532 nm continuous wave lasers yielding the particle velocity. A size calibration was performed using polystyrene latex spheres of known diameter to convert velocity to vacuum aerodynamic diameter. Aerosols were then desorbed and ionized at 266 nm using a Q-switched Nd:YAG laser. During ANARChE, the laser was operated at ~2.0 mJ and during AMIGAS, the laser power was 1.1 mJ from August 22-29 and 1.4-1.5 mJ thereafter.

Data analysis was performed by importing single-particle mass spectra into Matlab (The MathWorks, Inc.) using the YAADA toolkit.[22] Particles were clustered based on similarities in mass spectral peak identities and intensities using the ART-2a adaptive resonance theory method[23] with a vigilance factor of 0.8 (ANARChE) and 0.75 (AMIGAS), learning rate of 0.05, and 20 iterations. During AMIGAS, only a fraction of particles (32% of submicron, 80% of supermicron) yielded negative spectra, whereas 99% of particles during ANARChE contained dual-polarity spectra. This disparity is largely attributed to the evaporation of water in the aerodynamic lens inlet used during ANARChE;[24] the presence of water has been shown to suppress negative ion formation.[25] Data analysis was restricted to the subset of particles containing dual-polarity spectra since the organosulfate content could not be assessed for particles with only positive spectra; no corrections have been applied to account for the low fraction of negative spectra obtained during AMIGAS.

During AMIGAS, un-denuded high-volume filter samples were also collected in segregated day (10am-6pm) and night (10pm-6am) periods and were analyzed by ultra-performance liquid chromatography coupled to ESI-high-resolution time-of-flight mass spectrometry (UPLC/ESI-HR-TOFMS). The filter sampling and analysis protocols are described elsewhere.[26]

2.3.2 Organosulfate standard analysis

To test the detection capabilities of ATOFMS towards organosulfates and identify common marker ions for ambient aerosol apportionment, a synthesized standard of the

organosulfate derivative of 2,3-epoxy-1,4-butanediol (BEPOX) was analyzed as a proxy for the isoprene epoxydiol (IEPOX)-derived organosulfate.[27] The standard solution was a mixture of sodium sulfate, sulfuric acid, and the BEPOX-derived organosulfate. Because pure sulfate salts have been shown to poorly absorb the laser pulse at 266 nm,[28] dihydroxybenzoic acid (DHB) was added to the sample matrix as a chromophore to facilitate desorption and ionization of the standard particles and to better approximate the composition of ambient aerosols. The standard solution was analyzed by aerosolizing an aqueous solution with a Collison atomizer, drying the resulting aerosol with two diffusion driers, and introducing the particles directly into the ATOFMS.

2.4 Results and Discussion

2.4.1 Identification of Organosulfate Species

High mass species at *m/z* -139, -153, -155, -199, and -215 were observed in multi-year ATOFMS measurements conducted in Atlanta during the ANARChE and AMIGAS campaigns. The example spectrum shown in Figure 2.1 represents the average of an organic carbon particle cluster observed during ANARChE (~41,000 particles). The aforementioned peaks are hypothesized to be organosulfate species derived from isoprene oxidation products based on previous work by Surratt and coworkers who identified these compounds in chamber studies[5] and filter samples of ambient aerosols collected at the JST site.[26] These compounds have been identified as organosulfates derived from the following isoprene oxidation products: glycoaldehyde[5] (*m/z* -139), hydroxyacetone[5] (*m/z* -153), glyoxal[5] or glycolic acid[29] (*m/z* -155), 2-methylglyceric acid[5] (*m/z* -199), and IEPOX[27] (*m/z* -215). In those studies, organosulfates were detected as deprotonated molecular ions via ESI-MS. Since the LDI method used in ATOFMS is considered a "harder" ionization technique than ESI, a BEPOX-derived organosulfate standard (Figure 2.6) was aerosolized and analyzed by ATOFMS to confirm that it is capable of measuring intact organosulfate compounds. The synthetic standard is analogous to the compound attributed to the organosulfates of 2-methyltetrols formed through acid-catalyzed reactive uptake of IEPOX (structure included in Figure 2.1).[27,30] However, it lacks a methyl group (Figure 2.6), and thus appears 14 *m/z* units lower (*m/z* -201) than the IEPOX-derived compound (*m/z* -215). In the average ATOFMS spectrum (Figure 2.6), the predominant peak arising from the BEPOX-organosulfate standard is, in fact, the pseudomolecular ion at *m/z* -201. Additionally, ATOFMS analysis of a synthesized standard of the glycolic acid-derived organosulfate (*m/z* -155) was also dominated by the deprotonated ion (results not shown). These results indicate that the

pseudomolecular ion is the dominant species observed for organosulfate compounds under LDI at 266 nm and supports the assignment of the aforementioned ambient peaks to organosulfate species.

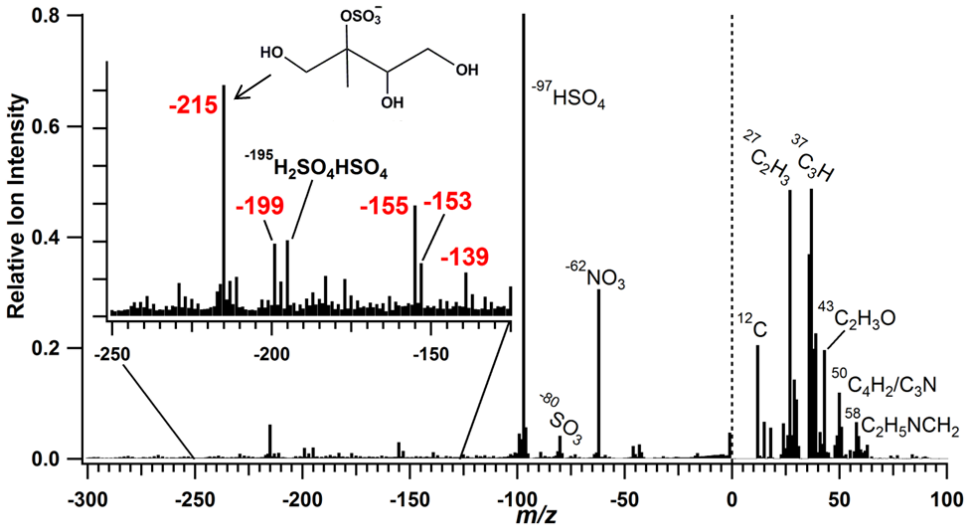

Figure 2.1 Average positive and negative-ion mass spectra of organic carbon-type particles measured during ANARChE. The spectra represent the average of ~41,000 particles. The inset molecule represents the IEPOX-derived organosulfate species (m/z -215).

2.4.2 Comparison between ATOFMS and Filter Samples during AMIGAS

Given the limitation of nominal mass resolution in the ATOFMS mass spectra, there remains the possibility that other isobaric species could yield these *m/z* values. To rule this out, ATOFMS results were compared with the chromatographic peak areas obtained by the UPLC/ESI-HR-TOFMS analysis of filter samples collected during the AMIGAS campaign (Figure 2.2). Only submicron particles measured by ATOFMS were included in this comparison, as the organosulfates were primarily detected on particles in this size range (discussed below). The ATOFMS and UPLC/ESI-HR-TOFMS methods show good agreement for the *m/z* -215 marker (R^2 = 0.53), further confirming that the peaks observed by ATOFMS can be attributed to the isoprene-derived organosulfates.

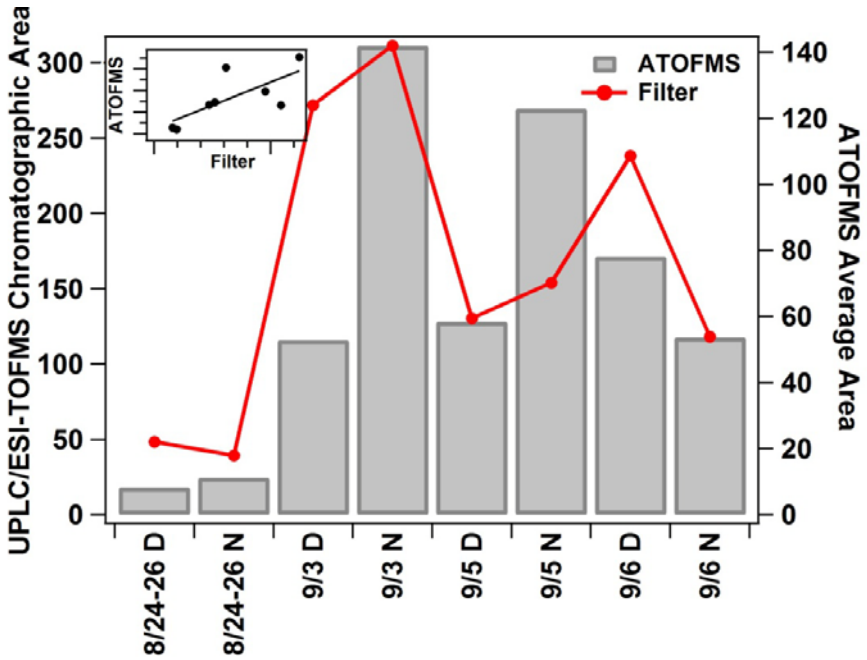

Figure 2.2 Comparison of *m/z* -215 abundance measured in single particles by ATOFMS with day/night filter samples analyzed by ultra-performance liquid chromatography (UPLC). For this comparison, the uncalibrated chromatographic peak area from the filter extracts was used; the ATOFMS absolute peak area of *m/z* -215 was averaged over the corresponding filter time periods; only submicron particles were included in the comparison. D = 10am – 6pm; N = 10pm – 6am. The inset shows the correlation plot between the two measurements (R^2=0.53).

There are several possible explanations for the significant, yet moderate correlation (R^2=0.53) between the ATOFMS *m/z* -215 peak area and the chromatographic peak area from the UPLC/ESI-HR-TOFMS analysis of the filter extracts. For example, positive artifacts could have influenced the filter sampling through increased uptake of organosulfate precursors from the gas-phase to a filter substrate with a pre-existing sulfate-rich aerosol loading and subsequent condensed-phase processing to non-volatile organosulfates. Minor contributions from matrix effects or other artifacts associated with laser/desorption ionization[31] during ATOFMS analysis were also possible. However, matrix effect are likely most significant when examining relatively pure particles, a condition that is rarely observed in atmospheric aerosols from a polluted region. Therefore, we expect that matrix effects played, at most, a minor role in the detection of organosulfates in Atlanta. A combination of factors likely played a role in the moderate correlation between the analysis methods and further studies are necessary to characterize the artifacts associated with each measurement technique. However, the correlation observed in the present study is sufficient to support the qualitative ATOFMS observations presented here and in Chapter 3.

2.4.3 Isoprene-Derived Organosulfate Markers

While standards from the other organosulfate markers (-139, -153, & -199) have not been analyzed by ATOFMS, the correlations between most of the markers and *m/z* -215 (Figure 2.7) show good correlations during both ANARChE (*m/z* -139, R^2=0.08; *m/z* -153, R^2=0.64; *m/z* -155, R^2=0.69; and *m/z* -199, R^2=0.50) and AMIGAS (*m/z* -139, R^2=0.23; *m/z* -153, R^2=0.54; *m/z* -155, R^2=0.51; and *m/z* -199, R^2=0.62). These correlations indicate that these species arise from similar formation mechanisms and further corroborate the assignment of these peaks to organosulfate species. The poor correlations between *m/z* -139 and *m/z* -215 are attributed to the lower peak area of *m/z* -139, and thus the reduced signal-to-noise ratio associated with this peak. While different correlations were observed between the minor organosulfate markers and *m/z* -215, they arise from different isoprene oxidation products, as described above, and display different product yields under different reaction conditions.[5] Therefore, a perfect correlation between the organosulfate markers is not necessarily expected.

Assuming the different isoprene-derived organosulfate markers exhibit similar ionization efficiency and degree of fragmentation under LDI, the peak areas can be used to indicate relative abundances. The same trends were observed during both ANARChE and AMIGAS with the marker at *m/z* -215 being the most abundant organosulfate, displaying ~4x higher peak area than the other species, followed by *m/z* -155 > -199 > -153 > -139. There are several potential explanations for the higher concentration of *m/z* -215 including differences in precursor concentrations or in organosulfate product yield/formation kinetics, but these effects could not be resolved in this study. However, additional characterization studies should also be performed to investigate the detection efficiency of various organosulfate compounds. In particular, it should be noted that clear ion signals from monoterpene-derived organosulfates were not observed in these ATOFMS datasets, despite their previous detection in Atlanta.[26] A discussion of the possible reasons for the absence of monoterpene-derived organosulfates is provided in the Supporting Information.

2.4.4 Size Dependence & Mixing State of Organosulfate Species

Measurements from both ANARChE and AMIGAS provide information on aerosols over a broad size range (50-3000 nm) to assess the possible size-dependence of organosulfates. The particle size distributions measured by ATOFMS are included in Figures 2.3 (AMIGAS) and 2.4 (ANARChE), separated by the presence or absence of organosulfate species and categorized by particle type. It is clear from the AMIGAS data that organosulfates were overwhelmingly

concentrated in submicron aerosols, with only minor contribution to supermicron particles. This trend is likely due to the secondary nature of these compounds: since particles a few hundred nanometers in diameter dominate the aerosol surface-area distribution,[32] they provide greater opportunity for collisions and subsequent uptake of gas-phase species. These findings are in general agreement with those of Lukács *et al.*[33] who detected the largest organosulfate mass concentrations in accumulation mode particles collected on impactor stages in K-puszta, Hungary. The ANARChE data provides additional insights into the organosulfate content of ultrafine particles. Since Lukács *et al* [33] did not observe significant organosulfate mass in the smallest impactor stage (~100 nm), it is noted that organosulfates were detected on nearly all (~85-95%) of the ultrafine particles (50-100 nm) sampled during ANARChE (Figure 2.4). However, the mass concentration of organosulfate species was not quantified from the ATOFMS data and therefore the overall mass contribution from these ultrafine particles could not be assessed for direct comparison to Lukács *et al.*[33]

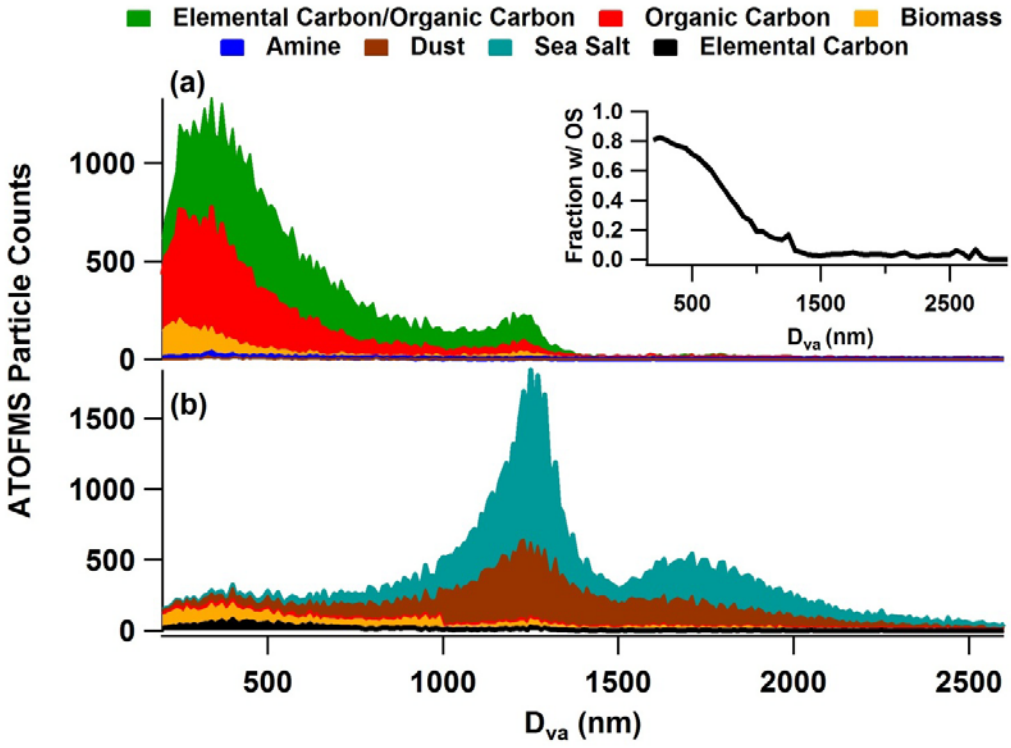

Figure 2.3 Size-dependent mixing state comparison of particles with dual-polarity spectra that contained (a) and did not contain (b) organosulfate species during AMIGAS. The y-axis represents particle counts measured by ATOFMS per 10 nm size bin, given in vacuum aerodynamic diameter. The inset shows the fraction of particles in each size bin that contained organosulfate species.

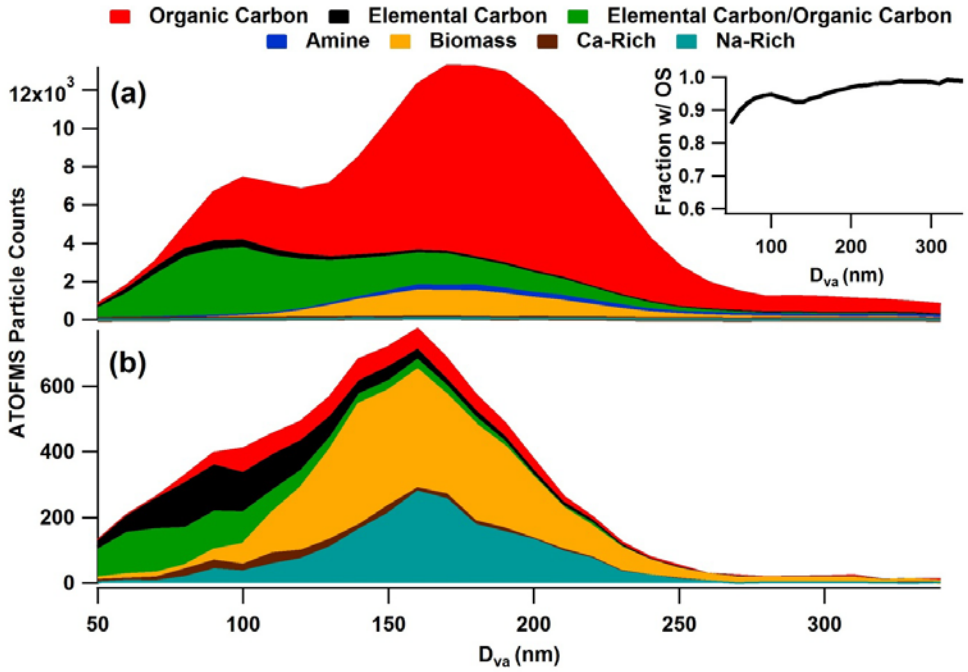

Figure 2.4 Size-dependent mixing state comparison of particles with dual-polarity spectra that contained (a) and did not contain (b) organosulfate species in 10 nm size bins during ANARChE. Note the difference in y-axis scales between (a) and (b). The inset shows the fraction of particles in each size bin that contained organosulfate species.

The size distribution of organosulfate-containing particles observed during ANARChE is shifted to slightly larger sizes than those lacking organosulfates (Figure 2.4). This observation indicates that the organosulfate-containing particles had possibly undergone a higher degree of atmospheric processing (aging) thereby acquiring a thicker coating of secondary species. The relationship between particle aging and organosulfate content was further explored using the ability of ATOFMS to determine the mixing state of individual particles. Difference spectra between all particles containing and lacking organosulfates during ANARChE are included in Figure 2.5. It is clear that the particles containing organosulfates (positive intensity) are strongly enriched in sulfate, relative to the particles lacking organosulfates (negative intensity), and indicating they had undergone a high degree of aging. However, simple aging is not sufficient to explain organosulfate formation as the organosulfate-deficient particles appear to be slightly aged as well, indicated by the presence of secondary nitrate (*m/z* – 46, NO_2^- & -62, NO_3^-). Rather, atmospheric processing leading to particles rich in sulfate, a necessary precursor to organosulfate formation is important, though the effect of sulfate—by either simply acting as a reactant or influencing aerosol acidity—cannot be determined from these studies. However, the trend of higher sulfate content in the organosulfate containing particles is true across the different particle

types and also holds for AMIGAS, as shown by the mass spectra for individual particle types provided in Figures 2.8-2.11. While not surprising, these observations demonstrate that a particle's sulfate content is likely a key parameter influencing organosulfate formation, consistent with the work of Minerath *et al.*[34] who observed an increase in organosulfate yield with increasing sulfate concentration.

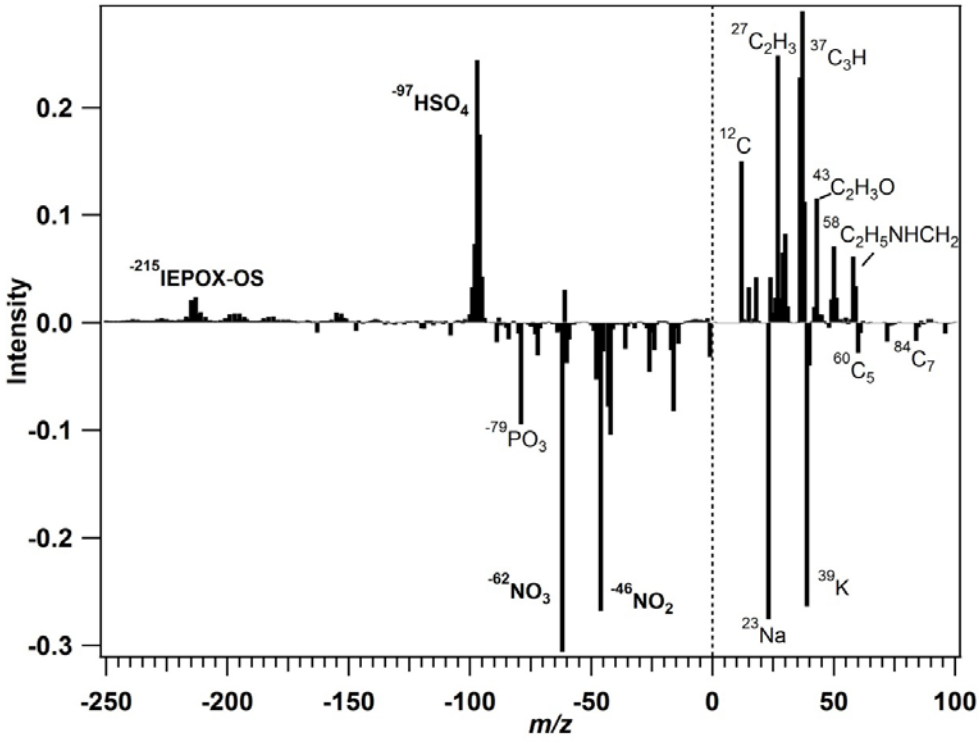

Figure 2.5 Difference spectra between particles (from all particle types) measured during ANARChE that contain organosulfate species (170,005) and those without (7991). The organosulfate-rich particles are strongly enriched in sulfate (*m/z* -97).

From this analysis, it appears that the predominant characteristics influencing organosulfate levels are particle size (i.e. surface area-to-volume ratio) and sulfate concentration, highlighting the role of atmospheric processing in leading to particulate organosulfate species. However, further research is necessary to better understand the role of particle aging and mixing state on the partitioning/formation of organosulfate species. The additional observation that organosulfates were primarily detected on carbonaceous particle types (e.g. organic carbon, elemental carbon/organic carbon) is described in the Supporting Information (Section 2.7.3). Possible organosulfate formation mechanisms will be explored in more detail in Chapter 3.

2.5 Conclusions and Implications

Organosulfate species were detected on ~90-95% of particles containing dual-polarity spectra during ANARChE and ~65% of submicron particles during the AMIGAS campaign. While the mass contribution of these organosulfate compounds to individual particles was not determined for this study, it is clear that they have the potential to influence a great number of particles. Given the high polarity and water solubility of these isoprene-derived organosulfate compounds, they may play a significant role in increasing the hygroscopicity and CCN activity of carbonaceous aerosols in regions influenced by biogenic and anthropogenic pollutants.

ATOFMS has been demonstrated to be an effective technique for measuring organosulfate compounds in real-time within individual atmospheric particles. Data from several past field campaigns have been reexamined for the presence of organosulfates derived from isoprene. Markers comparable to those measured during ANARChE and AMIGAS were also detected in other isoprene-rich locations, including New York, NY (2002); Boston, MA (2003); Chapel Hill, NC (2003); and the Sacramento, CA area (2010). Multi-year observations of organosulfate species in Atlanta, as well as their detection in other regions of the United States, highlight the significant contribution of these compounds to organic aerosols. It is also noteworthy that the IEPOX-derived organosulfate discussed herein has not been measured in Riverside, a region that has been extensively monitored by ATOFMS[35-37] and is generally characterized by lower emissions of isoprene and SO_2. These observations point to the regional nature of SOA processing and the strong influence of biogenic emissions in the southeastern United States.

2.6 Acknowledgements

The dissertation author was the primary researcher and author of this chapter. Stephanie Shaw and Eladio Knipping (EPRI) are gratefully acknowledged for coordinating the AMIGAS campaign. The authors thank the Prather group for extensive support throughout the studies. Additional assistance in Atlanta from Jerry Brown (ARA, Inc.) during AMIGAS was appreciated. Michele Sipin is acknowledged for assisting with data collection during ANARChE. We are grateful to Nathan Eddingsaas (Caltech) and Prof. Frank Keutsch (UW-Madison) for providing the BEPOX-derived and glycolic acid-derived organosulfate standards, respectively. ANARChE was supported by the University of Rochester EPA PM Center, Grant R827354. AMIGAS was

funded by the Electric Power Research Institute. L. Hatch has been funded by a National Science Foundation Graduate Research Fellowship (2008-2011).

Chapter 2 is reproduced with permission from the American Chemical Society: Hatch, L.E.; Creamean, J.M.; Ault, A.P.; Surratt, J.D.; Chan, M.N.; Seinfeld, J.H.; Edgerton, E.S.; Su, Y.; Prather, K.A., Measurements of isoprene-derived organosulfates in ambient aerosols by aerosol time-of-flight mass spectrometry, Part 1: Single particle observations. *Environ. Sci. Tech.,* **2011**, *45*(12), 5105-5111.

2.7 Supporting Information

2.7.1 Supplemental Figures

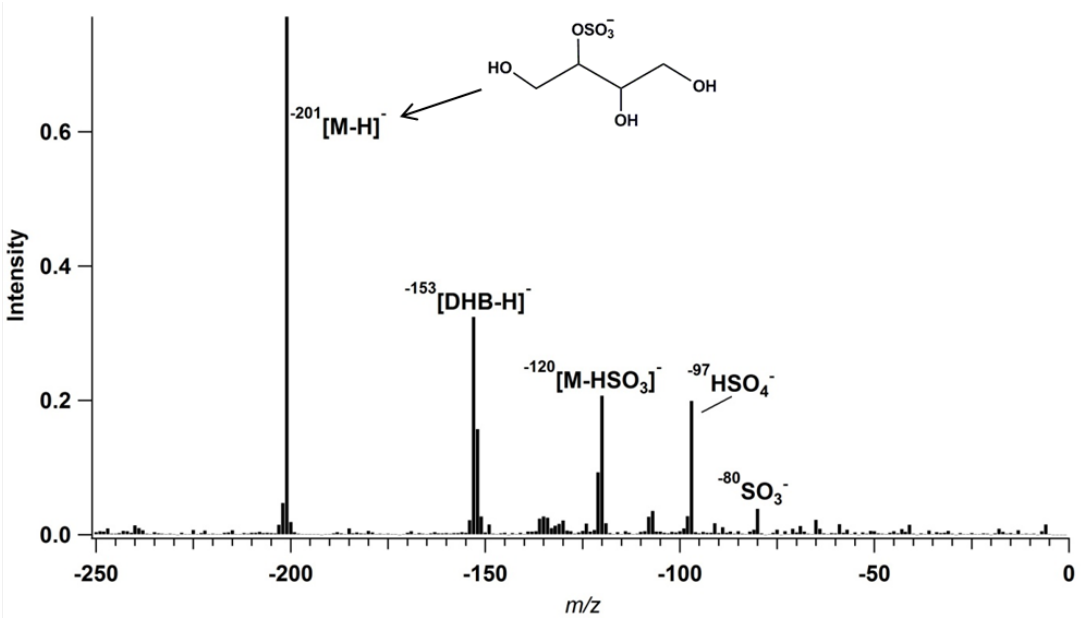

Figure 2.6 Average negative mass spectrum of a 2,3-epoxy-1,4-butanediol (BEPOX)-derived organosulfate standard. DHB is a matrix added to the standard solution.

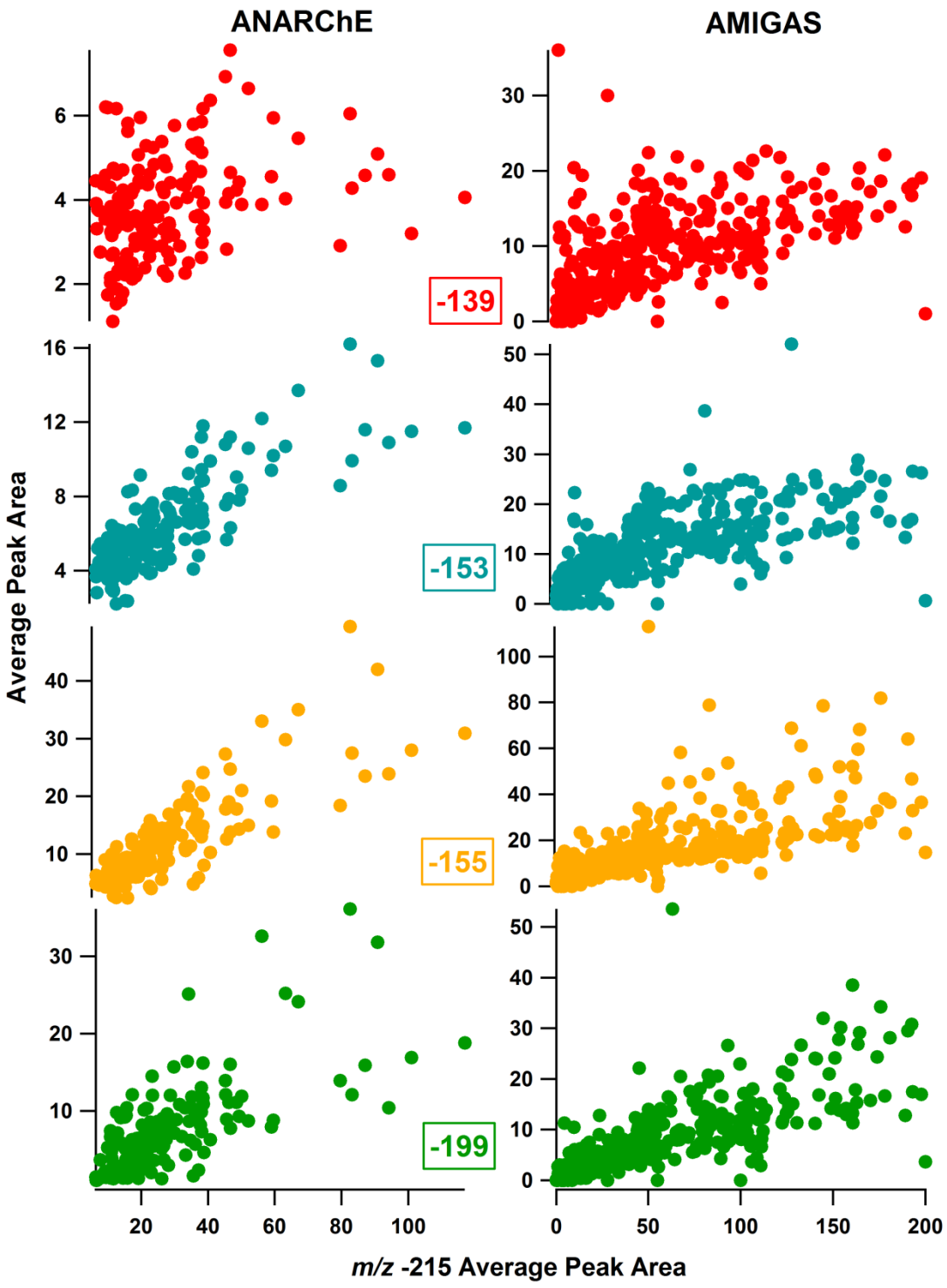

Figure 2.7 Correlations between the proposed organosulfate markers *m/z* -139, -153, -155, and -199 with *m/z* -215.

2.7.2 Monoterpene-derived organosulfates

Organosulfate species derived from monoterpenes have also been detected previously in the Atlanta region,[26] however, these species could not be unequivocally identified in the ATOFMS data. It is possible that the highly-branched and cyclic structure of these compounds make them more susceptible to fragmentation under laser desorption/ionization and thus were not detected as intact molecules that could be readily identified. Additionally, the ion transmission in the time-of-flight mass spectrometer utilized for these studies is significantly reduced at the high molecular weights characteristic of monoterpene-derived organosulfate species (> *m/z* 250). The reduced signal-to-noise ratio in this *m/z* range, combined with the mass calibration difficulties outlined in the Supporting Information of Chapter 3, likely prohibited the detection of monoterpene-derived organosulfates during AMIGAS. Additional characterization studies should be performed to assess the overall ATOFMS detection capabilities across the range of organosulfate compounds that have been detected in ambient aerosol particles.

2.7.3 Trends in aerosol mixing state

It is also interesting to note from Figures 2.3 & 2.4 that the organosulfate species are found primarily on the carbonaceous aerosol types (e.g. organic carbon, elemental carbon/organic carbon) while the inorganic types (e.g. sea salt) are lacking organosulfates. There are several possible explanations for this observation. The mixing state dependence could indicate preferential partitioning of the organosulfate precursors into a carbonaceous particle matrix. It is also possible that the disparity in organosulfate content between organic and inorganic particle types is simply due to the size ranges characteristic of these particle types- the carbonaceous types typically dominate the submicron mode, while the inorganic types are generally detected in the supermicron mode. Therefore, organosulfates could be found predominantly on the carbonaceous particle types simply because they dominate the size range with the highest surface-to-volume ratio as opposed to exhibiting more favorable gas-to-particle partitioning of organosulfate precursors. Also of note, previous ATOFMS studies have found that the acidity increases as particle size decreases,[35] consistent with the findings described in the main paper that the organosulfate-containing particles were more strongly enriched in sulfate.

2.7.4 ATOFMS particle types

Average mass spectra for each particle type are shown in Figure 2.8 for particles containing organosulfates and Figure 2.9 for particles that did not contain organosulfates during

AMIGAS and Figures 2.10 and 2.11 for ANARChE. Note that these mass spectra were averaged across particles with different mass calibrations. The particle types are assigned and named based on comparison between the mass spectral fingerprints and previously identified source libraries. A brief discussion of the key characteristics for each particle type is provided here for reference.

Elemental Carbon (EC). Elemental carbon particles display an intense series of carbon clusters ($^{12n}C_n$) in both positive and negative spectra. There were no EC particles that contained organosulfates during AMIGAS and 3125 (82%) that contained low levels during ANARChE.

Elemental Carbon/Organic Carbon (ECOC). This type is identified by the presence of small carbon clusters (C_n, n=1-3) mixed with less intense organic carbon fragments ($^{27}C_2H_3$, $^{43}C_2H_3O$) in the positive spectra. The negative spectra contain the secondary species, sulfate ($^{-97}HSO_4$) and nitrate ($^{-62}NO_3$, $^{-46}NO_2$). There were no ECOC particles detected that did not contain organosulfates during AMIGAS and 1067 (~3%) with undetectable amounts during ANARChE.

Organic Carbon (OC). OC is dominated by organic fragments in the positive spectra ($^{27}C_2H_3$, $^{39}C_3H_3$, $^{43}C_2H_3O$). The negative spectra contain primarily sulfate ($^{-97}HSO_4$) and nitrate ($^{-62}NO_3$, $^{-46}NO_2$). The OC particles that contained organosulfates (AMIGAS: 19892 particles, 96%; ANARChE: 110912, >99%) were significantly more abundant than those lacking organosulfates (AMIGAS: 913 particles, 4%; ANARChE: 706, <0.01%).

Amine. The positive spectra of the amine-type are enriched in the organic-nitrogen markers, $^{58}C_2H_5NCH_2$, $^{86}(C_2H_5)_2NCH_2$, $^{101}(C_2H_5)_3N$ with less intense organic carbon ($^{27}C_2H_3$, $^{39}C_3H_3$, $^{43}C_2H_3O$) fragments. The negative spectra are characterized by a large sulfate ($^{-97}HSO_4$) contribution with smaller nitrate ($^{-62}NO_3$, $^{-46}NO_2$) peaks. All of the amine particles contained organosulfates during both studies likely due to the highly aged nature of these particles as indicated by the high abundance of secondary amine species.

Biomass Burning. Particles attributed to biomass burning contain a dominant potassium (^{39}K) peak with smaller sodium (^{23}Na) and carbonaceous peaks (^{12}C, $^{27}C_2H_3$, $^{37}C_3H$) in the positive spectra. The negative spectra are primarily sulfate ($^{-97}HSO_4$) and nitrate ($^{-62}NO_3$, $^{-46}NO_2$). The biomass particles that contained organosulfates (AMIGAS: 4596 particles, 42%; ANARChE: 14505, 82%) were more strongly enriched in sulfate than those lacking organosulfates (AMIGAS: 6353 particles, 58%; ANARChE: 3248, 18%).

Dust. Dust particles are typified by the presence of minerals, such as sodium (^{23}Na), aluminum (^{27}Al), calcium (^{40}Ca), or iron (^{56}Fe). The negative spectra contain nitrate ($^{-62}NO_3$, $^{-46}NO_2$) and aluminosilicates ($^{-76}$ $AlO_2(OH)/SiO_3$). The positive and negative spectra included in Figure 8b are an average of multiple dust particle types. Only 208 (3%) iron-rich dust particles were found to contain organosulfates during AMIGAS.

Sea Salt. Sea salt contains primarily sodium (^{23}Na) with a smaller contribution from potassium/sodium oxide ($^{39}K/NaO$) in the positive spectra. Prominent negative ions include chloride ($^{-35,-37}Cl$), organonitrogen (^{-26}CN), sulfate ($^{-97}HSO_4$), and nitrate ($^{-62}NO_3$, $^{-46}NO_2$). Sea salt was introduced to the inland Atlanta region during AMIGAS by the tropical cyclones.[38] No sea salt particles were detected that contained organosulfates.

Ca-rich. The Ca-rich particle type observed during ANARChE is characterized by an intense calcium (^{40}Ca) peak, with a smaller sodium (^{23}Na) peak in the positive spectra. The negative spectra contain sulfate ($^{-97}HSO_4$), and nitrate ($^{-62}NO_3$, $^{-46}NO_2$). In ANARChE, 261 (48%) particles were found to contain organosulfates, while 280 (52%) did not.

Na-rich. The Na-rich particle type identified in the ANARChE campaign contains strong sodium (^{23}Na) and potassium (^{39}K) peaks in the positive-ion spectra. This particle type is distinguished from sea salt due the presence of carbon (^{12}C) and the absence of chloride. The negative spectra contain sulfate ($^{-97}HSO_4$), and nitrate ($^{-62}NO_3$, $^{-46}NO_2$). During ANARChE, 1025 (34%) Na-rich particles were detected with organosulfates, while 1991 (66%) displayed undetectable organosulfate levels.

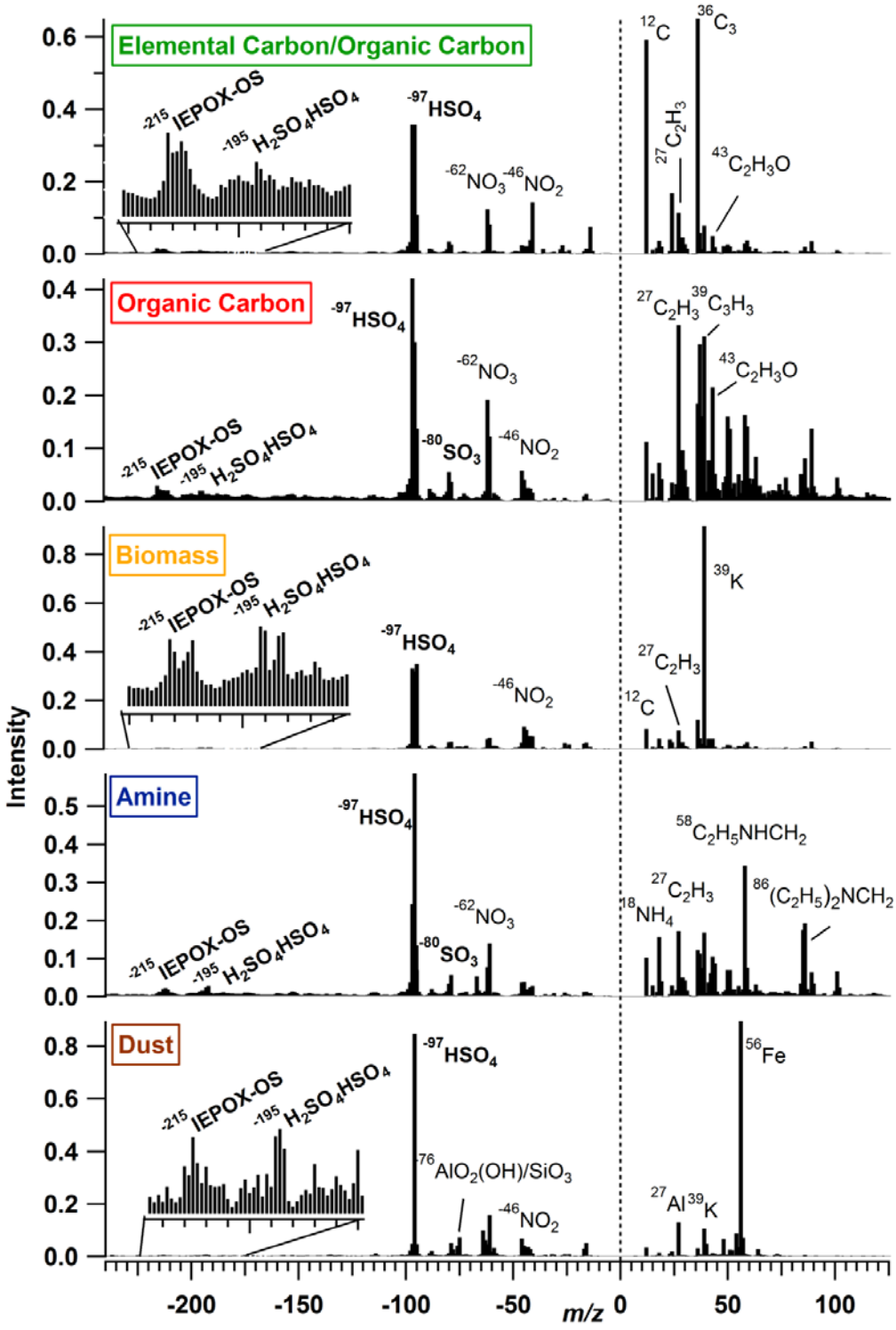

Figure 2.8 Average mass spectra for the dominant particle types containing organosulfate species during AMIGAS.

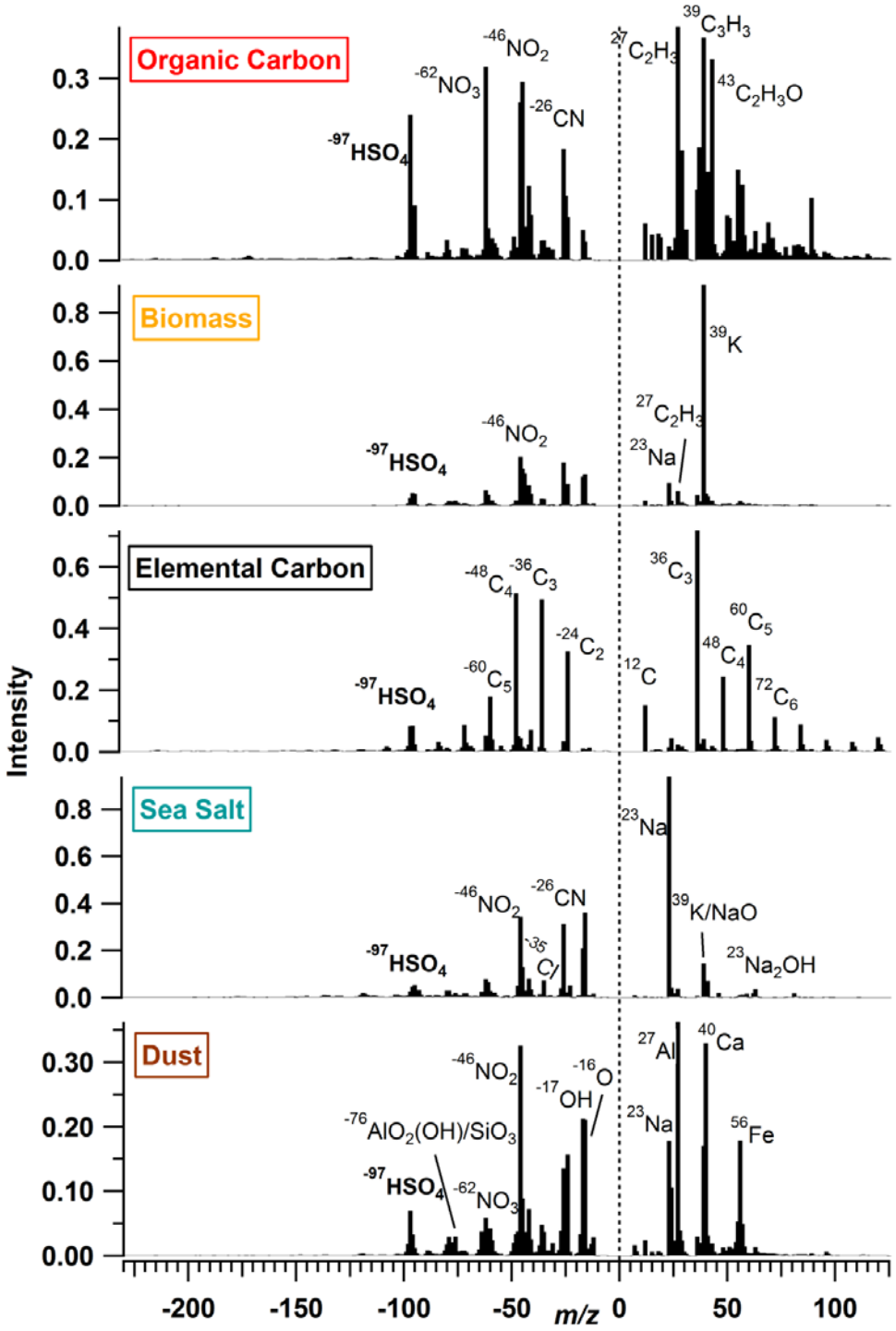

Figure 2.9 Average mass spectra for the dominant particle types that did not contain organosulfate species during AMIGAS.

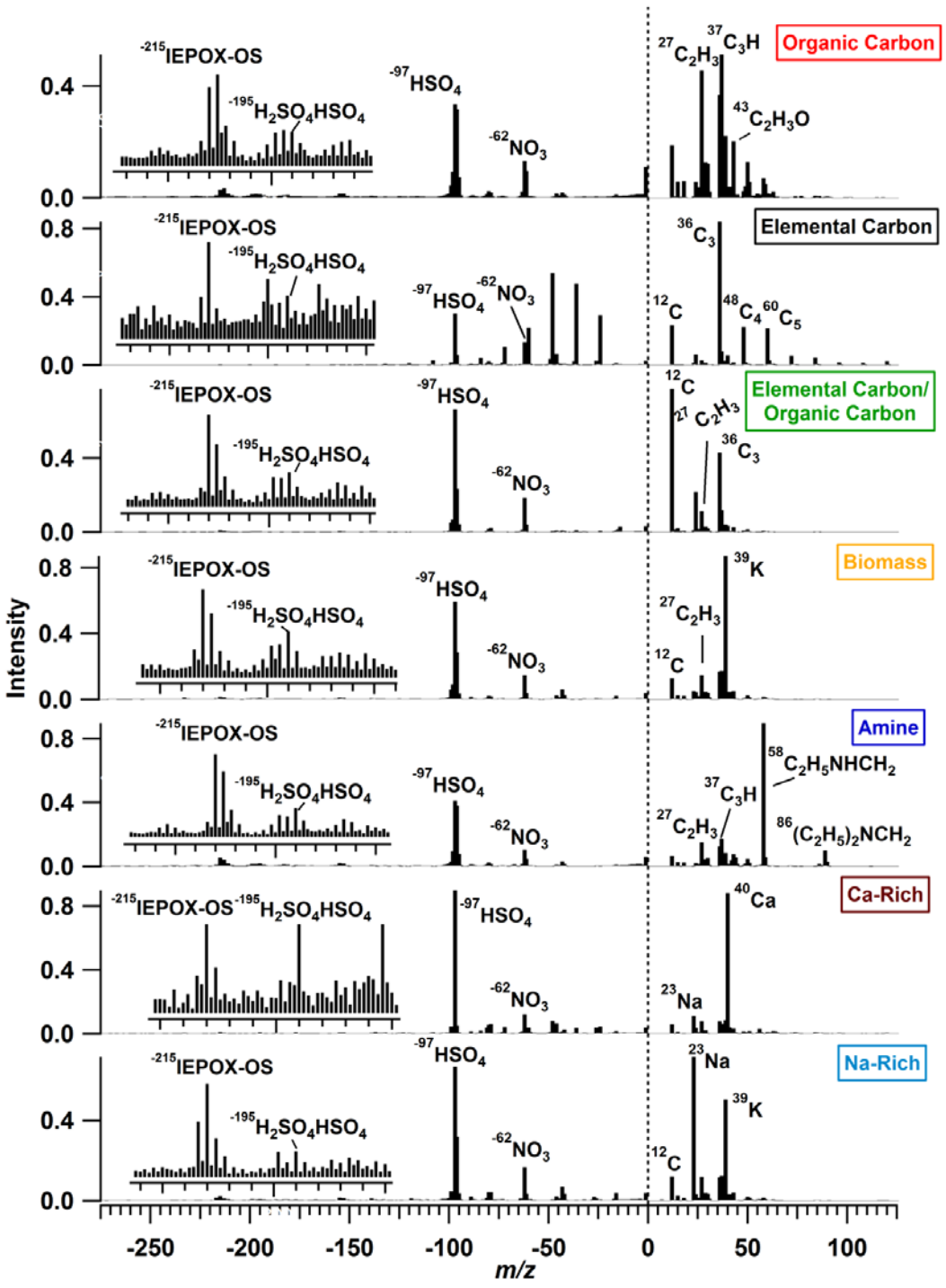

Figure 2.10 Average mass spectra for the dominant particle types containing organosulfate species during ANARChE.

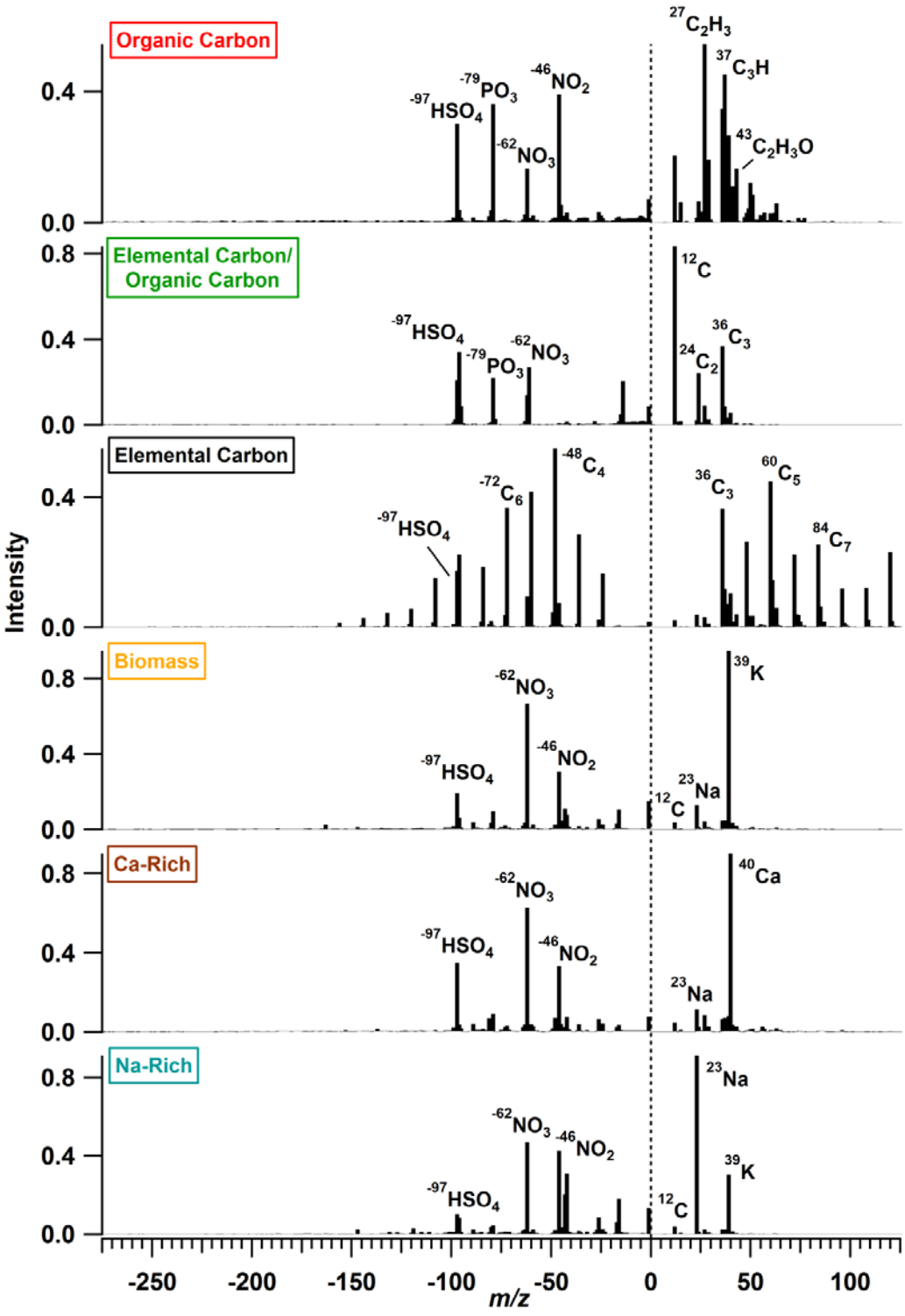

Figure 2.11 Average mass spectra for the dominant particle types that did not contain organosulfate species during ANARChE.

2.8 References:

1. Hallquist, M.; Wenger, J. C.; Baltensperger, U.; Rudich, Y.; Simpson, D.; Claeys, M.; Dommen, J.; Donahue, N. M.; George, C.; Goldstein, A. H.; Hamilton, J. F.; Herrmann, H.; Hoffmann, T.; Iinuma, Y.; Jang, M.; Jenkin, M. E.; Jimenez, J. L.; Kiendler-Scharr, A.; Maenhaut, W.; McFiggans, G.; Mentel, T. F.; Monod, A.; Prevot, A. S. H.; Seinfeld, J. H.; Surratt, J. D.; Szmigielski, R.; Wildt, J., The formation, properties and impact of secondary organic aerosol: current and emerging issues. *Atmos. Chem. Phys.* **2009,** *9*, (14), 5155-5236.

2. Carlton, A. G.; Wiedinmyer, C.; Kroll, J. H., A review of Secondary Organic Aerosol (SOA) formation from isoprene. *Atmos. Chem. Phys.* **2009,** *9*, (14), 4987-5005.

3. Claeys, M.; Graham, B.; Vas, G.; Wang, W.; Vermeylen, R.; Pashynska, V.; Cafmeyer, J.; Guyon, P.; Andreae, M. O.; Artaxo, P.; Maenhaut, W., Formation of secondary organic aerosols through photooxidation of isoprene. *Science* **2004,** *303*, (5661), 1173-1176.

4. Noziere, B.; Ekstrom, S.; Alsberg, T.; Holmstrom, S., Radical-initiated formation of organosulfates and surfactants in atmospheric aerosols. *Geophys. Res. Lett.* **2010,** *37*.

5. Surratt, J. D.; Kroll, J. H.; Kleindienst, T. E.; Edney, E. O.; Claeys, M.; Sorooshian, A.; Ng, N. L.; Offenberg, J. H.; Lewandowski, M.; Jaoui, M.; Flagan, R. C.; Seinfeld, J. H., Evidence for organosulfates in secondary organic aerosol. *Environ. Sci. Technol.* **2007,** *41*, (2), 517-527.

6. Gomez-Gonzalez, Y.; Surratt, J. D.; Cuyckens, F.; Szmigielski, R.; Vermeylen, R.; Jaoui, M.; Lewandowski, M.; Offenberg, J. H.; Kleindienst, T. E.; Edney, E. O.; Blockhuys, F.; Van Alsenoy, C.; Maenhaut, W.; Claeys, M., Characterization of organosulfates from the photooxidation of isoprene and unsaturated fatty acids in ambient aerosol using liquid chromatography/(-) electrospray ionization mass spectrometry. *J. Mass Spectrom.* **2008,** *43*, (3), 371-382.

7. Iinuma, Y.; Muller, C.; Berndt, T.; Boge, O.; Claeys, M.; Herrmann, H., Evidence for the existence of organosulfates from beta-pinene ozonolysis in ambient secondary organic aerosol. *Environ. Sci. Technol.* **2007,** *41*, (19), 6678-6683.

8. Altieri, K. E.; Turpin, B. J.; Seitzinger, S. P., Oligomers, organosulfates, and nitrooxy organosulfates in rainwater identified by ultra-high resolution electrospray ionization FT-ICR mass spectrometry. *Atmos. Chem. Phys.* **2009,** *9*, (7), 2533-2542.

9. Mazzoleni, L. R.; Ehrmann, B. M.; Shen, X. H.; Marshall, A. G.; Collett, J. L., Water-Soluble Atmospheric Organic Matter in Fog: Exact Masses and Chemical Formula Identification by Ultrahigh-Resolution Fourier Transform Ion Cyclotron Resonance Mass Spectrometry. *Environ. Sci. Technol.* **2010,** *44*, (10), 3690-3697.

10. Hawkins, L. N.; Russell, L. M.; Covert, D. S.; Quinn, P. K.; Bates, T. S., Carboxylic acids, sulfates, and organosulfates in processed continental organic aerosol over the southeast Pacific Ocean during VOCALS-REx 2008. *J. Geophys. Res.* **2010,** *115*.

11. Claeys, M.; Wang, W.; Vermeylen, R.; Kourtchev, I.; Chi, X. G.; Farhat, Y.; Surratt, J. D.; Gomez-Gonzalez, Y.; Sciare, J.; Maenhaut, W., Chemical characterisation of marine aerosol at Amsterdam Island during the austral summer of 2006-2007. *J. Aerosol Sci* **2010,** *41*, (1), 13-22.

12. Gard, E.; Mayer, J. E.; Morrical, B. D.; Dienes, T.; Fergenson, D. P.; Prather, K. A., Real-time analysis of individual atmospheric aerosol particles: Design and performance of a portable ATOFMS. *Anal. Chem.* **1997,** *69*, (20), 4083-4091.

13. Jayne, J. T.; Leard, D. C.; Zhang, X. F.; Davidovits, P.; Smith, K. A.; Kolb, C. E.; Worsnop, D. R., Development of an aerosol mass spectrometer for size and composition analysis of submicron particles. *Aerosol Sci. Technol.* **2000,** *33*, (1-2), 49-70.

14. Farmer, D. K.; Matsunaga, A.; Docherty, K. S.; Surratt, J. D.; Seinfeld, J. H.; Ziemann, P. J.; Jimenez, J. L., Response of an aerosol mass spectrometer to organonitrates and organosulfates and implications for atmospheric chemistry. *Proc. Natl. Acad. Sci. USA* **2010,** *107*, (15), 6670-6675.

15. Murphy, D. M.; Cziczo, D. J.; Froyd, K. D.; Hudson, P. K.; Matthew, B. M.; Middlebrook, A. M.; Peltier, R. E.; Sullivan, A.; Thomson, D. S.; Weber, R. J., Single-particle mass spectrometry of tropospheric aerosol particles. *J. Geophys. Res.* **2006,** *111*, (D23).

16. Froyd, K. D.; Murphy, S. M.; Murphy, D. M.; de Gouw, J. A.; Eddingsaas, N. C.; Wennberg, P. O., Contribution of isoprene-derived organosulfates to free tropospheric aerosol mass. *Proceedings of the National Academy of Sciences of the United States of America* **2010,** *107*, (50), 21360-21365.

17. Millet, D. B.; Jacob, D. J.; Boersma, K. F.; Fu, T. M.; Kurosu, T. P.; Chance, K.; Heald, C. L.; Guenther, A., Spatial distribution of isoprene emissions from North America derived from formaldehyde column measurements by the OMI satellite sensor. *J. Geophys. Res.* **2008,** *113*, (D2).

18. Levy, J. I.; Wilson, A. M.; Evans, J. S.; Spengler, J. D., Estimation of primary and secondary particulate matter intake fractions for power plants in Georgia. *Environ. Sci. Technol.* **2003,** *37*, (24), 5528-5536.

19. Hansen, D. A.; Edgerton, E. S.; Hartsell, B. E.; Jansen, J. J.; Kandasamy, N.; Hidy, G. M.; Blanchard, C. L., The Southeastern Aerosol Research and Characterization Study: Part 1-Overview. *J. Air Waste Manage. Assoc.* **2003,** *53*, (12), 1460-1471.

20. Su, Y. X.; Sipin, M. F.; Furutani, H.; Prather, K. A., Development and characterization of an aerosol time-of-flight mass spectrometer with increased detection efficiency. *Anal. Chem.* **2004,** *76*, (3), 712-719.

21. Marple, V. A.; Rubow, K. L.; Behm, S. M., A microorifice uniform deposit impactor (MOUDI) - Description, calibration, and use. *Aerosol Sci. Technol.* **1991,** *14*, (4), 434-446.

22. Allen, J. O., YAADA: software toolkit to anlayze single-particle mass spectral data. *Software Reference Manual* **2001**.

23. Song, X. H.; Hopke, P. K.; Fergenson, D. P.; Prather, K. A., Classification of single particles analyzed by ATOFMS using an artificial neural network, ART-2A. *Anal. Chem.* **1999,** *71*, (4), 860-865.

24. Zelenyuk, A.; Imre, D.; Cuadra-Rodriguez, L. A., Evaporation of water from particles in the aerodynamic lens inlet: An experimental study. *Anal. Chem.* **2006,** *78*, (19), 6942-6947.

25. Neubauer, K. R.; Johnston, M. V.; Wexler, A. S., Humidity effects on the mass spectra of single aerosol particles. *Atmos. Environ.* **1998,** *32*, (14-15), 2521-2529.

26. Surratt, J. D.; Gomez-Gonzalez, Y.; Chan, A. W. H.; Vermeylen, R.; Shahgholi, M.; Kleindienst, T. E.; Edney, E. O.; Offenberg, J. H.; Lewandowski, M.; Jaoui, M.; Maenhaut, W.; Claeys, M.; Flagan, R. C.; Seinfeld, J. H., Organosulfate formation in biogenic secondary organic aerosol. *J. Phys. Chem. A* **2008,** *112*, (36), 8345-8378.

27. Surratt, J. D.; Chan, A. W. H.; Eddingsaas, N. C.; Chan, M. N.; Loza, C. L.; Kwan, A. J.; Hersey, S. P.; Flagan, R. C.; Wennberg, P. O.; Seinfeld, J. H., Reactive intermediates revealed in secondary organic aerosol formation from isoprene. *Proc. Natl. Acad. Sci. USA* **2010,** *107*, (15), 6640-6645.

28. Wenzel, R. J.; Liu, D. Y.; Edgerton, E. S.; Prather, K. A., Aerosol time-of-flight mass spectrometry during the Atlanta Supersite Experiment: 2. Scaling procedures. *J. Geophys. Res.* **2003,** *108*, (D7).

29. Galloway, M. M.; Chhabra, P. S.; Chan, A. W. H.; Surratt, J. D.; Flagan, R. C.; Seinfeld, J. H.; Keutsch, F. N., Glyoxal uptake on ammonium sulphate seed aerosol: reaction products and reversibility of uptake under dark and irradiated conditions. *Atmos. Chem. Phys.* **2009,** *9*, (10), 3331-3345.

30. Chan, M. N.; Surratt, J. D.; Claeys, M.; Edgerton, E. S.; Tanner, R. L.; Shaw, S. L.; Zheng, M.; Knipping, E. M.; Eddingsaas, N. C.; Wennberg, P. O.; Seinfeld, J. H., Characterization and quantification of isoprene-derived epoxydiols in ambient aerosol in the southeastern United States. *Environ. Sci. Technol.* **2010,** *44*, (12), 4590-4596.

31. Reilly, P. T. A.; Lazar, A. C.; Gieray, R. A.; Whitten, W. B.; Ramsey, J. M., The elucidation of charge-transfer-induced matrix effects in environmental aerosols via real-time aerosol mass spectral analysis of individual airborne particles. *Aerosol Sci. Technol.* **2000,** *33*, (1-2), 135-152.

32. Finlayson-Pitts, B. J.; Pitts, J. N., Chemistry of the Upper and Lower Atmosphere: Theory, Experiments, and Applications. Academic Press: San Diego, 2000.

33. Lukacs, H.; Gelencser, A.; Hoffer, A.; Kiss, G.; Horvath, K.; Hartyani, Z., Quantitative assessment of organosulfates in size-segregated rural fine aerosol. *Atmos. Chem. Phys.* **2009,** *9*, (1), 231-238.

34. Minerath, E. C.; Elrod, M. J., Assessing the Potential for Diol and Hydroxy Sulfate Ester Formation from the Reaction of Epoxides in Tropospheric Aerosols. *Environ. Sci. Technol.* **2009,** *43*, (5), 1386-1392.

35. Denkenberger, K. A.; Moffet, R. C.; Holecek, J. C.; Rebotier, T. P.; Prather, K. A., Real-time, single-particle measurements of oligomers in aged ambient aerosol particles. *Environ. Sci. Technol.* **2007,** *41*, (15), 5439-5446.

36. Pastor, S. H.; Allen, J. O.; Hughes, L. S.; Bhave, P.; Cass, G. R.; Prather, K. A., Ambient single particle analysis in Riverside, California by aerosol time-of-flight mass spectrometry during the SCOS97-NARSTO. *Atmos. Environ.* **2003,** *37*, S239-S258.

37. Pratt, K. A.; Prather, K. A., Real-Time, Single-Particle Volatility, Size, and Chemical Composition Measurements of Aged Urban Aerosols. *Environ. Sci. Technol.* **2009,** *43*, (21), 8276-8282.

38. Creamean, J. M., Ault, A. P., Prather, K. A., Signature Marine Aerosol Chemistry Observed in an Inland Urban Location during Tropical Cyclones. *In preparation*.

3 Measurements of isoprene-derived organosulfates in ambient aerosols by aerosol time-of-flight mass spectrometry - Part 2: temporal variability & formation mechanisms

3.1 Abstract

Organosulfate species have recently gained attention for their potentially significant contribution to secondary organic aerosol (SOA); however their temporal behavior in the ambient atmosphere has not been probed in detail. In this work, organosulfates derived from isoprene were observed in single particle mass spectra in Atlanta, GA during the 2002 Aerosol Nucleation and Characterization Experiment (ANARChE) and the 2008 August Mini-Intensive Gas and Aerosol Study (AMIGAS). Real-time measurements revealed that the highest organosulfate concentrations occurred at night under a stable boundary layer, suggesting gas-to-particle partitioning and subsequent aqueous-phase processing of the organic precursors played key roles in their formation. Further analysis of the diurnal profile suggests possible contributions from multiple production mechanisms, including acid-catalysis and radical-initiation. This study highlights the potential for additional SOA formation pathways in biogenically-influenced urban regions to enhance the organic aerosol burden.

3.2 Introduction

Organic species can significantly influence the health and climate impacts of atmospheric particulate matter due to their potential toxicity and effect on hygroscopicity.[1] Organic aerosols can arise from both primary (directly emitted) and secondary (formed in the atmosphere) sources.[2] Despite extensive research in recent years,[2] models often under-predict the contribution of secondary organic species to aerosol mass[3] as a result of the remaining low scientific understanding of organic aerosol formation pathways.

Biogenic volatile organic compounds (BVOCs) can play a significant role in the formation of secondary organic aerosols (SOA) due to their high reactivity toward atmospheric oxidants. Indeed, radiocarbon dating has attributed a dominant fraction (~65%) of SOA to biogenic sources in heavily forested regions.[4] Isoprene (2-methyl-1,3-butadiene, C_5H_8) is the most abundant BVOC and has been implicated in SOA formation (ref (5) and references therein).

Further, in urban environments, BVOCs can interact with anthropogenic pollutants resulting in an enhancement of the organic aerosol mass.[6,7] Anthropogenic emissions can influence biogenic SOA in a number of ways,[8] including by introducing new chemical pathways to produce unique, low-volatility chemical species. Herein, we focus on a specific class of compounds, organosulfates, which have been demonstrated to form via reaction between BVOCs and particulate sulfate derived predominantly from industrial SO_2 emissions.[9]

Several mechanisms have been proposed from laboratory investigations to explain the formation of organosulfate compounds, including acid-catalyzed alcohol sulfate-esterification,[10] reaction with sulfate radicals ($SO_4^{-}\cdot$, $HSO_4\cdot$),[11-13] or acid-catalyzed epoxide hydrolysis.[14,15] The esterification mechanism has been shown to be kinetically limited and not likely to occur in the ambient atmosphere.[16] Radical-initiated formation has been proposed following the observation of organosulfate production in smog chamber reactions under irradiated conditions, which ceased in the dark.[11,17] Several studies have implicated the role of epoxide intermediates in leading to SOA compounds,[18-20] and in particular to organosulfate species.[14,21] The atmospheric fate of the isoprene-derived epoxide (IEPOX) largely depends on aerosol pH and liquid water content,[22] but has been shown to produce 2-methyltetrols and, in the presence of acidic sulfate aerosol, organosulfate species, as shown in Figure 3.1.

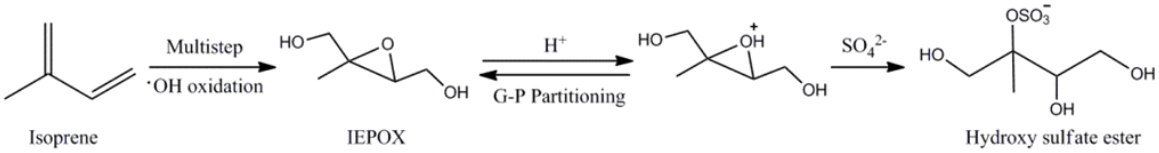

Figure 3.1 Reaction Mechanism for the formation of the IEPOX-derived organosulfate (adapted from ref 14).

In Chapter 2, observations of the size-resolved mixing state of organosulfates during the 2002 Aerosol Nucleation and Real-time Characterization Experiment (ANARChE) and the 2008 August Mini-Intensive Gas and Aerosol Study (AMIGAS) in Atlanta, GA were discussed.[23] The on-line mass spectrometry analysis employed in these studies provided the high time resolution necessary to monitor rapid changes in aerosol composition. Herein, we describe the temporal trends of organosulfate species and the resulting insights into the possible formation mechanisms occurring in the ambient atmosphere. To our knowledge, this is the first study to investigate in real-time the temporal variability of ambient particle-phase organosulfate species.

3.3 Experimental

3.3.1 Field Measurements.

Aerosol sampling was performed during two field studies at the Jefferson Street Southeastern Aerosol Research and Characterization (SEARCH) Network site (33.8º N, 84.4º W), a mixed residential-industrial location about 4 km northwest of metro Atlanta.[24] Data are presented in local time.

Real-time ATOFMS measurements were made of single particles during ANARChE from August 4-11, 2002 and during AMIGAS from August 22-September 10, 2008. Additional details of ATOFMS data collection and analysis are provided elsewhere.[23,25] Briefly, ATOFMS detected the size and chemical composition of individual particles from 50–350 nm during ANARChE and 200–3000 nm during AMIGAS. ATOFMS collects both positive and negative spectra for each particle; for the datasets considered here, some negative spectra displayed incorrect mass calibration in the mass range of interest (>100 *m/z*) due to instability in the mass spectrometer voltages. The manual correction method applied to the data is described in the Supporting Information. Further, as described in Chapter 2, organosulfates were predominantly detected in submicron particles; therefore, only the submicron particles (0.2-1 μm) with dual-polarity spectra collected during AMIGAS are included in the detailed analysis herein. All particles with dual-polarity spectra were included from ANARChE since these measurements were restricted to particles <350 nm.

Co-located instrumentation monitored meteorology (wind speed/direction, precipitation, temperature, relative humidity, solar radiation) and gas-phase pollutant levels (NO_x, CO, O_3, SO_2, HNO_3).[24] Continuous $PM_{2.5}$ samplers also monitored total carbon levels.[26] During AMIGAS, gas-phase water soluble organic carbon (WSOC) measurements were obtained by a mist-chamber.[27]

3.4 Results and Discussion

As discussed in Chapter 2, ATOFMS detected isoprene-derived organosulfates at *m/z* -139, -153, -155, -199, and -215 during both ANARChE and AMIGAS. Identification of these species was verified through ATOFMS analysis of chemical standards and comparison of ambient ATOFMS data to the accurate mass analysis obtained from co-located filter samples analyzed off-line by high resolution mass spectrometry.[23] For brevity, this chapter focuses on the

marker at *m/z* -215 since it was the most abundant isoprene-derived organosulfate compound observed in the ATOFMS data by a significant margin (~4x) and the other markers displayed similar temporal profiles, as shown in Figure 3.7 (Supporting Information) for the AMIGAS campaign. While the formation mechanism of *m/z* -215 will be explored below, for simplicity, it will be referred to as the IEPOX-derived organosulfate since both IEPOX and the corresponding organosulfate were detected in Atlanta during AMIGAS.[28]

3.4.1 Temporal trends of organosulfate species

Because both ANARChE and AMIGAS were conducted during summer, comparison of the datasets serves to provide verification of observations and improved understanding of the general behavior of organosulfate species. However, it should be noted at the outset that this work focuses on the qualitative trends of organosulfates during these Atlanta field campaigns. The ATOFMS mass spectral data have not been scaled to correct for potential instrumental differences (e.g., MS tuning) that could influence the absolute peak intensity measured during each campaign. Therefore only the relative trends in organosulfate mass spectral peak area observed in the two datasets will be compared herein (e.g. similarities in diurnal cycle); differences in the peak magnitude should not be used to infer differences in organosulfate concentrations between the two studies.

Using the high time resolution of real-time, single-particle data, the peak area of the IEPOX-derived organosulfate at *m/z* -215 was shown to fluctuate significantly throughout the ANARChE and AMIGAS campaigns (Figure 3.2). Much of this variation can be attributed to changes in meteorology. Both study periods exhibited several days characteristic of a diurnal cycle, as evidenced by regular patterns in meteorological (e.g. temperature, relative humidity) and gas-phase pollutant data (e.g. ozone) (ANARChE: 8/4-8/5/02, 8/8-8/11/02; AMIGAS: 8/29-8/31/08, 9/3/08, 9/6-9/10/08). Additionally, during AMIGAS, two tropical cyclones (TCs; Gustav, 8/24-9/4/08[29] and Hannah, 8/26-9/7/08[30]) influenced the southeastern United States. The time periods that TCs directly impacted the Atlanta region are inferred from the prevailing southeasterly winds and fast wind speeds (i.e. 8/23-8/27/08, 8/31-9/2/08, 9/4-9/5/08; Figure 3.2), and included a rain episode from 8/24-8/26/08. Tropical storm Bertha was also present in the Gulf of Mexico during ANARChE (8/4-8/9/02)[31] and may have slightly influenced the Atlanta region, as indicated by a shift in meteorology on 8/6-8/8/02 (Figure 3.2). The high temporal resolution of ATOFMS measurements provided unique observations of the behavior of

organosulfate species during both the calm days and the meteorological events, as described below.

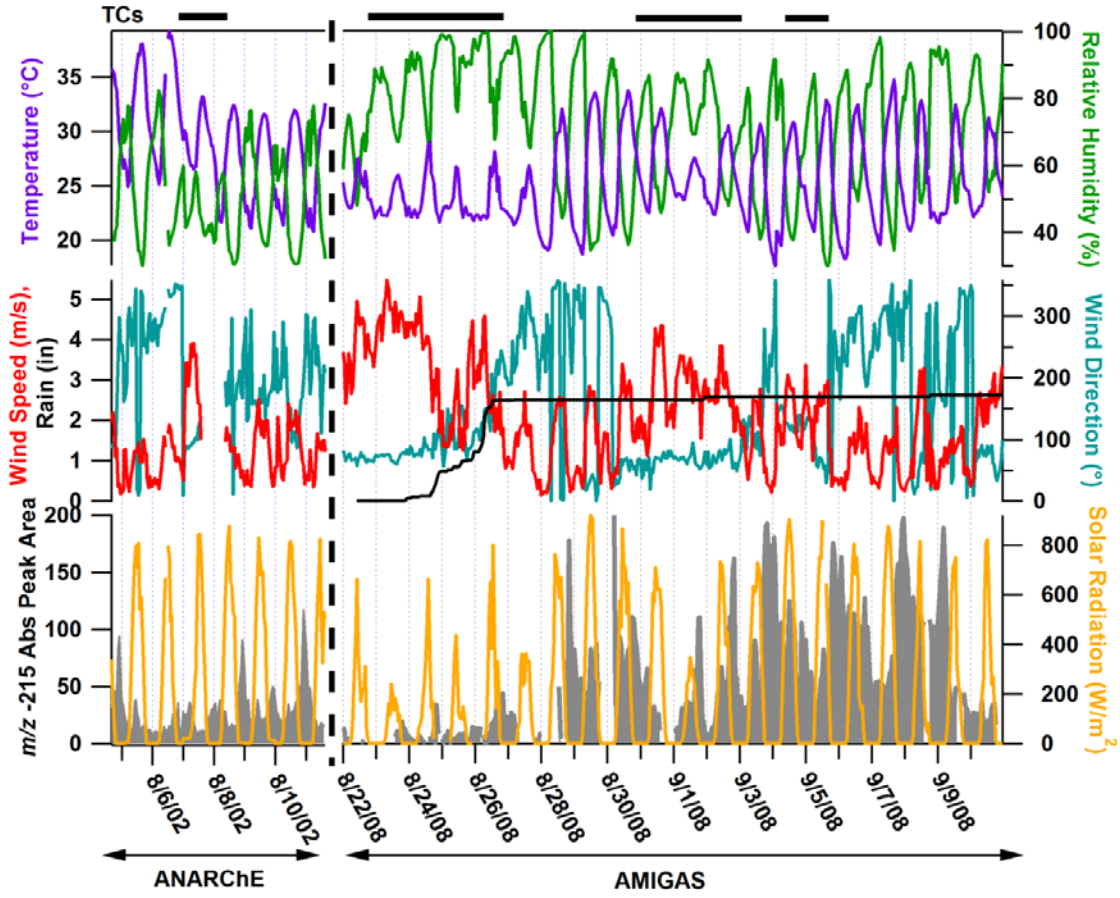

Figure 3.2 Hourly-averaged temporal variation in the absolute area of *m/z* -215, solar radiation, wind speed and direction, precipitation, temperature, and relative humidity. Black bars indicate time periods influenced by tropical cyclones (TCs). Data from both ANARChE and AMIGAS are included in the figure, separated by the dashed line.

3.4.1.1 Diurnal trends.

The non-TC days during ANARChE (8/4-8/5/02, 8/8-8/11/02) and AMIGAS (8/29-8/31/08, 9/3/08, 9/6-10/08) provided insight into the typical diurnal cycle of organosulfate species in Atlanta. Consistently during both campaigns, the highest abundance of organosulfate species occurred at night during periods with low wind speeds (Figure 3.2). The stagnant wind conditions and buildup of NO_x and CO (Figure 3.3) indicate that a stable boundary layer was present overnight. Radiosonde data was obtained from the NOAA Integrated Global Radiosonde Archive[32] to investigate the boundary layer stability; vertical temperature profiles are included in Figure 3.4. These soundings were taken at 12Z (7am EST), but are expected to be representative

of the nocturnal temperature profile since breakup of inversions in Atlanta has been observed to occur after 9am.[33] The radiosonde data confirmed the presence of nocturnal temperature inversions during these periods (Figure 3.4) yielding a very shallow mixed layer and increased pollutant levels (e.g. NO_x and CO; Figure 3.3). The nights characterized by the strongest inversions, as indicated by the temperature difference between the top and bottom of the inversion layer, are associated with the highest levels of organosulfates (e.g. 9/6/08, 9/8/08, Figures 3.2 & 3.4). Also of note, an inversion was not present on 9/10/08 (Figure 3.4), which could explain the lower abundance of organosulfates observed on this night during AMIGAS (Figure 3.2). These soundings and the diurnal trends observed by ATOFMS provide strong evidence for the role of a stable boundary layer in the formation of organosulfates in Atlanta.

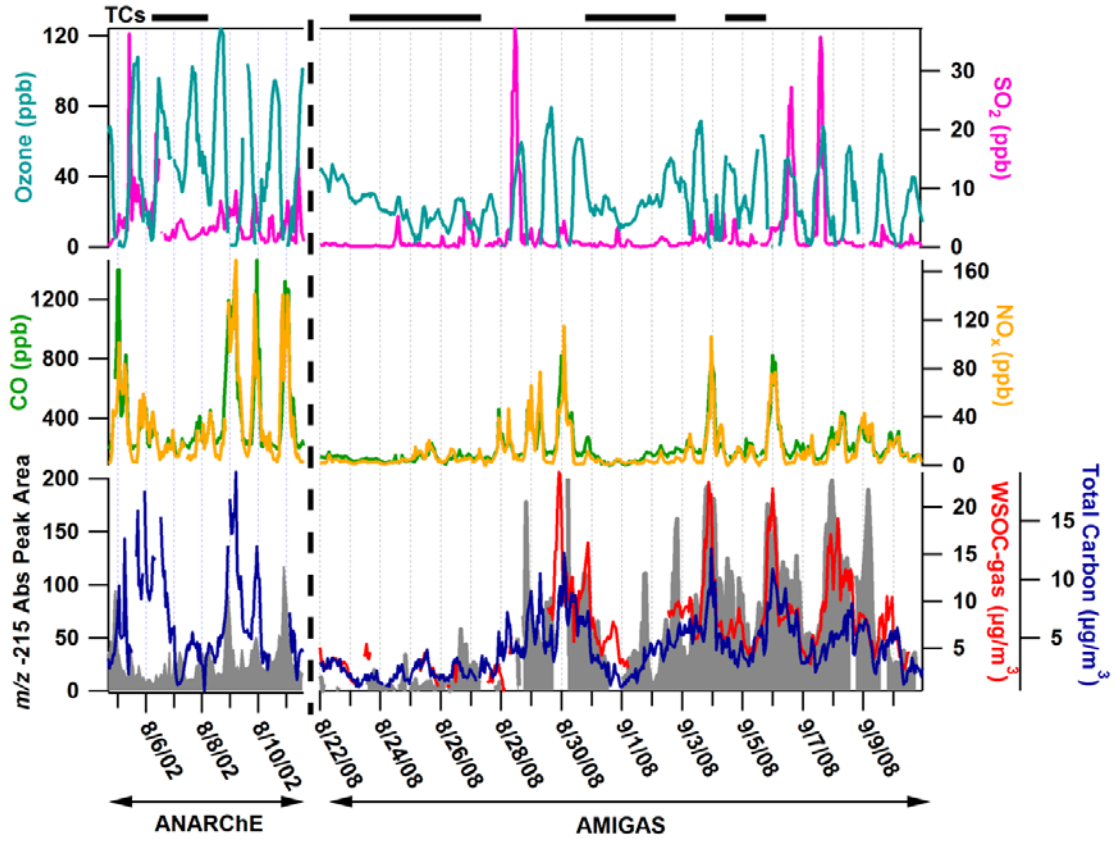

Figure 3.3 Hourly-averaged temporal variation in the *m/z* -215 absolute peak area, gas-phase water soluble organic carbon (WSOC), total $PM_{2.5}$ carbon mass concentration (Total Carbon), NO_x, CO, O_3, and SO_2. Black bars indicate time periods influenced by tropical cyclones (TCs). Data from both ANARChE and AMIGAS are included in the figure, separated by the dashed line.

The nighttime meteorology also displayed a characteristic decrease in temperature and increase in relative humidity (RH), providing favorable conditions for condensation of water and

semivolatile species. While IEPOX is not expected to partition appreciably to the organic phase,[28] Eddingsaas *et al.*[22] predicted an increase in IEPOX uptake with increasing aerosol water content, as would be expected under the high nocturnal RH conditions. It should also be noted that the presence of water can influence the ionization of species from a particle in the ATOFMS, and in particular has been shown to suppress negative ion formation.[34] Since organosulfate species were detected as negative ions and in higher abundance at night (higher RH and therefore higher aerosol water content), it is believed that the observed diurnal trend is not a measurement artifact, but rather, perhaps represents a lower bound on the nighttime organosulfate abundance relative to other species in the particles.

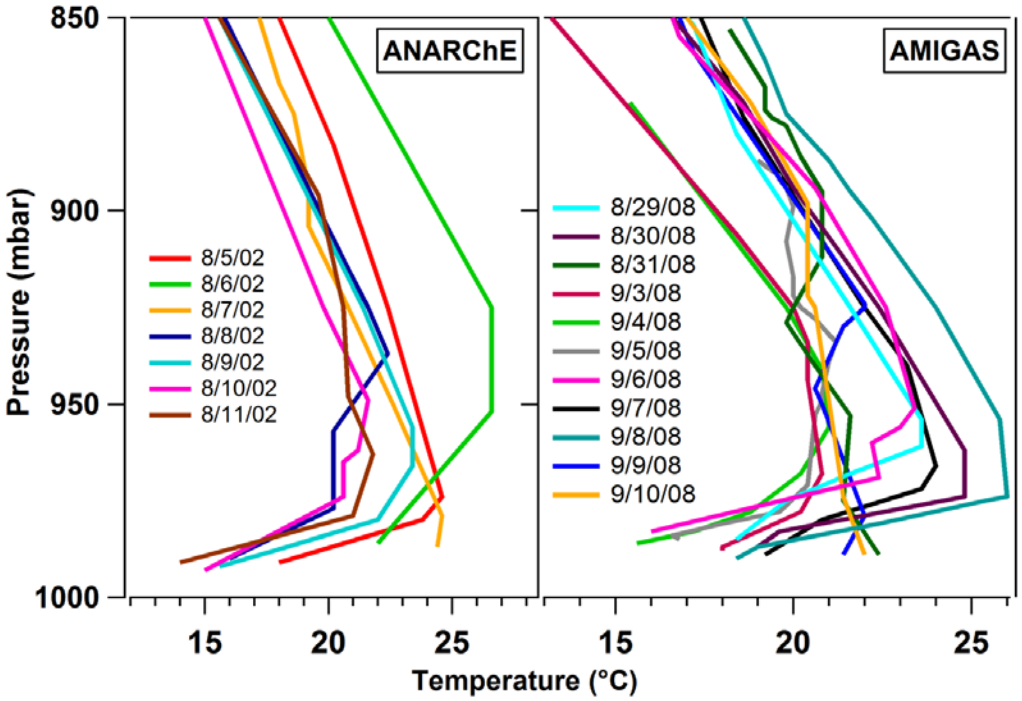

Figure 3.4 Vertical temperature profiles during ANARChE (left) and AMIGAS (right) obtained from the NOAA Integrated Global Radiosonde Archive.[32] Only non-TC days are shown for AMIGAS to avoid graph clutter.

The peak area of *m/z* -215 strongly tracks NO_x (NO_2 + NO) concentration during both ANARChE and AMIGAS (Figure 3.3). Interestingly, IEPOX has been shown to form under low-NO_x conditions,[14] making the correlation between the IEPOX-derived organosulfate and NO_x somewhat unexpected. Several possible explanations exist for this relationship: (1) Particulate organosulfate species and NO_x may have increased overnight independently of each other, driven predominantly by the lowering of the boundary layer. In this scenario, the organosulfate

precursors may have formed during the day under low-NO_x conditions, followed by condensation of the semi-volatile oxidized VOCs and organosulfate formation overnight. The overnight increase in NO_x would then be largely uninvolved in the organosulfate mechanism. (2) It is also possible that nocturnal nitrogen oxide chemistry played a role in the formation of organosulfates by raising aerosol acidity, an important parameter in the formation of organosulfates.[35] Overnight, NO_2 reacts with ozone to produce $NO_3\cdot$, which can subsequently react with NO_2 to form N_2O_5; heterogeneous hydrolysis of N_2O_5 yields $HNO_{3(aq)}$ (ref. 36 and references therein). Figure 3.5 shows the temporal trends of NO_2, $HNO_{3(g)}$, particulate nitrate, and *m/z* -215. The rise in NO_2 concentration overnight closely tracks the ATOFMS nitrate signal (*m/z* -62), indicating the possible of conversion of NO_x into HNO_3 by the reaction outlined above. Further, Brown *et al.* have demonstrated an increase in N_2O_5 uptake to aerosols with high sulfate content,[37] as is typical of Atlanta aerosol. While measurements of $NO_3\cdot$ and N_2O_5 were not available for these studies, previous work has shown that N_2O_5 is the dominant species under high NO_2 conditions,[36] as observed overnight in Atlanta (Figure 3.5). In addition, note that gas-phase nitric acid decreases as night falls (Figure 3.5), consistent with the partitioning of HNO_3 to the aerosol phase. Since the condensation of nitric acid and increase in particulate nitrate coincide with the rise in organosulfate abundance, it is possible that the reactive nitrogen species played a role in the formation of organosulfate by raising the aerosol acidity and thus enhancing the reactive uptake of organosulfate precursors. Although, based on these measurements, we cannot definitively establish a causal link between reactive nitrogen chemistry and organosulfate formation versus a dominant role of the nocturnal boundary layer, we note that both scenarios (1) and (2) involve partitioning/reactive uptake of the organosulfate precursors overnight. (3) A third possible explanation for the correlation between organosulfates and NO_x involves the indirect formation of organosulfates via an organonitrate intermediate. Organonitrates can arise from reaction of isoprene with OH under high-NOx conditions during the day[19] or at night with nitrate radical;[38] particulate nitrate can also act as a nucleophile toward epoxides similar to sulfate in Figure 3.1.[39] Tertiary organonitrates have been found to undergo rapid substitution by water or sulfate, leading to the formation of polyols and organosulfates.[39] Indeed, nitrooxy-organosulfate species derived from isoprene and have been previously observed in Atlanta by Surratt *et al.*,[40] wherein one or two nitrate groups are in the place of hydroxyl groups in the product compound of Figure 3.1. The hydrolysis of such compounds would produce the same *m/z* -215 ion described herein. In summary, the apparent correlation between organosulfates and reactive nitrogen

species could be driven by a combination of effects (1)-(3), or by some other mechanism, warranting further exploration.

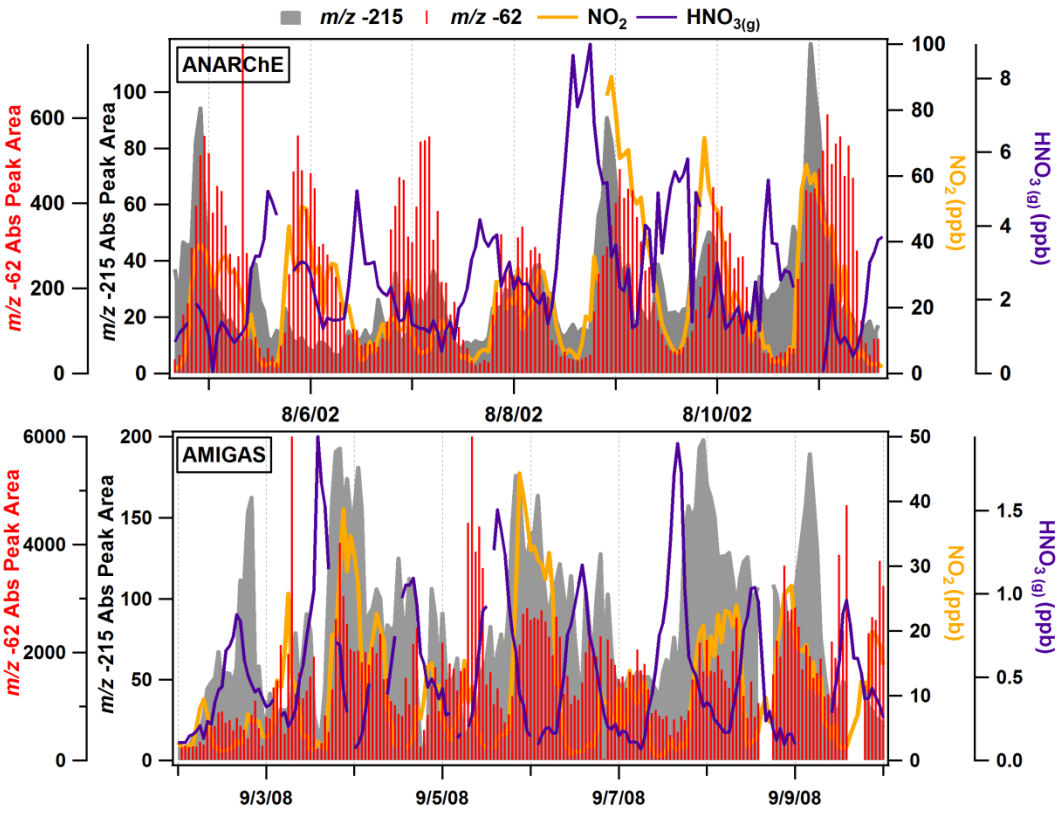

Figure 3.5 Hourly-averaged temporal trends in the absolute peak areas of *m/z* -215 & *m/z* -62 (NO_3^-), $HNO_{3(g)}$, and NO_2 during ANARChE (top) and AMIGAS (bottom). For graph clarity, only the period with highest organosulfate abundance (9/2-9/10/08) is shown for AMIGAS.

By peaking mostly at night, organosulfate species are largely anti-correlated with O_3, which forms by photochemical processes during the day. However, the highest nighttime concentrations of organosulfates generally follow days with high O_3 levels (e.g. 8/8-8/9/02 and 9/3-9/4/08, Figure 3.3). This relationship indicates that there was likely a high degree of photochemical isoprene oxidation contributing to the enhanced O_3 levels[41] and leading to the daytime formation of the organosulfate precursors, which then became concentrated under the low nocturnal boundary layer. These observations are supported by the water-soluble organic carbon (WSOC) measurements from AMIGAS (Figure 3.3). Gas-phase WSOC levels increased overnight, consistent with a low mixing height concentrating these species (likely including the organosulfate precursors) in the atmosphere, which likely enhanced the gas-to-particle partitioning.

Somewhat surprisingly, a clear trend between organosulfates and SO_2 was not observed: the large SO_2 spikes did not appear to significantly enhance the levels of organosulfates. However, a small afternoon increase in organosulfate abundance is noted on the afternoon of 8/5/02 during an SO_2 plume. Similarly during AMIGAS, an SO_2 spike on the afternoon of 9/6/08 led to one of the only days with higher organosulfate levels during the day than the following night.[23] It is possible that the semi-volatile nature of IEPOX prevented extensive partitioning during the day, even if there was an increase in aerosol acidity induced by SO_2 emissions.

The correlations of organosulfates with meteorological and gas-phase pollutant data described above suggest that gas-to-particle partitioning may be the key step in determining the concentration of particle-phase organosulfate species. As the boundary layer height and temperature decrease and RH increases at night, there is likely enhanced partitioning of the isoprene oxidation products (i.e. IEPOX in the case of the *m/z* -215 marker) followed by particle-phase reactions resulting in organosulfate formation. The relatively long gas-phase IEPOX lifetime of 18-22 hours[42] is consistent with this proposed delay between afternoon photochemical production of IEPOX and the nighttime formation of organosulfates. We note that IEPOX and other organosulfate precursors could have formed locally or advected from other locations during the day; indeed it is likely that the organosulfate precursors form regionally, given the similarities between the IEPOX concentration in Atlanta versus a rural Georgia site.[28]

3.4.1.2 Tropical cyclone influence

The lowest abundance of *m/z* -215 occurred during the rainy, TC-influenced period of AMIGAS (8/24-8/27/08) when the aerosols and pollutants were scavenged by precipitation or advected from the area, as evidenced by the low levels of gas-phase pollutants and total particulate carbon (Figure 3.3). This period and the additional TC periods (9/1-9/2/08, 9/4-9/5/08) were characterized by high wind speeds and predominantly southeasterly winds. During these storms, solar radiation and O_3 concentration decreased (Figures 3.2 & 3.3), consistent with a decrease in photochemical activity, resulting in reduced formation of isoprene oxidation products, and therefore lower organosulfate abundance.

During ANARChE, the levels of organosulfates were lowest from 8/6-8/8/02. A shift in meteorology is clear from the wind speed and relative humidity data (Figure 3.2); a decrease in barometric pressure was also observed on 8/6/02 (not shown). As mentioned above, TC Bertha present in the Gulf of Mexico may have induced the shift in meteorological patterns, though its

potential influence on Atlanta has not been verified. Additionally, a deeper temperature inversion was present on 8/6/02 and a negligible one existed on 8/7/02 (Figure 3.4); this change in boundary layer height could have also contributed to the lower organosulfate abundance on these nights.

3.4.2 Possible formation mechanisms of organosulfates

Since boundary layer stability appears to play a strong role in the absolute levels of particulate organosulfate species in Atlanta, the possible chemical mechanisms were further investigated by normalizing the organosulfate peak area by CO concentration. CO has been used as an inert chemical tracer to separate the effects of vertical mixing and chemical reactions on pollutant concentrations.[43] The CO-normalized temporal profiles are shown in Figure 3.6. During the ANARChE campaign, the normalized IEPOX-derived organosulfate levels exhibit a maximum in the afternoon on the days not influenced by a TC (8/4-8/5/02, 8/9-8/11/02) coinciding with high ozone concentrations indicative of high photochemical activity. The concurrent increase in the ATOFMS sulfuric acid marker *(m/z* -195, $HSO_4 \cdot H_2SO_4^-$)[44] is consistent with photochemical production from SO_2 and possibly indicates the importance of particle acidity in the formation of organosulfates. However, previous studies have also proposed a radical-initiated organosulfate formation mechanism via reaction between isoprene and sulfate/bisulfate radical giving rise to the *m/z* -215 organosulfate.[11,17] As these radical reactions occur under irradiated conditions, potential contribution of this mechanism to the daytime organosulfate concentration cannot be ruled out. It is noteworthy that organosulfate compounds have been observed with the same molecular formulas via both the radical-initiated and acid-catalyzed mechanisms[10,11] and thus these ATOFMS measurements cannot differentiate the afternoon contributions from these two potential pathways. It is therefore possible that the afternoon increase in organosulfate levels is due to either the radical formation mechanism or acid-catalyzed reactive uptake (or both).

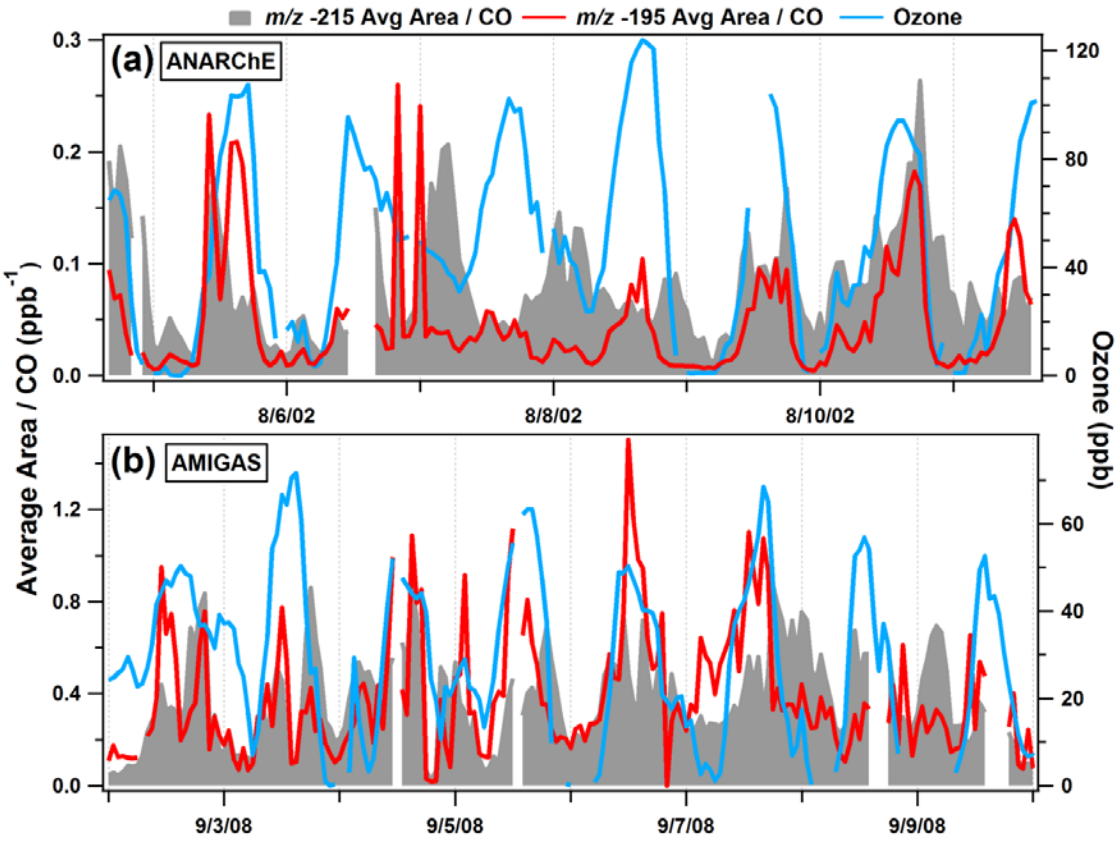

Figure 3.6 Hourly-averaged temporal trends of *m/z* -215 and -195 absolute peak area normalized by CO concentration during ANARChE (top) and AMIGAS (bottom). For graph clarity, only the period with highest organosulfate abundance (9/2-9/10/08) is shown for AMIGAS. The O_3 traces are overlaid to highlight the correlation with photochemical activity.

As described above, the highest absolute levels of organosulfates were detected overnight, primarily driven by the low boundary layer height. While the precursors may have formed elsewhere, it is likely that the organosulfates formed locally, as opposed to advection of organosulfate-containing particles to Atlanta, given the very low wind speed (<0.5 m/s) during these periods. The radical-initiated mechanism cannot explain the production of organosulfates overnight due to the lack of solar radiation required to form the sulfate radicals. Therefore, nocturnal organosulfate formation can likely be attributed to acid-catalyzed reactive uptake of the precursors. During AMIGAS both the particle size and temporal trends (Figures 3.8 & 3.9) demonstrate a relationship of increasing IEPOX-derived organosulfate with increasing *m/z* -195, an indicator of acidity. While the trends from ANARChE and AMIGAS are not in full agreement on the correlation between organosulfates and sulfuric acid (discussed in Section 3.6.3), it is important to note that nitric acid possibly contributed to the nocturnal aerosol acidity, as described above, with consistent trends during both studies (Figure 3.5). Further, particulate

IEPOX was detected during AMIGAS, including nighttime samples,[28] and its role in forming organosulfate species has been confirmed by smog chamber studies,[14] thus providing additional support for the hypothesized reactive-uptake of IEPOX in leading to the overnight formation of organosulfates.

In summary, the results from ANARChE and AMIGAS indicate that several formation mechanisms can contribute to the production of particulate organosulfate species in Atlanta. While further studies are necessary to better elucidate the conditions that favor a given formation pathway in the ambient atmosphere, the ATOFMS observations suggest that organosulfates form by the following atmospheric processes: During the daytime, isoprene is photochemically oxidized to IEPOX, with moderate organosulfate production from either a radical-initiated mechanism or acid-catalyzed reactive uptake. Since IEPOX is semivolatile and reactive uptake increases with aerosol water content,[22] it likely partitions to the aerosol phase to a greater extent as the RH increases and the temperature and boundary layer height decrease at night. Upon condensation, the acid-catalyzed mechanism likely dominates with subsequent particle-phase formation of organosulfate species. These results highlight the important roles of aqueous-phase processing and boundary layer stability in SOA formation.

3.5 Acknowledgements

The dissertation author was the primary researcher/author of this chapter. We gratefully acknowledge Stephanie Shaw and Eladio Knipping (EPRI) for coordinating the AMIGAS campaign. The authors thank the rest of the Prather group for extensive support throughout the studies. Additional assistance in Atlanta from Jerry Brown (ARA, Inc.) was appreciated during AMIGAS. Water soluble organic carbon measurements were provided by Xiaolu Zhang and Prof. Rodney Weber (Georgia Institute of Technology). Michele Sipin is acknowledged for assisting with data collection during ANARChE. The authors thank anonymous reviewers for insightful comments. ANARChE was supported by the University of Rochester EPA PM Center, Grant R827354. AMIGAS was funded by the Electric Power Research Institute. L. Hatch has been funded by a National Science Foundation Graduate Research Fellowship (2008-2011).

Chapter 3 is reproduced with permission from the American Chemical Society: Hatch, L.E.; Creamean, J.M.; Ault, A.P.; Surratt, J.D.; Chan, M.N.; Seinfeld, J.H.; Edgerton, E.S.; Su, Y.; Prather, K.A., Measurements of isoprene-derived organosulfates in ambient aerosols by

aerosol time-of-flight mass spectrometry, Part 2: Temporal variability & formation mechanisms**.** *Environ. Sci. Tech.*, **2011**, *45(20)*, 8648-8655.

3.6 Supporting Information

3.6.1 ATOFMS Measurements and Analysis.

For both the ANARChE and AMIGAS datasets considered here, some negative spectra displayed incorrect mass calibration in the mass range of interest (>100 *m/z*) due to instability in the mass spectrometer voltages. As a result, the majority (~ 90-95%) of particles containing organosulfates during AMIGAS (~50% during ANARChE) displayed a slight shift in *m/z* relative to the true value. Because the shift in *m/z* becomes more exaggerated at higher *m/z* due to the longer flight time in the TOF mass analyzer, the high-mass organosulfate peaks were impacted to a greater degree. In order to ensure data quality, a detailed analysis method was adopted for AMIGAS as follows. ART-2a clusters containing the proposed organosulfate markers were identified and each cluster was divided up by day. An average spectrum was obtained for each cluster on each day and the actual *m/z* (m/z_{actual}) of the peaks in question were identified by using known markers as an indication of the mass calibration. To determine mass spectral peak area as a function of time and/or particle size, the peak area search was performed on m/z_{actual} for each cluster on each day and the results from different clusters were combined accordingly. The ANARChE data was treated similarly, except the ART-2a clusters were treated intact and were not divided by day since the calibration issues were less severe than during AMIGAS.

3.6.2 Temporal trends of organosulfate markers.

The temporal profiles during AMIGAS of the organosulfate markers at *m/z* -215, -199, -155, and -153 are included in Figure 3.7. For the latter three ions, the diurnal trends are somewhat less definitive than *m/z* -215, however in general these markers track reasonably well, typically peaking overnight. Correlation plots between the markers can be found in Figure 2.7.

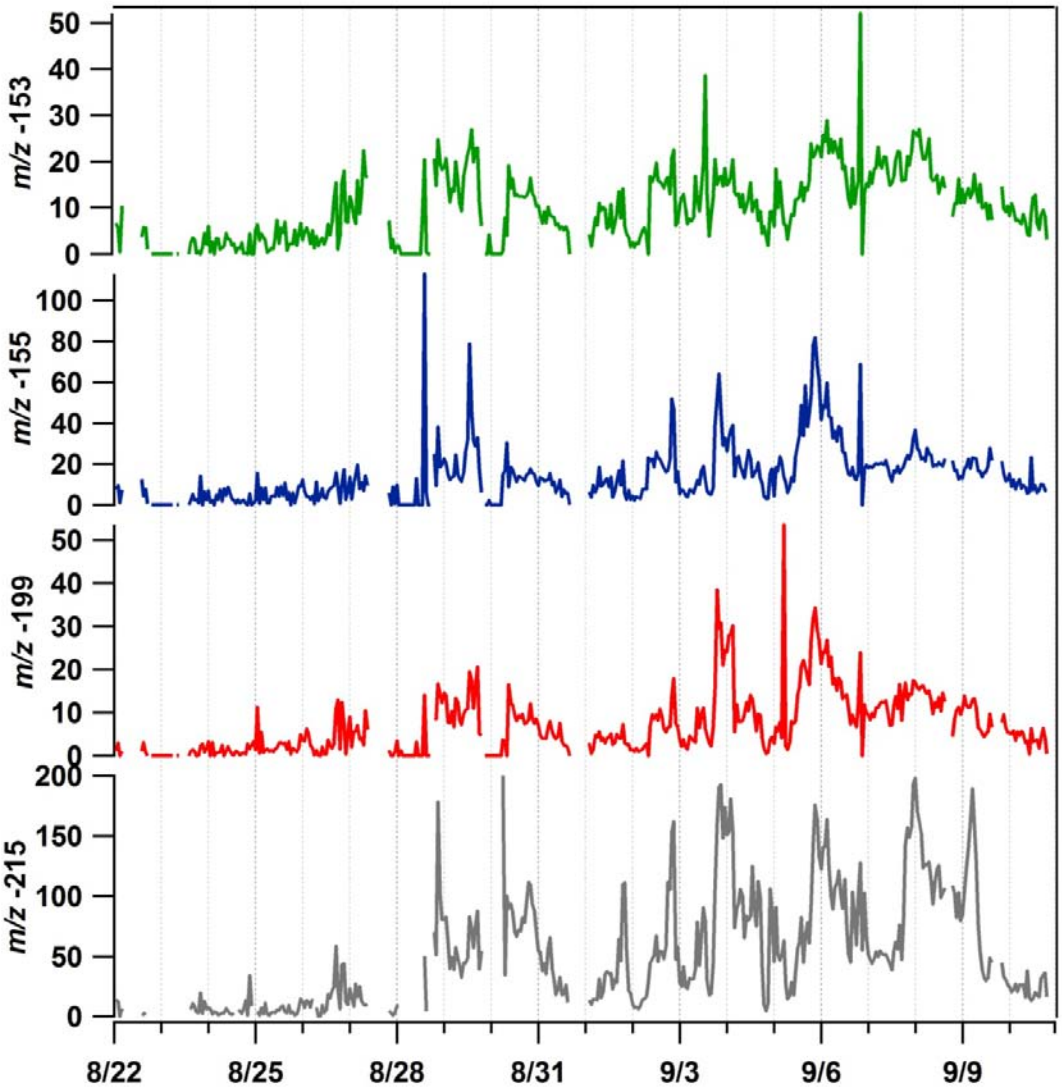

Figure 3.7 Hourly-averaged temporal variability in the absolute peak area of *m/z* -215 (gray), -199 (red), -155 (blue) and -153 (green) during AMIGAS.

3.6.3 Nocturnal acid-catalyzed organosulfate formation

The overnight formation of organosulfates observed in Atlanta is proposed to occur by acid-catalyzed reactive uptake, as the only other currently known formation mechanism requires radiation to form sulfate/bisulfate radicals.[11] While several observations seem to support this hypothesis, data from ANARChE and AMIGAS are not in full agreement. During AMIGAS, both the particle size and temporal trends demonstrate a relationship of increasing IEPOX-derived organosulfate with increasing *m/z* -195. The size distribution shows that the organosulfate and sulfuric acid concentrations increased as particle size decreased (R^2=0.83, Figure 3.8), consistent

with previous ATOFMS results that showed that particle phase acidity was highest at the smallest particle sizes.[45] Further, the correlation between these species in hourly time resolution is shown in Figure 3.9 for both daytime (6am – 6pm) and nighttime (6pm-6am) trends. A higher correlation was observed for the nighttime absolute peak area trend (R^2=0.56) than the daytime trend (R^2=0.36), possibly indicating a stronger relationship between acidity and organosulfate formation overnight. Further, the segregation of the day and night trends in the correlation plot, with a higher slope occurring overnight (1.13 vs. 0.66), suggests that organosulfate production may be driven largely by IEPOX uptake, as the increase in IEPOX gas-to-particle partitioning at night led to increased organosulfate formation for a given acidity level than would occur during the daytime under a reduced uptake regime.

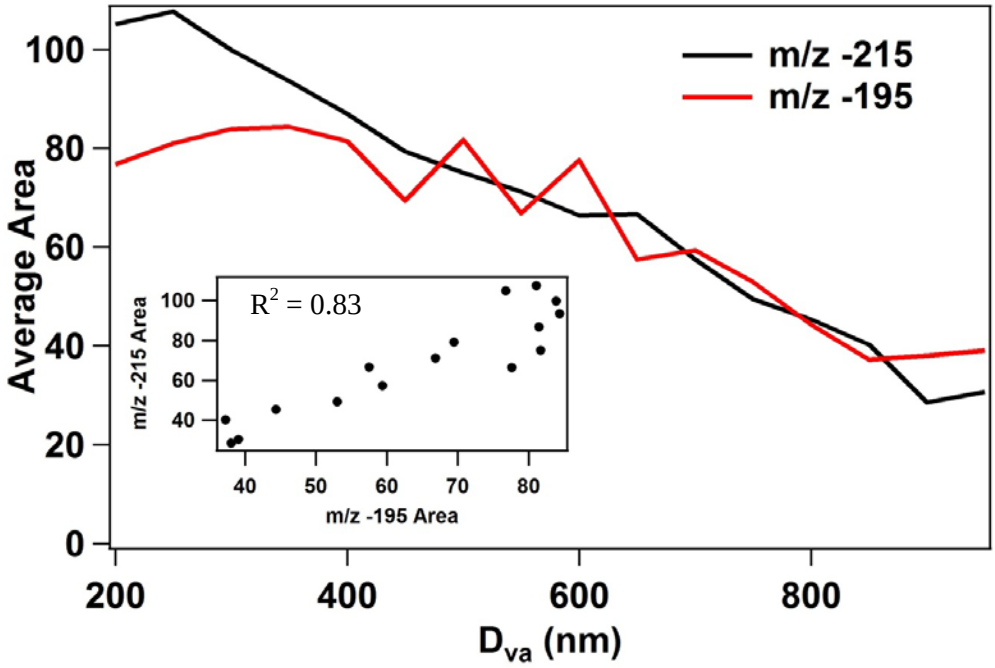

Figure 3.8 Size-dependence of *m/z* -215 and -195 absolute peak areas averaged over 50 nm size bins for the AMIGAS dataset. The inset shows the correlation between the two species as a function of size (R^2=0.83).

In contrast to AMIGAS, the temporal trends in the absolute areas of *m/z* -215 and -195 during ANARChE are anti-correlated (Figure 3.10), with *m/z* -195 peaking in the afternoon before the overnight increase in *m/z* -215. However, in this case, there are often increases in SO_2 concurrent with the increase in *m/z* -215, which perhaps contributed to the higher levels of organosulfates observed during periods of low *m/z* -195 peak area.

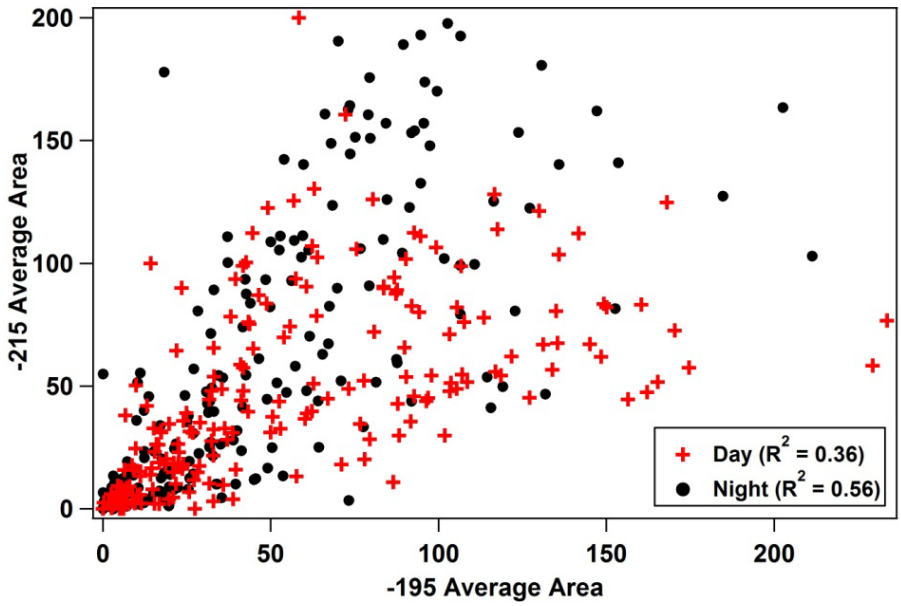

Figure 3.9 Daytime (6am-6pm; red) and nighttime (6pm-6am; black) correlation plots of the hourly-averaged absolute peak areas of *m/z* -215 (IEPOX-OS) and *m/z* -195 ($H_2SO_4HSO_4^-$) during AMIGAS.

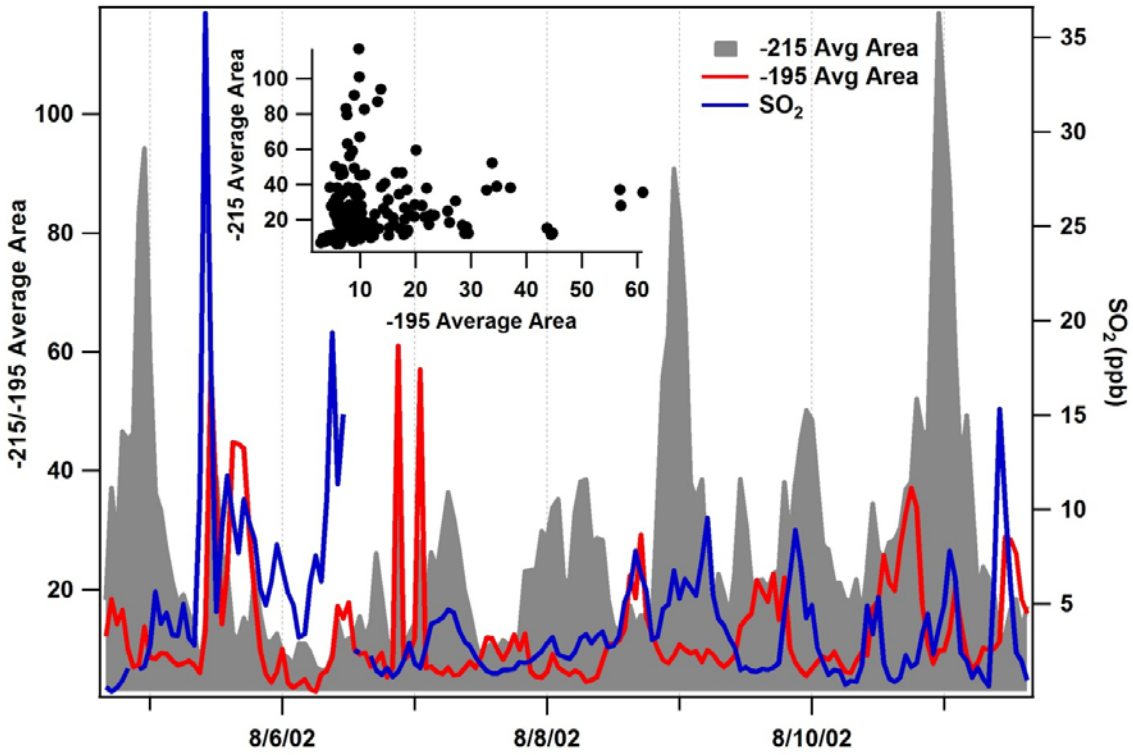

Figure 3.10 Temporal trends during ANARChE of the hourly-averged absolute area of *m/z* -215, m/z -195, and SO_2. The inset shows the correlation between *m/z* -215 and -195.

3.7 References:

1. Jacobson, M. C.; Hansson, H. C.; Noone, K. J.; Charlson, R. J., Organic atmospheric aerosols: Review and state of the science. *Rev. Geophys.* **2000,** *38*, (2), 267-294.

2. Hallquist, M.; Wenger, J. C.; Baltensperger, U.; Rudich, Y.; Simpson, D.; Claeys, M.; Dommen, J.; Donahue, N. M.; George, C.; Goldstein, A. H.; Hamilton, J. F.; Herrmann, H.; Hoffmann, T.; Iinuma, Y.; Jang, M.; Jenkin, M. E.; Jimenez, J. L.; Kiendler-Scharr, A.; Maenhaut, W.; McFiggans, G.; Mentel, T. F.; Monod, A.; Prevot, A. S. H.; Seinfeld, J. H.; Surratt, J. D.; Szmigielski, R.; Wildt, J., The formation, properties and impact of secondary organic aerosol: current and emerging issues. *Atmos. Chem. Phys.* **2009,** *9*, (14), 5155-5236.

3. Volkamer, R.; Martini, F. S.; Molina, L. T.; Salcedo, D.; Jimenez, J. L.; Molina, M. J., A missing sink for gas-phase glyoxal in Mexico City: Formation of secondary organic aerosol. *Geophys. Res. Lett.* **2007,** *34*, (19).

4. Lewis, C. W.; Klouda, G. A.; Ellenson, W. D., Radiocarbon measurement of the biogenic contribution to summertime PM-2.5 ambient aerosol in Nashville, TN. *Atmos. Environ.* **2004,** *38*, (35), 6053-6061.

5. Carlton, A. G.; Wiedinmyer, C.; Kroll, J. H., A review of Secondary Organic Aerosol (SOA) formation from isoprene. *Atmos. Chem. Phys.* **2009,** *9*, (14), 4987-5005.

6. Goldstein, A. H.; Koven, C. D.; Heald, C. L.; Fung, I. Y., Biogenic carbon and anthropogenic pollutants combine to form a cooling haze over the southeastern United States. *Proc. Natl. Acad. Sci. USA* **2009,** *106*, (22), 8835-8840.

7. Carlton, A. G.; Pinder, R. W.; Bhave, P. V.; Pouliot, G. A., To What Extent Can Biogenic SOA be Controlled? *Environ. Sci. Technol.* **2010,** *44*, (9), 3376-3380.

8. Hoyle, C. R.; Boy, M.; Donahue, N. M.; Fry, J. L.; Glasius, M.; Guenther, A.; Hallar, A. G.; Hartz, K. H.; Petters, M. D.; Petaja, T.; Rosenoern, T.; Sullivan, A. P., A review of the anthropogenic influence on biogenic secondary organic aerosol. *Atmos. Chem. Phys.* **2011,** *11*, (1), 321-343.

9. Hewitt, C. N., The atmospheric chemistry of sulphur and nitrogen in power station plumes. *Atmos. Environ.* **2001,** *35*, (7), 1155-1170.

10. Surratt, J. D.; Kroll, J. H.; Kleindienst, T. E.; Edney, E. O.; Claeys, M.; Sorooshian, A.; Ng, N. L.; Offenberg, J. H.; Lewandowski, M.; Jaoui, M.; Flagan, R. C.; Seinfeld, J. H., Evidence for organosulfates in secondary organic aerosol. *Environ. Sci. Technol.* **2007,** *41*, (2), 517-527.

11. Noziere, B.; Ekstrom, S.; Alsberg, T.; Holmstrom, S., Radical-initiated formation of organosulfates and surfactants in atmospheric aerosols. *Geophys. Res. Lett.* **2010,** *37*.

12. Perri, M. J.; Lim, Y. B.; Seitzinger, S. P.; Turpin, B. J., Organosulfates from glycolaldehyde in aqueous aerosols and clouds: Laboratory studies. *Atmos. Environ.* **2010,** *44*, (21-22), 2658-2664.

13. Rudzinski, K. J., Degradation of isoprene in the presence of sulphoxy radical anions. *Journal of Atmospheric Chemistry* **2004,** *48*, (2), 191-216.

14. Surratt, J. D.; Chan, A. W. H.; Eddingsaas, N. C.; Chan, M. N.; Loza, C. L.; Kwan, A. J.; Hersey, S. P.; Flagan, R. C.; Wennberg, P. O.; Seinfeld, J. H., Reactive intermediates revealed in secondary organic aerosol formation from isoprene. *Proc. Natl. Acad. Sci. USA* **2010,** *107*, (15), 6640-6645.

15. Iinuma, Y.; Boge, O.; Kahnt, A.; Herrmann, H., Laboratory chamber studies on the formation of organosulfates from reactive uptake of monoterpene oxides. *PCCP* **2009,** *11*, (36), 7985-7997.

16. Minerath, E. C.; Casale, M. T.; Elrod, M. J., Kinetics feasibility study of alcohol sulfate esterification reactions in tropospheric aerosols. *Environ. Sci. Technol.* **2008,** *42*, (12), 4410-4415.

17. Galloway, M. M.; Chhabra, P. S.; Chan, A. W. H.; Surratt, J. D.; Flagan, R. C.; Seinfeld, J. H.; Keutsch, F. N., Glyoxal uptake on ammonium sulphate seed aerosol: reaction products and reversibility of uptake under dark and irradiated conditions. *Atmos. Chem. Phys.* **2009,** *9*, (10), 3331-3345.

18. Minerath, E. C.; Schultz, M. P.; Elrod, M. J., Kinetics of the Reactions of Isoprene-Derived Epoxides in Model Tropospheric Aerosol Solutions. *Environ. Sci. Technol.* **2009,** *43*, (21), 8133-8139.

19. Paulot, F.; Crounse, J. D.; Kjaergaard, H. G.; Kroll, J. H.; Seinfeld, J. H.; Wennberg, P. O., Isoprene photooxidation: new insights into the production of acids and organic nitrates. *Atmos. Chem. Phys.* **2009,** *9*, (4), 1479-1501.

20. Wang, W.; Kourtchev, I.; Graham, B.; Cafmeyer, J.; Maenhaut, W.; Claeys, M., Characterization of oxygenated derivatives of isoprene related to 2-methyltetrols in Amazonian aerosols using trimethylsilylation and gas chromatography/ion trap mass spectrometry. *Rapid Commun. Mass Spectrom.* **2005,** *19*, (10), 1343-1351.

21. Iinuma, Y.; Muller, C.; Berndt, T.; Boge, O.; Claeys, M.; Herrmann, H., Evidence for the existence of organosulfates from beta-pinene ozonolysis in ambient secondary organic aerosol. *Environ. Sci. Technol.* **2007,** *41*, (19), 6678-6683.

22. Eddingsaas, N. C.; VanderVelde, D. G.; Wennberg, P. O., Kinetics and Products of the Acid-Catalyzed Ring-Opening of Atmospherically Relevant Butyl Epoxy Alcohols. *J. Phys. Chem. A* **2010,** *114*, (31), 8106-8113.

23. Hatch, L. E.; Creamean, J. M.; Ault, A. P.; Surratt, J. D.; Chan, M. N.; Seinfeld, J. H.; Edgerton, E. S.; Su, Y.; Prather, K. A., Measurements of Isoprene-Derived Organosulfates in Ambient Aerosols by Aerosol Time-of-Flight Mass Spectometry - Part 1: Single Particle Atmospheric Observations in Atlanta. *Environ. Sci. Technol.* **2011,** *45*, (12), 5105 - 5111.

24. Hansen, D. A.; Edgerton, E. S.; Hartsell, B. E.; Jansen, J. J.; Kandasamy, N.; Hidy, G. M.; Blanchard, C. L., The Southeastern Aerosol Research and Characterization Study: Part 1-Overview. *J. Air Waste Manage. Assoc.* **2003,** *53*, (12), 1460-1471.

25. Gard, E.; Mayer, J. E.; Morrical, B. D.; Dienes, T.; Fergenson, D. P.; Prather, K. A., Real-time analysis of individual atmospheric aerosol particles: Design and performance of a portable ATOFMS. *Anal. Chem.* **1997,** *69*, (20), 4083-4091.

26. Edgerton, E. S.; Hartsell, B. E.; Saylor, R. D.; Jansen, J. J.; Hansen, D. A.; Hidy, G. M., The Southeastern Aerosol Research and Characterization Study, part 3: Continuous measurements of fine particulate matter mass and composition. *J. Air Waste Manage. Assoc.* **2006,** *56*, (9), 1325-1341.

27. Hennigan, C. J.; Bergin, M. H.; Russell, A. G.; Nenes, A.; Weber, R. J., Gas/particle partitioning of water-soluble organic aerosol in Atlanta. *Atmos. Chem. Phys.* **2009,** *9*, (11), 3613-3628.

28. Chan, M. N.; Surratt, J. D.; Claeys, M.; Edgerton, E. S.; Tanner, R. L.; Shaw, S. L.; Zheng, M.; Knipping, E. M.; Eddingsaas, N. C.; Wennberg, P. O.; Seinfeld, J. H., Characterization and quantification of isoprene-derived epoxydiols in ambient aerosol in the southeastern United States. *Environ. Sci. Technol.* **2010,** *44*, (12), 4590-4596.

29. Beven, J. L. K., T.B., National Hurricane Center Tropical Cyclone Report: Hurricane Gustav. **2009**.

30. Brown, D. P. K., T., National Hurricane Center Tropical Cyclone Report: Hurricane Hanna. **2008**.

31. Beven, J. L., National Hurricane Center Tropical Cyclone Report: Tropical Storm Bertha. **2002**.

32. Durre, I.; Vose, R. S.; Wuertz, D. B., Overview of the Integrated Global Radiosonde Archive. *J. Clim.* **2006,** *19*, (1), 53-68.

33. Duncan, B. N.; Stelson, A. W.; Kiang, C. S., Estimated Contribution of Power-Plants to Ambient Nitrogen-Oxides Measured in Atlanta, GA in August 1992. *Atmos. Environ.* **1995,** *29*, (21), 3043-3054.

34. Neubauer, K. R.; Johnston, M. V.; Wexler, A. S., Humidity effects on the mass spectra of single aerosol particles. *Atmos. Environ.* **1998,** *32*, (14-15), 2521-2529.

35. Surratt, J. D.; Lewandowski, M.; Offenberg, J. H.; Jaoui, M.; Kleindienst, T. E.; Edney, E. O.; Seinfeld, J. H., Effect of acidity on secondary organic aerosol formation from isoprene. *Environ. Sci. Technol.* **2007,** *41*, (15), 5363-5369.

36. Chang, W. L.; Bhave, P. V.; Brown, S. S.; Riemer, N.; Stutz, J.; Dabdub, D., Heterogeneous Atmospheric Chemistry, Ambient Measurements, and Model Calculations of N2O5: A Review. *Aerosol Sci. Technol.* **2011,** *45*, (6), 665-695.

37. Brown, S. S.; Ryerson, T. B.; Wollny, A. G.; Brock, C. A.; Peltier, R.; Sullivan, A. P.; Weber, R. J.; Dube, W. P.; Trainer, M.; Meagher, J. F.; Fehsenfeld, F. C.; Ravishankara, A. R.,

Variability in nocturnal nitrogen oxide processing and its role in regional air quality. *Science* **2006,** *311*, (5757), 67-70.

38. Rollins, A. W.; Kiendler-Scharr, A.; Fry, J. L.; Brauers, T.; Brown, S. S.; Dorn, H. P.; Dube, W. P.; Fuchs, H.; Mensah, A.; Mentel, T. F.; Rohrer, F.; Tillmann, R.; Wegener, R.; Wooldridge, P. J.; Cohen, R. C., Isoprene oxidation by nitrate radical: alkyl nitrate and secondary organic aerosol yields. *Atmos. Chem. Phys.* **2009,** *9*, (18), 6685-6703.

39. Darer, A. I.; Cole-Filipiak, N. C.; O'Connor, A. E.; Elrod, M. J., Formation and Stability of Atmospherically Relevant Isoprene-Derived Organosulfates and Organonitrates. **2011,** *45*, (5), 1895 - 1902.

40. Surratt, J. D.; Gomez-Gonzalez, Y.; Chan, A. W. H.; Vermeylen, R.; Shahgholi, M.; Kleindienst, T. E.; Edney, E. O.; Offenberg, J. H.; Lewandowski, M.; Jaoui, M.; Maenhaut, W.; Claeys, M.; Flagan, R. C.; Seinfeld, J. H., Organosulfate formation in biogenic secondary organic aerosol. *J. Phys. Chem. A* **2008,** *112*, (36), 8345-8378.

41. Chameides, W. L.; Lindsay, R. W.; Richardson, J.; Kiang, C. S., The role of biogenic hydrocarbons in urban photochemical smog - Atlanta as a case-study *Science* **1988,** *241*, (4872), 1473-1475.

42. Paulot, F.; Crounse, J. D.; Kjaergaard, H. G.; Kurten, A.; St Clair, J. M.; Seinfeld, J. H.; Wennberg, P. O., Unexpected Epoxide Formation in the Gas-Phase Photooxidation of Isoprene. *Science* **2009,** *325*, (5941), 730-733.

43. Blanchard, C. L.; Hidy, G. M.; Tanenbaum, S.; Edgerton, E. S., NMOC, ozone, and organic aerosol in the southeastern United States, 1999-2007: 3. Origins of organic aerosol in Atlanta, Georgia, and surrounding areas. Atmos. Environ. 2011, 45, (6), 1291-1302.

44. Pratt, K. A.; Prather, K. A., Aircraft measurements of vertical profiles of aerosol mixing states. J. Geophys. Res. 2010, 115.

45. Denkenberger, K. A.; Moffet, R. C.; Holecek, J. C.; Rebotier, T. P.; Prather, K. A., Real-time, single-particle measurements of oligomers in aged ambient aerosol particles. Environ. Sci. Technol. 2007, 41, (15), 5439-5446.

4 Impacts of aerosol aging on laser desorption/ionization in single-particle mass spectrometers

4.1 Abstract

Single-particle mass spectrometry has been widely applied to characterize the chemical mixing state of ambient aerosol particles. However, the laser desorption/ionization (LDI) method utilized in these instruments is known to be affected by artifacts occurring during particle ablation and ionization, effects that remain poorly characterized for complex atmospheric particles. During the 2005 Study of Organic Aerosols in Riverside (SOAR), a thermodenuder was used to heat ambient aerosol in several temperature steps up to 230 ˚C; the residual aerosol particles were sampled by an aerosol mass spectrometer (AMS) and a single-particle aerosol time-of-flight mass spectrometer (ATOFMS). Removal of the secondary species (e.g., ammonium nitrate, organics) through heating permitted assessment of the change in ionization patterns as the composition changed for a given particle type. It was observed that a coating of secondary species can reduce the ionization efficiency by changing the degree of laser absorption, which significantly impacted the measured peak areas. Non-volatile aerosol components were used as internal standards to correct for this LDI effect, which subsequently produced strong agreement between the corrected ATOFMS ion peak areas and the AMS measurements of the same species. Covariance mapping of the major aerosol constituents was further utilized to probe matrix effects caused by collisions during the ionization process. This analysis demonstrated that these effects may not be constant as particles acquire high levels of secondary species (effectively the reciprocal of heating) that may alter the collision dynamics occurring within the LDI plume. This work represents the first systematic assessment of ionization matrix effects in the analysis of ambient atmospheric aerosol particles by single particle mass spectrometry.

4.2 Introduction

Single-particle mass spectrometry (SPMS) is a prominent analytical tool used to probe the mixing state (chemical associations) of aerosol particles in the atmosphere.[1,2] The real-time SPMS instruments typically utilize an ultraviolet (UV) laser to desorb and ionize both refractory and non-refractory aerosol material from single particles in a single step, with subsequent analysis of ionized components by time-of-flight mass spectrometers, yielding a full mass spectrum per

particle. However, there are several known ionization effects that can complicate the mass spectral interpretation, including shot-to-shot variability due to laser inhomogeneities[3] and matrix effects caused by reactions within the laser plume.[4,5]

Many aspects of the ion formation process during LDI have been probed in laboratory studies. The effects of laser wavelength and energy in the ablation process have been reported for a number of studies using laboratory-generated aerosol particles.[3,6-8] Molecular dynamics simulations of the laser disintegration for picosecond laser pulses found that aerosol morphology can significantly influence particle ablation.[9,10] Additional experimental work has demonstrated that particle morphology can also influence the resulting mass spectra.[11,12] The laser ablation process has been studied for matrix-assisted laser desorption ionization (MALDI). As described by Knochenmuss,[13] ablation and primary ionization occur during the laser pulse (several nanoseconds for the Nd:YAG laser utilized in this work), with subsequent plume expansion and secondary reactions occurring over microseconds. These reactions can significantly influence the ion distribution in the resulting mass spectrum. Reinard and Johnston[14] utilized covariance matrices to characterize the ionization mechanism using simple mixtures of common aerosol components. They determined that the desorption/ionization process likely proceeds through desorption of neutral species, with subsequent photoionization producing cations and electrons; formation of anions occurs through electron capture by components with high electron affinities. Reilly *et al.*[5] characterized the effect of plume reactions using soil samples from the National Institute of Standards and Technology Standard Reference Material archive and determined that extensive charge transfer can occur. In these reactions, the component with the lowest ionization potential (IP) is favored, thereby suppressing the formation of components with higher IPs in positive ion mass spectra.[4,5] The resulting mass spectral ion intensities are, therefore, dependent on the other chemical components present in the particle (the matrix). As a result of these matrix effects, a trace particle constituent with a low IP can dominate the resulting spectrum due to these charge-transfer processes. Similar processes occur for negative ions, where the species with the highest electron affinity are detected most easily and appear to be in higher abundance.[14]

Several studies have shown that one can account for these matrix effects by determining relative sensitivity factors to reconstruct the actual particle composition from mass spectral ion peak areas.[4,15] Several studies have also successfully quantified SPMS data by scaling peak areas of ambient particles using collocated quantitative measurements[16-18] or laboratory calibrations.[19] However, it is not clear if and how the LDI process and resulting mass spectra change as particles

undergo significant processing (aging) during their atmospheric lifetime, acquiring semi-volatile species, such as ammonium sulfate/nitrate and many organics, via condensation, coagulation, and heterogeneous reactions.[20] While laboratory studies are essential for the systematic characterization of the ion formation mechanism in SPMS instruments, atmospheric particles display vastly more complex composition and morphologies. Therefore, it is important to attempt to characterize ionization effects in ambient particles to account for composition changes with aging to help improve the quantitative capabilities of SPMS instruments.

In this work, SPMS measurements were conducted using an aerosol time-of-flight mass spectrometer (ATOFMS) in the highly polluted urban environment of Riverside, CA, a receptor site for emissions from Los Angeles and extensive agricultural operations.[21] A thermodenuder (TD) was used upstream of the ATOFMS inlet to systematically remove the semi-volatile constituents through heating.[22-24] The TD system used herein was developed by Huffman and coworkers to characterize the volatility of aerosol particles; it consists of a heated region to evaporate semi-volatile components followed by a charcoal denuder to prevent re-condensation.[25] The heated section steps through several temperatures up to 230 ºC, thereby removing different particle constituents as a function of their volatility. For example, more volatile constituents (e.g., ammonium nitrate) evaporate at low temperatures, leaving behind less volatile species. In this way, changes in ionization could be assessed as different chemical components were systematically removed from the individual particles. Further, an aerosol mass spectrometer (AMS) simultaneously measured the aerosol residuals from the TD, thereby providing an independent and quantitative assessment of the changes in aerosol composition with heating.

4.3 Experimental

Measurements of thermally-conditioned aerosol particles were conducted during the first Study of Organic Aerosols in Riverside (SOAR-1) campaign in Riverside, CA; SOAR-1 has been previously described in detail.[26,27] Data presented herein represent measurements conducted on August 12, 2005 only (0:00-24:00 PST). Single particle analysis was performed using the ground-based prototype of the aircraft-ATOFMS, which has been described in detail previously;[28] a brief summary is provided here. Aerosols (100 – 1000 nm) entered the instrument via an aerodynamic lens inlet and were accelerated to a size-dependent terminal velocity. In the particle sizing region, aerosols traverse (and scatter light from) two 532 nm continuous wave lasers yielding the particle velocity, which is converted to aerodynamic diameter via calibration with polystyrene latex spheres of known diameter. The individual particles were then desorbed and

ionized at 266 nm using a Q-switched Nd:YAG laser; the laser power was ~0.9-1.0 mJ throughout the study.

The TD was used to remove semi-volatile constituents from ambient particles with the heated portion stepping through 7 temperatures from 54 – 230 ºC.[25] Sampling switched between unheated and heated channels every ten minutes; a full cycle was completed in 160 minutes and thus each TD temperature (Figure 4.1a) was sampled periodically (~8x) throughout the day. The aerosol residuals were sampled simultaneously by ATOFMS and an AMS (C-ToF-AMS).[29] The AMS data was analyzed similar to previous TD-AMS studies.[22,23] For ATOFMS data analysis, all sampling periods at the same temperature were merged to bolster particle number statistics. Data analysis was performed by importing single-particle mass spectra into Matlab (The MathWorks, Inc.) using the YAADA toolkit.[30] Particles were clustered based on similarities in mass spectral peak identities and intensities using the ART-2a adaptive resonance theory method[31] with a vigilance factor of 0.8, learning rate of 0.05, and 20 iterations. Similar ART-2a clusters were identified as different particle types based on the predominant ion peaks or known source signatures.

4.4 Results & Discussion

4.4.1 General Ambient Particle Observations

The size-resolved chemical mixing state of individual particles measured by ATOFMS at ambient temperature during SOAR-1 has been summarized by Qin *et al.*[27] The relative number fraction of each particle type identified during SOAR-1 is shown in Figure 4.1a for each TD temperature from ambient temperature to 230 ºC. The predominant particle type was classified as organic carbon (OC), comprising up to ~70% of the detected particles by number. The positive ion mass spectral pattern (Figure 4.1b) of the OC particle type shows organic fragments $^{27}C_2H_3^+$, $^{37}C_3H^+$, and $^{43}C_2H_3O^+$ with smaller contributions from elemental carbon markers, C_n^+ (n=1-3) (Figure 4.1b). As shown in the average mass spectrum, unheated OC particles were internally mixed with ammonium, amines, nitrate, and sulfate (Figure 4.1b). The high abundance of these secondary species and oxidized OC reflects the highly aged nature of aerosol particles in Riverside, as well as the extensive photochemical processing occurring during the summertime leading to secondary organic aerosol formation.[32] The second most abundant submicron particle type (up to ~ 11% by number) was classified as Vanadium-rich, due to the strong ion peaks attributed to $^{51}V^+$ and $^{67}VO^+$ (Figure 4.1c). Particles enriched in vanadium have been observed in

emissions from ships[33,34] and vehicles.[35-37] Similar to the OC particles, these particles were also internally mixed with organic markers and ammonium/aminium nitrate/sulfate salts, suggesting transport from the coast.[38] Other minor particle classes included biomass burning, a mixed elemental carbon (EC)-OC class, EC, aromatic (characterized by markers of polycyclic aromatic hydrocarbons), amine particles (characterized by a dominant $^{86}(C_2H_5)_2NCH_2^+$ ion marker), dust, and sea salt. All of these particle types were strongly enriched in nitrate and sulfate due to atmospheric aging, as discussed by Qin *et al.*[27] An extensive discussion of the changes in each particle type with heating during SOAR-2 (fall 2005) has been given by Pratt and Prather.[24]

From Figure 4.1a, it is clear that the relative number fractions of particle types did not change dramatically with heating during SOAR-1 (the relevant changes will be described below). However, the fraction of hit particles (hit efficiency) nearly doubled, increasing from ~8% at ambient temperature to ~14% at 230˚ C. This indicates that the existing particle types became easier to ablate following heating and removal of secondary coatings. For comparison, the hit efficiency of polystyrene latex spheres used as calibration standards was ~20% during SOAR-1. The hit efficiency—defined as the number of particles that generated a mass spectrum ("hit") divided by the total number of particles that were sized (hit/hit+missed)—is a function of the inlet transmission efficiency, laser alignment, and the degree of laser absorption at 266 nm by particles within the source region.[39] The laser alignment was not adjusted during the measurement period, and thus such effects can be neglected. In contrast, the transmission efficiency can be influenced by particle shape, which possibly changed and became more fractal/irregular as secondary coatings were removed with increasing temperature. However, non-spherical particles would experience greater divergence in the aerodynamic lens,[40,41] and subsequent pumping chambers, which would degrade the transmission efficiency and thereby reduce the hit efficiency, rather than enhance it. Therefore, the increase in the fraction of hit particles can be predominantly attributed changes in laser-particle interactions, consistent with previous ATOFMS studies of ambient aerosols have attributed changes in particle hit percentages to changes in LDI laser absorption due to particle aging.[16,18,42] The changes observed herein were likely due to enhanced absorption of the laser pulse following removal of secondary coatings and water (generally referred to as LDI efficiency herein), and will be explored in more detail in the following sections.

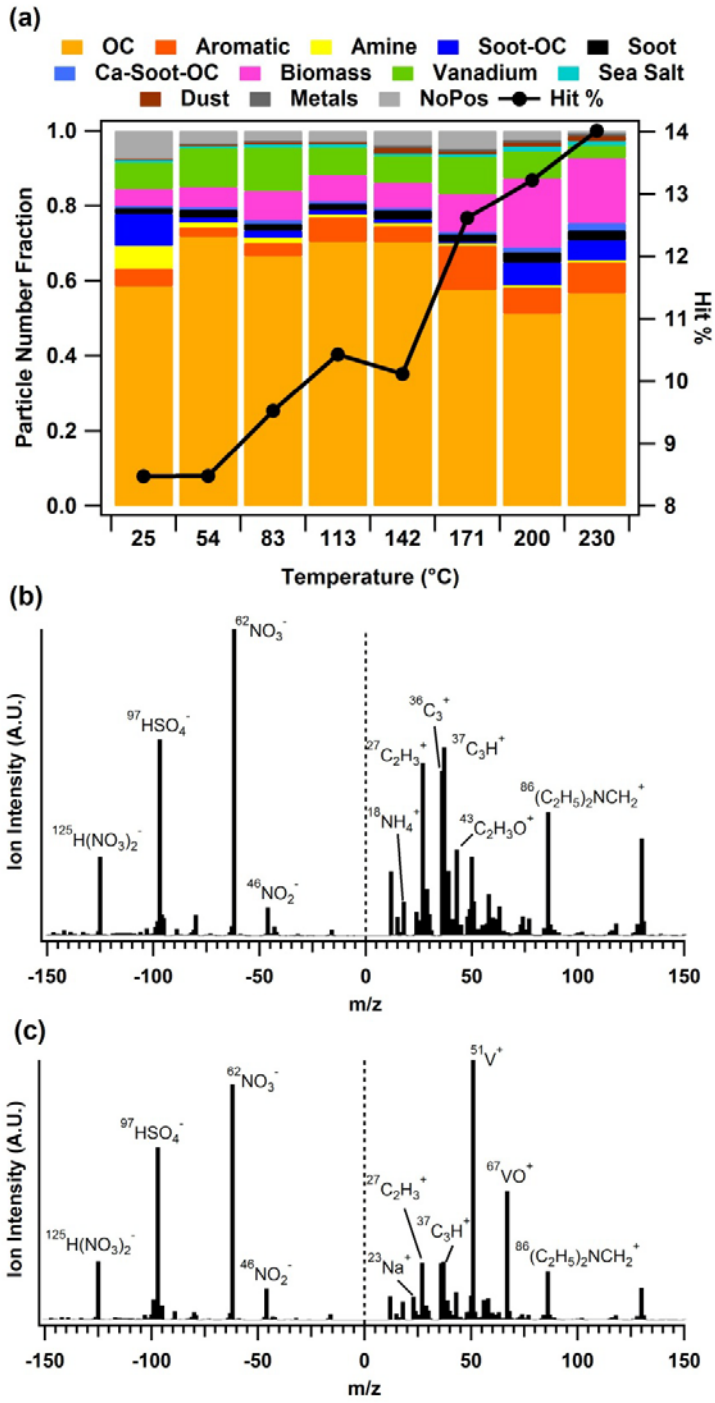

Figure 4.1 (a) Number fraction of particle classes at each thermodenuder temperature. The black trace represents the fraction of hit particles: hit/(hit+missed). (b) Average mass spectrum of unheated organic carbon particles. (c) Average mass spectrum of unheated vanadium-rich particles.

The changes in the LDI process due to aging were further probed by interpreting the trends in ion peak areas of individual particle types measured by ATOFMS. This study of thermally-conditioned ambient aerosols provides a unique opportunity to systematically examine the changes in LDI efficiency that occurred concurrently with the removal of secondary species. In this work, we focused on the OC and vanadium particle types because they were the most abundant and therefore provided the best statistics at all temperatures. In addition, these particle types also provide an opportunity to compare the ionization effects for metal-containing particles compared to those without metal species. We first discuss the observed changes in particle ablation/ionization inferred from the trends in ion peak intensities with heating, followed by a discussion of possible changes in collision-induced matrix effects.

4.4.2 Variations in LDI Efficiency & Matrix Effects with Particle Age

Atmospheric processing can lead to dramatic changes in the composition of a given particle and therefore the chemical matrix present during the ionization process. To accurately relate SPMS ion peak areas measured in ambient particles to the actual species concentration, a better understanding of the ionization process and matrix behavior is needed. To this end, the changes in ATOFMS ion peak areas measured at increasing TD temperatures (a proxy for decreasing particle age) were compared to the collocated AMS, which simultaneously sampled the aerosol residuals from the TD. For each instrument, heated particles were referenced to the unheated case, yielding the species' "fraction remaining" as a function of temperature ("thermogram"). The AMS data were used as an independent and quantitative measure of the fraction of the *non-refractory* mass remaining at each temperature, which is shown as the black thermograms in Figures 4.2 and 4.4. In the ATOFMS data, large deviations were observed in comparison to the AMS measurements when the traditional SPMS absolute and relative ion peak area metrics were used in the analysis. These deviations were used to better understand how the LDI process changed for two different ambient particle types (OC and Vanadium) significantly coated by secondary species in the eastern LA basin. Based on this study, an alternative approach for utilizing ion peak areas is proposed to correct for the ATOFMS biases in order to ultimately improve quantification via SPMS.

4.4.2.1 Organic Carbon Particles

4.4.2.1.1 LDI Efficiency

For the secondary species of interest herein (sulfate, nitrate, ammonium, amines, organics), the OC particle type likely contains predominantly non-refractory forms (e.g., ammonium nitrate/sulfate) that will evaporate at the operating temperatures of the TD (up to 230 ºC). The absence of metals in the OC spectrum (Figure 4.1b) suggests that non-volatile salts (e.g., sodium nitrate) were likely negligible in these particles. The OC particle type is therefore an ideal system for comparison with the AMS data because the volatility trends should be similar for these two instruments.

The single-particle absolute peak area (APA) denotes the raw intensity of each ion marker averaged over all particles in a given class at each TD temperature. APA has been used in a number of prior SPMS studies.[e.g.,17-19,43] Figure 4.2 shows the thermograms calculated using APAs for the ion markers of sulfate ($^{97}HSO_4^-$), nitrate ($^{62}NO_3^-$), ammonium ($^{18}NH_4^+$), amines ($^{86}(C_2H_5)_2NCH_2^+$), and organic carbon ($^{27}C_2H_3^+$ as a representative marker). It is apparent that the APA fractions remaining (solid, colored lines) for all species are significantly higher than the AMS thermograms at all temperatures. In particular, note that the ion peak area actually *increased* with temperature for several of these ion markers (sulfate, ammonium, OC). In addition, the ion intensity of the non-volatile EC marker ($^{36}C_3^+$) and the average integrated (total) positive and negative ion intensity per particle were all observed to increase with temperature (Figure 4.2f). These trends are only possible if: (1) the particles had more material/mass available to form ions (e.g., by larger particles shrinking into the detectable size range, thus increasing the average particle size) or (2) the ion yield per particle increased due to changes in absorption or ablation/ionization efficiency. The contribution from shrinking supermicron OC particles was likely minor since the AMS and ATOFMS utilized herein have similar aerodynamic lens inlets and the AMS mass fractions for each species predominantly decreased with increasing temperature, as expected with the removal of semi-volatile components (Figure 4.2). Further, the median size of the OC particles, as measured by ATOFMS, decreased by 56 nm from ambient temperature to 171 ºC, as shown in Figure 4.3. Note, however, that the median size is biased by the transmission of the aerodynamic lens inlet. The transmission efficiency of the ATOFMS utilized herein drops off steeply below 200 nm (D_{va}),[28] and thus the particles likely shrank to an even greater extent. Because the particles shrank with heating, an increase in overall particle mass can be ruled out, implying that the ion yield increased following heating. This is supported by the fact that the ion intensity increased for both positive and negative ion markers (e.g., $^{97}HSO_4^-$, $^{36}C_3^+$) and considering that charge-transfer induced matrix effects are largely decoupled

once positive and negative ions form. Therefore, the change in laser-particle interactions impacted the entire particle, rather than just individual species. This explanation is consistent with the observed increase in hit efficiency with temperature described above.

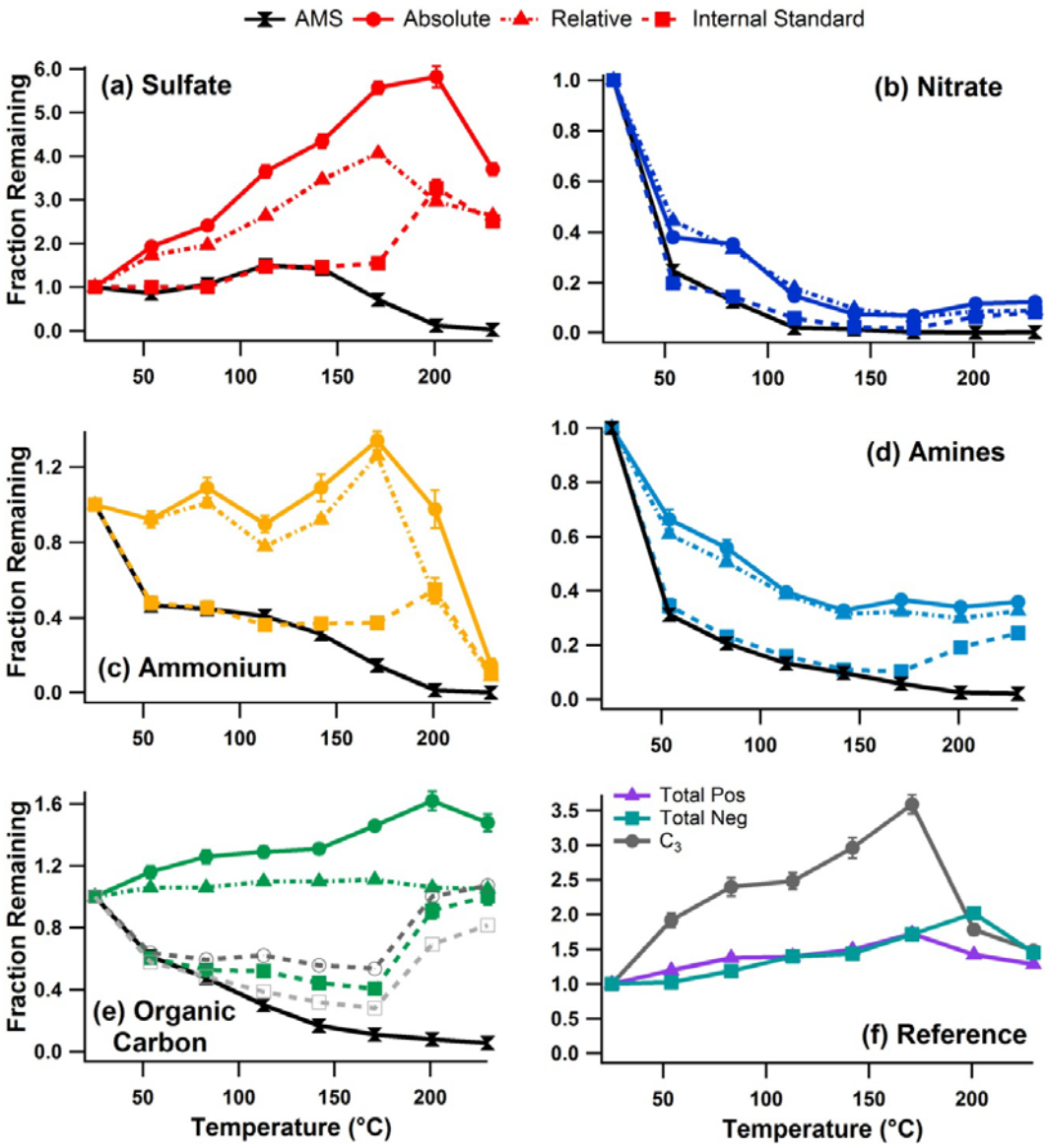

Figure 4.2 Thermograms of the organic carbon particle type for several aerosol constituents demonstrating the different peak area metrics for ATOFMS data (colors) compared to AMS (black). The ATOFMS ion peaks represented in each panel are as follows: (a) $^{97}HSO_4^-$; (b) $^{62}NO_3^-$, (c) $^{18}NH_4^+$, (d) $^{86}(C_2H_5)_2NCH_2^+$, (e) organic carbon marker $^{27}C_2H_3^+$. The dark grey, dashed line represents the thermogram calculated via and internal standard method for $^{37}C_3H^+$ and light grey, $^{43}C_2H_3O^+$. The AMS curve in panel (e) represents total organic aerosol. Panel (f) displays the fractional total negative and positive ion intensities and the fraction of C_3^+ (*m/z* 36), used as the internal standard for the OC type. Error bars represent 95% confidence intervals, and may be hidden by the data marker.

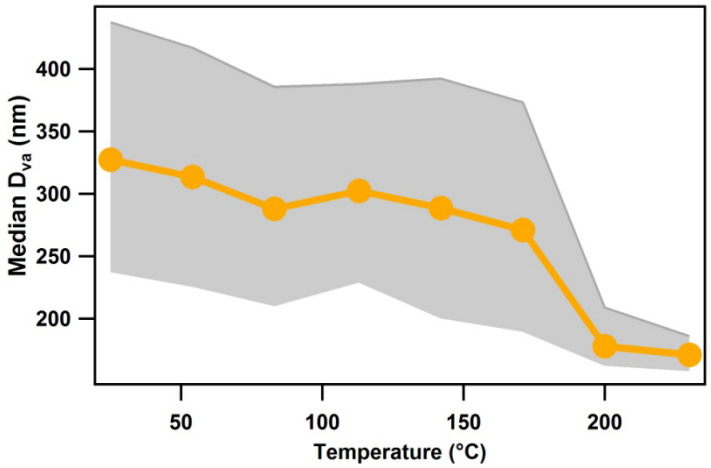

Figure 4.3 Change in median vacuum aerodynamic diameter with heating for the organic carbon particles. The shaded region represents the interquartile range.

To investigate the reason for the increased ion yield, the mass spectral patterns of the heated and unheated OC particles were compared: a subtraction plot of the OC particles measured at 83 ºC minus the unheated OC particles is shown in Figure 4.3. It is clear that the carbon cluster peaks (C_n^+, n=1-3) became more prominent with heating, indicating that these particles were likely composed of a soot core, coated in secondary species (organics, ammonium nitrate/sulfate) and is consistent with prior studies of aged soot morphologies.[44] As the particle coating was stripped away with heating, more of the strongly absorbing soot core was exposed. Therefore, a possible explanation for the increase in ion peak area is that the secondary coating, which absorbs less efficiently than soot (if not largely transparent), inhibited the absorption. Once those shell components were removed, or at least thinned, the particles absorbed the laser more efficiently and generated more cations, and therefore more electrons available to generate sulfate and nitrate ions. Thomson *et al.*[6] observed that the ionization threshold decreased with increasing absorption coefficient; in other words, more ions were produced from particles composed of more strongly absorbing species, consistent with this hypothesis. An additional explanation is that the increased peak area was due to changes in the extent of particle ablation rather than absorption. Schoolcraft *et al.*[9] observed a decrease in particle disintegration using molecular dynamics simulations of an absorbing particle core coated with a thick, amorphous, and transparent coating. In their simulations, the particle core absorbed the laser pulse and expanded upon vaporization; however the coating stretched around the expanding core and prevented the particle from ablating. A similar phenomenon may have played a role here, where a thinner secondary coating could have led to ablation of a greater fraction of the particle and therefore more ions formed. Both effects

likely contributed to some degree, with the net result being an increase in the LDI efficiency and total number of ions formed per particle as the secondary coating was removed.

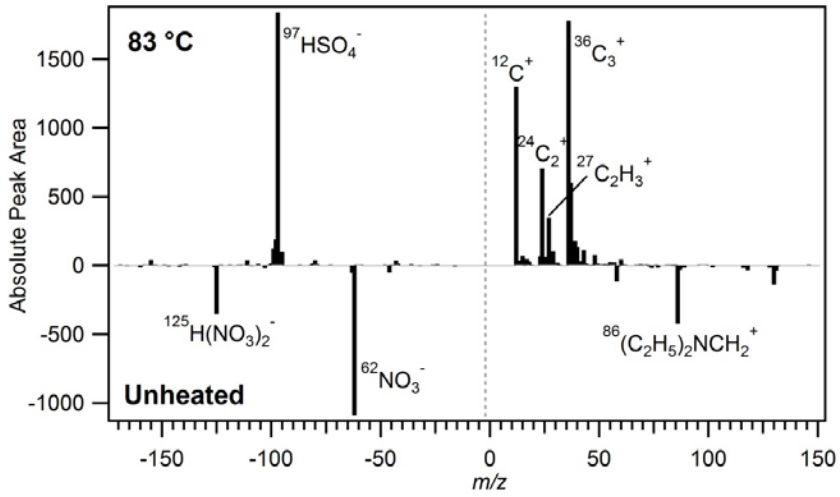

Figure 4.4 Mass spectral subtraction plot of the average mass spectrum corresponding to OC particles at 83˚C minus unheated OC particles. Positive intensity peaks correspond to higher abundance in the 83˚C particles, whereas negative intensity peaks show higher in tensity in the unheated particles.

Due to the increase in LDI efficiency, the APA method predicted artificially high fractions remaining, even for the highly volatile components (nitrate, amines- Figure 4.2). Sulfate displayed the largest increase in ion intensity because it is non-volatile below 150 ºC,[45,46] and therefore the primary factor contributing to the change in APA was the increase in ion yield. Previous studies have used the APAs of ammonium and nitrate to scale ATOFMS mass spectral data to collocated impactor measurements in Riverside.[17] It is likely that this quantification study was successful because the high degree of secondary coatings resulted in similar chemical matrices and therefore similar responses for the particles measured at ambient temperature only. Indeed, measurements during SOAR-1 indicated that different unheated particle types had similar densities due to the thick coating of secondary material (organics, ammonium nitrate/sulfate).[47]

Normalized peak areas are also commonly used in SPMS studies as a means of correcting for different ion intensities commonly observed among different particle types and other LDI artifacts, including shot-to-shot variability.[e.g.,4,16] "Relative Area" herein refers to absolute peak areas normalized by the total ion intensity of the spectrum at the single particle level, then averaged over all particles in the class. Using RPA, the thermograms generally improved

compared to using APAs, but remained significantly above the AMS measurements. In this case, the deviation was caused by the loss of volatile species, thereby reducing the total ion intensity. This becomes clear by comparing the higher APA fractions for individual, non-volatile species (i.e., $^{97}HSO_4^-$, $^{36}C_3^+$) with the total negative/positive ion intensities up to 142 ˚C (Figure 4.2). The total ion intensity displayed much smaller fractional increases than individual non-volatile components because semi-volatile components evaporated and reduced the amount of material available for ionization. As an example, nitrate evaporation reduced the total negative ion intensity, thereby lowering the normalization factor for sulfate and increasing its apparent intensity. Therefore, the total ion intensity cannot be used as an independent indicator of the changes in LDI efficiency in order to correct individual species.

As an alternative to the APA and RPA methods that were unable to accurately represent the TD data, a third case is proposed in which a single ion marker serves as an "internal standard" (IS) to normalize all aerosol constituents. In this way, the change in ion peak areas relative to the ion peak area of the IS was investigated to account for the changes in LDI efficiency with limited influence from other particle constituents. Internal standards were chosen by the following criteria such that their particle-phase mass could reasonably be assumed to stay constant across all temperatures. An appropriate IS should: (1) be non-volatile and emitted by a primary source so that gas-particle partitioning is not a factor; (2) be non-reactive or not react in a way that changes the mass spectral response to that component; and (3) be a significant component of the spectrum, without saturating the detector. For the OC particles, we use the elemental carbon marker, $^{36}C_3^+$, as the best option because it represents a component that is non-volatile at the temperatures considered here and is also one of the predominant peaks in the mass spectrum of this particle type (Figure 4.1b). As discussed above, the OC type is likely comprised of a soot core emitted from combustion sources (e.g., vehicles[36,37]) and coated with secondary species during transport.[48] A previous ATOFMS study found that normalizing OC components by EC ion markers (including C_3^+) produced good agreement with a collocated instrument measuring OC/EC ratios via thermal/optical measurements.[49] Herein, we extend this method and use the EC marker to normalize all particle components within the OC particle type. Although the ionization mechanisms of positive and negative ions are largely decoupled (once electrons are generated), we take the $^{36}C_3^+$ marker as the normalization factor for both positive and negative ions because the absolute intensities indicated that the predominant influence on peak areas (aside from evaporation) was due to an increase in the overall ion yield from the particles. Therefore the

greater degree of ionization likely influenced both polarities approximately equally. There was also not a suitable ion peak in the negative spectrum to act as an IS because all components can evaporate to some extent in the TD temperature range.

In this internal standard approach, the APA of each ion peak of interest was divided by the APA of the IS at the corresponding temperature; the normalized peak areas of the heated particles were then referenced to the unheated case to generate the thermograms for several secondary ion markers (dashed lines in Figure 4.2). Using the IS as a normalization factor produced thermograms in agreement with those from the AMS for ammonium and sulfate at temperatures up to 142 ºC (Figure 4.2a,c) and amines and nitrate up to 171 ºC (Figure 4.2b,d). The organic carbon markers were consistently above the AMS data at temperatures greater than 83 ºC (Figure 4.2e) for reasons that are described below. Above 171 ºC, the marked increase in the fraction remaining of all components via the IS method is attributed to a change in particle classification. Sudden evaporation of components above 171 ºC (likely ammonium sulfate) is indicated by the large change in the median diameter (93 nm, Figure 4.3) at 200 ºC. This loss of material changed the ion peak area trends and caused the particles to be reclassified as the ECOC particle type. The change in classification is demonstrated by the increase in the fraction of ECOC particles above 200ºC (Figure 4.1a), and the associated drop in $^{36}C_3^+$ ion peak area (Figure 4.2f), since particles with greater EC ion peak intensity were moved to the ECOC particle class. In an attempt to account for this issue, the OC and ECOC particle classes were combined. Thermograms for the merged OC and ECOC classes were calculated for each species of interest by taking a particle-number weighted average of the absolute peak areas. The averaged peak areas were then treated via the internal standard (IS) method using $^{36}C_3^+$ as the IS. Figure 4.5 shows example thermograms for the individual and combined OC/ECOC classes, in addition to the peak area of the IS. In Figures 4.5a and b, it can be seen that combining the OC and ECOC particles eliminated the problem of increasing fraction remaining at the highest temperatures. The shape of the combined thermograms indeed follows the AMS data well at all temperatures; however, it is systematically higher despite the fact that the separate OC and ECOC particle are each reasonably similar to the AMS up to 171 ºC.

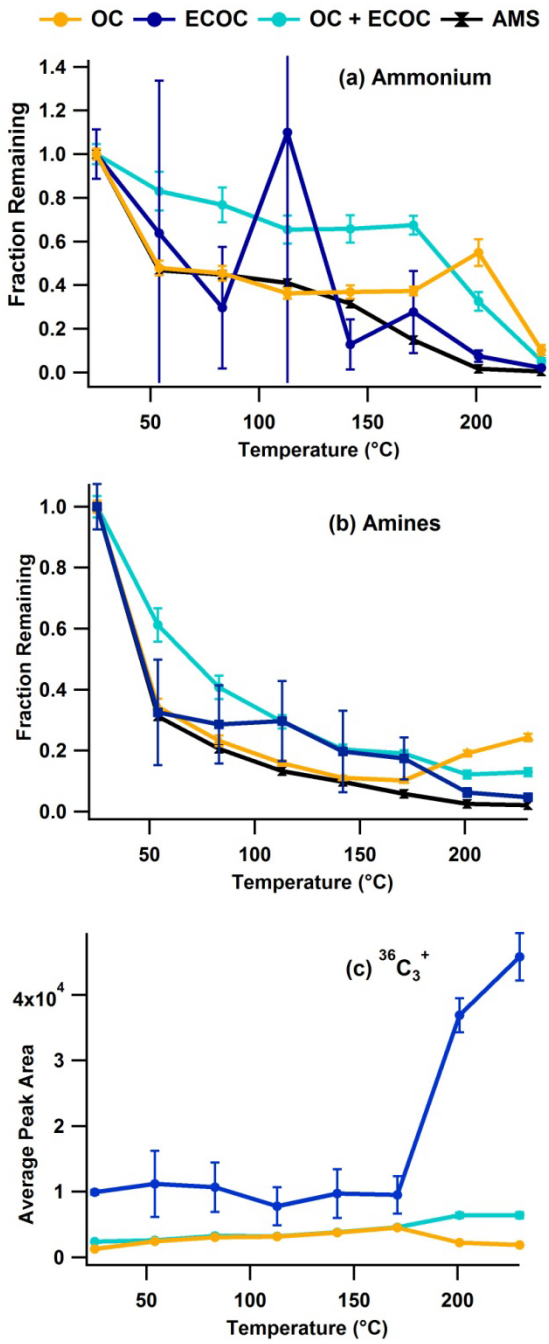

Figure 4.5 Example thermograms merging OC particles and ECOC particles (light blue) for (a) ammonium), $^{18}NH_4^+$, (b) amines, $^{86}(C_2H_5)_2NCH_2^+$. The internal standard method was applied in panels (a) and (b), using $^{36}C_3^+$. The peak areas for $^{36}C_3^+$ are included in panel (c). The distinct particle types are shown for comparison.

The greater apparent fraction remaining for the combined class (Figure 4.5a and b) occurs because the relative contribution from the ECOC type is low at the intermediate TD temperatures. Figure 4.6 shows the size-resolved number fractions of each particle type observed in SOAR-1

for particles sampled in the unheated and 54 ºC cases. In the unheated particles (Figure 4.6a), a significant fraction of the ECOC particles were present in the smallest size bins. With heating (Figure 4.6b), these particles shrank below the lower end of the ATOFMS transmission window and thus were not measured, similar to that observed during SOAR-2.[24] The size-resolved fractions at TD temperatures up to 171 ºC are similar to the 54 ºC case. Therefore, the unheated particles were disproportionately impacted when merging the OC and ECOC particle classes. The resulting impact on the combined peak areas is demonstrated in Figure 4.5c, showing the peak areas of the $^{36}C_3^+$ IS. The combined peak area (light blue) is greater than the OC case for unheated particles, but is then nearly identical to OC at the intermediate temperatures. The higher IS peak area would reduce the apparent peak area of the analyte, and by extension—because the TD temperatures are normalized by the unheated peak area—the fraction remaining will appear greater than the true value. Therefore, we keep the particle types separate and refrain from drawing conclusions about the volatility of components from the OC type at temperatures >171 ºC. However, we note that the inaccuracy resulting from combining these particle types was largely due to particles shifting out of the size range and loss of the corresponding information. Combining particle types to account for changing particle classification may work if both particle types remain in the detectable ATOFMS size range, but this should be tested in future work.

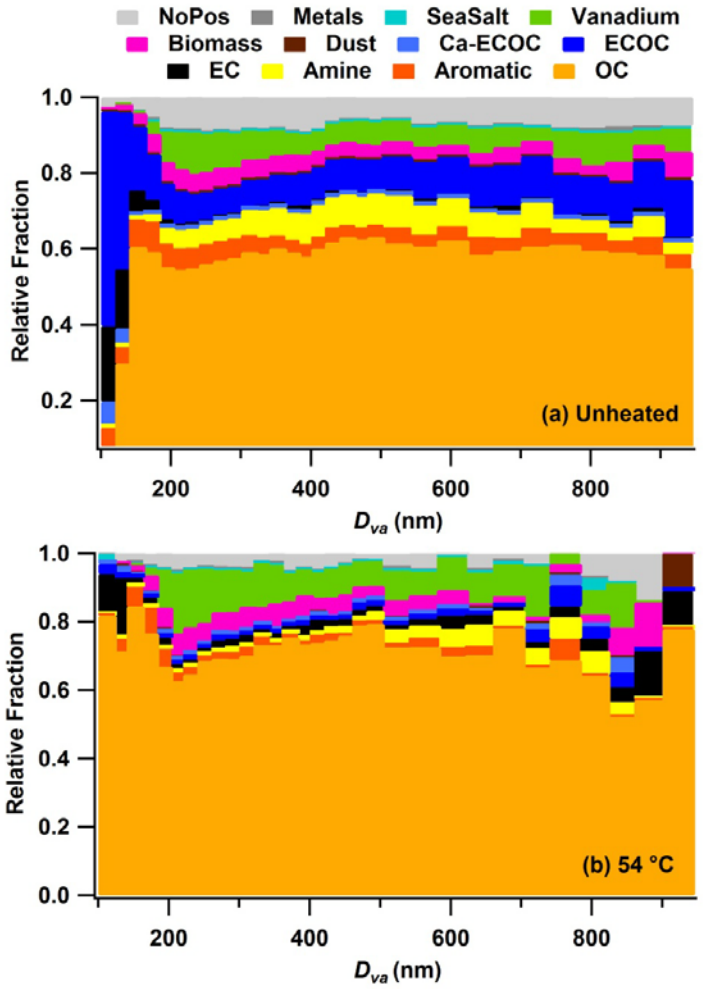

Figure 4.6 Relative number fractions of each particle type in 20 nm size bins up to D_{va} = 500 nm and 40 nm bins thereafter for (a) unheated and (b) 54 °C particles. Note the significant fraction of ECOC particles less than 200 nm in the unheated particles, which shrink out of the size range at 54 °C.

The strong agreement with the AMS at most temperatures via the IS method for nearly all ion markers (positive and negative) confirms the above hypothesis that the deviations in the APAs from the AMS measurements were largely due to effects that impacted the whole particle. If the APA trends had been the result of changes in competitive charge-transfer or collision-induced matrix effects, then the intensity of each ion marker would have been affected to different extents. Therefore, normalizing by an "inert" component of the particle most accurately reproduced the volatility of these secondary species because the IS gave an unbiased measure of how the LDI efficiency changed with heating. Note however, that this method relies on fully ablating the particle to ensure that the relative amount of the core species is accurately represented. If the surface components had been preferentially ionized at lower TD temperatures,

then the relative EC ion intensity would have been underpredicted and this internal standard method would have failed. Given that the EC marker could be successfully used as an internal standard implies that the particles sampled herein, were indeed fully ablated, which is consistent with previous ATOFMS studies that determined that laboratory-generated particles were fully ablated for diameters < 1.4 μm in diameter[50] (i.e., encompassing the size range measured with the ATOFMS used herein). Therefore, the increasing ionization efficiency can be likely attributed to increased absorption of the laser pulse generating more ions in the plume. Also note that these corrected peak areas can explain the difference in previously published ATOFMS and AMS amine volatility studies,[19,22] as discussed by Docherty, *et al.*[26] When the ionization artifacts of ATOFMS are properly taken into account, the two methods agree quite well.

4.4.2.1.2 Collision-Induced Matrix Effects

The results outlined above indicate that changes in laser-particle interactions significantly impacted ion intensities with heating. However, note that the thermograms of the organic ions did not accurately match the AMS thermograms by any peak area metric (Figure 4.2e). Since it is well-established that reactions within the ion plume can also alter the ion distributions in the mass spectrum,[5] changes in collision-induced matrix effects may have further influenced the observed changes in peak areas with heating. To this end, we follow Reinard and Johnston[14] in performing covariance mapping to investigate how ion peaks correlate with each other at the single-particle level. In this analysis, ion pairs that are (anti) correlated will yield (negative) positive correlation coefficients; ion pairs with no relationship will yield null values. The TD data was used to probe possible changes in matrix effects as components were removed with heating. It has previously been shown that the particle residues at 230°C strongly matched the source signatures of fresh particle emissions.[24] Therefore, utilization of a thermodenuder permits observations of the changes in matrix effects due to aging through comparison of the particles cores with their counterparts at lower temperatures. In the covariance analysis, the relative peak areas for single particles were used as the input, which is justified in this instance because peak areas are compared within a given temperature, not across temperatures and for individual particle types. Only particles with dual-polarity mass spectra were included in the analysis. We take correlation coefficients to be significantly different from zero if they had less than 5% probability of occurring by chance; values exceeding this threshold were reassigned to zero, shown as white in the covariance plots. Because the resulting correlation coefficients were influenced by real particle-to-particle differences in composition in addition to matrix effects, the following results

are interpreted in the context of the laboratory studies of Reinard and Johnston,[14] as well as known aging processes in eastern Los Angeles Basin.[27,48] Because Reinard and Johnston[14] used ~5x higher laser fluence (4 J/cm^2 vs. 0.8 J/cm^2) and 193 nm instead of 266 nm radiation, the ion distributions may differ between the two studies; however, the collision-induced matrix effects should be comparable.

Figure 4.7 shows the covariance analysis for the main ion markers in the OC particles, comparing the full matrices for unheated particles and particles at 171°C, which we used as the particle core due to the conversion of OC to the ECOC particle class at higher temperatures discussed above. Due to the large number of particles in the unheated case, a random sampling of 50% of the particles (40,000) were used; all particles were used in the covariance analysis at the elevated temperatures (>10,000 particles each).

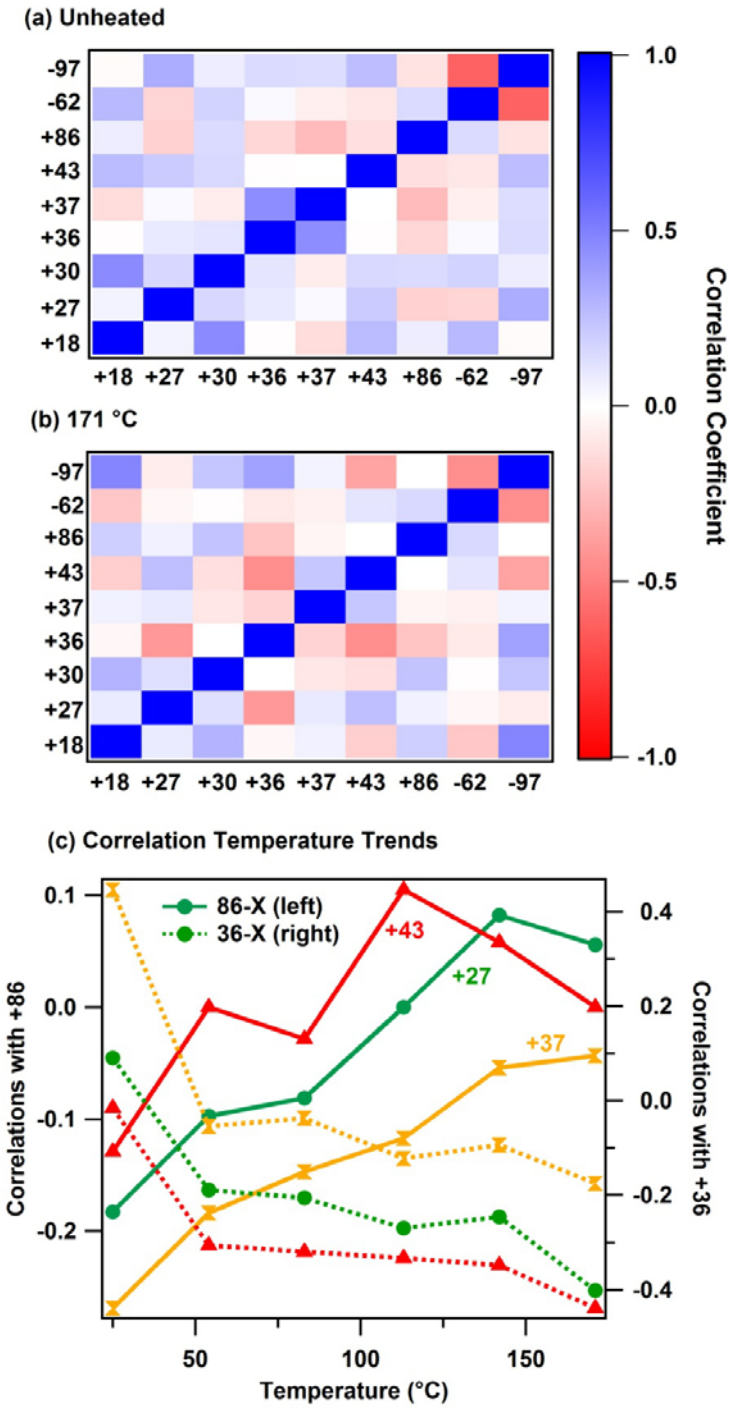

Figure 4.7 Covariance analysis of the OC particle type. (a) unheated; (b) 171˚C; (c) correlation coefficients between the ions indicated and the amine marker $^{86}(C_2H_5)_2NCH_2^+$ (solid, left axis) and $^{36}C_3^+$ EC marker (dashed, right axis) as a function of temperature. In (a) and (b), the x- and y-axes list the ion markers included in the covariance analysis. *m/z* values correspond to the following ions: +18, NH_4^+; +27, $C_2H_3^+$; +30, NO^+; +37 C_3H^+; +36 C_3^+; +43, $C_2H_3O^+$;. +86, $(C_2H_5)_2NCH_2^+$; -62, NO_3^-; -97, HSO_4^-.

We observe that the amine ion marker is anti-correlated with other carbonaceous ions in the unheated OC particles (Figure 4.7a). Amines have low ionization potentials (IP); for example, the IP of triethylamine, which has been shown to produce the $^{86}(C_2H_5)_2NCH_2^+$ marker,[51] is ~7.5 eV[52] compared to ~9-12 eV for most organic molecules.[53] Therefore, it is likely that amines suppressed the ionization of internally-mixed organic components through competitive charge transfer and would explain the common occurrence of amine-dominant spectra in ATOFMS studies.[e.g.,51,54,55] A steady increase in the correlations between these organic ions with the amine marker is apparent with heating and evaporation of the amines (Figure 4.7c). Additionally, in the unheated particles, the organic fragments $^{27}C_2H_3^+$ and $^{37}C_3H^+$ are positively correlated with $^{36}C_3^+$, whereas $^{43}C_2H_3O^+$ is very weakly anti-correlated, which is reasonable since $^{27}C_2H_3^+$ and $^{37}C_3H^+$ are more likely to be associated with primary organics co-emitted with EC and $^{43}C_2H_3O^+$ with secondary organics.[27] As shown in Figure 4.7c, these correlations became negative with heating (dotted lines), which coincided with loss of ~70% of the amine mass by ~64°C (Figure 4.2d); once the amines largely evaporated, the formation of other organic ions was less suppressed and became more favorable relative to $^{36}C_3^+$. At high temperature, $^{36}C_3^+$ is anti- (or not significantly) correlated with all of the organic components (Figure 4.7b), indicating that this is likely the least preferred species formed in the plume, consistent with its high IP of 12-13 eV.[52] These apparent changes in matrix effects could explain why the organic ions appear elevated relative to the AMS organics (Figure 4.2e)—the greater suppression of the organics by amines in the unheated particles lowered their apparent ion intensity, which would result in an elevated fraction remaining at higher temperatures. These results also indicate that, despite the strong improvement over the absolute and relative peak area metrics for correcting the LDI efficiency, the internal standard method is not ideal because it cannot correct these collision-induced matrix effects.

Although amines are the apparent preferred cation in this particle matrix, $^{86}(C_2H_5)_2NCH_2^+$ is weakly positively correlated with $^{18}NH_4^+$ and $^{30}NO^+$, likely a nitrate fragment[17] (Figure 4.7a). In previous covariance analysis of laboratory mixtures of ammonium sulfate and nitrate, $^{18}NH_4^+$ was strongly anti-correlated with $^{30}NO^+$ due to matrix effects.[14] Therefore, the positive correlations herein are likely due to real chemical correlations, in particular, the co-condensing of ammonium and aminium nitrate salts. Extensive animal operations in the Chino area upwind of Riverside are known to emit very high levels of ammonia[21,56] and likely amines as well.[57,58] Ammonia and amines can partition by a similar mechanism, (i.e., acid-base reactions with nitric

acid forming less volatile salts[19,59]) and therefore, it is not surprising that these species are correlated at the single particle level since particles acquire ammonium/aminium nitrate coatings during transport from the LA area.[48]

Sulfate and nitrate were strongly anti-correlated (Figure 4.7a), as was observed by Reinard and Johnston.[14] The anti-correlation became weaker as nitrate evaporated (Figure 4.7b) because the lower nitrate concentration reduced the competition for electrons. The strong agreement between the ATOFMS-IS peak area and the AMS nitrate fraction remaining indicate that the change in matrix effects did not impact the apparent nitrate volatility.

4.4.2.2 Vanadium Particles.

4.4.2.2.1 LDI Efficiency

The Vanadium-rich particles displayed different behavior than the OC particle type and are briefly described in this section. Figure 4.8 shows the ion peak areas observed for this particle type using the same metrics described above. Here, the average total ion intensity per particle is relatively flat up to 177°C, indicating that the ioni zation efficiency was roughly constant up to that temperature, after which it increased substantially (Figure 4.8f). The average absolute intensity of the species attributed to the particle core, $^{51}V^{+}$ and $^{23}Na^{+}$, also follow this trend (Figure 4.8f). The median diameter was roughly flat up to 171 ºC, at which point it started decreasing (Figure 4.9), demonstrating that the increase in ion peak areas at high temperature coincided with material evaporating, rather than larger particles shrinking into the detectable range. This transition occurred within the temperature range of ammonium sulfate evaporation, indicating that this component suppressed the laser absorption at lower temperatures. It is well known in the SPMS community that ammonium sulfate is transparent in the UV range and pure ammonium sulfate particles are difficult to measure using LDI at 266 nm due to lack of absorption of the laser beam.[6,39,42] These results indicate that the sudden evaporation of secondary components, particularly ammonium sulfate, led to greater absorption of the D/I laser pulse and therefore greater ion formation. The different temperature trends in ion intensity between the OC and Vanadium-rich particle types can perhaps be attributed to the stronger absorption by soot and a larger change in the LDI efficiency as the coating thinned at low temperatures. The OC particles also showed a larger decrease in the median diameter with heating (Figures 4.3, 4.9), which may implicate the impacts of coating thickness on the LDI process.

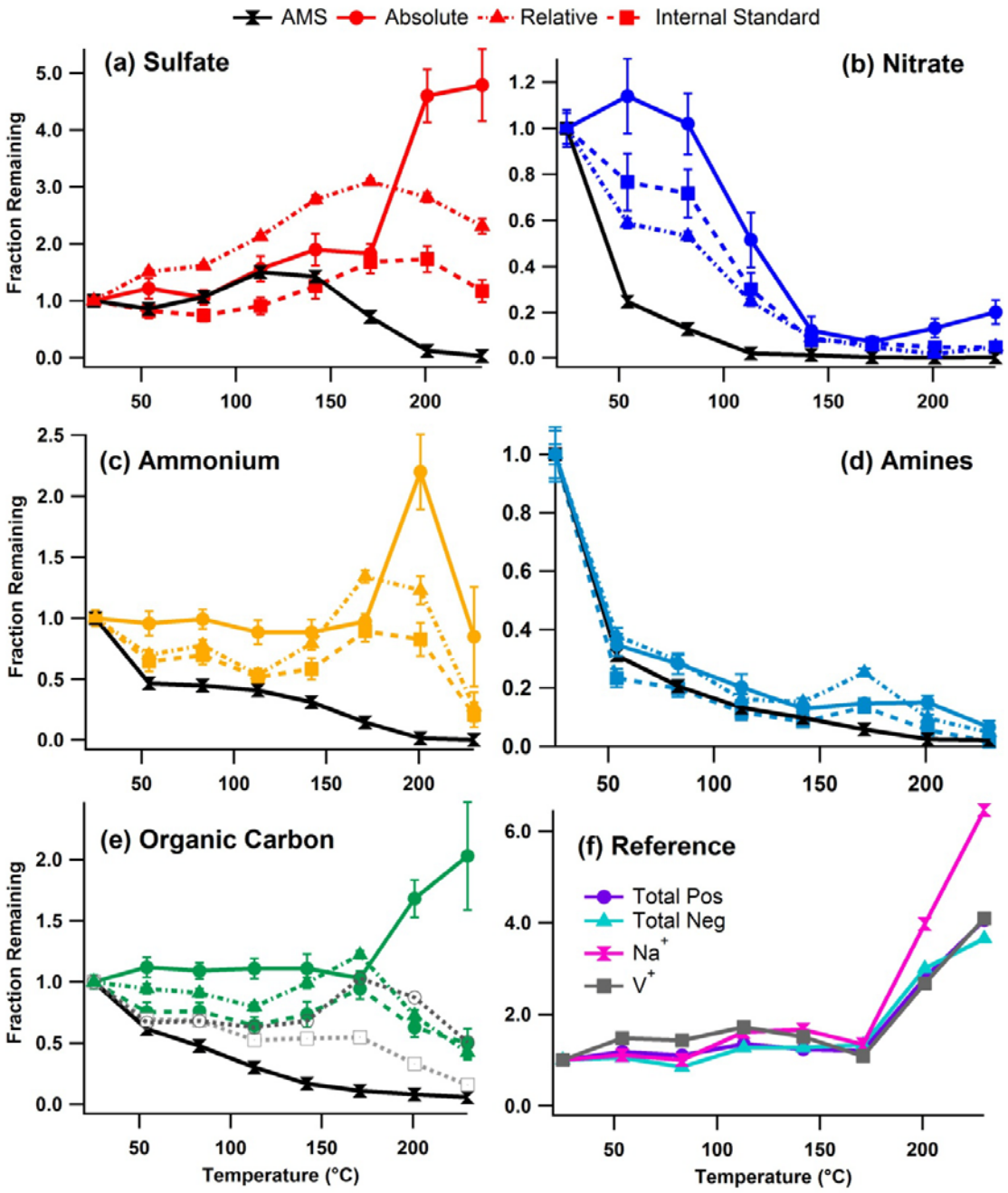

Figure 4.8 Thermograms of the vanadium-type particle type for several aerosol constituents demonstrating the different peak area metrics for ATOFMS data (colors) compared to AMS (black). The ATOFMS ion peaks represented in each panel are as follows: (a) $^{97}HSO_4^-$; (b) $^{62}NO_3^-$, (c) $^{18}NH_4^+$, (d) $^{86}(C_2H_5)_2NCH_2^+$, (e) organic carbon marker $^{27}C_2H_3^+$. The dark grey, dashed line represents the thermogram calculated via and internal standard method for $^{37}C_3H^+$ and light grey, $^{43}C_2H_3O^+$. The AMS curve in panel (e) represents total organic aerosol. Panel (f) displays the fractional total negative and positive ion intensities and the fraction of $^{23}Na^+$, and $^{51}V^+$. The latter was used as the internal standard for these particles. Error bars represent 95% confidence intervals, and may be hidden by the data marker.

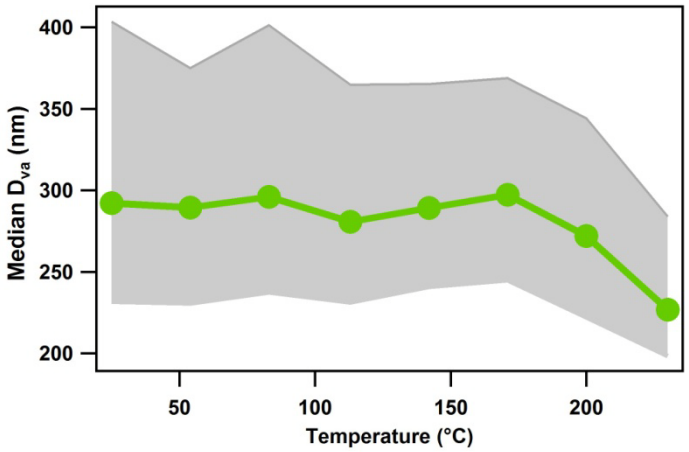

Figure 4.9 Change in median vacuum aerodynamic diameter with heating for the vanadium-rich particles. The shaded region represents the interquartile range.

The stronger ion formation at high temperature is apparent in the thermograms of less-volatile constituents, namely sulfate (Figure 4.8a), ammonium (Figure 4.8c), and organic carbon (Figure 4.8e), wherein the APAs increased markedly at 200 ºC. Normalizing these peak areas by $^{51}V^{+}$ as the internal standard removed this artifact and shows that these components actually decreased with heating, as expected. For the more volatile components (e.g., amines- Figure 4.8d), the APA, RPA, and IS methods all produced similar thermograms. Therefore, at the low temperatures where the ionization efficiency did not change appreciably, the change in APA reasonably represented the evaporation of these species, though the IS-normalized thermogram does agree slightly better with AMS measurements at $T \geq 83$ ºC. In the case of nitrate, even the normalized peak area of $^{62}NO_3^-$ remains significantly above the AMS thermogram (Figure 4.8b), and likely reflects a true difference in nitrate volatility. The chemical mixing-state dependence of nitrate volatility will be described in Chapter 5.

Previous work has noted a morphology dependence on the extent of plasma formation in the LDI of laboratory-generated metal particles.[60] Zhou *et al.*[60] coated an absorbing aluminum oxide core with a transparent coating of NaCl and observed diminished aluminum ion formation up to high aluminum mole fraction, which they attributed to weakened plasma formation due to a poor coupling of the laser energy from the core to the shell and therefore less overall ionization. In contrast, homogeneously-mixed particles of the same composition produced the expected increase in aluminum ion intensity with increasing aluminum mole fraction due to stronger plasma formation caused by the absorbing material being present throughout the particle.[60] Therefore it is possible that the observed ion intensity trends of the vanadium particles indicated

that these particles also existed in a core-shell-type morphology in Riverside, however there were no collocated measurements able to confirm this hypothesis for this specific particle type. Future studies should couple the TD-ATOFMS measurements with microscopy studies to directly correlate the change in ionization efficiency of ambient particles with changes in particle morphology. Alternatively, the morphology could be probed by SPMS through variations in the laser power.[12,61]

4.4.2.2.2 Matrix Effects

The vanadium particle type contained many metal cations (Figure 4.1c), which are known to display significant charge-transfer matrix effects due to their low IPs.[5,14] The significant metals observed in the V-rich type include (with their IP's[52] in parentheses): Na (5.1-5.6 eV), Ca (6.0 eV), V (6.7 eV), and VO (7.2-7.8 eV). The covariance matrix for all 9,045 unheated particles and 280 particle residuals at 230 ºC are shown in Figure 4.10a & b. In the unheated particles, all metal cations were positively correlated with each other and in turn are negatively correlated with all other cations. Additionally, the anti-correlations between the metals and organic components, $^{27}C_2H_3^+$ and $^{43}C_2H_3O^+$, were stronger in the unheated case, than at 230 ºC. These results indicate that the dominant collisions of the metal cations were likely with secondary species in the highly aged particles; in other words, the metals were competing for charge with non-metals due to the low relative abundance of metals in the highly aged particles. If the non-metals were more strongly suppressed in the unheated case, it could explain why the thermograms of $^{18}NH_4^+$ and the organic components were elevated relative to the AMS up to 142 ºC (Figure 4.8c,e). It is not clear if this discrepancy is the result of a real change in volatility because $^{18}NH_4^+$, for instance, was still likely in the form of nitrate and sulfate salts in these particles, which should be detectable by the AMS.

The correlations between the core species also changed with heating. At high temperature, $^{23}Na^+$ became the most favorable ion, as indicated by the negative correlations with all metal and non-metal cations and the IPs listed above. As the secondary species were removed, Na and V began to compete for charge, consistent with the increase in ion peak area of $^{23}Na^+$ relative to $^{51}V^+$ at high temperature (Figure 4.8f). The fact that $^{23}Na^+$ (which has the lowest IP of the observed metals) is not the dominant ion in the spectrum, even at 230 ºC (not shown), indicates that it is likely in significantly lower abundance relative to vanadium in these particles. This finding is consistent with a previous elemental analysis of ship fuel.[62] Because $^{51}V^+$ and $^{67}VO^+$ remain positively correlated, they likely form by non-competitive processes, perhaps

fragmentation from more oxidized forms of vanadium, e.g., V_2O_5, which is the most abundant vanadium species emitted from vehicles.[35]

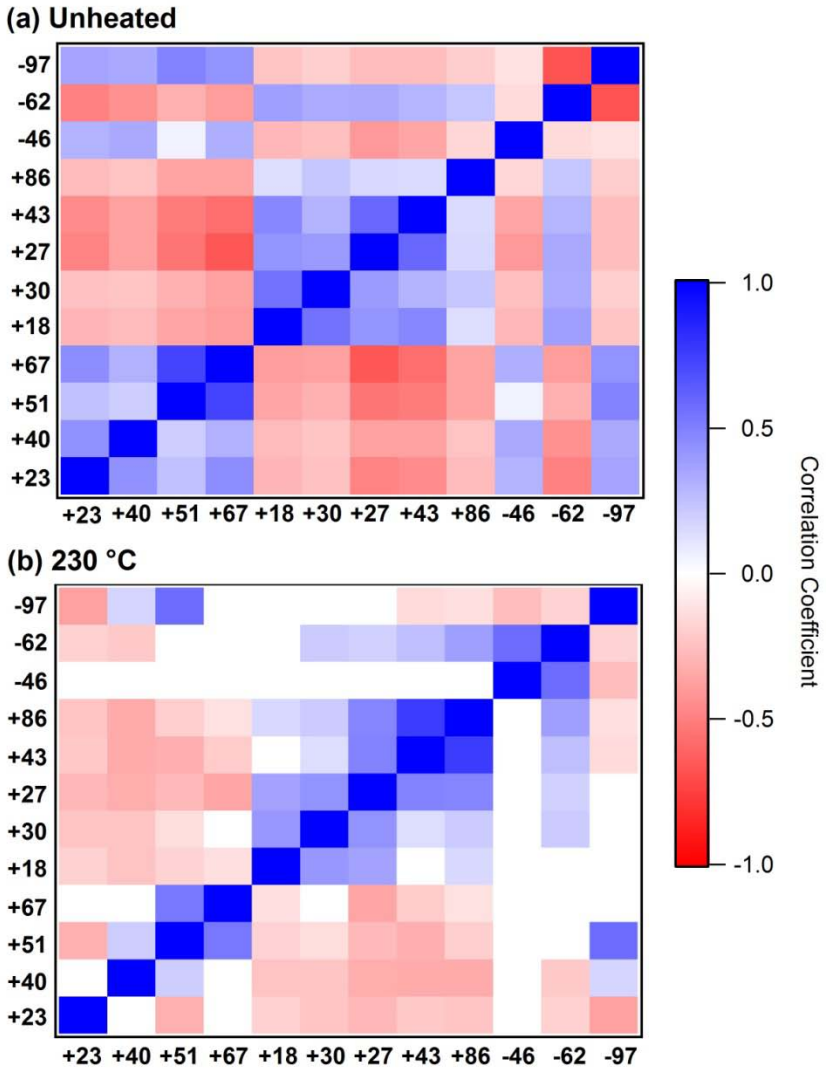

Figure 4.10 Covariance analysis of the Vanadium particle type (a) unheated; (b) 230°C. In (a) and (b), the x- and y-axes list the ion markers included in the covariance analysis. *m/z* values correspond to the following species/fragments: +23, Na^+; +40, Ca^+; +51, V^+; +67, VO^+; +18, NH_4^+; +27, $C_2H_3^+$; +30, NO^+; +37 C_3H^+; +43, $C_2H_3O^+$;. +86, $(C_2H_5)_2NCH_2^+$; -46, NO_2^-; -62, NO_3^-; -97, HSO_4^-.

This correlation analysis was also used to explain the increase in the thermograms for sulfate, ammonium, organics ($^{27}C_2H_3^+$, $^{37}C_3H^+$), and amines at 142-171 ºC using the IS peak area method, which indicates that these components increased relative to $^{51}V^+$. In the same temperature range, the correlations of these ions with $^{51}V^+$ also change (Figure 4.11a). The

correlation of $^{23}Na^+$ and $^{51}V^+$ increased to similar levels as the unheated particles, whereas the correlations between sulfate, ammonium, organics (represented by $^{27}C_2H_3^+$) with $^{51}V^+$ all decrease. These changes coincided with a large spike in the ion peak area of the $^{195}H_2SO_4 \cdot HSO_4^-$ marker (Figure 4.11b), which can be used as an indicator of un-neutralized sulfate.[63] Only at these temperatures is the correlation between $^{51}V^+$ and the $^{195}H_2SO_4 \cdot HSO_4^-$ marker anti-correlated and coincides with a decrease in the correlation between $^{97}HSO_4^-$ and $^{51}V^+$ (Figure 4.11a). Larson *et al.*[64] reported an increase in the scattering coefficient during nephelometry measurements of ammonium sulfate at ~150 ºC that was attributed to decomposition to ammonium bisulfate. Yao *et al.*[63] observed a decrease in their ATOFMS hit efficiency as they reduced the extent of sulfate neutralization in laboratory mixtures; they postulated that sulfuric acid formed a coating around neutral metal salts, which decreased the laser absorption. Therefore, it is plausible that a conversion from ammonium sulfate to ammonium bisulfate/sulfuric acid in this temperature range induced a change in ionization efficiency and/or weakened the plasma formation, resulting in a greater sensitivity to the surface components. We note that the absolute peak area of vanadium decreased slightly at this temperature, as well (Figure 4.8f), which may indicate shallower ablation depth. This "shielding" of the particle core could explain the anti-correlations of the secondary components with $^{51}V^+$ and also the stronger positive correlations between the $^{23}Na^+$ and $^{51}V^+$ at 171 ºC, since both metals would be present at higher concentrations if the core was more efficiently ionized.

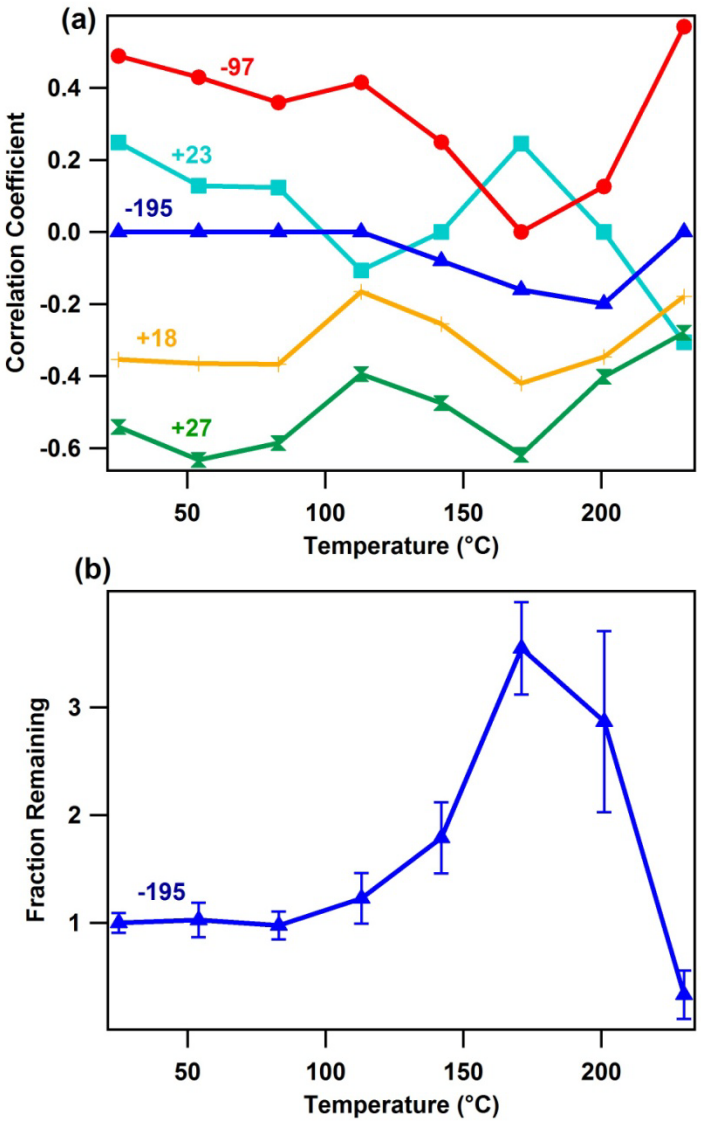

Figure 4.11 (a) Correlation coefficient between $^{51}V^{+}$ and the ions indicated at each TD temperature. *m/z* values shown correspond to the following ions: +18, NH_4^+; +23, Na^+; +27, $C_2H_3^+$; -97, HSO_4^-; -195, $H_2SO_4 \cdot HSO_4^-$. (b) Thermogram of the $^{195}H_2SO_4 \cdot HSO_4^-$ ion marker in Vanadium-rich particles.

4.5 Conclusions and Implications

In this work, a thermodenuder was used in-line with ATOFMS to characterize the ionization effects of ambient aerosol particles as the effects of aging were removed. It was demonstrated that the efficiency of the LDI process is reduced as particles become coated with secondary species. Jeong and coworkers[16] have previously postulated that an observed decrease in ATOFMS hit efficiency during measurements in Canada could have been due to a coating of high albedo secondary species such as ammonium sulfate and ammonium nitrate. The results herein

support their hypothesis, as the hit efficiency increased as secondary coatings were removed and exposed a more absorbing core. Our results further indicate that secondary coatings may influence the ionization efficiency for hit particles, as demonstrated herein for two particle types of different composition. After transparent coatings were removed, the laser pulse was absorbed more strongly, resulting in greater photoionization. When viewed in reverse (decreasing temperature) these results highlight that particle aging in the atmosphere can significantly influence the degree of ionization from a single particle and thus the resulting ion peak areas measured by ATOFMS. It was demonstrated herein that these ionization effects can be corrected by utilizing relatively inert aerosol components as internal standards; the resulting normalized ion peak areas were clearly proportional to the species' mass, as demonstrated by the strong agreement with the AMS. However, a few components (e.g., the organic ions in the OC type) were impacted by collision-induced matrix effects, as demonstrated through covariance analysis. It was observed that amines can suppress the formation of other organic constituents in positive ion spectra and that the matrix effects induced by metals may change with aging or morphology. This underscores the importance of better understanding how SPMS measurements of ambient aerosols change as a function of atmospheric processing in order to ultimately achieve quantitative measurements of chemical mixing state. The methods outlined herein provide a significant step in that direction.

4.6 Acknowledgements

The dissertation author was the primary researcher and author of this chapter. Dr. Kerri Pratt is acknowledged for collecting the TD-ATOFMS data. Drs. Alex Huffman and Jose Jimenez (University of Colorado-Boulder) are also thanked for providing the TD-AMS data (and use of the TD). Prof. Paul Ziemann (UC-Riverside), Ken Docherty (CU-Boulder), the UC Riverside Air Pollution Research Center, and the entire Prather Group are thanked for support during SOAR. The SOAR campaign was funded by the National Science Foundation (NSF-ATM 0321362) and the California Air Resources Board (CARB 04-336). L. Hatch and K. Pratt were funded by National Science Foundation Graduate Research Fellowships (2008-2011 and 2006-2009, respectively). K. Pratt was additionally funded by an EPA STAR Graduate Fellowship (2005-2006). The EPA has not officially endorsed this publication, and the views expressed herein may not reflect the views of the EPA. Helpful discussions and manuscript reviews by John Cahill are gratefully acknowledged. Cassandra Gaston is also thanked for reviewing this chapter.

Chapter 4 is in preparation for submission to Aerosol Science & Technology: Hatch, L.E.; Pratt, K. A.; Huffman, J. A.; Jimenez, J. L.; and Prather, K. A., Impacts of aerosol aging on laser desorption/ionization in single particle mass spectrometers.

4.7 References

1. Pratt, K. A.; Prather, K. A., Mass spectrometry of atmospheric aerosols: Recent developments and applications. Part II: On-line mass spectrometry techniques. *Mass Spectrom. Rev.* **2012,** *31*, (1), 17-48.

2. Murphy, D. M.; Cziczo, D. J.; Froyd, K. D.; Hudson, P. K.; Matthew, B. M.; Middlebrook, A. M.; Peltier, R. E.; Sullivan, A.; Thomson, D. S.; Weber, R. J., Single-particle mass spectrometry of tropospheric aerosol particles. *J. Geophys. Res.* **2006,** *111*, (D23).

3. Zelenyuk, A.; Yang, J.; Imre, D., Comparison between mass spectra of individual organic particles generated by UV laser ablation and in the IR/UV two-step mode. *Int. J. Mass spectrom.* **2009,** *282*, (1-2), 6-12.

4. Gross, D. S.; Galli, M. E.; Silva, P. J.; Prather, K. A., Relative sensitivity factors for alkali metal and ammonium cations in single particle aerosol time-of-flight mass spectra. *Anal. Chem.* **2000,** *72*, (2), 416-422.

5. Reilly, P. T. A.; Lazar, A. C.; Gieray, R. A.; Whitten, W. B.; Ramsey, J. M., The elucidation of charge-transfer-induced matrix effects in environmental aerosols via real-time aerosol mass spectral analysis of individual airborne particles. *Aerosol Sci. Technol.* **2000,** *33*, (1-2), 135-152.

6. Thomson, D. S.; Middlebrook, A. M.; Murphy, D. M., Thresholds for laser-induced ion formation from aerosols in a vacuum using ultraviolet and vacuum-ultraviolet laser wavelengths. *Aerosol Sci. Technol.* **1997,** *26*, (6), 544-559.

7. Wade, E. E.; Farquar, G. R.; Steele, P. T.; McJimpsey, E. L.; Lebrilla, C. B.; Fergenson, D. P., Wavelength and size dependence in single particle laser aerosol mass spectra. *J. Aerosol Sci* **2008,** *39*, (8), 657-666.

8. Carson, P. G.; Johnston, M. V.; Wexler, A. S., Real-time monitoring of the surface and total composition of aerosol particles. *Aerosol Sci. Technol.* **1997,** *26*, (4), 291-300.

9. Schoolcraft, T. A.; Constable, G. S.; Jackson, B.; Zhigilei, L. V.; Garrison, B. J., Molecular dynamics simulations of laser disintegration of amorphous aerosol particles with spatially nonuniform absorption. *Nuclear Instruments & Methods in Physics Research Section B-Beam Interactions with Materials and Atoms* **2001,** *180*, 245-250.

10. Schoolcraft, T. A.; Constable, G. S.; Zhigilei, L. V.; Garrison, B. J., Molecular dynamics simulation of the laser disintegration of aerosol particles. *Anal. Chem.* **2000,** *72*, (21), 5143-5150.

11. Cai, Y.; Zelenyuk, A.; Imre, D., A high resolution study of the effect of morphology on the mass spectra of single PSL particles with Na-containing layers and nodules. *Aerosol Sci. Technol.* **2006,** *40*, (12), 1111-1122.

12. Zelenyuk, A.; Yang, J.; Song, C.; Zaveri, R. A.; Imre, D., "Depth-profiling" and quantitative characterization of the size, composition, shape, density, and morphology of fine particles with SPLAT, a single-particle mass spectrometer. *J. Phys. Chem. A* **2008,** *112*, (4), 669-677.

13. Knochenmuss, R., Ion formation mechanisms in UV-MALDI. *Analyst* **2006,** *131*, (9), 966-986.

14. Reinard, M. S.; Johnston, M. V., Ion formation mechanism in laser desorption ionization of individual nanoparticles. *J. Am. Soc. Mass. Spectrom.* **2008,** *19*, (3), 389-399.

15. Ge, Z. Z.; Wexler, A. S.; Johnston, M. V., Laser desorption/ionization of single ultrafine multicomponent aerosols. *Environ. Sci. Tech.* **1998,** *32*, (20), 3218-3223.

16. Jeong, C. H.; McGuire, M. L.; Godri, K. J.; Slowik, J. G.; Rehbein, P. J. G.; Evans, G. J., Quantification of aerosol chemical composition using continuous single particle measurements. *Atmos. Chem. Phys.* **2011,** *11*, (14), 7027-7044.

17. Bhave, P. V.; Allen, J. O.; Morrical, B. D.; Fergenson, D. P.; Cass, G. R.; Prather, K. A., A field-based approach for determining ATOFMS instrument sensitivities to ammonium and nitrate. *Environ. Sci. Tech.* **2002,** *36*, (22), 4868-4879.

18. Dall'Osto, M.; Harrison, R. M.; Beddows, D. C. S.; Freney, E. J.; Heal, M. R.; Donovan, R. J., Single-particle detection efficiencies of aerosol time-of-flight mass spectrometry during the North Atlantic marine boundary layer experiment. *Environ. Sci. Tech.* **2006,** *40*, (16), 5029-5035.

19. Pratt, K. A.; Hatch, L. E.; Prather, K. A., Seasonal Volatility Dependence of Ambient Particle Phase Amines. *Environ. Sci. Tech.* **2009,** *43*, (14), 5276-5281.

20. Seinfeld, J. H.; Pandis, S. N., *Atmospheric Chemistry & Physics: From Air Pollution to Climate Change*. 2nd. ed.; John Wiley & Sons, Inc.: New Jersey, 2006.

21. Russell, A. G.; Cass, G. R., Verification of a Mathematical-Model for Aerosol Nitrate and Nitric-Acid Formation and Its Use for Control Measure Evaluation. *Atmos. Environ.* **1986,** *20*, (10), 2011-2025.

22. Huffman, J. A.; Docherty, K. S.; Aiken, A. C.; Cubison, M. J.; Ulbrich, I. M.; DeCarlo, P. F.; Sueper, D.; Jayne, J. T.; Worsnop, D. R.; Ziemann, P. J.; Jimenez, J. L., Chemically-resolved aerosol volatility measurements from two megacity field studies. *Atmos. Chem. Phys.* **2009,** *9*, (18), 7161-7182.

23. Huffman, J. A.; Docherty, K. S.; Mohr, C.; Cubison, M. J.; Ulbrich, I. M.; Ziemann, P. J.; Onasch, T. B.; Jimenez, J. L., Chemically-Resolved Volatility Measurements of Organic Aerosol from Different Sources. *Environ. Sci. Tech.* **2009,** *43*, (14), 5351-5357.

24. Pratt, K. A.; Prather, K. A., Real-Time, Single-Particle Volatility, Size, and Chemical Composition Measurements of Aged Urban Aerosols. *Environ. Sci. Tech.* **2009,** *43*, (21), 8276-8282.

25. Huffman, J. A.; Ziemann, P. J.; Jayne, J. T.; Worsnop, D. R.; Jimenez, J. L., Development and Characterization of a Fast-Stepping/Scanning Thermodenuder for Chemically-Resolved Aerosol Volatility Measurements. *Aerosol Sci. Technol.* **2008,** *42*, 395-407.

26. Docherty, K. S.; Aiken, A. C.; Huffman, J. A.; Ulbrich, I. M.; DeCarlo, P. F.; Sueper, D.; Worsnop, D. R.; Snyder, D. C.; Peltier, R. E.; Weber, R. J.; Grover, B. D.; Eatough, D. J.; Williams, B. J.; Goldstein, A. H.; Ziemann, P. J.; Jimenez, J. L., The 2005 Study of Organic Aerosols at Riverside (SOAR-1): instrumental intercomparisons and fine particle composition. *Atmos. Chem. Phys.* **2011,** *11*, (23), 12387-12420.

27. Qin, X.; Pratt, K. A.; Shields, L. G.; Toner, S. M.; Prather, K. A., Seasonal comparison of single-particle chemical mixing state in Riverside, CA. *Atmos. Environ.* **2012,** *Accepted Manuscript*.

28. Pratt, K. A.; Mayer, J. E.; Holecek, J. C.; Moffet, R. C.; Sanchez, R. O.; Rebotier, T. P.; Furutani, H.; Gonin, M.; Fuhrer, K.; Su, Y. X.; Guazzotti, S.; Prather, K. A., Development and Characterization of an Aircraft Aerosol Time-of-Flight Mass Spectrometer. *Anal. Chem.* **2009,** *81*, (5), 1792-1800.

29. Drewnick, F.; Hings, S. S.; DeCarlo, P.; Jayne, J. T.; Gonin, M.; Fuhrer, K.; Weimer, S.; Jimenez, J. L.; Demerjian, K. L.; Borrmann, S.; Worsnop, D. R., A new time-of-flight aerosol mass spectrometer (TOF-AMS) - Instrument description and first field deployment. *Aerosol Sci. Technol.* **2005,** *39*, (7), 637-658.

30. Allen, J. O., YAADA: software toolkit to analyze single-particle mass spectral data. *Software Reference Manual* **2001**.

31. Song, X. H.; Hopke, P. K.; Fergenson, D. P.; Prather, K. A., Classification of single particles analyzed by ATOFMS using an artificial neural network, ART-2A. *Anal. Chem.* **1999,** *71*, (4), 860-865.

32. Docherty, K. S.; Stone, E. A.; Ulbrich, I. M.; DeCarlo, P. F.; Snyder, D. C.; Schauer, J. J.; Peltier, R. E.; Weber, R. J.; Murphy, S. M.; Seinfeld, J. H.; Grover, B. D.; Eatough, D. J.; Jimenez, J. L., Apportionment of Primary and Secondary Organic Aerosols in Southern California during the 2005 Study of Organic Aerosols in Riverside (SOAR-1). *Environ. Sci. Tech.* **2008,** *42*, (20), 7655-7662.

33. Ault, A. P.; Gaston, C. J.; Wang, Y.; Dominguez, G.; Thiemens, M. H.; Prather, K. A., Characterization of the Single Particle Mixing State of Individual Ship Plume Events Measured at the Port of Los Angeles. *Environ. Sci. Tech.* **2010,** *44*, (6), 1954-1961.

34. Healy, R. M.; O'Connor, I. P.; Hellebust, S.; Allanic, A.; Sodeau, J. R.; Wenger, J. C., Characterisation of single particles from in-port ship emissions. *Atmos. Environ.* **2009,** *43*, (40), 6408-6414.

35. Shafer, M. M.; Toner, B. M.; Oyerdier, J. T.; Schauer, J. J.; Fakra, S. C.; Hu, S. H.; Herner, J. D.; Ayala, A., Chemical Speciation of Vanadium in Particulate Matter Emitted from Diesel Vehicles and Urban Atmospheric Aerosols. *Environ. Sci. Tech.* **2012,** *46*, (1), 189-195.

36. Sodeman, D. A.; Toner, S. M.; Prather, K. A., Determination of single particle mass spectral signatures from light-duty vehicle emissions. *Environ. Sci. Tech.* **2005,** *39*, (12), 4569-4580.

37. Toner, S. M.; Sodeman, D. A.; Prather, K. A., Single particle characterization of ultrafine and accumulation mode particles from heavy duty diesel vehicles using aerosol time-of-flight mass spectrometry. *Environ. Sci. Tech.* **2006,** *40*, (12), 3912-3921.

38. Gaston, C. J.; Pratt, K. A.; Qin, X. Y.; Prather, K. A., Real-Time Detection and Mixing State of Methanesulfonate in Single Particles at an Inland Urban Location during a Phytoplankton Bloom. *Environ. Sci. Tech.* **2010,** *44*, (5), 1566-1572.

39. Kane, D. B.; Johnston, M. V., Size and composition biases on the detection of individual ultrafine particles by aerosol mass spectrometry. *Environ. Sci. Tech.* **2000,** *34*, (23), 4887-4893.

40. Huffman, J. A.; Jayne, J. T.; Drewnick, F.; Aiken, A. C.; Onasch, T.; Worsnop, D. R.; Jimenez, J. L., Design, modeling, optimization, and experimental tests of a particle beam width probe for the aerodyne aerosol mass spectrometer. *Aerosol Sci. Technol.* **2005,** *39*, (12), 1143-1163.

41. Liu, P.; Ziemann, P. J.; Kittelson, D. B.; Mcmurry, P. H., Generating Particle Beams of Controlled Dimensions and Divergence .1. Theory of Particle Motion in Aerodynamic Lenses and Nozzle Expansions. *Aerosol Sci. Technol.* **1995,** *22*, (3), 293-313.

42. Wenzel, R. J.; Liu, D. Y.; Edgerton, E. S.; Prather, K. A., Aerosol time-of-flight mass spectrometry during the Atlanta Supersite Experiment: 2. Scaling procedures. *J. Geophys. Res.* **2003,** *108*, (D7).

43. Mansoori, B. A.; Johnston, M. V.; Wexler, A. S., Quantitation of Ionic Species in Single Microdroplets by Online Laser Desorption/Ionization. *Anal. Chem.* **1994,** *66*, (21), 3681-3687.

44. Moffet, R. C.; Prather, K. A., In-situ measurements of the mixing state and optical properties of soot with implications for radiative forcing estimates. *Proc. Nat. Acad. Sci.* **2009,** *106*, (29), 11872-11877.

45. Qiu, C.; Zhang, R. Y., Physiochemical Properties of Alkylaminium Sulfates: Hygroscopicity, Thermostability, and Density. *Environ. Sci. Tech.* **2012,** *46*, (8), 4474-4480.

46. Johnson, G.; Ristovski, Z.; Morawska, L., Application of the VH-TDMA technique to coastal ambient aerosols. *Geophysical Research Letters* **2004,** *31*, (16).

47. Spencer, M. T.; Shields, L. G.; Prather, K. A., Simultaneous measurement of the effective density and chemical composition of ambient aerosol particles. *Environ. Sci. Tech.* **2007,** *41*, (4), 1303-1309.

48. Hughes, L. S.; Allen, J. O.; Salmon, L. G.; Mayo, P. R.; Johnson, R. J.; Cass, G. R., Evolution of nitrogen species air pollutants along trajectories crossing the Los Angeles area. *Environ. Sci. Tech.* **2002,** *36*, (18), 3928-3935.

49. Spencer, M. T.; Prather, K. A., Using ATOFMS to determine OC/EC mass fractions in particles. *Aerosol Sci. Technol.* **2006,** *40*, (8), 585-594.

50. Zauscher, M. D. Extending the Physicochemical Characterization of Aerosol Particles in California. Ph.D. Thesis, University of California, San Diego, La Jolla, CA, 2012.

51. Angelino, S.; Suess, D. T.; Prather, K. A., Formation of aerosol particles from reactions of secondary and tertiary alkylamines: Characterization by aerosol time-of-flight mass spectrometry. *Environ. Sci. Tech.* **2001,** *35*, (15), 3130-3138.

52. Linstrom, P. J.; Mallard, W. G. NIST Chemistry WebBook, NIST Standard Reference Database Number 69. National Institute of Standards and Technology, Gaithersburg, MD, USA, http://webbook.nist.gov, 2012.

53. McLafferty, F. W., *Interpretation of Mass Spectra*. 3rd ed.; University Science Books: Mill Valley, CA, USA, 1980.

54. Creamean, J. M.; Ault, A. P.; Ten Hoeve, J. E.; Jacobson, M. Z.; Roberts, G. C.; Prather, K. A., Measurements of Aerosol Chemistry during New Particle Formation Events at a Remote Rural Mountain Site. *Environ. Sci. Tech.* **2011,** *45*, (19), 8208-8216.

55. Hatch, L. E.; Creamean, J. M.; Ault, A. P.; Surratt, J. D.; Chan, M. N.; Seinfeld, J. H.; Edgerton, E. S.; Su, Y. X.; Prather, K. A., Measurements of Isoprene-Derived Organosulfates in Ambient Aerosols by Aerosol Time-of-Flight Mass Spectrometry - Part 1: Single Particle Atmospheric Observations in Atlanta. *Environ. Sci. Tech.* **2011,** *45*, (12), 5105-5111.

56. Nowak, J. B.; Neuman, J. A.; Bahreini, R.; Middlebrook, A. M.; Holloway, J. S.; McKeen, S. A.; Parrish, D. D.; Ryerson, T. B.; Trainer, M., Ammonia sources in the California South Coast Air Basin and their impact on ammonium nitrate formation. *Geophysical Research Letters* **2012,** *39*.

57. Schade, G. W.; Crutzen, P. J., Emission of Aliphatic-Amines from Animal Husbandry and Their Reactions - Potential Source of N2o and Hcn. *Journal of Atmospheric Chemistry* **1995,** *22*, (3), 319-346.

58. Sorooshian, A.; Murphy, S. N.; Hersey, S.; Gates, H.; Padro, L. T.; Nenes, A.; Brechtel, F. J.; Jonsson, H.; Flagan, R. C.; Seinfeld, J. H., Comprehensive airborne characterization of aerosol from a major bovine source. *Atmos. Chem. Phys.* **2008,** *8*, (17), 5489-5520.

59. Ge, X. L.; Wexler, A. S.; Clegg, S. L., Atmospheric amines - Part II. Thermodynamic properties and gas/particle partitioning. *Atmos. Environ.* **2011,** *45*, (3), 561-577.

60. Zhou, L.; Rai, A.; Zachariah, M. R., Component and morphology biases on quantifying the composition of nanoparticles using single-particle mass spectrometry. *Int. J. Mass spectrom.* **2006,** *258*, (1-3), 104-112.

61. Vaden, T. D.; Song, C.; Zaveri, R. A.; Imre, D.; Zelenyuk, A., Morphology of mixed primary and secondary organic particles and the adsorption of spectator organic gases during aerosol formation. *Proc. Nat. Acad. Sci.* **2010,** *107*, (15), 6658-6663.

62. Moldanova, J.; Fridell, E.; Popovicheva, O.; Demirdjian, B.; Tishkova, V.; Faccinetto, A.; Focsa, C., Characterisation of particulate matter and gaseous emissions from a large ship diesel engine. *Atmos. Environ.* **2009,** *43*, (16), 2632-2641.

63. Yao, X. H.; Rehbein, P. J. G.; Lee, C. J.; Evans, G. J.; Corbin, J.; Jeong, C. H., A study on the extent of neutralization of sulphate aerosol through laboratory and field experiments using an ATOFMS and a GPIC. *Atmos. Environ.* **2011,** *45*, (34), 6251-6256.

64. Larson, T. V.; Ahlquist, N. C.; Weiss, R. E.; Covert, D. S.; Waggoner, A. P., Chemical Speciation of H2SO4-(NH4)2SO4 Particles Using Temperature and Humidity Controlled Nephelometry. *Atmos. Environ.* **1982,** *16*, (6), 1587-1590.

5 Mixing-state dependence of nitrate volatility from atmospheric particles

5.1 Abstract

Nitric acid is one of the major semi-volatile inorganic components of the atmosphere; its distribution between the gas and particle phases can significantly influence its atmospheric lifetime and environmental impacts. Most studies of atmospheric aerosol chemistry assume that the distribution of nitrate is largely dictated by ammonium nitrate partitioning and/or that all particle constituents are homogeneously dispersed among the aerosol population. Herein, we studied the role of different particle core composition in altering the volatility of particulate nitrate. During the summer 2005 Study of Organic Aerosols in Riverside field campaign, the mixing state of thermally-conditioned particle residuals was measured by aerosol time-of-flight mass spectrometry. It is demonstrated herein through these single-particle volatility measurements and thermodynamic modeling that the presence of metal ions impacts the partitioning of semi-volatile nitrate. The modeling results suggest that reduced availability of ammonium and increased liquid water content contributed to the suppression of nitrate volatility even at low relative concentrations of metal ions. Comparisons between measurements and model results imply that complex particle morphologies may exist in the Riverside region due to the extensive secondary organic and inorganic aerosol formation occurring during summertime.

5.2 Introduction

Nitric acid is a major global air pollutant that forms photochemically through the gas-phase reaction of OH radical with NO_x ($NO+NO_2$).[1] NO_x species are predominantly emitted from combustion sources (e.g., vehicular and industrial).[2] Nitric acid is semi-volatile and highly water soluble and can thus partition significantly to the particle phase, making nitrate one of the dominant aerosol components in California.[3] The gas-particle distribution of nitrate can impact the nitrogen cycle by influencing the atmospheric lifetime of reactive nitrogen species.[4] For instance, the dry deposition velocity of gas-phase nitric acid is ~20 times faster than that of the aerosol phase.[4] The resulting difference in lifetime can impact the transport of nitrogen species and therefore regional nutrient deposition.[5] Particulate nitrate can also influence the water uptake and optical properties of aerosols. Nitrate salts are highly hygroscopic/water soluble and can therefore promote cloud droplet formation.[6,7] Nitrate aerosols have also been shown to directly

scatter incoming solar radiation and can therefore act to cool the climate system.[8,9] These effects are expected to increase in relative importance over the next few decades due to air quality regulations aimed at reducing sulfate aerosol.[10,11]

Formation of particulate nitrate can occur by a number of reactions: (1) by co-condensing with ammonia, the dominant Brønsted base in the atmosphere, forming NH_4NO_3:

$$NH_{3(g)} + HNO_{3(g)} \rightleftarrows NH_4NO_{3(p)} \rightleftarrows NH_{4(aq)}^{+} + NO_{3(aq)}^{-} \quad (5.1)$$

The dissociation of ammonium nitrate into solvated ions reduces the volatility since acids and bases can only evaporate in their neutral form,[12] which thus increases the partitioning to the particle phase. Nitrate partitioning by Equation 5.1 is very sensitive to temperature and relative humidity (RH) through their impacts on vapor pressure and liquid water content, respectively.[13,14] (2) Nitric acid can also react with sea salt[15] (shown here) or mineral dust particles,[16] to form non-volatile nitrate salts:

$$NaCl_{(p)} + HNO_{3(g)} \rightarrow NaNO_{3(p)} + HCl_{(g)} \quad (5.2)$$

(3) Another significant pathway to the formation of particulate nitrate is the nighttime heterogeneous uptake of N_2O_5, a nocturnal reservoir for NO_x species:[17]

$$N_2O_{5(g)} + H_2O_{(p)} \rightarrow 2HNO_{3(p)} \quad (5.3)$$

In the above reactions, the subscript (p) indicates species in the particle phase, which could be solid or aqueous. From these reactions, it is clear that nitrate is a secondary aerosol component and may condense onto particles from all sources. Therefore nitrate may experience different chemical environments in particles of different composition that could influence the gas-particle partitioning. The work herein probes the effect of mixing state in altering the volatility of nitrate.

Measurements of ambient aerosol volatility were obtained during the Study of Organic Aerosols in Riverside (SOAR-1) field campaign in the summer of 2005.[18-20] Riverside is located in the inland region of the South Coast Air Basin downwind of Los Angeles. The high levels of NO_x and volatile organic compounds from vehicular emissions in the LA area undergo extensive photochemical aging during inland transport that generates high atmospheric loadings of nitric acid and secondary organic aerosol.[21] During transit to Riverside, air masses originating at the coast also pass through the Chino area that is home to vast agricultural and animal husbandry

operations.[22] These industries represent the largest source (~60%) of NH_3 emissions in Southern California.[22,23] The high ammonia concentrations drive the formation of particulate ammonium nitrate (Equation 5.1);[24,25] indeed, 51-68% of the nitric acid has been measured in the particle phase downwind of the dairies compared to 16% directly downwind of LA.[23] As a result, this region is characterized by some of the highest particulate matter concentrations in the country,[26] more than half of which has been attributed to ammonium nitrate.[3] Amines are also emitted from animal husbandry operations and can similarly act as bases to neutralize atmospheric acids analogous to Equation 5.1.[19] In addition, single-particle measurements in the Riverside region have demonstrated the presence of transported sea salt, dust, biomass burning, and other metal-containing particles.[27,28] Nitric acid or N_2O_5 (at night), can react with these particles via reactions similar to Equation 5.2 and 5.3, forming non-volatile nitrate salts within the particle phase. Since different forms of nitrate display a range of volatilities, vaporization of nitrate can be significantly impacted by the chemical mixing state of the aerosol population, in particular the presence of metals.

Model studies have investigated the role of sea salt and mineral ions on the partitioning of nitrate.[2,29-32] However, to our knowledge, most studies have based the metal ion concentrations on bulk measurements, and assume that aerosols contain equal amounts of these metal species. Previous model results underpredicted measured nitrate loadings in the South Coast Air Basin, with the discrepancy partly attributed to the assumption of internal mixing.[33] Kleeman *et al.*[34] developed a model to characterize the aging of externally mixed aerosol populations; however, the model was initialized with bulk-phase measurements and therefore required assumptions regarding the chemical associations within individual particles. Single-particle measurements are uniquely suited to determine the chemical mixing state of aerosols and clearly show that not all particles contain metals. Therefore internal mixing assumptions essentially dilute the metal concentration by taking the ensemble-averaged ion concentration. The relative metal concentration within the subset of the aerosol population that does contain metals will certainly be higher than the average and correspondingly will be zero for those that are free of metal ions. It is demonstrated herein through single-particle volatility measurements and thermodynamic modeling that the distribution of metals does indeed impact the partitioning of semi-volatile nitrate.

5.3 Experimental

Field measurements and subsequent data analysis were performed as described in Chapter 4. Briefly, a thermodenuder was used in line with ATOFMS and AMS on August 12th, 2005 during the SOAR-1 campaign. The heated particle residuals were used to determine the volatility of nitrate from particles of different composition that were identified based on their mass spectral fingerprints and source signatures.

5.4 Results & Discussion

5.4.1 Nitrate Volatility Measurements

The mixing state of aerosols detected in Riverside during SOAR-1 has been previously described.[19,27] The relative number fractions of the particle types detected at each TD temperature were shown in Chapter 4 (Figure 4.1a). Mass spectra for unheated particles from the 3 dominant particle classes are shown in Figure 5.1. Organic carbon (OC) particles were the dominant particle type, and are characterized by organic fragments at $^{27}C_2H_3^+$, $^{37}C_3H^+$, and $^{43}C_2H_3O^+$ internally mixed with elemental carbon (EC) markers, C_n^+ (n = 1-3). The next most abundant particle types are classified as vanadium-rich and biomass burning. Vanadium-rich particles are emitted from ships[35,36] and light-duty vehicles[37,38] and contain dominant $^{51}V^+$ and ^{67}VO+ peaks with smaller mass spectral contributions from organics and other metals (e.g., $^{23}Na^+$). Biomass burning (BB) particles contain a strong potassium ($^{39}K^+$) ion signal associated with organic markers and $^{23}Na^+$.[39] Other minor particle classes (see Figure 4.1a) included a mixed EC-OC class, EC, aromatic (which contains markers for polycyclic aromatic hydrocarbons), amine class (which contains a dominant $^{86}(C_2H_5)_2NCH_2^+$ ion marker), dust, and sea salt. Each of these particle types was internally mixed with nitrate and sulfate, as well as ammonium ($^{18}NH_4^+$) and amines ($^{86}(C_2H_5)_2NCH_2^+$), as clearly indicated in the spectra for the 3 representative particle types in Figure 5.1.

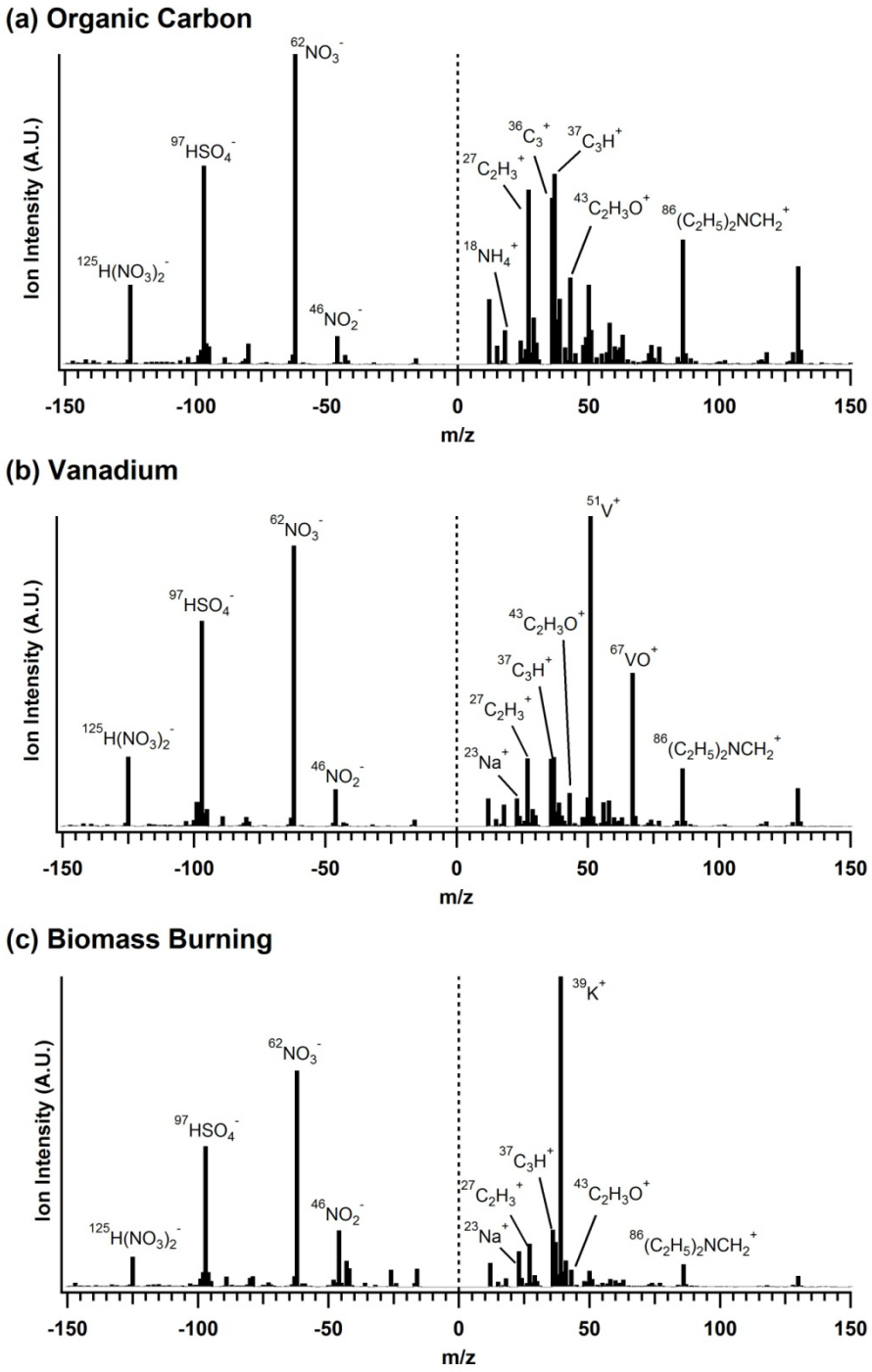

Figure 5.1 Average mass spectra for unheated (a) organic carbon, (b) vanadium-rich, and (c) biomass burning particles.

ATOFMS detects three main markers for nitrate species: $^{46}NO_2^-$, $^{62}NO_3^-$, and $^{125}H(NO_3)_2^-$ (Figure 5.1). The $^{46}NO_2^-$ and $^{62}NO_3^-$ ion peaks can arise from both non-refractory and refractory nitrate (e.g., KNO_3). Since a proton is required to generate the $^{125}H(NO_3)_2^-$ ion cluster, this

marker indicates that non-refractory counter ions were present within the particles (e.g., H^+, NH_4^+). Acidic particles are unlikely to exist in the Riverside area that is characterized by very high ammonia/amine levels; it is therefore postulated that the $^{125}H(NO_3)_2^-$ ion marker is representative of ammonium or aminium nitrate salts. This assessment is supported by previous positive matrix factorization analysis of ATOFMS measurements from aging BB plumes, wherein the $^{125}H(NO_3)_2^-$ ion marker was predominantly associated with ammonium or aminium nitrate factors, but the $^{46}NO_2^-$ and $^{62}NO_3^-$ ions were associated with both an ammonium nitrate factor and nitrate factors associated with potassium.[40]

The particle residues following heating were analyzed to investigate the volatility of nitrate from the OC, BB, and vanadium particle types. The thermograms for total particulate nitrate (i.e., $^{46}NO_2^- + {}^{62}NO_3^- + {}^{125}H(NO_3)_2^-$) are shown in Figure 5.2 for these representative particle types. These thermograms are dominated by the contribution from $^{62}NO_3^-$ due to its strong peak intensity (Figure 5.1). The fraction remaining plots represent the change in normalized peak areas calculated following the internal standard method described in Chapter 4 using $^{36}C_3^+$, $^{51}V^+$, and $^{39}K^+$ as the internal standards for the OC, vanadium, and BB particle types, respectively. This method has demonstrated good agreement between ATOFMS and the independent, quantitative AMS measurements of non-refractory nitrate (Chapter 4). The nitrate thermogram measured by the AMS for the same aerosol population is included in Figure 5.2, as a reference point for the changes in bulk, non-refractory nitrate mass with heating.

As discussed by Huffman *et al.*,[18] and shown in Figure 5.2a, the measured volatility of pure ammonium nitrate particles is significantly higher than nitrate within ambient non-refractory aerosols, highlighting that different chemical interactions can influence evaporation. ATOFMS can further probe the evaporation as a function of chemical mixing-state, wherein more extreme behaviors may be observed among particles of different composition. Figure 5.2a shows that significantly higher nitrate fractions remaining were observed for the BB and vanadium-rich particle types than in the OC particles, indicating that nitrate was more strongly bound in these particles. However, since different particle matrices are known to exhibit different ionization effects in single particle mass spectrometers,[41] the thermogram of the individual $^{125}H(NO_3)_2^-$ ion marker are also included in Figure 5.2b. In all three particle types, the $^{125}H(NO_3)_2^-$ thermograms were well correlated with each other and the AMS data, indicating that ionization effects were likely not the main factor influencing the nitrate thermograms. Otherwise, all nitrate markers would be expected to experience similar effects. It remains possible that there was a small

instrumental bias impacting the $^{46}NO_2^-$ and $^{62}NO_3^-$ ion markers; however, it seems unlikely that an artifact could fully account for the large differences in the fractions remaining relative to the OC type (0.72 and 0.55 higher than the OC thermogram for the BB and vanadium types, respectively, at 54 ºC), given the good agreement with the independent AMS measurements for the $^{125}H(NO_3)_2^-$ ion marker across all particle types (Figure 5.2b). Therefore, the differences observed among these particle types in Figure 5.2a can be attributed to real differences in nitrate volatility from these particles that can be attributed to chemical interactions. The different behavior for the $^{125}H(NO_3)_2^-$ ion marker will be discussed below (Section 5.4.3).

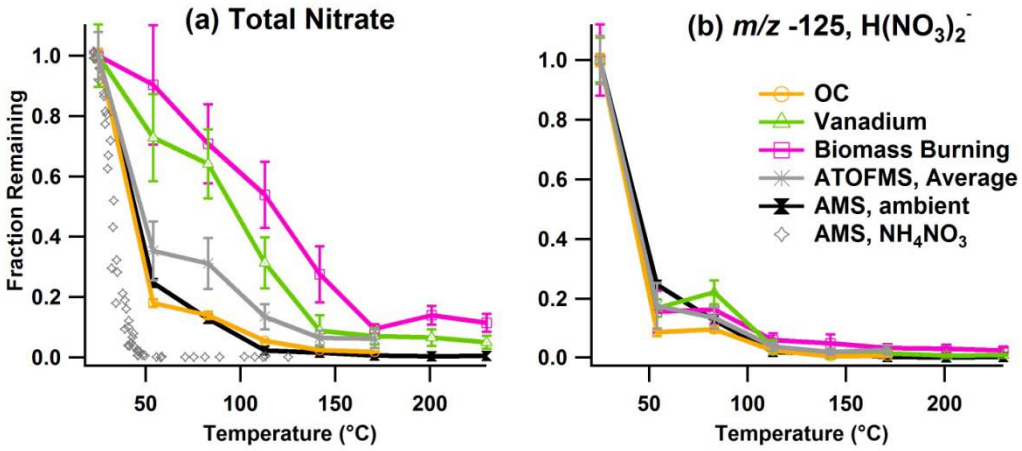

Figure 5.2 ATOFMS and AMS nitrate thermograms. Panel (a) represents the change in the total nitrate ($^{46}NO_2^- + {}^{62}NO_3^- + {}^{125}H(NO_3)_2^-$) for the OC, vanadium, and BB particle types and the average thermogram across all ATOFMS particle types. Gray diamonds represent laboratory AMS measurements of pure ammonium nitrate.[42] (b) Thermogram of the $^{125}H(NO_3)_2^-$ ion marker only. Error bars represent 95% confidence intervals. Note that the data for the 'OC' and 'ATOFMS, Average' curves end at 171 °C due to a known artifact with the OC particle type at higher temperatures described in Chapter 4.

The key difference between the BB and vanadium particle types compared to the OC particles is the presence of refractory material (alkali and transition metals- Figure 5.1), indicating that nitrate volatility was influenced by metal cations. It should be noted that the strong peak intensities of the metal components in the vanadium and BB spectra (Figure 5.1 b & c) do not necessarily indicate that they were the dominant species in these particles. Rather, these metals were preferentially ionized in the LDI process due to their lower ionization potentials.[43,44] Therefore the actual concentration of metal cations cannot be deduced from the mass spectra, but were likely a small percentage of the particle mass. For instance, potassium represents only 0.5-16% of the particulate mass in smoke emissions,[39] whereas it is the overwhelming component in the BB mass spectra (Figure 5.1c). Further, collocated measurements during SOAR-1 indicated

that particles from different sources exhibited similar effective densities due to the high degree of secondary components,[45] indicating that the particle cores made a small contribution to the particle mass. Although, note that the total nitrate thermogram from BB particles is systematically higher than vanadium-rich particles, with more than twice as much nitrate remaining at 230 ºC (11±3 vs. 5±2%), indicating that BB particles may contain more refractory metal ions resulting in higher levels of non-volatile metal-nitrate salts. However, vanadium has also been hypothesized to catalyze the production of sulfuric acid within these particles,[35,46] thus it is also possible that a greater fraction of the metal ions were neutralized by sulfate rather than nitrate. From Figure 5.1, the sulfate/nitrate ion peak ratios ($^{97}HSO_4^-$ / $^{62}NO_3^-$) are 0.73, 0.64, and 0.65 for the vanadium, OC, and BB particles, respectively, indicating that higher sulfate content within the vanadium particles may have also affected the evaporation of nitrate from these particles, due to reduced presence of refractory nitrate salts. Therefore, further studies are necessary to better constrain the relative concentrations of refractory material within these particles.

It follows from the above discussion and Figure 5.2 that ~89±3% and 95±2% of the total particulate nitrate evaporated by 230 ºC from the BB and vanadium particles, respectively. Therefore, most of the nitrate could not have existed as metal-nitrate salts, which would be non-volatile at these TD temperatures. The high fractions remaining at low TD temperatures thus imply that the metal ions influenced even non-refractory nitrate. There also appears to have been distinct volatility behaviors, as indicated by the thermogram of $^{125}H(NO_3)_2^-$ (non-refractory nitrate) compared to the total nitrate signal. A thermodynamic model was applied to address these questions and better elucidate the role of metal cations on the volatility of nitrate, as described below.

To further demonstrate the impact of the internal vs. external mixing assumptions, the thermograms of total nitrate from all ATOFMS particle types (including the minor classes) were averaged on a particle number-weighted basis and are included in Figure 5.2. The average thermogram provides the bulk perspective (i.e., akin to filter measurements), assuming the metal ions were distributed evenly over all measured particles. However, the ATOFMS data cannot quantify the nitrate mass within each particle type, therefore weighting the individual thermograms by particle number implicitly assumes that each particle contained the same nitrate mass at ambient temperature. This assumption is reasonable to a first approximation given the high degree of secondary ammonium nitrate in the Riverside area, as described above, so this

analysis can provide some insight into the role of particle mixing state. It can be seen in Figure 5.2 that the nitrate fractions remaining in the BB and vanadium particle types are significantly higher than the average thermogram, which in turn is higher than the thermogram of the OC particle type. As described in the Introduction, when refractory material is externally mixed in an aerosol population, the relative concentration of metals within single particles can be significantly higher than the average composition would suggest. Herein, the metals were confined to a small fraction of the particle population (~20% by number- Figure 4.1a) and correspondingly exert a much larger effect on nitrate volatility within these particles. In contrast, the OC particles did not contain metal ions and behaved as purely non-refractory nitrate, as indicated by the agreement with the AMS thermogram and the similarities between the total nitrate and $^{125}H(NO_3)_2^-$ ion marker thermograms (Figure 5.2). Therefore, individual particles can display vastly different volatility behaviors relative to the average composition of the aerosol population. Therefore assumptions of internal mixing can skew estimates of climate-relevant properties which will depend on the relative amounts of soluble material within each particle.

5.4.2 Model Studies

The Extended Aerosol Inorganics Model (E-AIM, http://www.aim.env.uea.ac.uk/aim/aim.php) was used to probe the effect of metal ions on the partitioning of nitrate. 'Model IV' of E-AIM treats systems containing H^+, NH_4^+, Na^+, SO_4^{2-}, NO_3^-, Cl^-, and H_2O.[47] E-AIM calculates the distribution of a given input composition among the gas, liquid, and solid phases assuming thermodynamic equilibrium. The equilibrium condition is determined by minimizing the Gibbs free energy of the system. Of particular interest herein, is the evaporation of particulate nitrate, which for these model systems will occur via Equation 5.1. The equilibrium expression is given by:[31,47]

$$K = \frac{x_{NH_4^+} f_{NH_4^+} x_{NO_3^-} f_{NO_3^-}}{p_{NH_3} p_{HNO_3}} \quad (5.4)$$

where x is the mole fraction, f is the mole fraction-scale activity coefficient, and p is the partial pressure. In Equation 5.4, Henry's Law has been modified to account for the equilibria of the aqueous dissociation of HNO_3 and the protonation of NH_3 because the presence of the neutral species (NH_3, HNO_3) in the aqueous phase of ambient particles can generally be neglected.[47,48] Aerosol particles in the sub-saturated RH regime are also highly concentrated (tens of molal) and thus non-ideality cannot be ignored.[49] Activity coefficients for electrolytes are calculated in E-AIM via parameterizations of measured interaction parameters.[48] The activity parameterizations

of the model used herein are valid for both dilute and saturated solutions.[47] Because E-AIM was designed for accuracy rather than computational efficiency, it can be regarded as a complete and robust thermodynamic model.[50] However, it is a bulk-phase model, so it assumes all components are internally mixed.

5.4.2.1 Initial Model Test: Pure Ammonium Nitrate

As an initial test of the ability of the model to represent the TD data, the predicted volatility of pure ammonium nitrate was compared to measurements of the pure salt measured by the TD-AMS system.[18] In these tests, the mass concentration of NH_4NO_3 was 6.4 µg/m^3 (4.96 µg/m^3 as nitrate), noted as 'Low Mass' in Figure 5.3). During the experimental measurements, the aerosol was dried to <20% RH;[18] therefore, the model was run at 20% RH for the most accurate comparison. For this model calculation, deliquescence behavior was assumed; therefore all modeled particulate nitrate existed in the solid form. The resulting thermograms are shown in Figure 5.3.

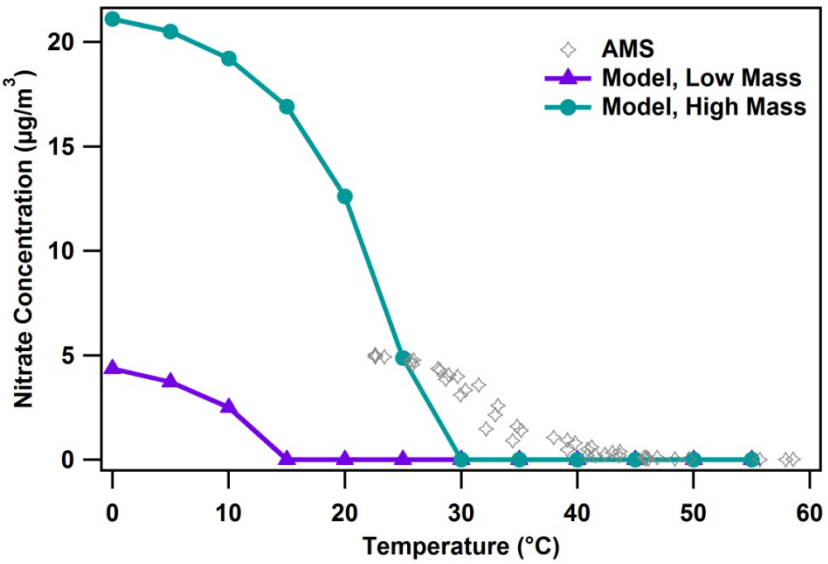

Figure 5.3 Measured (AMS) and modeled volatility of pure ammonium nitrate particles. In the 'low mass' model case, the AMS-measured nitrate mass at ambient temperature was used as model input; for the 'high mass' case, the input mass was adjusted to match the AMS mass at 25 °C. All concentrations represent nitrate mass only.

When the ammonium nitrate mass measured by the AMS was used as the model input (the 'low mass' case in Figure 5.3), full evaporation was predicted by 15 ºC. It is likely that a substantial fraction of the initial ammonium nitrate mass evaporated prior to analysis during the experimental measurement. More than 4-fold higher mass (21.1 µg/m^3 of nitrate) was required in

the model input for the model to match the measured nitrate mass at 25 ºC (the 'high mass' case in Figure 5.3). However, even with a high ammonium nitrate mass loading, it still completely evaporated by 30 ºC and under predicted the measured nitrate mass, which persisted up to ~40 ºC. It is clear from Figure 5.3 that the assumption of thermodynamic equilibrium cannot accurately recreate the TD measurements. This finding is consistent with the current prevailing thought that the residence times in TDs (generally <20 seconds[51]) are far too short to achieve equilibrium,[52,53] which can take minutes to hours for ambient submicron particles.[54] Dzepina *et al.*[55] found that a thermodynamic model predicted evaporation of organic aerosols at significantly lower temperatures than a kinetic model fully describing TD processes. The ammonium nitrate measurements in the TD likely had not equilibrated, and would therefore require a kinetic modeling approach to recreate the extent of evaporation within the TD, as has been achieved for organic aerosols.[56] Such kinetic limitations within TDs therefore preclude any attempts to accurately model the ambient TD data thermodynamically. However, a thermodynamic model can still be used to assist in the interpretation of the ambient measurements by shedding light on the behavior of nitrate in solutions containing metal electrolytes. It is also more representative of the behavior in the atmosphere, where submicron particles are likely to equilibrate within a few hours.[54] Therefore, the model calculations focus on the more atmospherically-relevant temperature range from 0-55 ºC, rather than the full TD range of 25-230 ºC. The upper end of this new range (55 ºC) is the highest temperature modeled by E-AIM, yet also overlaps with the lowest TD temperature used for the ambient data collection (54 ºC). The impacts of aerosol composition on nitrate volatility should be clearly observable over this range given the strong temperature dependence of ammonium nitrate evaporation below 30 ºC (Figure 5.3).

5.4.2.2 Effect of Metals on Nitrate Partitioning

In these calculations, a metal-free "base-case" composition (sulfate, nitrate, ammonia) was defined at levels consistent with measured values observed in SOAR-1.[57] Nitrate and sulfate values were based on the average measured AMS mass concentrations on August 12th, 2005 (K. Docherty, personal communication) and are given in Table 1. Note that sulfate and nitrate were internally mixed during SOAR-1 (Figure 5.1). Although nitric acid was in equilibrium between the gas and particle phases, only the particle-phase concentration was used, since the total (gas + particle) nitrate concentration during the measurements is unknown. Ammonia was input as a gas-phase component to keep its levels in excess of the acid concentration (Table 1), in

accordance with previous measurements in the region.[2,23] The equilibrium concentrations were calculated over the temperature range 0-55 ºC in 5 ºC steps.

Table 5.1 Concentration of components used for model initialization in the base case scenario.

Component	Mass Concentration ($\mu g/m^3$)	Molar Concentration (mol/m^3)
Nitrate	12.4	2×10^{-7}
Sulfate	4.44	0.5×10^{-7}
Ammonia	8.5	5×10^{-7}

As seen in Figure 5.1, a variety of alkali and transition metals were observed in the predominant particle types in SOAR-1, in particular K^+, Na^+, and V/VO^+. However, only sodium ions can be modeled in E-AIM and so we assume that all metals behave as sodium. Moya *et al.*[30] demonstrated that mineral cations could be modeled effectively as equivalent amounts of sodium. However, later studies expressed that this should be considered only as an approximation due to the different deliquescence (D)RHs for different salts.[29] Potassium salts, for instance, have higher DRH than the corresponding sodium salts,[58,59] and will therefore remain solid at higher RHs. The potassium salts of BB may therefore behave slightly differently, but this approach is reasonable given the general understanding sought herein. E-AIM cannot model metastable salts for systems containing sodium and therefore the model exclusively follows deliquescence behavior. Under such conditions, for RH < 80%, sulfate salts precipitated out at 30 ºC, which eliminated all liquid water and drove ammonium nitrate to the gas phase. Under such conditions, sodium had no effect on keeping nitrate in the particle phase to high temperature (> 30 ºC). Using high RH (90%) was found to maintain an aqueous solution for most systems with sodium up to 55 ºC; therefore the RH was fixed at 90% in order to simulate the effect of sodium in aqueous solutions. This assumption is reasonable since the nitrate salts considered herein do not effloresce and the sulfate salts effloresce below 60% RH (55% for Na_2SO_4 and 35% for $(NH_4)_2SO_4$).[59] Ansari and Pandis[33] modeled the influence of efflorescence vs. deliquescence behavior on the partitioning of ammonium nitrate and generally found that nitrate loadings are higher along the efflorescence curve. Rood *et al.*[60] also found that aerosols in Riverside existed as metastable solutions more the half of the time for RHs in the range of 45-75%. For comparison, the average RH during the SOAR-1 measurements was 68%, with a range of 37-93%. Thus, there was a significant likelihood that the ambient aerosol particles existed as aqueous solutions during the measurement period.

The model was run by adding sodium to the base-case composition, with Na^+ concentrations ranging from 0-6.9 µg/m^3. The highest concentration (3 x 10^{-7} mol/m^3) represents the case where sodium fully balanced both nitrate and sulfate. While these calculations represent the total mass in the system, the range of sodium concentrations can be related to the *relative* concentrations for various mixing-state assumptions. For instance, low sodium concentrations could represent the internally-mixed case where the metals were spread over all particles; whereas the base case composition and high sodium concentrations could represent the particles in an externally-mixed population. The model results are shown in Figure 5.4b, with the color contours demonstrating the change in nitrate concentration relative to the base case, shown for reference in Figure 5.4a. The dashed line in Figure 5.4b indicates the Na^+ concentration that balances sulfate. Below this line, all of the nitrate is able to evaporate as ammonium nitrate; above this level, a fraction of the nitrate will be necessary to neutralize the excess Na^+ ($[Na^+] - 2[SO_4^{2-}]$).

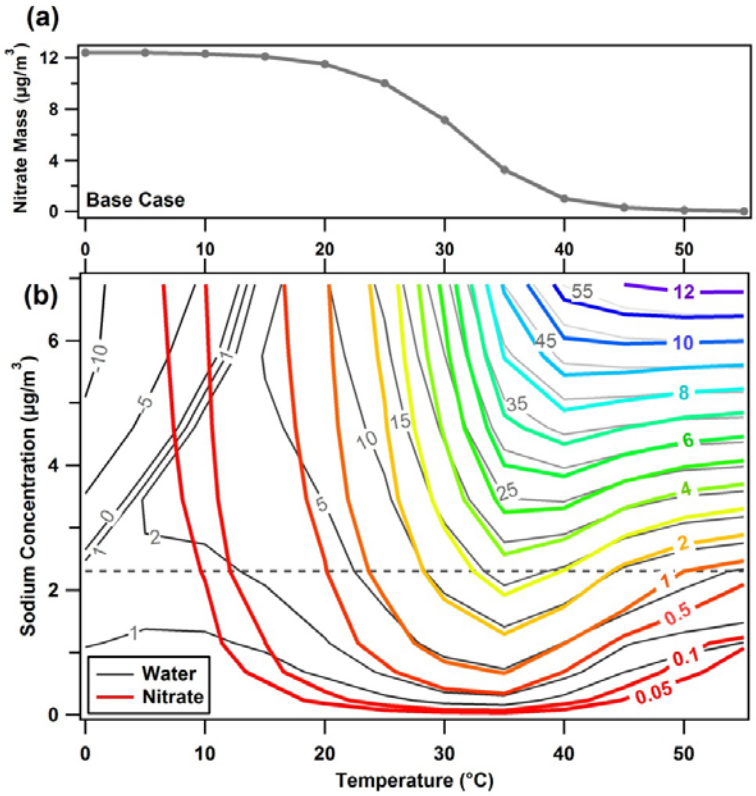

Figure 5.4 E-AIM model results at 90% RH for (a) the temperature-dependent nitrate mass assuming the base-case composition (sodium-free); and (b) the difference in nitrate (color) and water (gray) mass concentrations (µg/m³) for cases with sodium minus the base case. The dashed line represents the point at which sodium balances sulfate; above this line, nitrate is necessary to balance the excess sodium.

At low temperature, the vapor pressure of ammonium nitrate is sufficiently low that nearly 100% of the nitrate partitioned to the particle phase, even in the base case (top panel). Therefore, a negligible difference was observed between the base case and the addition of sodium at all concentrations. Sodium began to have an influence starting at ~10 ºC, around the point at which NH_4NO_3 began to evaporate in the absence of sodium ions. However, varying the sodium concentration did not have much effect until about 20 ºC, where significant evaporation began in the base case. Above 20 ºC, increasing sodium concentrations significantly impacted the particulate nitrate mass. Even very low levels of sodium influenced nitrate partitioning. At concentrations where nitrate was not required to balance sodium (below the dashed line), particulate nitrate was as much as ~3 μg/m^3, or about 2-fold greater than the base case at 35 ºC. This result can be understood in terms of the equilibrium Equation 5.4. Because the system is always charge neutral and the inputs for sulfate and nitrate were fixed, the proton concentration for each case was reduced by the [Na^+]. Therefore, for fixed anion concentrations and the requirement of electroneutrality, the concentration of NH_4^+ must decrease in the presence of Na^+ due to the reduced availability of protons in solution, with a corresponding increase in the partial pressure of NH_3. These effects would act to decrease the reaction quotient and therefore the concentration of NO_3^- must increase (and the partial pressure of HNO_3 must decrease) to maintain equilibrium (Equation 5.4). For instance, at 35 ºC the nitrate mole fraction increased from 0.0274 in the base case to 0.0374 at [Na^+] = 2.3 μg/m^3 (dashed line in Figure 5.4b). In contrast, the ammonium mole fraction decreased from 0.0781 to 0.037 over the same range. The activity coefficients for these species changed only marginally over this range: nitrate increased from 0.383 to 0.401 and ammonium decreased from 0.412 to 0.411, highlighting that the reduced availability of ammonium contributed to the suppression of nitrate volatility rather than changes in solution non-ideality effects. At higher temperatures, while ammonium nitrate did evaporate to some extent (as indicated by the bend in the contours toward higher sodium concentration) there was still as much as 1 μg/m^3, or ~8% of the total nitrate, remaining in the particle phase at 55 ºC for low sodium levels. Note that for these low sodium levels (below the dashed line) the ammonium concentration still exceeded that of nitrate. Therefore, the presence of sodium reduced the volatility of ammonium nitrate even when nitrate was not necessary to maintain charge balance. With increasing sodium levels (above the dashed line), nitrate became necessary to balance the sodium ions, thus suppressing the evaporation even more at high temperatures: the curves flatten out above 35 ºC due to the higher fraction of $NaNO_3$. At the highest sodium

concentration, where the anions existed exclusively as sodium salts, 100% (12.4 μg/m^3) of the nitrate remains, as expected, due to the lack of volatilizable forms of nitrate.

Liquid water content also played a significant role in the partitioning of nitrate. The change in liquid water content relative to the base case is included in Figure 5.4b (gray contours). It is clear that the trends in water follow the trends in nitrate very well, with nitrate and water content increasing with increasing sodium concentration. In the region of low temperature and high [Na^+], where the water content is lower than the base case (negative values), E-AIM predicted the formation of solid sodium sulfate decahydrate, for which the DRH is 93%[59] (i.e., above the 90% RH used in the model run). The presence of solid inclusions would lower the amount of electrolytes and therefore the associated water content. However, it should be mentioned that for all cases where a solid phase was predicted in this system, the result failed an internal test of equilibrium by E-AIM between the aqueous and solid phases and so the validity of this result is suspect. However, since most of the nitrate is in the particle phase at these temperatures (Figure 5.4a), the formation of solid sodium sulfate had little impact on the assessment of nitrate volatility. The remaining regions of Figure 5.4b demonstrate that liquid water increased coincident with the increase in nitrate mass concentration. Since the sodium salts of nitrate and sulfate are more hygroscopic than the corresponding ammonium salts,[61] the condensed phase will experience greater hygroscopic growth when sodium is present. Previous work has also shown that even low concentrations of sodium nitrate in ammonium nitrate can lower the DRH,[62] and therefore increase the water uptake properties. The link between liquid water content and particulate nitrate loadings is likely a synergistic effect: ammonium nitrate is less volatile as an aqueous solution than as a solid,[63] so the increased water content at low sodium levels helped to keep nitrate in the particle phase up to higher temperatures. The increased electrolyte content also induced additional water uptake.

The enhanced nitrate and liquid water content can influence aerosol optical properties. As discussed by Martin *et al.*,[63] the radiative forcing attributed to sulfate-nitrate-ammonium systems is higher along the efflorescence curve than the deliquescence curve due to higher ammonium nitrate and aerosol water, which impact the aerosol size and refractive index. Further, Moffet *et al.*[64] measured different refractive indices between fresh BB particles and those that had acquired nitrate/water via atmospheric processing. As shown by these model results, the addition of even small relative concentrations of sodium may further enhance these optical effects by retaining additional nitrate and water. Since individual particles can behave very differently than

the average composition, as described above, it is important to account for the external mixing effects in predictions of aerosol radiative properties.

5.4.3 Measurement-Model Comparison

The model results imply that the presence of sodium can impact the volatility of nitrate, even without explicitly forming sodium nitrate salts, but rather by reducing the availability of ammonium and increasing the liquid water content. These results could help explain the observations from the ambient measurements (Figure 5.2) where the presence of metals influenced the volatility of nitrate, even though only 5±2% and 11±3% of the nitrate existed as non-volatile salts in the vanadium-rich and BB particles, respectively. Given that only these small fractions of the total nitrate were required to balance the charge from the metals, these particles likely fall in the region of relative sodium concentration just above the dashed line in Figure 5.4, where significant enhancements in nitrate mass were observed. However, we note that the temperature ranges of evaporation are substantially different between the measurements and model. During SOAR-1, evaporation of nitrate was essentially complete by 142 ºC and 171 ºC for the vanadium and BB types (Figure 5.2a), compared to significant evaporation between 40-55 ºC predicted by the model (Figure 5.4). This discrepancy can be partly attributed to the non-equilibrium conditions of the TD,[52,53] as discussed in Section 5.4.2.1.

In addition to the short time-scales used in TDs, the complexity of the ambient particles may have induced further mass-transfer limitations that suppressed the evaporation within the TD, in particular the presence of SOA coatings. Aerosols undergo extensive photochemical aging during summer throughout the South Coast Air Basin that result in accumulation of thick coatings of secondary organic carbon.[21,27,65] Previous laboratory studies have demonstrated that organic films on ammonium nitrate particles could reduce the evaporation rate of ammonium nitrate by limiting the diffusion to the particle surface.[66] Another study showed that even a monolayer of SOA could cause sodium nitrate particles to retain water, an effect that increased with coating thickness.[67] Therefore, coatings of SOA on particles comprised of highly hygroscopic metals present within the core could help to keep the particles aqueous to higher temperatures within the TD and therefore exacerbate the effect of water in reducing nitrate volatility. Diffusion of ammonium nitrate to the particle-air interface would be further limited by the organic coating.

These effects were not accounted for in the model representation that assumes the particle phase is homogeneously mixed. However, it is possible that the ambient aerosol morphology

displayed such complex morphologies. Both the BB and vanadium particle types may have been transported significant distances between the source and Riverside. Vanadium particles arising from ship emissions are transported from the coast over many hours.[28] Further, limited fire activity in Southern California during SOAR-1 implies that the observed biomass burning particles were transported from other regions[20,57] and may have undergone significant processing during transit.[65] It is therefore likely that these particle cores were aged to some extent via reactions 5.1—5.3 before arriving in Riverside; indeed, significant levels of particulate nitrate have been detected upwind of the dairy regions.[24] It is therefore possible that the metal cations were predominantly within the core of the particle along with nitrate from initial aging processes. Indeed, the ionization trends following heating presented in Chapter 4 implied that the vanadium particle type could have existed in Riverside as a core-shell morphology; and, while not shown, the biomass burning particle type displayed similar behavior and thus may also have acquired a similar morphology. Further, previous microscopy studies of ambient aerosols have shown the presence of inorganic inclusions within otherwise organic biomass burning particles,[68,69] as well as coatings of SOA surrounding inorganic cores.[70] Thus it is reasonable to speculate that SOA coatings may have played a role in reducing the volatility of ammonium nitrate that was mixed with metal species within the particle cores. Therefore, the combination of water uptake by hygroscopic metal ions and diffusion limitations induced by SOA coatings likely contributed to the higher ammonium nitrate evaporation temperatures observed for the BB and vanadium particles relative to the OC particles (Figure 5.2a).

If such core-shell morphology existed during SOAR-1, then the evaporation of nitrate in these particles would have been subject to significant mass-transfer limitations within the TD and thus higher temperatures would be necessary to remove the organic coatings and evaporate ammonium nitrate/water from the particle cores. Interestingly, the thermogram of ammonium from the vanadium particle type shown in Figure 4.4 was slightly higher than the AMS measurements, which may support this hypothesis. However, it is unknown if this difference in ammonium observations was due to matrix effects or real differences in volatility. It is expected that the AMS would have also measured nitrate that was not bound to metal ions, with fractions remaining, then, lying closer to the average ATOFMS curve shown in Figure 5.2a. However, we note that the average ATOFMS thermogram (Figure 5.2), weighted by the relative number fraction of each particle type, is only slightly higher than the AMS (e.g., 0.35 vs. 0.25 at 54 ºC). The reason for the discrepancy is currently unknown, but could arise from a bias in either (or

both) instruments, for example a change in the AMS collection efficiency as coatings were removed from these particles or an ATOFMS oversensitivity to particles with metal ions that have low ionization potentials. Clearly more extensive ATOFMS-AMS comparisons are warranted.

Finally, recall that the non-refractory nitrate marker, $^{125}H(NO_3)_2^-$, exhibited similar volatility across all particle types (Figure 5.2b). Since substantial partitioning of ammonium nitrate occurs in the vicinity of Riverside due to the nearby dairies upwind, it is possible that ammonium nitrate condensing locally and on the outside of the particles was somewhat decoupled from the metal components in the core. If nitrate was present in different layers throughout the particle, it could be impacted by the metal ions to different extents and thus the rates of evaporation would be different. To assess whether two nitrate regimes existed, the unheated particles were divided into 3 separate categories based on their total ion intensities: low, medium, and high. Particles displaying lower overall ion intensity likely were not "hit as hard" by the D/I laser and therefore the surface components would be preferentially ionized; in contrast, particles producing high intensity spectra were likely ablated more completely, with higher contributions from the particle core. This approach is akin to depth-profiling experiments in SPMS instruments wherein the laser power is intentionally varied to change the ablation depth.[71] For particles within the 3 ion intensity regimes, the ion peak areas of $^{125}H(NO_3)_2^-$ and $^{62}NO_3^-$ were normalized by the internal standard peak areas of each particle type, which represent the core components (Figure 5.5). For species that were enriched at the surface, this ratio will shift to lower values in particles that were more strongly ablated due to the higher contributions from the particle core to the total ion intensity.

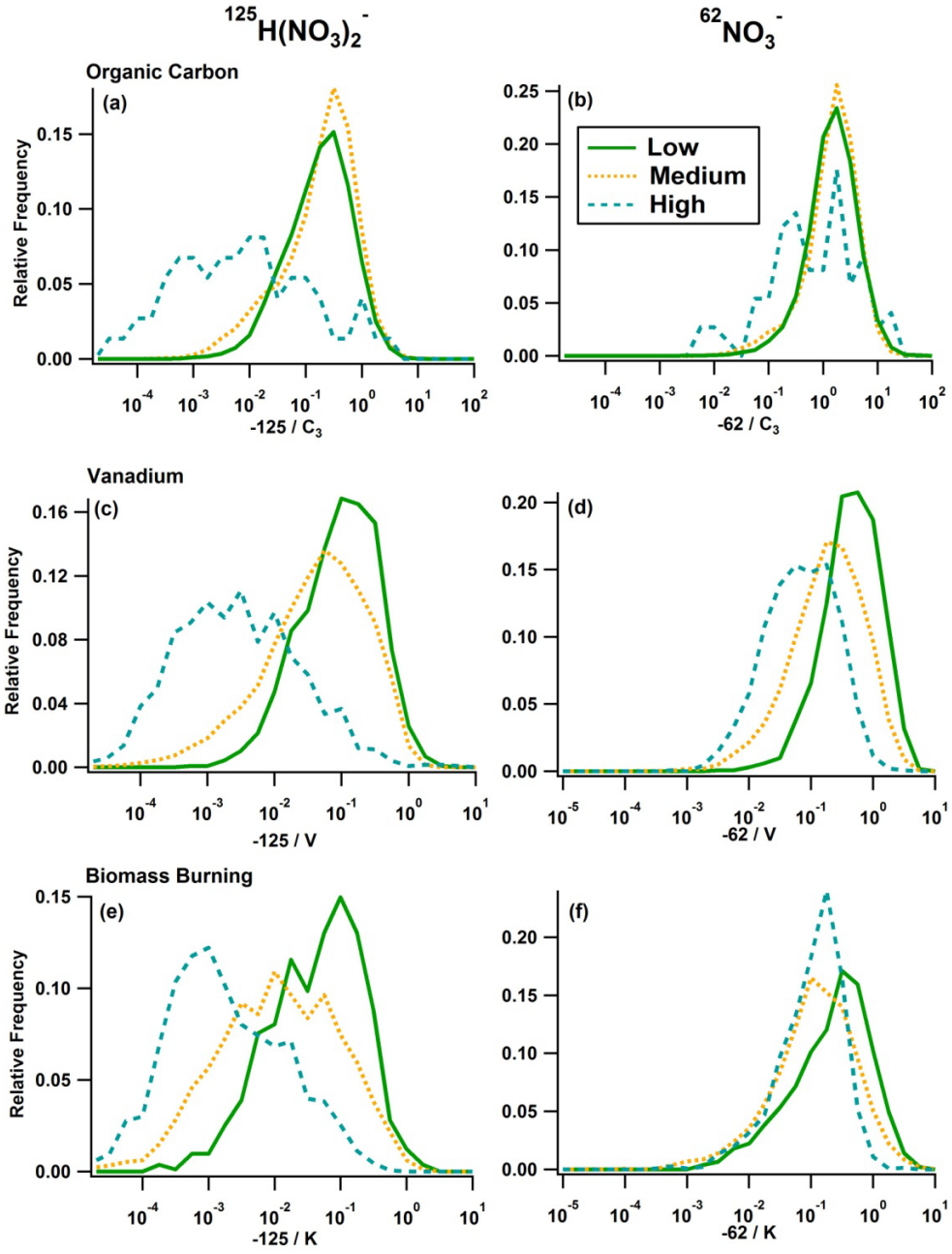

Figure 5.5 Histograms of the ratio of the ion peak areas for the ion markers $^{125}H(NO_3)_2^-$ (left column) and $^{62}NO_3^-$ (right column) relative to the peak areas of the internal standards for each particle type. Single particles were categorized by the total ion intensity: Low = $<10^{-4}$; Medium = 10^{-4} – 10^{-5}; High = $>10^{-5}$ (in arbitrary area units). On the left side, only particles containing $^{125}H(NO_3)_2^-$ were included in this analysis (>~70% of the particles in each category). All cases represent unheated particles.

As shown in Figure 5.5, for the three particle types considered herein, the ratio for the $^{125}H(NO_3)_2^-$ ion marker shifts approximately two orders of magnitude to lower values as the spectral intensity increased, demonstrating that the non-refractory nitrate associated with

$^{125}H(NO_3)_2^-$ was indeed enriched on the particle surfaces. In contrast, the $^{62}NO_3^-$ marker shifts to a significantly smaller degree (about 1 order of magnitude or less), indicating that nitrate producing this marker (refractory + non-refractory) was more dispersed throughout the particle. This analysis shows that there was likely nitrate present in different chemical environments even within single particles. Such morphologies could therefore explain the two apparent volatility behaviors observed for nitrate by ATOFMS (Figure 5.2). Given the high degree of secondary aerosol formation in the South Coast Air Basin described above, the outermost layer(s) of ammonium nitrate likely experienced a similar environment on all particle types and would thus evaporate similarly, consistent with Figure 5.2b. In contrast, nitrate within the particle cores would be significantly affected by the composition, and in particular, the presence of metals. We note that the core of the OC type was soot, which would not influence the volatility of nitrate as the metal salts did. Multi-layer kinetic models are currently in development by other groups[72] that may better assess the potential for multiple evaporation regimes from complex atmospheric particles.

5.5 Conclusions & Implications

In this work, a thermodenuder was coupled to an aerosol time-of-flight mass spectrometer to probe the influence of aerosol mixing-state on nitrate volatility. Nitrate was observed to evaporate at significantly higher temperatures in particles that contained metal cations (K^+, Na^+, V^+/VO^+). The results presented herein demonstrate that the unequal distribution of refractory material resulted in very different volatility behavior for the individual particle types relative to the average composition. Thermodynamic modeling indicated that the presence of sodium can reduce the volatility of non-refractory nitrate by lowering the ammonium concentrations and enhancing the liquid water content, even when nitrate is not required to balance the charge of the metal ions. Further, the comparisons between the measurement and model discussed herein implied that complex morphologies may have existed, wherein two nitrate regimes were present: (1) with the outermost layer(s) of ammonium nitrate decoupled from the metal ions, which evaporated similarly from all particle types and (2) with nitrate mixed with metals in the core that evaporated at higher temperatures. The findings herein highlight that partitioning in the atmosphere is highly complex and depends on the single-particle mixing state. Nitrate should not be assumed to exist simply as ammonium nitrate or mixed with the ensemble-averaged concentration of metal ions. The different partitioning behavior of nitrate to different aerosol mixing states would impact predicted aerosol mass and liquid water content over a broad

range of RHs, which may have important implications for optical properties and estimates of aerosol radiative forcing.[63]

5.6 Acknowledgements

The dissertation author was the primary researcher and author of this chapter. Dr. Kerri Pratt is acknowledged for collecting the TD-ATOFMS data. Drs. Alex Huffman and Jose Jimenez (University of Colorado-Boulder) are also thanked for providing the TD-AMS data (and use of the TD). Dr. Kelley Barsanti is thanked for assisting with the modeling work. Prof. Paul Ziemann (UC-Riverside), Ken Docherty (CU-Boulder), the UC Riverside Air Pollution Research Center, and the entire Prather Group are thanked for support during SOAR. The SOAR campaign was funded by the National Science Foundation (NSF-ATM 0321362) and the California Air Resources Board (CARB 04-336). L. Hatch and K. Pratt were funded by National Science Foundation Graduate Research Fellowships (2008-2011 and 2006-2009, respectively). K. Pratt was additionally funded by an EPA STAR Graduate Fellowship (2005-2006). The EPA has not officially endorsed this publication, and the views expressed herein may not reflect the views of the EPA. Dr. Melanie Zauscher is thanked for helpful comments that improved the quality of this manuscript.

Chapter 5 is in preparation for submission to Environmental Science & Technology: L. E. Hatch, K. C. Barsanti, K. A. Pratt, J. A. Huffman, J. L. Jimenez, and K. A. Prather, Mixing-state dependence of nitrate volatility from atmospheric particles.

5.7 Appendix: Additional preliminary model studies

In addition to metal ions, other aerosol components could influence the volatility of nitrate from atmospheric particles, as demonstrated by the higher thermogram of ambient non-refractory particles (e.g., OC-type particles) and pure ammonium nitrate measured in the laboratory (Figure 5.2). In particular, amines and other organic compounds were internally-mixed with nitrate in all particle types during SOAR-1 (Figure 5.1). Preliminary model investigations regarding the impact of these aerosol constituents on nitrate volatility are discussed in the following sections.

All model studies in this section utilized E-AIM Model 2, which treats systems containing H^+, NH_4^+, SO_4^{2-}, and NO_3^-, and H_2O.[48] Additionally, E-AIM includes the option to add both hydrophobic and hydrophilic organic compounds to the system and calculates their

partitioning between the organic and aqueous phases. Activity coefficients for organic compounds are calculated via UNIFAC (UNIQUAC functional-group activity coefficients).[73] UNIFAC estimates activity coefficients via functional-group contributions based on the volume and surface area of each group, combined with its interactions with other functional groups.[73] Peng *et al.*[74] modified the parameters for interactions between carboxylic acid groups, hydroxyl groups, and water; these parameters have been shown to improve model-measurement agreement[75] and were used herein for compounds containing these functional groups. For all systems, the base-case composition was used, as indicated in Table 5.1. Solid formation was not permitted and thus systems were treated as metastable (efflorescence behavior) at 70% RH.

5.7.1 Amines

Amines have been identified as significant players in atmospheric nucleation[76,77] and particle growth.[78,79] But their potential influence on nitrate volatility has not been sufficiently explored. Aliphatic amines are stronger bases than ammonia,[80] and therefore form a stronger salt[78] that potentially retains nitrate in the particle phase to higher temperatures. Salo *et al.*[81] performed laboratory experiments on the volatility of pure aminium nitrate salts and determined that their vapor pressures were within a factor of ~2 that of ammonium nitrate. However, since amines are typically present in low concentrations relative to ammonia, pure aminium nitrate salts are unlikely to exist in the atmosphere. Docherty *et al.*[57] concluded that amines had little influence on the nitrate charge balance during SOAR-1. However, as discussed in Chapter 4, significant correlations at the single-particle level between nitrate and the amine markers were observed during SOAR-1 (Figures 4.7 and 4.10), indicating the potential existence of amine-nitrate salts in these particles. Therefore the effect of amines on nitrate volatility should be explored further.

Triethylamine (TEA) was used as a proxy amine because it has been shown to yield the $^{86}(C_2H_5)_2NCH_2^+$ and $^{118}(C_2H_5)_3NOH^+$ ion markers observed in the ambient spectra (Figure 5.1).[82] E-AIM contains a library of amine compounds and their associated thermodynamic data.[80] For reference, the pK_a's of $TEAH^+$ and NH_4^+ are 9.2[48] and 10.75,[80] respectively. E-AIM treats the gas-particle partitioning of TEA on a Raoult's law basis, via its liquid vapor pressure. In these investigations, the relative molar concentration of TEA was varied, while keeping the total base level (NH_3 + TEA) constant. Therefore any change in particulate nitrate mass was due to the change in the identity of the base. The effect of varying TEA concentrations on nitrate mass is shown in Figure 5.6, where the contours represent the change in nitrate mass relative to the base

case (TEA = 0); the change in nitrate mass with temperature for the base case is included for reference (gray curve).

It is clear that the effect of TEA is confined to the intermediate temperatures (10 – 40 ºC). At low temperatures (< 15 ºC), nearly 100% of nitrate is in the particle phase and therefore adding a stronger base will have little impact on nitrate partitioning. At high temperatures (> 40 ºC), it is clear that TEA did not significantly enhance the nitrate mass. TEA-nitrate salts are still too volatile to remain in the particle phase at these temperatures, even when TEA is the only base. In the intermediate temperature range, there is a clear enhancement of nitrate mass as the proportion of amine increased. The largest enhancement occurred at 25 ºC, with increased nitrate ranging from ~0.3 to 2.4 μg/m^3 for TEA = 10% and 100% of the base concentration, respectively; these enhancements represent 5.8 and 48% more nitrate at 25 ºC relative to the base case. These findings are consistent with the small difference in vaporization temperature between pure ammonium nitrate and dimethylamine nitrate observed by Salo *et al.*[81] These model results demonstrate that TEA can influence the volatility of nitrate at reasonable atmospheric temperatures, but that amine-nitrate salts are not significantly more strongly bound to the particle phase than ammonium nitrate. Future model studies should explore the role of different amines that may be stronger bases or lower vapor pressure/higher Henry's Law constants.

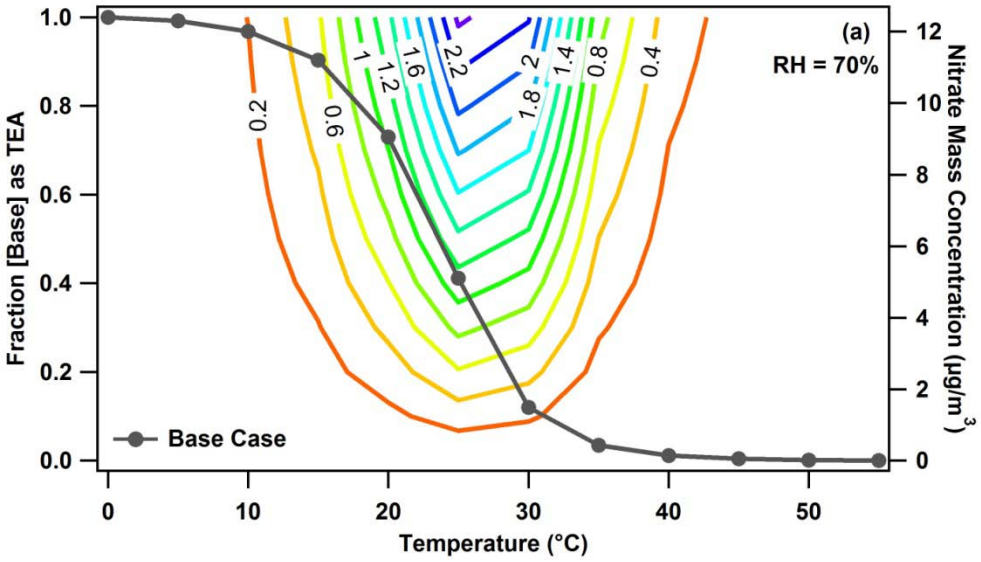

Figure 5.6 E-AIM model results showing the difference in nitrate mass concentration (μg/m^3) for cases with TEA minus the base case. The fraction of TEA (total [base] = 5 x 10^{-7} mol/m^3) was varied with fixed RH = 70%. For comparison, the gray curve represents the nitrate mass calculated for the base case ([TEA] = 0), right axis.

5.7.2 Organonitrates

Organonitrates can form in the atmosphere via reaction between organic radicals (e.g., formed via reaction with OH radical) and NO.[83] Addition of a nitrate moiety can decrease the vapor pressure of a given organic molecule ~50-fold.[83] Studies have shown that organonitrates can fragment to HNO_3 during mass spectral analysis,[84] which could subsequently be detected as any of the major nitrate markers in ATOFMS spectra. Organonitrates also break down to organic ions and inorganic nitrate in AMS, thus evading direct detection.[85] Therefore, it is possible that organonitrates contributed to a fraction of the mass spectral signal from inorganic nitrate during SOAR, particularly since organonitrate groups have been detected in Southern California.[86] While Farmer *et al.*[85] estimated that organonitrates likely represented less than 10% of the inorganic nitrate signal measured by AMS, organonitrates could have influenced the resulting thermogram if they were significantly less volatile than ammonium nitrate. These effects were investigated via E-AIM.

An 18 carbon, 1,4 hydroxynitrate (1,4-HN) was chosen as the proxy organonitrate molecule[83] (Figure 5.7a). The vapor pressure and enthalpy of vaporization were estimated from the online calculation tool, SPARC ('SPARC Performs Automated Reasoning in Chemistry', http://archemcalc.com/sparc/)[87] to be 2.2 x 10^{-11} atm and 138.3 kJ/mol, respectively and were used in the compound definition within E-AIM. The activity coefficient was calculated by UNIFAC; however, parameters for organic nitrate ($RONO_2$) groups are not available in UNIFAC parameter set within E-AIM. Nitro (RNO_2) groups are included, and primary nitro groups display similar volume and surface area parameters as secondary nitrate groups determined by Compernolle *et al.*[88] Therefore, the structure was modified slightly (Figure 5.7b) to accommodate the UNIFAC parameter set within E-AIM (www.aim.env.uea.ac.uk/aim/info/UNIFACgroups.html).

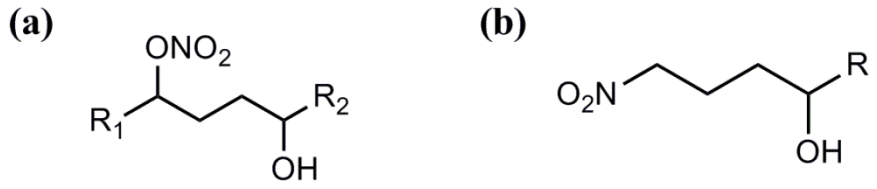

Figure 5.7(a) Structure of the 1,4 hydroxynitrate chosen as the proxy organonitrate.[83] (b) The structure representation used to determine UNIFAC groups. The R groups represent alkyl chains yielding a total 18-carbon chain length.

In the presence of electrolytes, the 1,4-HN existed entirely in the hydrophobic phase and the behavior was largely decoupled from the aqueous phase. Since partitioning is strongly dependent on the mass of the absorbing phase,[89] the presence of additional organic mass will significantly alter the partitioning and volatility of the organonitrate; therefore the influence of OA mass on the volatility of 1,4-HN was investigated first. Dodecanedione was chosen as a proxy organic compound because it and other compounds with similar functionality (but differing chain lengths) were detected during SOAR-1.[65] The dodecanedione mass concentration was varied over the range 0 - 20 $\mu g/m^3$; for reference the measured organic aerosol mass during SOAR-1 on August 12th peaked at ~18 $\mu g/m^3$.[65] For simplicity, it was assumed that dodecanedione was non-volatile, so the absorbing mass remained constant at all temperatures. The organonitrate concentration was determined by assuming that the nitrate group contributed 10% of the molar concentration of inorganic nitrate (i.e., 0.2×10^{-7} mol/m^3); the organonitrate mass was not factored into the organic mass. The results are shown in Figure 5.8a, where the contours represent the fraction of 1,4-HN remaining relative to 25 °C. Up to 25 °C, 100% of the hydroxynitrate was in the particle phase for all conditions. When 1,4-HN was the sole constituent within the hydrophobic phase (dodecanedione = 0), it completely evaporated by 55 °C. In contrast, with 20 $\mu g/m^3$ of dodecanedione, there was 48% of 1,4-HN remaining at 55 °C, demonstrating the influence of organic mass in reducing the volatility.

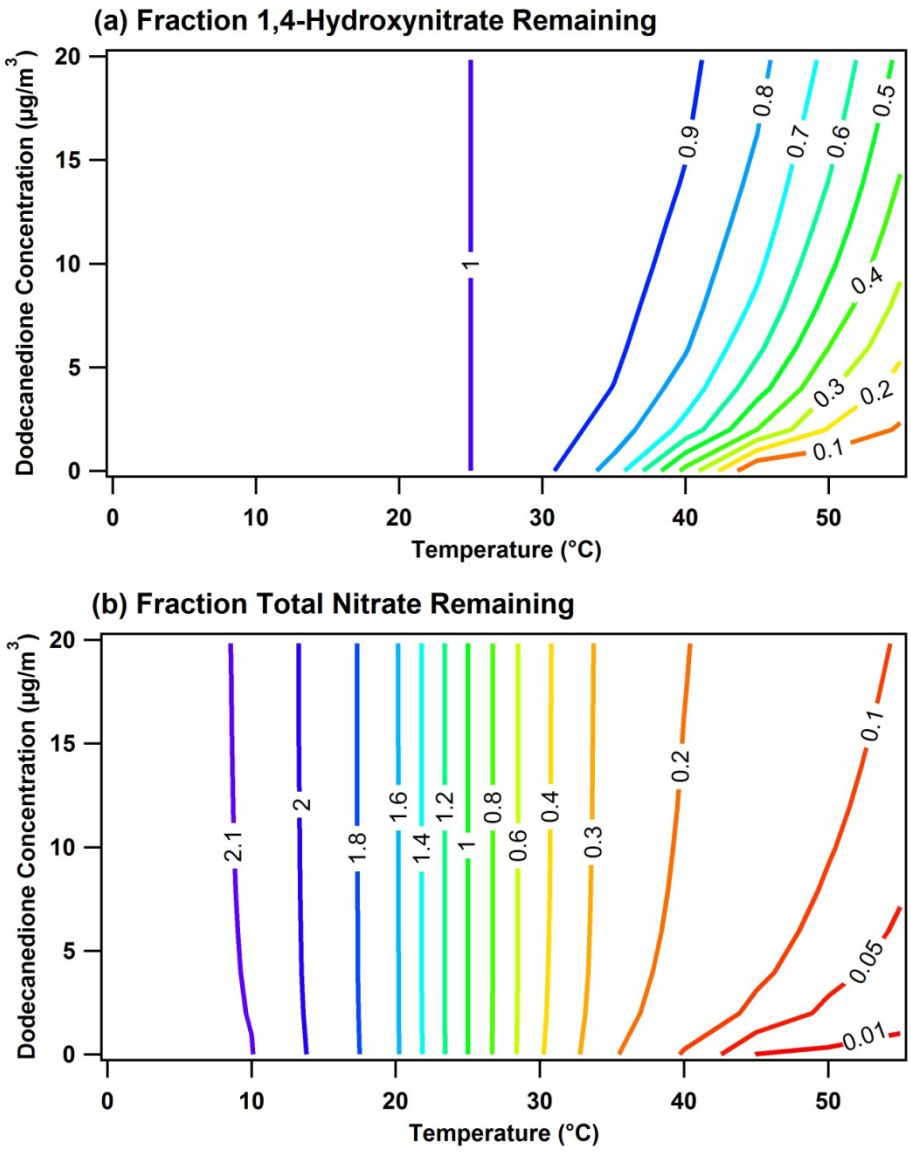

Figure 5.8 Influence of the organic absorbing phase on the volatility of 1,4-hydroxynitrate. Contours represent either the fraction of (a) 1,4-hydroxynitrate or (b) total nitrate (inorganic nitrate + 1,4-HN) remaining relative to 25 °C. RH=70%.

As the goal herein is to determine if organonitrates can contribute to the apparent volatility of nitrate, the fraction remaining was calculated for total nitrate (nitrate + 1,4-HN) on a molar basis (Figure 5.8b) and relative to 25 °C. This provides a similar perspective to the mass spectral measurements. The only variable here (besides temperature) is the organic mass available to absorb 1,4-HN, which was assumed to be 100% dodecanedione. If all of the organic mass during SOAR-1 (~18 µg/m^3) was able to absorb 1,4-HN, then there would appear to be ~10% of nitrate remaining at 55 °C (Figure 5.8b). Even if about half (~9 µg/m^3) of the OA mass

acted as an absorbing phase, there is still as much as ~6% of the total nitrate remaining at high temperature. It is important to note that dodecanedione and 1,4-HN were entirely within the organic phase for these investigations and therefore had no effect on the partitioning of aqueous inorganic nitrate (the two phases behaved as though they were decoupled). Note that the thermogram for inorganic nitrate alone is included in Figure 5.6 (base case), and demonstrated full evaporation by 55 °C. Therefore the nitrate remaining at high temperature is due to residual 1,4-HN. Organonitrates can therefore influence the apparent volatility of inorganic nitrate and may account for part of the difference between pure ammonium nitrate volatility and the volatility of nitrate from non-refractory ambient particles.

Atmospheric organic aerosols are highly complex and therefore preclude accurate representation using a single proxy compound as the absorbing phase. Additional representative organic compounds can be obtained from the speciated organic aerosol composition during SOAR-1, as determined by Williams *et al.*[65] via thermal-desorption aerosol gas chromatography (TAG). It would also be useful to investigate smaller organonitrate compounds, as the large 18-carbon 1,4-HN utilized herein represents substantial organic mass (6 $\mu g/m^3$) when set to contribute 10% of the inorganic nitrate levels. Smaller molecules with greater polarity could exert the same influence on the nitrate thermograms, while comprising a smaller fraction of the organic mass. Further, given the high SOA fraction of the total OA mass during SOAR-1,[21,65] it is likely that a significant portion of the organics were water soluble and therefore present in the aqueous phase. Thus, the effect of water-soluble organics on inorganic nitrate volatility should also be explored.

5.8 References

1. Seinfeld, J. H.; Pandis, S. N., *Atmospheric Chemistry & Physics: From Air Pollution to Climate Change*. 2nd. ed.; John Wiley & Sons, Inc.: New Jersey, 2006.

2. Russell, A. G.; Cass, G. R., Verification of a Mathematical-Model for Aerosol Nitrate and Nitric-Acid Formation and Its Use for Control Measure Evaluation. *Atmos. Environ.* **1986,** *20*, (10), 2011-2025.

3. Christoforou, C. S.; Salmon, L. G.; Hannigan, M. P.; Solomon, P. A.; Cass, G. R., Trends in fine particle concentration and chemical composition in Southern California. *Journal of the Air & Waste Management Association* **2000,** *50*, (1), 43-53.

4. Kajino, M.; Ueda, H.; Nakayama, S., Secondary acidification: Changes in gas-aerosol partitioning of semivolatile nitric acid and enhancement of its deposition due to increased emission and concentration of SO(x). *J. Geophys. Res.* **2008,** *113*, (D3).

5. Vitousek, P. M.; Aber, J. D.; Howarth, R. W.; Likens, G. E.; Matson, P. A.; Schindler, D. W.; Schlesinger, W. H.; Tilman, D., Human alteration of the global nitrogen cycle: Sources and consequences. *Ecological Applications* **1997,** *7*, (3), 737-750.

6. Kulmala, M.; Korhonen, P.; Laaksonen, A.; Vesala, T., Changes in-Cloud Properties Due to Nox Emissions. *Geophysical Research Letters* **1995,** *22*, (3), 239-242.

7. Kulmala, M.; Toivonen, A.; Mattila, T.; Korhonen, P., Variations of cloud droplet concentrations and the optical properties of clouds due to changing hygroscopicity: A model study. *J. Geophys. Res.* **1998,** *103*, (D13), 16183-16195.

8. Veefkind, J. P.; vanderHage, J. C. H.; tenBrink, H. M., Nephelometer derived and directly measured aerosol optical depth of the atmospheric boundary layer. *Atmospheric Research* **1996,** *41*, (3-4), 217-228.

9. Wang, T. J.; Li, S.; Shen, Y.; Deng, J. J.; Xie, M., Investigations on direct and indirect effect of nitrate on temperature and precipitation in China using a regional climate chemistry modeling system. *J. Geophys. Res.* **2010,** *115*.

10. Bauer, S. E.; Koch, D.; Unger, N.; Metzger, S. M.; Shindell, D. T.; Streets, D. G., Nitrate aerosols today and in 2030: a global simulation including aerosols and tropospheric ozone. *Atmos. Chem. Phys.* **2007,** *7*, (19), 5043-5059.

11. Adams, P. J.; Seinfeld, J. H.; Koch, D.; Mickley, L.; Jacob, D., General circulation model assessment of direct radiative forcing by the sulfate-nitrate-ammonium-water inorganic aerosol system. *J. Geophys. Res.* **2001,** *106*, (D1), 1097-1111.

12. Pankow, J. F., Gas/particle partitioning of neutral and ionizing compounds to single and multi-phase aerosol particles. 1. Unified modeling framework. *Atmos. Environ.* **2003,** *37*, (24), 3323-3333.

13. Mozurkewich, M., The Dissociation-Constant of Ammonium-Nitrate and Its Dependence on Temperature, Relative-Humidity and Particle-Size. *Atmospheric Environment Part a-General Topics* **1993,** *27*, (2), 261-270.

14. Stelson, A. W.; Seinfeld, J. H., Relative-Humidity and Temperature-Dependence of the Ammonium-Nitrate Dissociation-Constant. *Atmos. Environ.* **1982,** *16*, (5), 983-992.

15. Gard, E. E.; Kleeman, M. J.; Gross, D. S.; Hughes, L. S.; Allen, J. O.; Morrical, B. D.; Fergenson, D. P.; Dienes, T.; Galli, M. E.; Johnson, R. J.; Cass, G. R.; Prather, K. A., Direct observation of heterogeneous chemistry in the atmosphere. *Science* **1998,** *279*, (5354), 1184-1187.

16. Gibson, E. R.; Hudson, P. K.; Grassian, V. H., Physicochemical properties of nitrate aerosols: Implications for the atmosphere. *J. Phys. Chem. A* **2006,** *110*, (42), 11785-11799.

17. Chang, W. L.; Bhave, P. V.; Brown, S. S.; Riemer, N.; Stutz, J.; Dabdub, D., Heterogeneous Atmospheric Chemistry, Ambient Measurements, and Model Calculations of N2O5: A Review. *Aerosol Sci. Technol.* **2011,** *45*, (6), 665-695.

18. Huffman, J. A.; Docherty, K. S.; Aiken, A. C.; Cubison, M. J.; Ulbrich, I. M.; DeCarlo, P. F.; Sueper, D.; Jayne, J. T.; Worsnop, D. R.; Ziemann, P. J.; Jimenez, J. L., Chemically-resolved aerosol volatility measurements from two megacity field studies. *Atmos. Chem. Phys.* **2009,** *9*, (18), 7161-7182.

19. Pratt, K. A.; Hatch, L. E.; Prather, K. A., Seasonal Volatility Dependence of Ambient Particle Phase Amines. *Environ. Sci. Tech.* **2009,** *43*, (14), 5276-5281.

20. Pratt, K. A.; Prather, K. A., Real-Time, Single-Particle Volatility, Size, and Chemical Composition Measurements of Aged Urban Aerosols. *Environ. Sci. Tech.* **2009,** *43*, (21), 8276-8282.

21. Docherty, K. S.; Stone, E. A.; Ulbrich, I. M.; DeCarlo, P. F.; Snyder, D. C.; Schauer, J. J.; Peltier, R. E.; Weber, R. J.; Murphy, S. M.; Seinfeld, J. H.; Grover, B. D.; Eatough, D. J.; Jimenez, J. L., Apportionment of Primary and Secondary Organic Aerosols in Southern California during the 2005 Study of Organic Aerosols in Riverside (SOAR-1). *Environ. Sci. Tech.* **2008,** *42*, (20), 7655-7662.

22. Russell, A. G.; Mcrae, G. J.; Cass, G. R., Mathematical-Modeling of the Formation and Transport of Ammonium-Nitrate Aerosol. *Atmos. Environ.* **1983,** *17*, (5), 949-964.

23. Nowak, J. B.; Neuman, J. A.; Bahreini, R.; Middlebrook, A. M.; Holloway, J. S.; McKeen, S. A.; Parrish, D. D.; Ryerson, T. B.; Trainer, M., Ammonia sources in the California South Coast Air Basin and their impact on ammonium nitrate formation. *Geophysical Research Letters* **2012,** *39*.

24. Hughes, L. S.; Allen, J. O.; Salmon, L. G.; Mayo, P. R.; Johnson, R. J.; Cass, G. R., Evolution of nitrogen species air pollutants along trajectories crossing the Los Angeles area. *Environ. Sci. Tech.* **2002,** *36*, (18), 3928-3935.

25. Neuman, J. A.; Nowak, J. B.; Brock, C. A.; Trainer, M.; Fehsenfeld, F. C.; Holloway, J. S.; Hubler, G.; Hudson, P. K.; Murphy, D. M.; Nicks, D. K.; Orsini, D.; Parrish, D. D.; Ryerson, T. B.; Sueper, D. T.; Sullivan, A.; Weber, R., Variability in ammonium nitrate formation and nitric acid depletion with altitude and location over California. *J. Geophys. Res.* **2003,** *108*, (D17).

26. Chow, J. C.; Liu, C. S.; Cassmassi, J.; Watson, J. G.; Lu, Z. Q.; Pritchett, L. C., A Neighborhood-Scale Study of Pm-10 Source Contributions in Rubidoux, California. *Atmospheric Environment Part a-General Topics* **1992,** *26*, (4), 693-706.

27. Qin, X.; Pratt, K. A.; Shields, L. G.; Toner, S. M.; Prather, K. A., Seasonal comparison of single-particle chemical mixing state in Riverside, CA. *Atmos. Environ.* **2012,** *Accepted Manuscript*.

28. Gaston, C. J.; Pratt, K. A.; Qin, X. Y.; Prather, K. A., Real-Time Detection and Mixing State of Methanesulfonate in Single Particles at an Inland Urban Location during a Phytoplankton Bloom. *Environ. Sci. Tech.* **2010,** *44*, (5), 1566-1572.

29. Metzger, S.; Mihalopoulos, N.; Lelieveld, J., Importance of mineral cations and organics in gas-aerosol partitioning of reactive nitrogen compounds: case study based on MINOS results. *Atmos. Chem. Phys.* **2006,** *6*, 2549-2567.

30. Moya, M.; Ansari, A. S.; Pandis, S. N., Partitioning of nitrate and ammonium between the gas and particulate phases during the 1997 IMADA-AVER study in Mexico City. *Atmos. Environ.* **2001,** *35*, (10), 1791-1804.

31. Jacobson, M. Z., Studying the effects of calcium and magnesium on size-distributed nitrate and ammonium with EQUISOLV II. *Atmos. Environ.* **1999,** *33*, (22), 3635-3649.

32. Myhre, G.; Grini, A.; Metzger, S., Modelling of nitrate and ammonium-containing aerosols in presence of sea salt. *Atmos. Chem. Phys.* **2006,** *6*, 4809-4821.

33. Ansari, A. S.; Pandis, S. N., The effect of metastable equilibrium states on the partitioning of nitrate between the gas and aerosol phases. *Atmos. Environ.* **2000,** *34*, (1), 157-168.

34. Kleeman, M. J.; Cass, G. R.; Eldering, A., Modeling the airborne particle complex as a source-oriented external mixture. *J. Geophys. Res.* **1997,** *102*, (D17), 21355-21372.

35. Ault, A. P.; Gaston, C. J.; Wang, Y.; Dominguez, G.; Thiemens, M. H.; Prather, K. A., Characterization of the Single Particle Mixing State of Individual Ship Plume Events Measured at the Port of Los Angeles. *Environ. Sci. Tech.* **2010,** *44*, (6), 1954-1961.

36. Healy, R. M.; O'Connor, I. P.; Hellebust, S.; Allanic, A.; Sodeau, J. R.; Wenger, J. C., Characterisation of single particles from in-port ship emissions. *Atmos. Environ.* **2009,** *43*, (40), 6408-6414.

37. Sodeman, D. A.; Toner, S. M.; Prather, K. A., Determination of single particle mass spectral signatures from light-duty vehicle emissions. *Environ. Sci. Tech.* **2005,** *39*, (12), 4569-4580.

38. Toner, S. M.; Sodeman, D. A.; Prather, K. A., Single particle characterization of ultrafine and accumulation mode particles from heavy duty diesel vehicles using aerosol time-of-flight mass spectrometry. *Environ. Sci. Tech.* **2006,** *40*, (12), 3912-3921.

39. Silva, P. J.; Liu, D. Y.; Noble, C. A.; Prather, K. A., Size and chemical characterization of individual particles resulting from biomass burning of local Southern California species. *Environ. Sci. Tech.* **1999,** *33*, (18), 3068-3076.

40. Zauscher, M. D.; Wang, Y.; Moore, M. J. K.; C.J., G.; Prather, K. A., Mixing state and aging of individual biomass burning aerosols during the 2007 San Diego Wildfires. *In Preparation* **2012**.

41. Kane, D. B.; Johnston, M. V., Size and composition biases on the detection of individual ultrafine particles by aerosol mass spectrometry. *Environ. Sci. Tech.* **2000,** *34*, (23), 4887-4893.

42. Huffman, J. A.; Docherty, K. S.; Mohr, C.; Cubison, M. J.; Ulbrich, I. M.; Ziemann, P. J.; Onasch, T. B.; Jimenez, J. L., Chemically-Resolved Volatility Measurements of Organic Aerosol from Different Sources. *Environ. Sci. Tech.* **2009,** *43*, (14), 5351-5357.

43. Reilly, P. T. A.; Lazar, A. C.; Gieray, R. A.; Whitten, W. B.; Ramsey, J. M., The elucidation of charge-transfer-induced matrix effects in environmental aerosols via real-time aerosol mass spectral analysis of individual airborne particles. *Aerosol Sci. Technol.* **2000,** *33*, (1-2), 135-152.

44. Reinard, M. S.; Johnston, M. V., Ion formation mechanism in laser desorption ionization of individual nanoparticles. *J. Am. Soc. Mass. Spectrom.* **2008,** *19*, (3), 389-399.

45. Spencer, M. T.; Shields, L. G.; Prather, K. A., Simultaneous measurement of the effective density and chemical composition of ambient aerosol particles. *Environ. Sci. Tech.* **2007,** *41*, (4), 1303-1309.

46. Barbaray, B.; Contour, J. P.; Mouvier, G., Effects of Nitrogen-Dioxide and Water-Vapor on Oxidation of Sulfur-Dioxide over V2o5 Particles. *Environ. Sci. Tech.* **1978,** *12*, (12), 1294-1297.

47. Friese, E.; Ebel, A., Temperature Dependent Thermodynamic Model of the System H+-NH4+-Na+-SO42-NO3--Cl--H2O. *J. Phys. Chem. A* **2010,** *114*, (43), 11595-11631.

48. Clegg, S. L.; Brimblecombe, P.; Wexler, A. S., Thermodynamic model of the system H+-NH4+-SO42--NO3--H2O at tropospheric temperatures. *J. Phys. Chem. A* **1998,** *102*, (12), 2137-2154.

49. Stelson, A. W.; Seinfeld, J. H., Chemical Mass Accounting of Urban Aerosol. *Environ. Sci. Tech.* **1981,** *15*, (6), 671-679.

50. Yu, S. C.; Dennis, R.; Roselle, S.; Nenes, A.; Walker, J.; Eder, B.; Schere, K.; Swall, J.; Robarge, W., An assessment of the ability of three-dimensional air quality models with current thermodynamic equilibrium models to predict aerosol NO3-. *J. Geophys. Res.* **2005,** *110*, (D7).

51. Huffman, J. A.; Ziemann, P. J.; Jayne, J. T.; Worsnop, D. R.; Jimenez, J. L., Development and Characterization of a Fast-Stepping/Scanning Thermodenuder for Chemically-Resolved Aerosol Volatility Measurements. *Aerosol Sci. Technol.* **2008,** *42*, 395-407.

52. Saleh, R.; Shihadeh, A.; Khlystov, A., On transport phenomena and equilibration time scales in thermodenuders. *Atmospheric Measurement Techniques* **2011,** *4*, (3), 571-581.

53. Riipinen, I.; Pierce, J. R.; Donahue, N. M.; Pandis, S. N., Equilibration time scales of organic aerosol inside thermodenuders: Evaporation kinetics versus thermodynamics. *Atmos. Environ.* **2010,** *44*, (5), 597-607.

54. Meng, Z. Y.; Seinfeld, J. H., Time scales to achieve atmospheric gas-aerosol equilibrium for volatile species. *Atmos. Environ.* **1996,** *30*, (16), 2889-2900.

55. Dzepina, K.; Volkamer, R. M.; Madronich, S.; Tulet, P.; Ulbrich, I. M.; Zhang, Q.; Cappa, C. D.; Ziemann, P. J.; Jimenez, J. L., Evaluation of recently-proposed secondary organic aerosol models for a case study in Mexico City. *Atmos. Chem. Phys.* **2009,** *9*, (15), 5681-5709.

56. Cappa, C. D.; Jimenez, J. L., Quantitative estimates of the volatility of ambient organic aerosol. *Atmos. Chem. Phys.* **2010,** *10*, (12), 5409-5424.

57. Docherty, K. S.; Aiken, A. C.; Huffman, J. A.; Ulbrich, I. M.; DeCarlo, P. F.; Sueper, D.; Worsnop, D. R.; Snyder, D. C.; Peltier, R. E.; Weber, R. J.; Grover, B. D.; Eatough, D. J.; Williams, B. J.; Goldstein, A. H.; Ziemann, P. J.; Jimenez, J. L., The 2005 Study of Organic Aerosols at Riverside (SOAR-1): instrumental intercomparisons and fine particle composition. *Atmos. Chem. Phys.* **2011,** *11*, (23), 12387-12420.

58. Freney, E. J.; Martin, S. T.; Buseck, P. R., Deliquescence and Efflorescence of Potassium Salts Relevant to Biomass-Burning Aerosol Particles. *Aerosol Sci. Technol.* **2009,** *43*, (8), 799-807.

59. Martin, S. T., Phase transitions of aqueous atmospheric particles. *Chem. Rev.* **2000,** *100*, (9), 3403-3453.

60. Rood, M. J.; Shaw, M. A.; Larson, T. V.; Covert, D. S., Ubiquitous Nature of Ambient Metastable Aerosol. *Nature* **1989,** *337*, (6207), 537-539.

61. Petters, M. D.; Kreidenweis, S. M., A single parameter representation of hygroscopic growth and cloud condensation nucleus activity. *Atmos. Chem. Phys.* **2007,** *7*, (8), 1961-1971.

62. Prideaux, E. B. R., The deliquescence and drying of ammonium and alkali nitrates and a theory of the absorption of water vapour by mixed salts. *J. Soc. Chem. Ind.* **1920,** *39*, 182-185.

63. Martin, S. T.; Hung, H. M.; Park, R. J.; Jacob, D. J.; Spurr, R. J. D.; Chance, K. V.; Chin, M., Effects of the physical state of tropospheric ammonium-sulfate-nitrate particles on global aerosol direct radiative forcing. *Atmos. Chem. Phys.* **2004,** *4*, 183-214.

64. Moffet, R. C.; Qin, X. Y.; Rebotier, T.; Furutani, H.; Prather, K. A., Chemically segregated optical and microphysical properties of ambient aerosols measured in a single-particle mass spectrometer. *J. Geophys. Res.* **2008,** *113*, (D12).

65. Williams, B. J.; Goldstein, A. H.; Kreisberg, N. M.; Hering, S. V.; Worsnop, D. R.; Ulbrich, I. M.; Docherty, K. S.; Jimenez, J. L., Major components of atmospheric organic aerosol in southern California as determined by hourly measurements of source marker compounds. *Atmos. Chem. Phys.* **2010,** *10*, (23), 11577-11603.

66. Cruz, C. N.; Dassios, K. G.; Pandis, S. N., The effect of dioctyl phthalate films on the ammonium nitrate aerosol evaporation rate. *Atmos. Environ.* **2000,** *34*, (23), 3897-3905.

67. Zelenyuk, A.; Ezell, M. J.; Perraud, V.; Johnson, S. N.; Bruns, E. A.; Yu, Y.; Imre, D.; Alexander, M. L.; Finlayson-Pitts, B. J., Characterization of organic coatings on hygroscopic salt particles and their atmospheric impacts. *Atmos. Environ.* **2010,** *44*, (9), 1209-1218.

68. Li, J.; Posfai, M.; Hobbs, P. V.; Buseck, P. R., Individual aerosol particles from biomass burning in southern Africa: 2, Compositions and aging of inorganic particles. *J. Geophys. Res.* **2003,** *108*, (D13).

69. Posfai, M.; Simonics, R.; Li, J.; Hobbs, P. V.; Buseck, P. R., Individual aerosol particles from biomass burning in southern Africa: 1. Compositions and size distributions of carbonaceous particles. *J. Geophys. Res.* **2003,** *108*, (D13).

70. Laskin, A.; Laskin, J.; Nizkorodov, S. A., Mass spectrometric approaches for chemical characterisation of atmospheric aerosols: critical review of the most recent advances. *Environmental Chemistry* **2012,** *9*, (3), 163-189.

71. Zelenyuk, A.; Yang, J.; Song, C.; Zaveri, R. A.; Imre, D., "Depth-profiling" and quantitative characterization of the size, composition, shape, density, and morphology of fine particles with SPLAT, a single-particle mass spectrometer. *J. Phys. Chem. A* **2008,** *112*, (4), 669-677.

72. Shiraiwa, M.; Pfrang, C.; Koop, T.; Poschl, U., Kinetic multi-layer model of gas-particle interactions in aerosols and clouds (KM-GAP): linking condensation, evaporation and chemical reactions of organics, oxidants and water. *Atmos. Chem. Phys.* **2012,** *12*, (5), 2777-2794.

73. Fredenslund, A.; Jones, R. L.; Prausnitz, J. M., Group-Contribution Estimation of Activity-Coefficients in Nonideal Liquid-Mixtures. *Aiche Journal* **1975,** *21*, (6), 1086-1099.

74. Peng, C.; Chan, M. N.; Chan, C. K., The hygroscopic properties of dicarboxylic and multifunctional acids: Measurements and UNIFAC predictions. *Environ. Sci. Technol.* **2001,** *35*, (22), 4495-4501.

75. Peckhaus, A.; Grass, S.; Treuel, L.; Zellner, R., Deliquescence and Efflorescence Behavior of Ternary Inorganic/Organic/Water Aerosol Particles. *J. Phys. Chem. A* **2012,** *116*, (24), 6199-6210.

76. Smith, J. N.; Barsanti, K. C.; Friedli, H. R.; Ehn, M.; Kulmala, M.; Collins, D. R.; Scheckman, J. H.; Williams, B. J.; McMurry, P. H., Observations of aminium salts in

atmospheric nanoparticles and possible climatic implications. *Proc. Natl. Acad. Sci. USA* **2010,** *107*, (15), 6634-6639.

77. Kurten, T.; Loukonen, V.; Vehkamaki, H.; Kulmala, M., Amines are likely to enhance neutral and ion-induced sulfuric acid-water nucleation in the atmosphere more effectively than ammonia. *Atmos. Chem. Phys.* **2008,** *8*, (14), 4095-4103.

78. Barsanti, K. C.; McMurry, P. H.; Smith, J. N., The potential contribution of organic salts to new particle growth. *Atmos. Chem. Phys.* **2009,** *9*, (9), 2949-2957.

79. Creamean, J. M.; Ault, A. P.; Ten Hoeve, J. E.; Jacobson, M. Z.; Roberts, G. C.; Prather, K. A., Measurements of Aerosol Chemistry during New Particle Formation Events at a Remote Rural Mountain Site. *Environ. Sci. Tech.* **2011,** *45*, (19), 8208-8216.

80. Ge, X. L.; Wexler, A. S.; Clegg, S. L., Atmospheric amines - Part II. Thermodynamic properties and gas/particle partitioning. *Atmos. Environ.* **2011,** *45*, (3), 561-577.

81. Salo, K.; Westerlund, J.; Andersson, P. U.; Nielsen, C.; D'Anna, B.; Hallquist, M., Thermal Characterization of Aminium Nitrate Nanoparticles. *J. Phys. Chem. A* **2011,** *115*, (42), 11671-11677.

82. Angelino, S.; Suess, D. T.; Prather, K. A., Formation of aerosol particles from reactions of secondary and tertiary alkylamines: Characterization by aerosol time-of-flight mass spectrometry. *Environ. Sci. Tech.* **2001,** *35*, (15), 3130-3138.

83. Ziemann, P. J., Effects of molecular structure on the chemistry of aerosol formation from the OH-radical-initiated oxidation of alkanes and alkenes. *Int. Rev. Phys. Chem.* **2011,** *30*, (2), 161-195.

84. LeClair, J. P.; Collett, J. L.; Mazzoleni, L. R., Fragmentation Analysis of Water-Soluble Atmospheric Organic Matter Using Ultrahigh-Resolution FT-ICR Mass Spectrometry. *Environ. Sci. Technol.* **2012,** *46*, (8), 4312-4322.

85. Farmer, D. K.; Matsunaga, A.; Docherty, K. S.; Surratt, J. D.; Seinfeld, J. H.; Ziemann, P. J.; Jimenez, J. L., Response of an aerosol mass spectrometer to organonitrates and organosulfates and implications for atmospheric chemistry. *Proc. Natl. Acad. Sci. USA* **2010,** *107*, (15), 6670-6675.

86. Day, D. A.; Liu, S.; Russell, L. M.; Ziemann, P. J., Organonitrate group concentrations in submicron particles with high nitrate and organic fractions in coastal southern California. *Atmos. Environ.* **2010,** *44*, (16), 1970-1979.

87. Hilal, S. H.; Karickhoff, S. W.; Carreira, L. A., Prediction of the vapor pressure, boiling point, heat of vaporization, and diffusion coefficient of organic compounds. *Qsar & Combinatorial Science* **2003,** *22*, (6), 565-574.

88. Compernolle, S.; Ceulemans, K.; Muller, J. F., Influence of non-ideality on condensation to aerosol. *Atmos. Chem. Phys.* **2009,** *9*, (4), 1325-1337.

89. Seinfeld, J. H.; Pankow, J. F., Organic atmospheric particulate material. *Annual Review of Physical Chemistry* **2003,** *54*, 121-140.

6 Implementation of an ion funnel in proton-transfer-reaction mass spectrometry

6.1 Abstract

Proton-transfer-reaction mass spectrometry (PTRMS) is a widely used tool for the analysis of trace gases in the atmosphere. In the last few years, significant progress has been made in applying this technique toward the analysis of organic aerosol particles; however, the analytical capabilities have been rather limited due to poor sensitivity. High pressures are required for efficient ionization in PTRMS, which can hinder ion transmission efficiencies due to the need for differentially-pumped chambers connecting the ion source to the low-pressure mass analyzer. Ion funnels have been demonstrated in other mass-spectrometric-based applications to yield near unit ion transmission efficiency in relatively high pressure regions. Therefore, incorporating these devices into PTRMS instruments could provide substantial sensitivity improvements. In this chapter, implementation of an ion funnel into a PTRMS instrument and its initial characterization are described. Through ion simulations, transmission efficiencies up to 90% were estimated for analyte ions. It is further demonstrated that RF heating in the ion funnel can be used to efficiently break apart water clusters that can complicate PTRMS mass spectra. Water adducts of protonated reagent and analyte ions were observed to decluster at RF amplitudes of only 10-20 V_{p-p}. These results highlight the potential benefits that ion funnels can provide in the PTRMS field and atmospheric analytical chemistry.

6.2 Introduction

Organic compounds comprise a large fraction of atmospheric aerosol mass.[1] The extensive sources and atmospheric transformation processes contributing to organic aerosols result in a very large number of possible compounds, many of which have not been identified.[2-4] The complexity and low volatility of the organic species in aerosols make them extremely difficult to analyze using traditional analytical techniques.[5] It has been an elusive challenge to come up with a universal analytical approach which can analyze a broad range of compounds with such highly variable chemical and physical properties (e.g., solubility and volatility).[6] Current analytical methods targeting aerosols fall into two broad categories: off-line and on-line methods. The most common off-line analysis methods targeting organics entail particle

collection (e.g., via filtration or impaction) with subsequent sample preparation and analysis. Extraction of aerosol components into organic solvent misses the water soluble fraction (and vice-versa). While this post-analysis can provide comprehensive molecular characterization (e.g., through chromatographic separation[e.g.,7,8] and/or high-resolution mass spectrometry methods[e.g.,9,10]), the long sampling times involved in filter collection averages the composition over the entire aerosol population and further limits our understanding of their temporal evolution. Further, polar, multifunctional compounds, which are common following atmospheric oxidation, are often not amenable to chromatographic separation and typically require derivatization prior to analysis,[2,11] thus further complicating and extending sample preparation.

To circumvent the long sample preparation and poor time resolution of off-line methods, significant efforts over the last couple decades have pushed towards development of on-line aerosol analysis methods.[12] In particular, single-particle mass spectrometry (SPMS) techniques have provided insight into the chemical associations (i.e., mixing state) of species among individual particles, which is vital for source apportionment and studies of aerosol processing. However, the ability to speciate organic molecules within individual particles and quantify their concentrations using on-line SPMS techniques has been extremely limited.[13,14] The high laser power of laser desorption/ionization (LDI) typically used in SPMS instruments can fragment organic species resulting in limited molecular information. Aerosol mass spectrometry (AMS) has become widely used for the quantitative characterization of organic aerosols in real-time.[15,16] However, the 70-eV electron impact ion source used in this instrument is also known to cause extensive fragmentation of organic molecules. Thus, in these methods, the mass spectra of atmospheric particles are a convolution of fragment ions from the numerous organic species present. Further, many compounds break down to the same fragment ions, severely limiting the molecular information that can be gained.

Improving the ability to speciate molecular components could significantly enhance the scientific understanding regarding the sources, reactivity, and environmental impacts of organic aerosols in the atmosphere. To this end, new analytical techniques are desired and chemical ionization mass spectrometry (CIMS) is one approach that has recently gained attention for the on-line analysis of atmospheric aerosol constituents.[e.g.,17-20] Chemical ionization (CI) utilizes ion-molecule reactions between primary reagent ions and neutral analyte gases to ionize the analyte via a lower energy process than SPMS and AMS methods, thereby reducing fragmentation of the analyte molecules. Further, the reagent ions and ionization mechanisms can be varied, including

charge exchange, proton transfer, and ion association, that can selectively target different molecular classes. In this work, proton transfer was used as the ionization scheme, and is described in detail in the following section.

6.2.1 *Proton-Transfer-Reaction Mass Spectrometry*

Proton-transfer-reaction mass spectrometry (PTRMS) is the most common CI method and has emerged as a powerful tool for the on-line analysis of trace gases in the atmosphere.[21] This technique was first pioneered in the mid-to-late 90's by Armin Hansel and Werner Lindinger.[22-27] In PTRMS instruments, protonated water (H_3O^+) is used as the reagent ion and reacts with neutral analyte molecules (R) through:

$$H_3O^+ + R \rightarrow H_2O + RH^+ \qquad (6.1)$$

In order to ionize, the analyte molecule must have a higher proton affinity (PA) than the reagent ion. The PA of water (7.16 eV)[28] is high enough that it will not ionize the major gases in the atmosphere (e.g., N_2, O_2, CO_2, CH_4), but is lower than most organic molecules (~7-10 eV) and can therefore act as a nearly universal reagent ion (alkanes are not efficiently ionized by water).[23] The internal energy (and thus the likelihood of fragmentation) of the product ion is dictated by the difference in PA between the analyte molecule and water.[29] For H_3O^+ CI, this difference is relatively low—on the order of 2-3 eV or less—resulting in little fragmentation of the analyte species. Water proton-transfer ionization can therefore be considered a relatively soft ionization mechanism that generally permits detection of molecular ions.

PTRMS is not without its own challenges. In particular, the reagent and analyte ions tend to form clusters with additional neutral water molecules (i.e., $H_3O\cdot(H_2O)_n^+$ and $RH\cdot(H_2O)_n^+$). The presence of these clusters can significantly complicate mass spectral identification, since species are typically identified solely by their *m/z*. Water-bound clusters of the reagent ions can also impact the ion chemistry because these adducts have higher proton affinity than bare H_3O^+.[30] To eliminate these clusters, PTRMS instruments to date have utilized drift tubes wherein a large potential (several hundred volts or more) is applied across a series of electrodes at a pressure of generally 1 Torr or greater. The high electric field increases the kinetic energy of the ions, which, in combination with collisions between the ions and the bath gas, breaks apart these clusters. The relatively high pressures within the drift tube also result in high ionization efficiency for analytes with sufficient PA due to the high number of collisions occurring between the reagent ion and analyte gas combined with reaction rates occurring near the collisional limit.[29] However, the

difficulty lies in efficiently transferring ions to the mass analyzer that typically operates at least 5 orders of magnitude lower pressure than the reaction chamber. To achieve the necessary pressure drop, ions are generally extracted from the drift region via pinhole orifices, which tend to have low transmission efficiencies and subsequently traverse additional pumping stages en route to the mass spectrometer. Traditional ion optics (e.g., Einzel lenses and RF-only multipole ion guides) are generally not effective at typical CI pressures. Therefore it is advantageous to explore methods other than the typical drift tube-orifice configuration in order to provide higher sensitivity analysis.

The ultimate aim of this project is to build a highly-sensitive CIMS capable of analyzing the molecular constituents of single organic aerosols. A number of groups have developed PTRMS instruments for the analysis of an ensemble of organic aerosols. Because ionization requires gas-phase ion-molecule reactions, aerosol components must first be vaporized. The most widely used method is thermal desorption, wherein aerosols are passed through a continuously heated desorption tube or collected onto a substrate for a period of time followed by substrate heating. Voisin *et al.*[19] first described the CI of ultrafine particles by collecting aerosols via electrostatic precipitation onto a heated filament with subsequent analysis by CIMS. This system has made important progress into the chemical analysis of atmospheric nanoparticles.[31] Hearn and Smith[17] specifically targeted organic aerosols by coupling a heated-tube aerosol inlet to CIMS. Their aerosol CIMS instrument is capable of utilizing a variety of reagent ions to target different types of molecules[17] and has been applied primarily to the analysis of laboratory chamber experiments.[32,33] They were able to analyze ambient aerosols only after collecting off-line for 6 hours.[33] Thornberry *et al.*[34] developed an ion-trap PTRMS system and first demonstrated the use of a resistive glass drift tube to provide a more homogeneous field than the common discrete electrodes used in drift regions. Their instrument was deployed for shipboard ambient measurements and identified a handful of ions above their detection limit.[34] Mikoviny *et al.*[35] followed in their footsteps and incorporated a resistive glass drift tube into a high-temperature PTRMS that is capable of operating continuously at 250 ºC. Their work represents a significant step toward reducing wall losses due to the condensation of low volatility gases. Yatavelli and Thornton[20] developed a micro-orifice virtual impactor for high efficiency *in-situ* aerosol collection and demonstrated its use by characterizing laboratory ozonolysis reactions. Holzinger *et al.*[36] designed an aerosol collection/thermal desorption cell and coupled it to a commercial PTRMS instrument. They successfully applied their method toward the

characterization of ambient aerosols after collecting for 2.5 - 3 hours.[18,36] Collectively, these works have made significant inroads regarding the chemical ionization of aerosol particles. However, few of these systems provide adequate sensitivity for high-level analysis of ambient aerosols and typically require long collection times. Most of these instruments utilize the conventional drift tube-orifice configuration for ion-molecule reaction regions; the poor transmission efficiency of this geometry could be limiting the sensitivity of these instruments. It is therefore essential to explore alternative methods that could achieve improved ion transmission, while still providing the drift tube functionality (i.e., declustering). To this end, an electrodynamic ion funnel was applied as a potential means of improving upon the standard PTRMS methods.

6.2.2 *Ion funnel*

Ion funnels (IF) were developed about 15 years ago to achieve high ion transmission across differentially pumped stages in mass spectrometers.[37,38] In particular, these devices filled a critical need by providing efficient ion transfer from high pressure ionization sources to low pressure mass analyzers. The IF principle was based on the stacked ring ion guide first described by Gerlich[39] and consists of a series of parallel plates (electrodes) with progressively decreasing inner diameters (Figure 6.1). Each plate receives both a static (DC) and oscillating (radio frequency, RF) voltage. A DC gradient is applied across the plates to drive ions down the axis toward the exit. The RF signals are applied 180° out of phase to adjacent plates, as shown in Figure 6.1a. The interaction of the fields from adjacent plates cancels out a short distance from the plates, and thus creates a near field-free region in the center of the IF (Figure 6.1b). Further, the radial effective potential of a stacked ring ion guide is approximately proportional to the exponential of the radius, yielding a steep potential at the electrode surface that quickly drops to nearly zero at the center.[39] These fields therefore provide a very large acceptance area to confine ions. In comparison, the effective potential of quadrupoles that are commonly used as ion transfer devices, scales as $\sim r^2$,[39] resulting in a very narrow trapping and transfer region. IFs thus provide very large space-charge capacity relative to standard ion optics.[40] IFs have been shown to achieve near unity transfer of ions across the interfaces of differential pumping stages and have further been shown to operate effectively in relatively high pressure regions (~0.1 – 30 Torr).[41] In their implementation with electrospray ionization sources, IFs have demonstrated a 10-fold improvement over typical skimmer interfaces.[37]

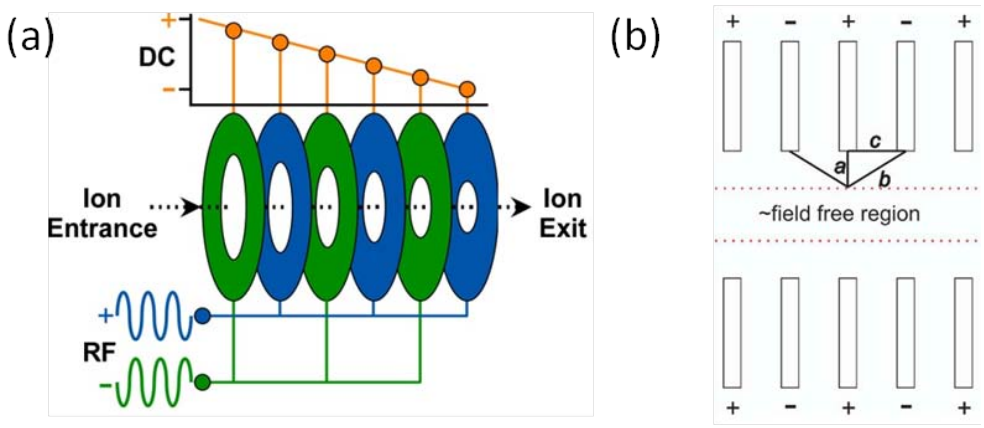

Figure 6.1 (a) Schematic of the ion funnel electrodes and applied potentials. (b) Cancellation of the RF field from adjacent plates. The figure in panel (b) was reprinted from Julian *et al.*[42] Copyright 2005, with permission, from Elsevier.

Researchers have also found that adduct ions can be either broken apart or transmitted through the IF by adjusting the RF amplitude[43] and that RF heating—the increase in internal energy of the ions due to the energetic collisions induced by the RF oscillations—increases with increasing RF amplitude.[44] The key features of IFs—high pressure operation, high efficiency ion transfer, and adduct removal—indicate that their implementation in PTRMS instruments could yield substantial improvements over existing instruments. However, IFs are most broadly applied to the characterization of large biomolecules.[37,38,42,43] Comparatively few studies have utilized ion funnels for the analysis of low molecular weight species (m/z < 200).[44,45] Kukui *et al.*[45] were the first to utilize an IF in a CIMS instrument, which used SO_2 reagent gas to target OH radicals. Herein, an IF was implemented into a home-built PTRMS instrument as proof-of-concept for their utility in these instruments. Results are described regarding the effects of RF heating on ion declustering. Computer simulations were also performed to characterize the ion transmission properties of the IF design used in this work. While the ultimate goal is for the analysis of atmospheric organic aerosol particles, initial characterization studies were performed with gas-phase analytes. Preliminary aerosol analysis will be discussed at the end.

6.3 Instrument Description

A schematic diagram of the recently constructed instrument is shown in Figure 6.2. A radioactive ion source (Po-210) was used to generate H_3O^+ reagent ions. Ultra-high purity nitrogen was bubbled at ~1.5 lpm through a reservoir of water (Milli-Q, 18.2 MΩ) and subsequently introduced into the ion source via a 0.33 mm orifice (0.865 liters per minute (lpm)). The source was operated at 30-35 Torr, maintained by a dry scroll pump (SH-110, 110 lpm,

Agilent Technologies, Lexington, MA) with a baffle valve to provide necessary pressure adjustments. The source region is separated from the ion funnel reaction region via a 1 mm orifice to both step down the pressure and reduce the interaction between the radiation and analyte gases. The ion funnel region was operated at ~1.4 Torr, via a second scroll pump (TS600, 500 lpm, Agilent Technologies, Lexington, MA). Scroll pumps are oil-free and therefore eliminate the potential of organic contamination from the pumping system. The ion funnel utilized here is similar to that described by Moision et al.[44] It consists of 40 0.5 mm thick brass plates, separated by 0.5 mm thick Teflon washers. The ion funnel entrance plate has an inner diameter (i.d.) of 16.6 mm, with subsequent plates tapering linearly down to the exit plate of 0.74 mm i.d. The electrodes were designed and constructed in house. A low-voltage power supply was designed to provide the ion source voltages and DC potentials for the ion funnel. A function/waveform generator (Model 3320A, Agilent Technologies, Englewood, CO) provides the RF signal, which was amplified by a 50 db broadband amplifier (Model 155LCRH, Kalmus Engineering). The amplified waveform was passed through a trifilar-wrapped balun to transform the signal into two equal-intensity and 180º out of phase waveforms. A custom printed circuit board was designed to pass the necessary DC and RF potentials to each IF plate. The PCB contains the resistor (200 kΩ) chain that defines the linear DC gradient across the ion funnel and 1 nF capacitors that pass the RF signal. Electrical connections were made directly to each plate within the vacuum chamber via individual leads and clips. A DC-only lens was also added at the end of the ion funnel to help focus ions into the subsequent pumping chamber. The potentials used in the instrument front end were: Source, 50.2 V; Sample Inlet, 51.9 V; IF DC gradient, 23.5→14.5 V; Lens, 14.3 V.

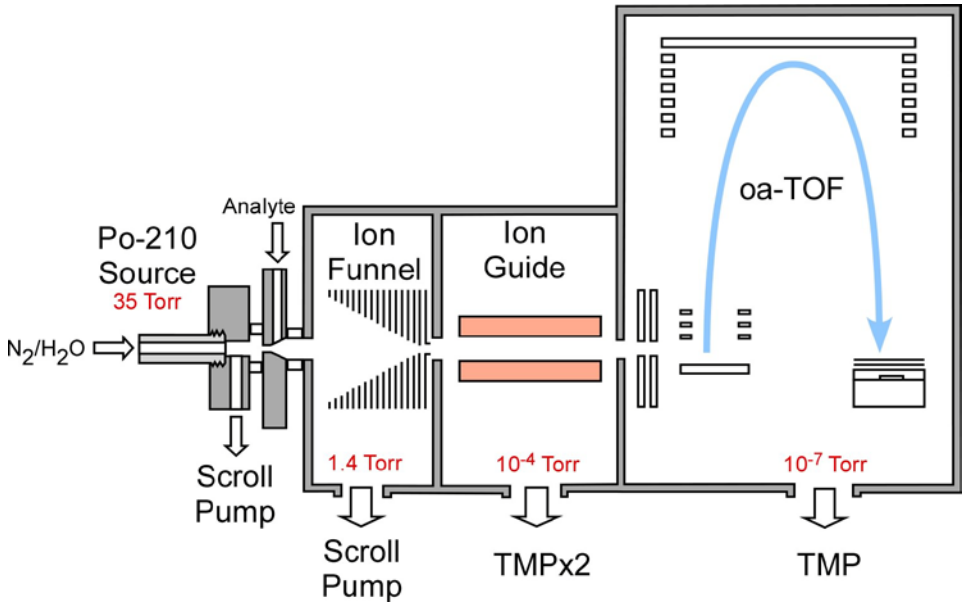

Figure 6.2 Schematic of the ion funnel-PTRMS instrument. Not drawn to scale. TMP = turbomolecular pump.

Following the IF, ions enter an intermediate pumping chamber equipped with an RF-only quadrupole (Aerodyne, Inc., Billerica, MA) to transfer ions to the mass analyzer. This region was pumped by two 250 L/s turbo molecular pumps (V-301, Agilent Technologies, Lexington, MA). The mass analyzer is an orthogonal acceleration (oa), reflectron time-of-flight mass spectrometer (c-TOF, Aerodyne, Inc., Billerica, MA) and is pumped by one 250 L/s turbo molecular pump (V-301, Agilent Technologies, Lexington, MA). The TOFMS was operated at a repetition rate of 65 kHz and the signal was integrated over 1 second. An additional practical, yet important, component was a custom sliding gate valve installed in between the IF and quadrupole regions to isolate the high vacuum chambers from the source region when necessary. This valve greatly facilitated development and cleaning of the ion funnel without adding undue strain to the turbo pumps and microchannel plate detector due to frequent venting.

Analytes were introduced to the sample inlet upstream of the ion funnel (Figure 6.2). Initial instrument characterization experiments utilized gas-phase analytes that were introduced by flowing nitrogen over a reservoir containing the compounds of interest. Acetone and triethylamine were used herein without further purification. The analytes were passed into the instruments via either a mass flow controller (5 sccm, MKS Instruments, Andover, MA) or a critical orifice (15 sccm, O'Keefe Controls, Trumbull, CT).

6.4 Results & Discussion

While the ultimate goal of incorporating an IF into PTRMS is to provide high detection sensitivity, this chapter will explore its ability to replace conventional drift tubes. To this end, IFs must be able to effectively break apart water adducts while maintaining high ion transmission. These properties were characterized experimentally and theoretically using ion simulation software. Because RF heating is proportional to RF voltage, these properties were assessed as a function of RF amplitude. Although the instrument is being developed for aerosol analysis, initial characterization studies were performed using gas-phase analytes and will comprise the bulk of this chapter. Preliminary analysis of aerosol standards will be discussed at the end.

Changes in the RF amplitude can impact the detected ion signal in two distinct ways: by altering the ion transmission efficiency and the extent of water clustering. Therefore, two representative gas-phase analytes were chosen to best decouple these effects during IF characterization: triethylamine (TEA, MW = 101 amu) and acetone (Ac, MW = 58 amu). TEA does not cluster efficiently with water due to its high proton affinity (10.2 eV[28]) and therefore the $^{102}TEAH^+$ ion signal should change primarily due to changes in transmission efficiency. Acetone was also used because experience with earlier instrument prototypes showed that protonated acetone clustered significantly with water ($^{77}AcH(H_2O)^+$) and itself ($^{117}Ac_2H^+$). This is consistent with its lower PA of 8.4 eV.[28] Amines and ketones are also commonly found in atmospheric organic aerosol particles,[14,31,46,47] and therefore these representative compounds are relevant to future applications of this instrument for aerosol analysis. Example spectra obtained at low (10 $V_{peak\text{-}to\text{-}peak}$, $V_{p\text{-}p}$) and high (22 $V_{p\text{-}p}$) RF are shown in Figure 6.3 for acetone and TEA analysis. At low RF amplitude (panel a), the presence of extensive water clusters of both reagent ($H(H_2O)_n^+$, *n*=2-4) and analyte ($^{77}AcH(H_2O)^+$) ions were clearly observed. At elevated RF amplitudes (panel b), the cluster ions from both reagent and analyte ions were largely eliminated and the spectrum was substantially simplified. However, small contributions from fragment ions (e.g., $^{31}CH_3O^+$) were present in the mass spectra obtained in high RF mode and will be discussed in Section 6.4.3. Detailed characterization of the *m/z*- and RF-dependent ion transmission and the effect of RF amplitude on ion declustering were performed and will be described in the following sections.

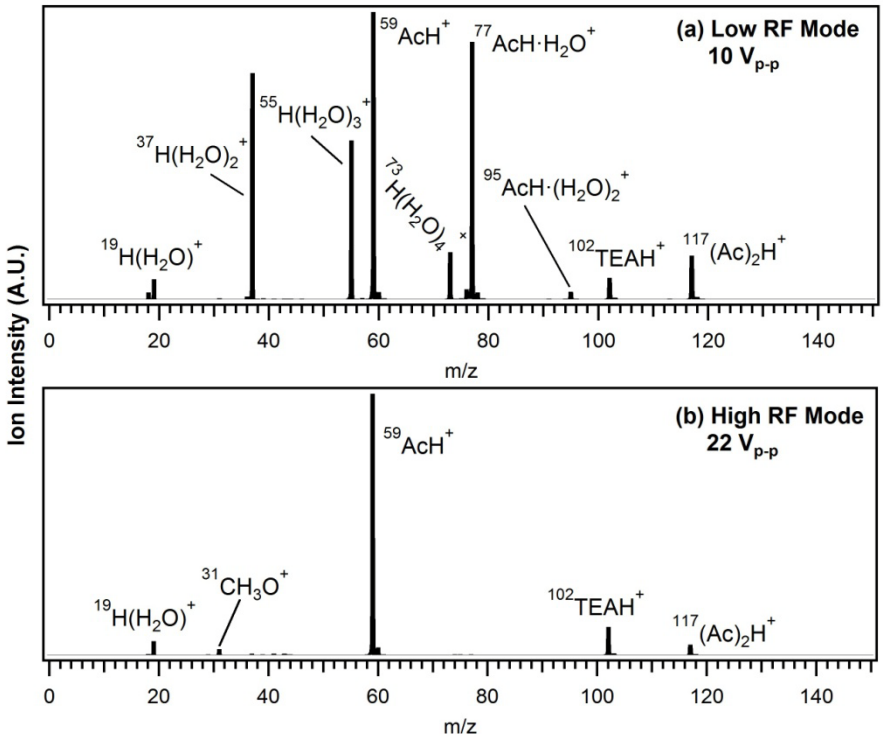

Figure 6.3 Example Spectra at low (a) and high (b) RF amplitudes. RF frequency = 2.41 MHz; Ac = Acetone, TEA = triethylamine.

6.4.1 *Ion Transmission*

Given the high relative intensity of the reagent ion water clusters ($H(H_2O)_n^+$, n=2-4) in low RF mode (Figure 6.3a), one would expect a corresponding increase in the H_3O^+ ion signal as these clusters break apart at high RF amplitude. The peak intensity of H_3O^+, however, remained low in high RF mode (Figure 6.3b); it was therefore postulated that the IF was biased against low mass ions. Ion trajectory calculations were performed using the ion simulation software SIMION (Version 8.0.6, Scientific Instrument Services, Inc., Ringoes, NJ) to better characterize the transmission properties of the IF configuration. This software calculates the electrostatic fields for the user-defined electrode geometry; ion motion is then predicted based on the potential energy surface. Further, SIMION can mimic collisions with a simulated bath gas using a built-in hard-sphere collision model. This was utilized with the pressures set to 1.4 Torr in the ion funnel region and 1.2 x 10^{-4} Torr in the region following the IF exit orifice (i.e., the ion guide region in the real instrument). The collision cross section of N_2 was used for all trajectories. Ions were started with ~0 kinetic energy (KE); initial trials indicated that any initial ion KE was quickly dissipated at 1.4 Torr via collisional cooling and thus had no effect on the resulting ion trajectory, consistent with previous simulations.[48] Ion trajectories for individual ions were calculated

sequentially and thus space-charge effects were not considered. An example simulation for $^{102}TEAH^+$ is included in Figure 6.4a to show the electrode geometry and resulting trajectories. In the simulations, gas flow was necessary for successful transmission; a gas velocity of 300 m/s along the IF axis was used herein, which is consistent with jet velocities under choked flow conditions, which are expected from the gas expansion through the orifice in the sample inlet. For comparison, previous IF simulations have used supersonic gas velocities (500 m/s).[48] When no gas flow was used, the ions crashed out at the grounded electrodes, as seen in Figure 6.4b. Therefore, the geometry could be modified to eliminate the ion line of sight to all grounded components and perhaps improve the sensitivity. All subsequent simulations assumed choked-flow gas velocities, as described above. For each ion and RF voltage considered, 1000 trajectories were calculated and the transmission efficiency was based on the number of ions hitting the splat plate at the far right edge of the model domain (Figure 6.4a).

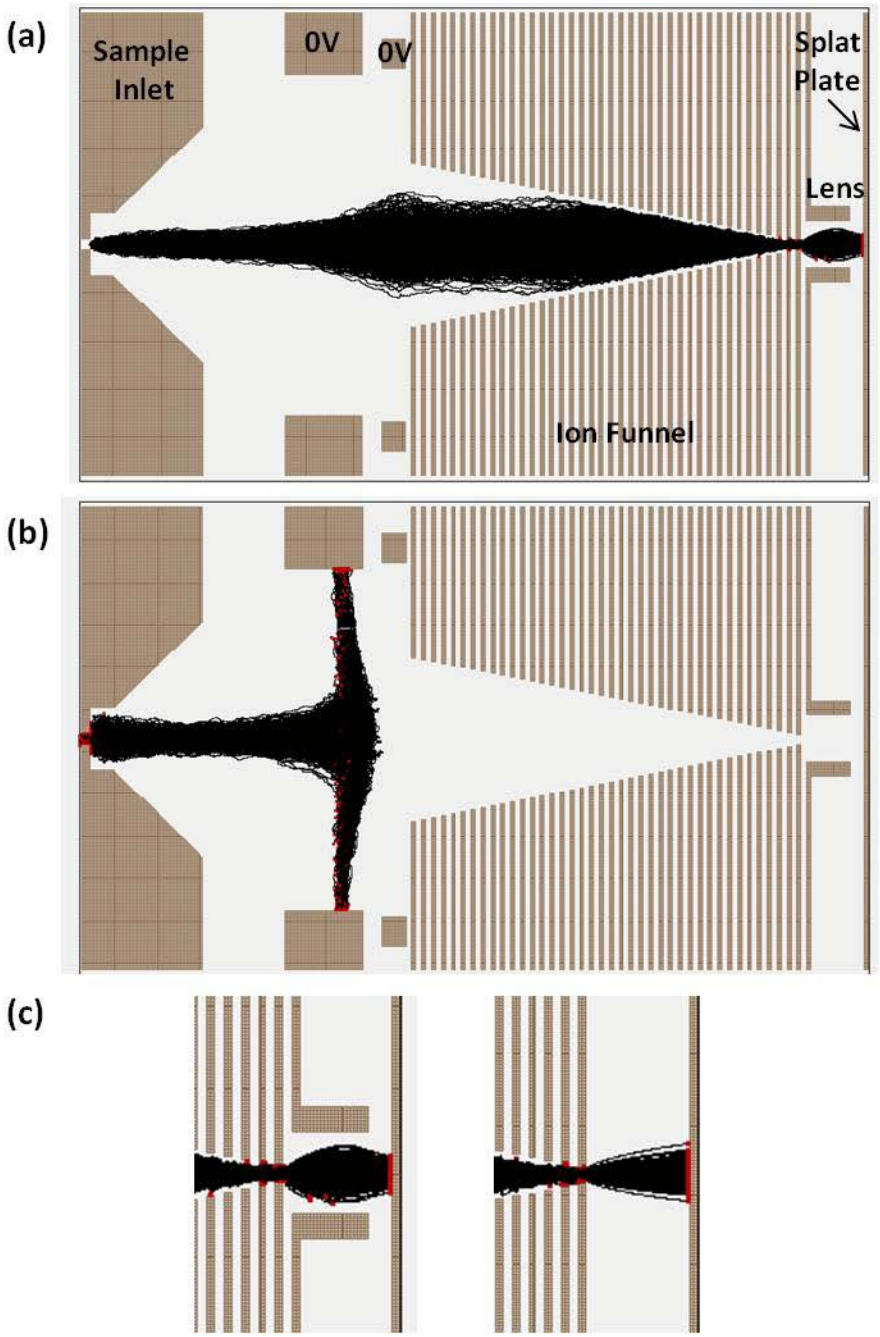

Figure 6.4 Screen shots of SIMION simulations for $^{102}TEAH^+$ (1000 Trajectories). Grounded electrodes are indicated with '0V'. For all simulations: RF = 2.4 MHz, 30 V_{p-p}; IF pressure = 1.4 Torr; Ion guide pressure = 1.2 x 10^{-4} Torr. Red dots indicate ions hitting an electrode or the splat plate. (a) Full simulation, with gas flow (300 m/s in the x-direction) and exit lens; (b) no gas flow; and (c) comparison of simulations with (left) and without (right) the exit lens.

The example simulation in Figure 6.4a shows the effective radial confinement of ions within the IF. Under the conditions of this simulation, minimal (10.6%) of ions were lost to

electrodes (as indicated by red dots before the splat plate) and only 1 ion was lost before the third-to-last IF plate. The performance of the exit lens at refocusing divergent ions is also clearly demonstrated in Figure 6.4c (left panel). A comparison of simulations run with and without the exit lens is included in Figure 6.4c. The divergence in the ion beam is significantly wider without the exit lens: at the splat plate, the ions spread as much as 1.9 mm from the central axis, compared to 1.1 mm with the lens. The low pressure region following the IF is in the free molecular regime, with mean free paths (~42 cm) far too long for ions to be collisionally focused. Therefore, the divergent ion trajectories in the absence of an exit lens will continue to travel away from the central axis and may not be efficiently transferred to the quadrupole ion guide in the following chamber. The exit lens therefore helped to reduce ion losses between the differentially pumping stages.

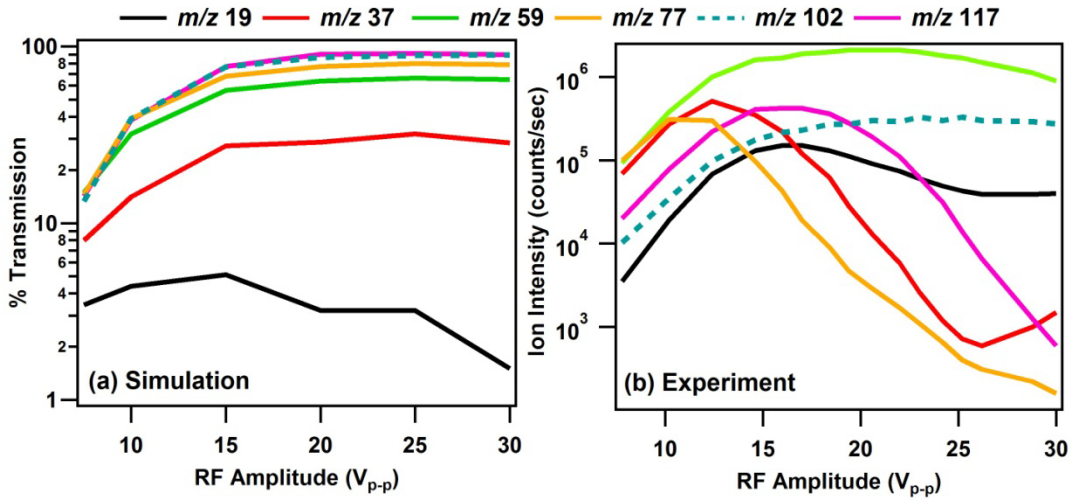

Figure 6.5 (a) Transmission efficiencies calculated from SIMION simulations and (b) Ion intensities observed experimentally.

Similar ion trajectories were calculated for the range of ions and RF amplitudes considered herein. The resulting transmission curves are included in Figure 6.5a with measured ion intensity curves shown for comparison in panel b (note that the simulations results are given in terms of % of ions transmitted whereas the experimental measurements are presented as the ion signal, counts/sec). The simulation results can be validated against the experimental measurements of $^{102}TEAH^+$ (blue dashed line), since clusters of this analyte were not observed at any RF amplitude (Figure 6.3). The general trends agree very well: both simulations and measurements indicate an increase in ion transmission as the RF amplitude was initially raised, which leveled off at ~20 V_{p-p}. The magnitude of the change between low and high RF amplitude

were similar, but differed slightly. The simulations predicted a ~8-9-fold increase in transmission from 7.5 – 30 V_{p-p}, whereas the experimental results displayed a ~25-fold increase in the ion intensity from 7.8 – 31 V_{p-p}. The measured ion intensity drops off more steeply in the low RF range. The general agreement between the simulations and measurements for $^{102}TEAH^+$ demonstrates that the simulations can be used to provide insight into the IF properties.

The simulations demonstrate that low RF fields are not strong enough to effectively confine ions in this IF, as indicated by the increase in transmission efficiency up to 20 V_{p-p} (Figure 6.5a). Above 20 V_{p-p}, the calculated transmission curves plateau for all *m/z* >37, indicating that ions above an *m/z* threshold will reach their maximum transmission at about the same RF amplitude. The fraction of ions transmitted, however, improved with increasing *m/z*; higher mass ions (*m/z* >102) reached ~90% transmission at >~20 V_{p-p}, compared to ~30% for *m/z* 37. Because of the theoretical plateau in transmission at high RF amplitude, the decrease in measured ion signal for the cluster ions, $^{37}H(H_2O)_2^+$, $^{77}AcH\cdot(H_2O)^+$, and $^{117}Ac_2H^+$ (Figure 6.5b) can be attributed to declustering, which will be described in Section 6.4.2. Low mass ions displayed very low ion transmission, with less than 5% of $^{19}H_3O^+$ transmitted under all conditions (Figure 6.5a). In previous studies, poor low mass ion transmission was attributed to IF geometries wherein the diameter of the last IF plate is of similar dimension to the plate spacing.[48] In such a configuration, potential wells form as the electrode diameters decrease toward the IF exit, as shown in Figure 6.6 (near r = 0 mm, z = 3.5 mm) that can trap ions.[48] The ion motion of low mass ions will become unstable in these wells and are thus most likely to be lost to the electrodes.

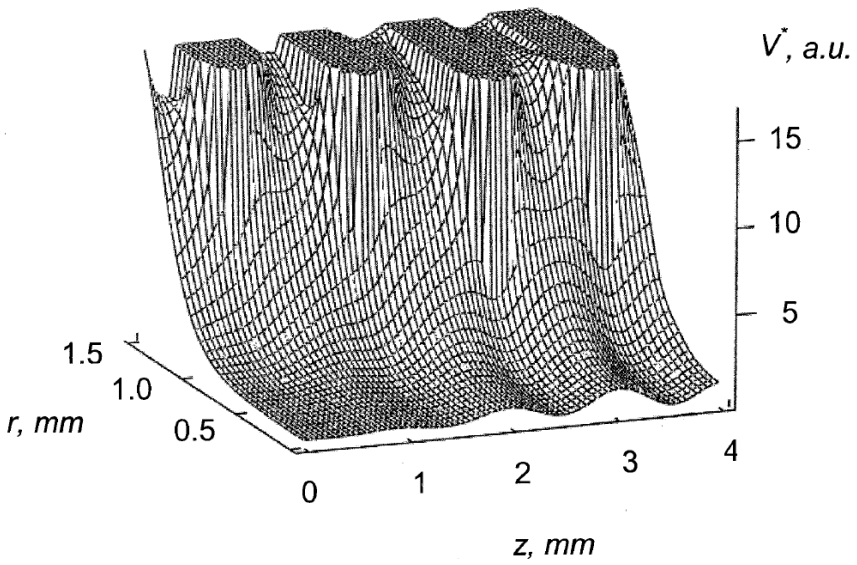

Figure 6.6 Ion Funnel Effective Potential. The flat tops represent the electrode surfaces; the electrode inner diameters decrease along the x-axis. *r* represents the radial position in the IF (*r* = 0 is the IF center). Note the increased potential well depth as the plate i.d. decreases (near *r* = 0 mm, *z* = 3.5 mm). Reprinted from Tolmachev *et al.*[48]. Copyright 2000, with permission from Elsevier.

The depth of these potential wells, or the trapping potential (V_{trap}), is related to the ratio of the electrode inner diameter (r) to the electrode spacing:[41]

$$V_{trap} = V_{max} 2\pi \frac{r}{\delta} exp\left(-\frac{2r}{\delta}\right). \tag{6.2}$$

V_{max} represents the effective potential at the surface of the IF electrodes and is given by:[48]

$$V_{max} = \frac{zeV_{RF}^2}{4m\omega^2\delta^2} \tag{6.3}$$

where z is the charge of the ion, e is the elementary charge, V_{RF} is the RF amplitude (0-p), m is the ion mass, ω is the angular frequency ($\omega = 2\pi f$), and δ is related to the spacing (d) between electrodes ($\delta = d/\pi$). To minimize ion trapping (and loss), V_{trap} should be very small relative to V_{max} and thus,[41]

$$2\pi \frac{r}{\delta} exp\left(-\frac{2r}{\delta}\right) \ll 1. \tag{6.4}$$

Equation 6.4 was evaluated for the electrode geometry used herein. With a 0.74 mm i.d. exit orifice and 0.5 mm electrode spacing, V_{trap} is ~15% of V_{max}, indicating that the potential wells

were significant at the IF exit and likely explain the very poor transmission efficiency of low mass ions observed in our system. In contrast, the trapping potential at the second to last plate (1.14 mm i.d.) was ~1.7% of V_{max}, demonstrating that expanding the exit orifice could enhance the ion transmission. However, the small exit diameter was necessary to achieve sufficiently low pressure in the mass spectrometer downstream.

The low transmission efficiency of reagent ions, particularly $^{19}H(H_2O)^+$, should not limit the analytical capabilities of the instrument. Quantitative analyses could still be achieved provided the relative transmission efficiencies between the analyte and reagent ions are known;[21] these values can be approximated with the SIMION simulations (Figure 6.5a). Calibrations could also be performed for target compounds. Additionally, the high transmission efficiency for analyte ions, up to ~90% for *m/z* > 100, is very promising for providing high sensitivity measurements.

6.4.2 *Ion Declustering*

In addition to providing high ion transmission, the IF must be able to decluster water adducts to avoid over-complicated mass spectra. To better probe the declustering capability of the IF, the ion signals were monitored over a range of RF amplitudes (~8-31 V_{p-p}), as shown in Figure 6.7. It is clear that both reagent and analyte ions clusters were effectively broken up, as indicated by the decreasing ion intensity of the cluster ions with increasing RF amplitude. As discussed above, the ion transmission efficiency was predicted to plateau above 20 V_{p-p}, so the decrease in the ion intensity cannot be attributed to diminished ion transmission; this is further demonstrated by the steady $^{102}TEAH^+$ ion intensity (Figure 6.7b) at high RF amplitude. Above ~17 V_{p-p}, $^{19}H(H_2O)^+$ became the dominant reagent ion, representing >95% of the measured reagent ion intensity. The percentage is likely even higher, due to the very low transmission efficiency of *m/z* 19 described above. In the high RF range, $^{59}AcH^+$ also represents more than 99% of the protonated acetone signal, demonstrating the efficient removal of cluster ions.

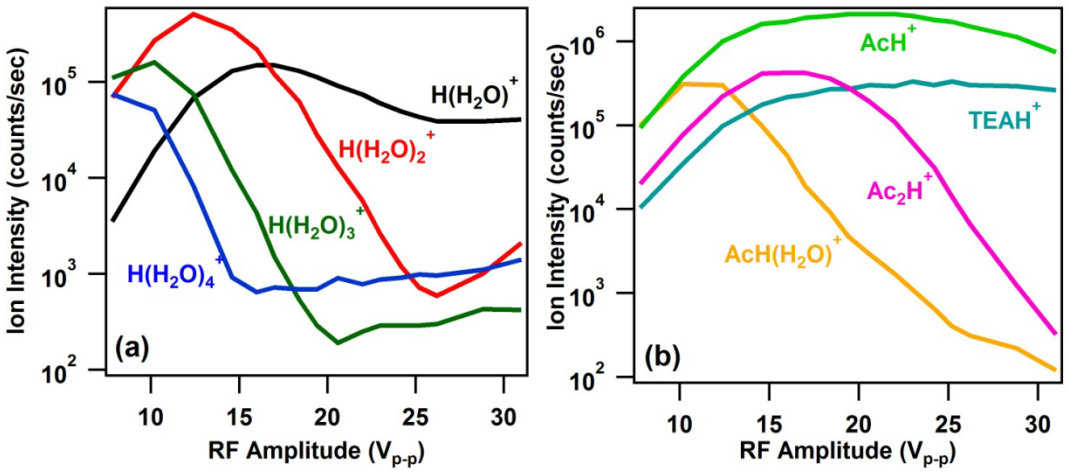

Figure 6.7 Cluster ion signals as a function of RF amplitude for the reagent ions (a) and analyte ions (b) (Ac = acetone, TEA = triethylamine). The RF frequency was fixed at 2.41 MHz in these experiments.

For comparison to the experimental results, reported values of the cluster dissociation energies obtained from the NIST database[28] are given in Table 6.1. These dissociation energies represent sequential dehydration (i.e., loss of one water molecule). The measured declustering trend among the reagent ions, follows the trends in dissociation energies, wherein clusters with higher dissociation energy thresholds persisted to higher RF amplitudes. For instance, dissociation of $^{37}H(H_2O)_2^+$ occurred at higher amplitude than the n = 3,4 water clusters (~15 V_{p-p} vs. ~10 V_{p-p}, Figure 6.7a), because it required a stronger RF field to exceed the dissociation threshold (Table 6.1). The same trend holds for the analyte ions, as well, with $^{117}Ac_2H^+$ dissociating at higher RF amplitudes than $^{77}AcH(H_2O)^+$ (Figure 6.7b). Note that cluster ions with similar dissociation thresholds break apart at similar RF amplitudes; in particular $^{77}AcH(H_2O)^+$ and $^{55}H(H_2O)_3^+$ began to dissociate at ~10 V_{p-p}. Interestingly, the dissociation energy of $^{117}Ac_2H^+$ is slightly lower than $^{37}H(H_2O)_2^+$ (Table 6.1), but it dissociates at higher amplitude (~15 vs. 12 V_{p-p}, Figure 6.7 a and b). This can perhaps be attributed to the inverse dependence of the effective potential on mass (Equation 6.3). In other words, higher mass ions do not acquire as much energy from the RF field, and therefore, higher RF amplitudes may be required to cross their dissociation threshold.

Table 6.1 Ion Dissociation Energies (obtained from NIST[28])

	Declustering Reaction	Dissociation Energy (eV)
Reagent Ions	$^{37}H(H_2O)_2^+ \rightarrow {}^{19}H(H_2O)^+ + H_2O$	1.41
	$^{55}H(H_2O)_3^+ \rightarrow {}^{37}H(H_2O)_2^+ + H_2O$	0.87
	$^{73}H(H_2O)_4^+ \rightarrow {}^{55}H(H_2O)_3^+ + H_2O$	0.76
Analyte Ions	$^{77}AcH(H_2O)^+ \rightarrow {}^{59}AcH^+ + H_2O$	0.89
	$^{117}Ac_2H^+ \rightarrow {}^{59}AcH^+ + Ac$	1.23

Typical PTRMS instruments apply hundreds to thousands of volts (~30-60 V/cm)[30,34] across a drift tube in order to limit the extent of water clustering. These drift tubes are therefore susceptible to discharging[49] which can damage power supplies and destroy the analytical capabilities of the instrument. Using an IF in place of a conventional drift tube effectively declustered reagent and analyte ions with significantly lower potentials; the DC potential across the IF during these measurements was only 9 V (2.25 V/cm). In this instrument, cluster break up can be attributed to collisional activation induced by the RF field.[50] This likely occurred at the small diameter electrodes toward the exit of the IF where the ions are forced closer to the electrode surface and thus experience the strongest field. To illustrate this point, consider Figure 6.1b in comparison to the IF dimensions utilized herein. As discussed by Julian *et al.*,[42] the RF fields from adjacent plates cancel out at a position (dimension a in Figure 6.1b) that is ~60% of the center-to-center distance between the plates (dimension c in Figure 6.1b, 1 mm in the IF geometry used herein). Therefore, in the present IF, the RF field will cancel out at ~0.6 mm from the inner plate surface; thus IF plates with inner diameters >1.2 mm are required for a field-free region to exist within the center of the IF. This condition is achieved along the IF up to the last two plates (i.d. = 1.14 and 0.74 mm) and therefore, ions will experience the strongest RF heating at the exit of IF.

The IF described herein successfully declustered ions at RF amplitudes on the order of 10-20 $V_{p\text{-}p}$. In work conducted in parallel to that described here, Barber *et al.*[51] recently reported the use of an ion funnel to dehydrate ions in their PTRMS instrument. Their ion funnel geometry is substantially different, with wider electrode spacing and inner diameters, resulting in peak-to-peak amplitudes ~10x higher than those utilized in this work and an additional superimposed DC

field of ~10 V/cm. Our system accomplished similar effects using much lower voltages, largely due to the smaller diameter electrodes.

6.4.3 Ion Fragmentation

At RF amplitudes >25 V_{p-p}, the intensity of $^{59}AcH^+$ decreased (Figure 6.5b) despite the theoretical prediction that the transmission should plateau above ~15 V_{p-p} (Figure 6.5a). The decrease in ion signal can be attributed to fragmentation of the protonated molecular ion. Figure 6.8 shows the trends in the dominant fragments produced in the collision-induced dissociation of protonated acetone, namely $^{31}CH_3O^+$ and $^{41}C_3H_5^+$.[52,53] The dominant fragment ion, $^{31}CH_3O^+$, results from loss of ethylene and rearrangement to protonated formaldehyde, whereas $^{41}C_3H_5^+$ reflects loss of water.[53]

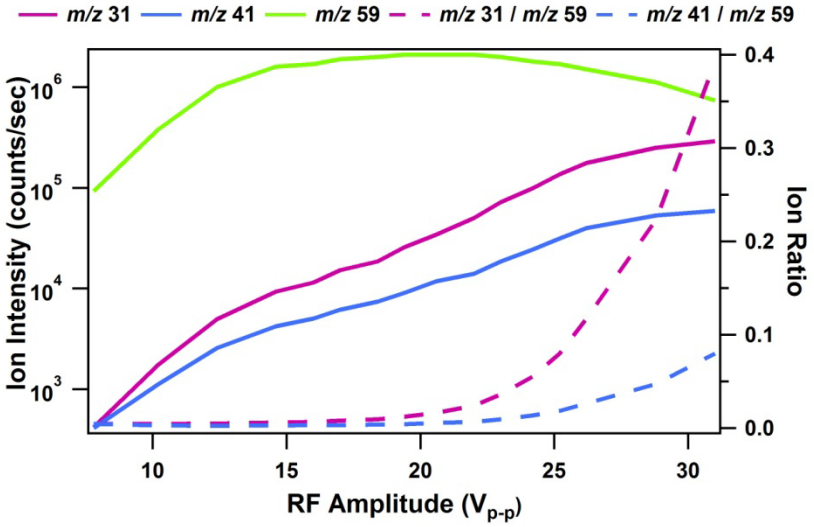

Figure 6.8 Ion intensities observed for the fragments of protonated acetone (solid lines, left axis). *m/z* 59 = AcH^+; *m/z* 31 = CH_3O^+; *m/z* 41 = $C_3H_5^+$. The ratio of the fragment ions to AcH^+ are shown for comparison (dashed lines, right axis).

The initial increase in fragment ion intensity (< ~20 V_{p-p}, Figure 6.8), is due to an increase in ion transmission (as observed for *m/z* 37 in Figure 6.5a), rather than an increase in the extent of fragmentation. This is clear by noting that each fragment remained <1% of the $^{59}AcH^+$ intensity in this RF range (Figure 6.8, dashed lines). The energy barriers for these fragmentation pathways of protonated acetone have been previously determined to be the same and equal to 2.6 eV.[54] The onset of fragmentation at higher RF amplitudes than declustering (~20 V_{p-p} vs. <15 V_{p-p}), is consistent with these energy barriers relative to those in Table 6.1. At higher RF amplitudes, the contribution from the $^{31}CH_3O^+$ and $^{41}C_3H_5^+$ ions increased markedly and reached

nearly 40% and 8% of the protonated acetone signal at 31 V_{p-p}, respectively. Given the equal fragmentation thresholds, it is not entirely clear why the loss of ethylene ($^{31}CH_3O^+$) would occur to a far greater extent than loss of water ($^{41}C_3H_5^+$), though it is possible the high water concentrations present from the ion source reduced the driving force via Le Chatelier's Principle. The measured increase in fragment ion intensity did not fully account for the loss of $^{59}AcH^+$, which decreased by ~65% from 20 to 31 V_{p-p}, due to the reduced ion transmission for lower mass ions (Figure 6.5a). Therefore, the contribution of fragment ions is likely even higher than the mass spectra indicate at high RF amplitudes. From this analysis, it is clear that care must be taken to find an optimal setting that minimizes both ion clusters and fragments, while maximizing ion transmission. In this system, it appears that ~20 V_{p-p} achieved these criteria (Figures 6.5, 6.7, & 6.8).

6.4.4 Preliminary Aerosol Analysis

The instrument described herein is ultimately being developed to target organic aerosol species. As an initial test of aerosol analysis, a simple heated aerosol vaporization tube was constructed that is similar to the thermodenuder described by Huffman *et al.*[55] Succinic (MW = 118 amu) and malonic (MW = 104 amu) acids were ground into a fine powder and aerosolized by passing nitrogen over the agitated powders. The aerosol particles were vaporized by flowing through the tube heated at 140 ºC. The evaporated aerosol was introduced into the sample inlet; the resulting spectrum is shown in Figure 6.9.

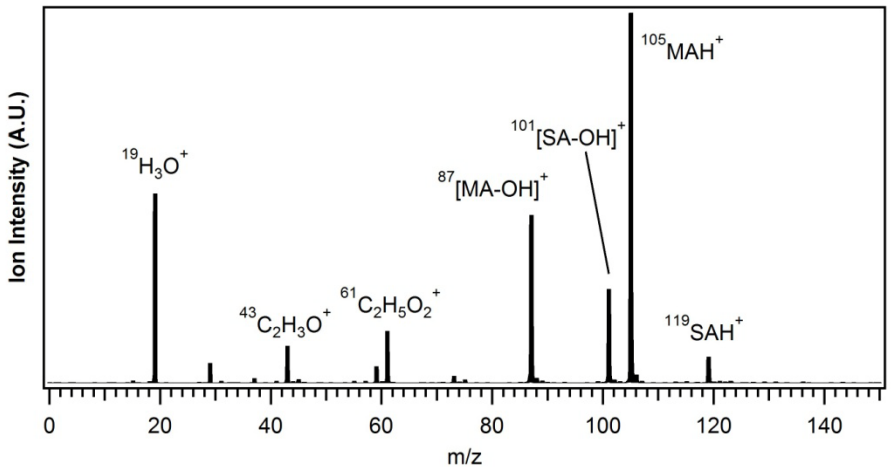

Figure 6.9 Example spectrum from the analysis of malonic (MA) and succinic (SA) acids.

From Figure 6.9 it is clear that these dicarboxylic acids underwent extensive fragmentation, as indicated by the large peak attributed to the loss of an –OH group. No RF amplitudes were found that eliminated (or even greatly reduced) the extent of this fragmentation pathway, indicating that the fragmentation was induced by the ionization step, rather than RF heating in the IF. Indeed, this fragmentation pattern is commonly observed following the protonation of dicarboxylic acids.[29] Upon protonation, the carboxylic acid groups interact and form a cyclic anhydride structure, subsequently eliminating water,[29] as shown in Figure 6.10 for succinic acid. This reaction mechanism can potentially explain the different fragment-to-protonated molecular ion ratios for succinic and malonic acid. Malonic acid has 1 carbon in between the acid groups, compared to 2 for succinic acid. Therefore, elimination of water would produce a more strained, 4-member ring for malonic acid, which likely reduces the driving force for fragmentation. Future experiments will explore a variety of other aerosol standards to determine the ability to detect molecular ions from aerosol particles.

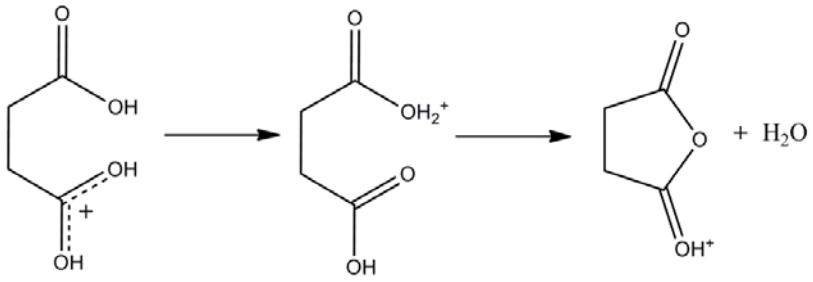

Figure 6.10 Dehydration of protonated succinic acid. Reaction mechanism obtained from ref. 29.

6.5 Conclusions & Future Directions

In this work, an ion funnel has been shown to be an effective tool to achieve ion declustering and high ion transmission efficiencies. Reagent and analyte ions were successfully declustered at RF amplitudes ~20 $V_{p\text{-}p}$, with the trends in good agreement with the relative dissociation energies. The highest potential in the instrument front end was only ~50 V, compared to the hundreds to thousands of volts utilized in typical PTRMS instruments. Ion simulations further estimated that analyte ions can be transmitted with ~90% efficiency, demonstrating the strong potential for IFs to provide substantial improvements in the PTRMS field.

While the sensitivity of the current system has yet to be fully characterized, it is expected that the detection limit is not yet suitable for sensitive ambient aerosol analyses. A number of

options exist for optimizing the ion funnel configuration to maximize sensitivity. First and foremost, the IF should be extended to provide longer interaction time between the analytes and reagent ions, thereby ensuring maximum protonation of the analyte molecules. The geometry of the vacuum chamber and ion funnel mounts should also be redesigned such that the analytes are introduced immediately in front of (or even, perhaps, through) the ion funnel to make sure that all ions are confined and transferred. A significant improvement would involve incorporating an IF trapping region, as developed by Ibrahim *et al.*[56,57] In their system, ion accumulation on the order of 100 ms resulted in 10-20-fold improvement in the signal intensity of low concentration analytes over the continuous mode.[56] In conjunction with an ion trap, the low mass filtering observed in the present ion funnel could be quite advantageous by significantly reducing the concentration of reagent ions in the trap, which may reach its space-charge capacity. An improved aerosol inlet should also be designed and implemented. Here, too, many options are possible with the choice of real-time introduction[17,58] or *in-situ* collection[20,36] being dependent on the instrument sensitivity. With these improvements, the ion funnel could provide a highly effective means of achieving sensitive molecular analysis of organic aerosols in the atmosphere.

6.6 Acknowledgments

The dissertation author was the primary researcher and author of this chapter. Dr. Robert Moision is acknowledged for introducing ion funnels to the Prather group and designing the electrodes and electronics of the ion funnel used herein. Joseph Mayer is thanked for design discussions and machining parts. Helpful discussions with Dr. Jean Futrell & Dr. M. Lizabeth Alexander (Pacific Northwest National Laboratory) and Dr. Timothy Guasco & Dr. Timothy Bertram (UCSD) are gratefully acknowledged. George Kassabian (UCSD) is also thanked for assisting with the design of the electronics. Assistance with the aerosol experiments by Camille Sultana and Katherine Nadler is also gratefully acknowledged. This work was funded by the National Science Foundation, Grant # AGS-0923581 and the Electric Power Research Institute. L. Hatch was funded by an NSF Graduate Research Fellowship (2008-2011). R. Moision received funding through a Dreyfus Foundation Postdoctoral Fellowship (2007-2009).

6.7 References

1. Zhang, Q.; Jimenez, J. L.; Canagaratna, M. R.; Allan, J. D.; Coe, H.; Ulbrich, I.; Alfarra, M. R.; Takami, A.; Middlebrook, A. M.; Sun, Y. L.; Dzepina, K.; Dunlea, E.; Docherty, K.; DeCarlo, P. F.; Salcedo, D.; Onasch, T.; Jayne, J. T.; Miyoshi, T.; Shimono, A.; Hatakeyama, S.; Takegawa, N.; Kondo, Y.; Schneider, J.; Drewnick, F.; Borrmann, S.; Weimer, S.; Demerjian, K.; Williams, P.; Bower, K.; Bahreini, R.; Cottrell, L.; Griffin, R. J.; Rautiainen, J.; Sun, J. Y.; Zhang, Y. M.; Worsnop, D. R., Ubiquity and dominance of oxygenated species in organic aerosols in anthropogenically-influenced Northern Hemisphere midlatitudes. *Geophys. Res. Lett.* **2007,** *34*, (13).

2. Goldstein, A. H.; Galbally, I. E., Known and unexplored organic constituents in the earth's atmosphere. *Environ. Sci. Technol.* **2007,** *41*, (5), 1514-1521.

3. Fuzzi, S.; Andreae, M. O.; Huebert, B. J.; Kulmala, M.; Bond, T. C.; Boy, M.; Doherty, S. J.; Guenther, A.; Kanakidou, M.; Kawamura, K.; Kerminen, V. M.; Lohmann, U.; Russell, L. M.; Poschl, U., Critical assessment of the current state of scientific knowledge, terminology, and research needs concerning the role of organic aerosols in the atmosphere, climate, and global change. *Atmos. Chem. Phys.* **2006,** *6*, 2017-2038.

4. Hallquist, M.; Wenger, J. C.; Baltensperger, U.; Rudich, Y.; Simpson, D.; Claeys, M.; Dommen, J.; Donahue, N. M.; George, C.; Goldstein, A. H.; Hamilton, J. F.; Herrmann, H.; Hoffmann, T.; Iinuma, Y.; Jang, M.; Jenkin, M. E.; Jimenez, J. L.; Kiendler-Scharr, A.; Maenhaut, W.; McFiggans, G.; Mentel, T. F.; Monod, A.; Prevot, A. S. H.; Seinfeld, J. H.; Surratt, J. D.; Szmigielski, R.; Wildt, J., The formation, properties and impact of secondary organic aerosol: current and emerging issues. *Atmos. Chem. Phys.* **2009,** *9*, (14), 5155-5236.

5. McMurry, P. H., A review of atmospheric aerosol measurements. *Atmos. Environ.* **2000,** *34*, (12-14), 1959-1999.

6. Jacobson, M. C.; Hansson, H. C.; Noone, K. J.; Charlson, R. J., Organic atmospheric aerosols: Review and state of the science. *Reviews of Geophysics* **2000,** *38*, (2), 267-294.

7. Vogt, L.; Groger, T.; Zimmermann, R., Automated compound classification for ambient aerosol sample separations using comprehensive two-dimensional gas chromatography-time-of-flight mass spectrometry. *J. Chromatogr. A* **2007,** *1150*, (1-2), 2-12.

8. Surratt, J. D.; Gomez-Gonzalez, Y.; Chan, A. W. H.; Vermeylen, R.; Shahgholi, M.; Kleindienst, T. E.; Edney, E. O.; Offenberg, J. H.; Lewandowski, M.; Jaoui, M.; Maenhaut, W.; Claeys, M.; Flagan, R. C.; Seinfeld, J. H., Organosulfate formation in biogenic secondary organic aerosol. *J. Phys. Chem. A* **2008,** *112*, (36), 8345-8378.

9. Bateman, A. P.; Nizkorodov, S. A.; Laskin, J.; Laskin, A., High-Resolution Electrospray Ionization Mass Spectrometry Analysis of Water-Soluble Organic Aerosols Collected with a Particle into Liquid Sampler. *Anal. Chem.* **2010,** *82*, (19), 8010-8016.

10. Laskin, J.; Laskin, A.; Roach, P. J.; Slysz, G. W.; Anderson, G. A.; Nizkorodov, S. A.; Bones, D. L.; Nguyen, L. Q., High-Resolution Desorption Electrospray Ionization Mass Spectrometry for Chemical Characterization of Organic Aerosols. *Anal. Chem.* **2010,** *82*, (5), 2048-2058.

11. Chan, M. N.; Surratt, J. D.; Claeys, M.; Edgerton, E. S.; Tanner, R. L.; Shaw, S. L.; Zheng, M.; Knipping, E. M.; Eddingsaas, N. C.; Wennberg, P. O.; Seinfeld, J. H., Characterization and Quantification of Isoprene-Derived Epoxydiols in Ambient Aerosol in the Southeastern United States. *Environ. Sci. Technol.* **2010,** *44*, (12), 4590-4596.

12. Pratt, K. A.; Prather, K. A., Mass spectrometry of atmospheric aerosols. Recent developments and applications. Part II: On-line mass spectrometry techniques. *Mass Spectrom. Rev.* **2012,** *31*, (1), 17-48.

13. Woods, E.; Smith, G. D.; Dessiaterik, Y.; Baer, T.; Miller, R. E., Quantitative detection of aromatic compounds in single aerosol particle mass spectrometry. *Anal. Chem.* **2001,** *73*, (10), 2317-2322.

14. Pratt, K. A.; Hatch, L. E.; Prather, K. A., Seasonal Volatility Dependence of Ambient Particle Phase Amines. *Environ. Sci. Technol.* **2009,** *43*, (14), 5276-5281.

15. Zhang, Q.; Jimenez, J. L.; Canagaratna, M. R.; Ulbrich, I. M.; Ng, N. L.; Worsnop, D. R.; Sun, Y. L., Understanding atmospheric organic aerosols via factor analysis of aerosol mass spectrometry: a review. *Anal. Bioanal. Chem.* **2011,** *401*, (10), 3045-3067.

16. Canagaratna, M. R.; Jayne, J. T.; Jimenez, J. L.; Allan, J. D.; Alfarra, M. R.; Zhang, Q.; Onasch, T. B.; Drewnick, F.; Coe, H.; Middlebrook, A.; Delia, A.; Williams, L. R.; Trimborn, A. M.; Northway, M. J.; DeCarlo, P. F.; Kolb, C. E.; Davidovits, P.; Worsnop, D. R., Chemical and microphysical characterization of ambient aerosols with the aerodyne aerosol mass spectrometer. *Mass Spectrom. Rev.* **2007,** *26*, (2), 185-222.

17. Hearn, J. D.; Smith, G. D., A chemical ionization mass spectrometry method for the online analysis of organic aerosols. *Anal. Chem.* **2004,** *76*, (10), 2820-2826.

18. Holzinger, R.; Kasper-Giebl, A.; Staudinger, M.; Schauer, G.; Rockmann, T., Analysis of the chemical composition of organic aerosol at the Mt. Sonnblick observatory using a novel high mass resolution thermal-desorption proton-transfer-reaction mass-spectrometer (hr-TD-PTR-MS). *Atmos. Chem. Phys.* **2010,** *10*, (20), 10111-10128.

19. Voisin, D.; Smith, J. N.; Sakurai, H.; McMurry, P. H.; Eisele, F. L., Thermal desorption chemical ionization mass spectrometer for ultrafine particle chemical composition. *Aerosol Sci. Technol.* **2003,** *37*, (6), 471-475.

20. Yatavelli, R. L. N.; Thornton, J. A., Particulate Organic Matter Detection Using a Micro-Orifice Volatilization Impactor Coupled to a Chemical Ionization Mass Spectrometer (MOVI-CIMS). *Aerosol Sci. Technol.* **2010,** *44*, (1), 61-74.

21. de Gouw, J.; Warneke, C., Measurements of volatile organic compounds in the earths atmosphere using proton-transfer-reaction mass spectrometry. *Mass Spectrom. Rev.* **2007,** *26*, (2), 223-257.

22. Lagg, A.; Taucher, J.; Hansel, A.; Lindinger, W., Applications of Proton-Transfer Reactions to Gas-Analysis. *Int. J. Mass Spectrom. Ion Processes* **1994,** *134*, (1), 55-66.

23. Hansel, A.; Jordan, A.; Holzinger, R.; Prazeller, P.; Vogel, W.; Lindinger, W., Proton-Transfer Reaction Mass-Spectrometry - Online Trace Gas-Analysis at the Ppb Level. *Int. J. Mass spectrom.* **1995,** *149*, 609-619.

24. Lindinger, W.; Hansel, A., Analysis of trace gases at ppb levels by proton transfer reaction mass spectrometry (PTR-MS). *Plasma Sources Sci. Technol.* **1997,** *6*, (2), 111-117.

25. Lindinger, W.; Hansel, A.; Jordan, A., Proton-transfer-reaction mass spectrometry (PTR-MS): on-line monitoring of volatile organic compounds at pptv levels. *Chem. Soc. Rev.* **1998,** *27*, (5), 347-354.

26. Hansel, A.; Jordan, A.; Warneke, C.; Holzinger, R.; Lindinger, W., Improved detection limit of the proton-transfer reaction mass spectrometer: On-line monitoring of volatile organic compounds at mixing ratios of a few PPTV. *Rapid Commun. Mass Spectrom.* **1998,** *12*, (13), 871-875.

27. Hansel, A.; Jordan, A.; Warneke, C.; Holzinger, R.; Wisthaler, A.; Lindinger, W., Proton-transfer-reaction mass spectrometry (PTR-MS): on-line monitoring of volatile organic compounds at volume mixing ratios of a few pptv. *Plasma Sources Sci. Technol.* **1999,** *8*, (2), 332-336.

28. Linstrom, P. J.; Mallard, W. G. NIST Chemistry WebBook, NIST Standard Reference Database Number 69. National Institute of Standards and Technology, Gaithersburg, MD, USA, http://webbook.nist.gov, retrieved 2012.

29. Harrison, A. G., *Chemical Ionization Mass Spectrometry*. 2nd ed.; CRC Press: Boca Raton, FL, 1992.

30. Blake, R. S.; Monks, P. S.; Ellis, A. M., Proton-Transfer Reaction Mass Spectrometry. *Chem. Rev.* **2009,** *109*, (3), 861-896.

31. Smith, J. N.; Barsanti, K. C.; Friedli, H. R.; Ehn, M.; Kulmala, M.; Collins, D. R.; Scheckman, J. H.; Williams, B. J.; McMurry, P. H., Observations of aminium salts in atmospheric nanoparticles and possible climatic implications. *Proc. Natl. Acad. Sci. USA* **2010,** *107*, (15), 6634-6639.

32. Hearn, J. D.; Smith, G. D., Kinetics and product studies for ozonolysis reactions of organic particles using aerosol CIMS. *J. Phys. Chem. A* **2004,** *108*, (45), 10019-10029.

33. Hearn, J. D.; Smith, G. D., Reactions and mass spectra of complex particles using Aerosol CIMS. *Int. J. Mass spectrom.* **2006,** *258*, (1-3), 95-103.

34. Thornberry, T.; Murphy, D. M.; Thomson, D. S.; de Gouw, J.; Warneke, C.; Bates, T. S.; Quinn, P. K.; Coffman, D., Measurement of Aerosol Organic Compounds Using a Novel Collection/Thermal-Desorption PTR-ITMS Instrument. *Aerosol Sci. Technol.* **2009,** *43*, (5), 486-501.

35. Mikoviny, T.; Kaser, L.; Wisthaler, A., Development and characterization of a High-Temperature Proton-Transfer-Reaction Mass Spectrometer (HT-PTR-MS). *Atmos. Meas. Tech.* **2010,** *3*, (3), 537-544.

36. Holzinger, R.; Williams, J.; Herrmann, F.; Lelieveld, J.; Donahue, N. M.; Rockmann, T., Aerosol analysis using a Thermal-Desorption Proton-Transfer-Reaction Mass Spectrometer (TD-PTR-MS): a new approach to study processing of organic aerosols. *Atmos. Chem. Phys.* **2010,** *10*, (5), 2257-2267.

37. Shaffer, S. A.; Prior, D. C.; Anderson, G. A.; Udseth, H. R.; Smith, R. D., An ion funnel interface for improved ion focusing and sensitivity using electrospray ionization mass spectrometry. *Anal. Chem.* **1998,** *70*, (19), 4111-4119.

38. Shaffer, S. A.; Tang, K. Q.; Anderson, G. A.; Prior, D. C.; Udseth, H. R.; Smith, R. D., A novel ion funnel for focusing ions at elevated pressure using electrospray ionization mass spectrometry. *Rapid Commun. Mass Spectrom.* **1997,** *11*, (16), 1813-1817.

39. Gerlich, D., Inhomogeneous RF Fields: A versatile tool for the study of processes with slow ions. In *State-Selected and State-to-State Ion Molecule Reaction Dynamics, Part 1: Experiment*, Ng, C.-Y.; Baer, M., Eds. John Wiley & Sons, Inc. : New York, 1992; Vol. LXXXII.

40. Tolmachev, A. V.; Udseth, H. R.; Smith, R. D., Charge capacity limitations of radio frequency ion guides in their use for improved ion accumulation and trapping in mass spectrometry. *Anal. Chem.* **2000,** *72*, (5), 970-978.

41. Kelly, R. T.; Tolmachev, A. V.; Page, J. S.; Tang, K. Q.; Smith, R. D., The Ion Funnel: Theory, Implementations, and Applications. *Mass Spectrom. Rev.* **2010,** *29*, (2), 294-312.

42. Julian, R. R.; Mabbett, S. R.; Jarrold, M. F., Ion funnels for the masses: Experiments and simulations with a simplified ion funnel. *J. Am. Soc. Mass. Spectrom.* **2005,** *16*, (10), 1708-1712.

43. Kim, T.; Tolmachev, A. V.; Harkewicz, R.; Prior, D. C.; Anderson, G.; Udseth, H. R.; Smith, R. D.; Bailey, T. H.; Rakov, S.; Futrell, J. H., Design and implementation of a new electrodynamic ion funnel. *Anal. Chem.* **2000,** *72*, (10), 2247-2255.

44. Moision, R. M.; Armentrout, P. B., An electrospray ionization source for thermochemical investigation with. the guided ion beam mass spectrometer. *J. Am. Soc. Mass. Spectrom.* **2007,** *18*, (6), 1124-1134.

45. Kukui, A.; Ancellet, G.; Le Bras, G., Chemical ionisation mass spectrometer for measurements of OH and Peroxy radical concentrations in moderately polluted atmospheres. *J. Atmos. Chem.* **2008,** *61*, (2), 133-154.

46. Williams, B. J.; Goldstein, A. H.; Kreisberg, N. M.; Hering, S. V.; Worsnop, D. R.; Ulbrich, I. M.; Docherty, K. S.; Jimenez, J. L., Major components of atmospheric organic aerosol in southern California as determined by hourly measurements of source marker compounds. *Atmos. Chem. Phys.* **2010,** *10*, (23), 11577-11603.

47. Hawkins, L. N.; Russell, L. M., Oxidation of ketone groups in transported biomass burning aerosol from the 2008 Northern California Lightning Series fires. *Atmos. Environ.* **2010,** *44*, (34), 4142-4154.

48. Tolmachev, A. V.; Kim, T.; Udseth, H. R.; Smith, R. D.; Bailey, T. H.; Futrell, J. H., Simulation-based optimization of the electrodynamic ion funnel for high sensitivity electrospray ionization mass spectrometry. *Int. J. Mass spectrom.* **2000,** *203*, (1-3), 31-47.

49. Hanson, D. R.; Greenberg, J.; Henry, B. E.; Kosciuch, E., Proton transfer reaction mass spectrometry at high drift tube pressure. *Int. J. Mass spectrom.* **2003,** *223*, (1-3), 507-518.

50. Tolmachev, A. V.; Vilkov, A. N.; Bogdanov, B.; Pasa-Tolic, L.; Masselon, C. D.; Smith, R. D., Collisional activation of ions in RF ion traps and ion guides: The effective ion temperature treatment. *J. Am. Soc. Mass. Spectrom.* **2004,** *15*, (11), 1616-1628.

51. Barber, S.; Blake, R. S.; White, I. R.; Monks, P. S.; Reich, F.; Mullock, S.; Ellis, A. M., Increased Sensitivity in Proton Transfer Reaction Mass Spectrometry by Incorporation of a Radio Frequency Ion Funnel. *Anal. Chem.* **2012**.

52. Warneke, C.; de Gouw, J. A.; Lovejoy, E. R.; Murphy, P. C.; Kuster, W. C.; Fall, R., Development of proton-transfer ion trap-mass spectrometry: On-line detection and identification of volatile organic compounds in air. *J. Am. Soc. Mass. Spectrom.* **2005,** *16*, (8), 1316-1324.

53. Prazeller, P.; Palmer, P. T.; Boscaini, E.; Jobson, T.; Alexander, M., Proton transfer reaction ion trap mass spectrometer. *Rapid Commun. Mass Spectrom.* **2003,** *17*, (14), 1593-1599.

54. Bowen, R. D.; Harrison, A. G., Chemical Ionization Mass-Spectra of Selected C3h6o Compounds. *Org. Mass Spectrom.* **1981,** *16*, (4), 159-166.

55. Huffman, J. A.; Ziemann, P. J.; Jayne, J. T.; Worsnop, D. R.; Jimenez, J. L., Development and Characterization of a Fast-Stepping/Scanning Thermodenuder for Chemically-Resolved Aerosol Volatility Measurements (vol 42, pg 395, 2008). *Aerosol Sci. Technol.* **2009,** *43*, (3), 273-273.

56. Ibrahim, Y.; Belov, M. E.; Tolmachev, A. V.; Prior, D. C.; Smith, R. D., Ion funnel trap interface for orthogonal time-of-flight mass spectrometry. *Anal. Chem.* **2007,** *79*, (20), 7845-7852.

57. Clowers, B. H.; Ibrahim, Y. M.; Prior, D. C.; Danielson, W. F.; Belov, M. E.; Smith, R. D., Enhanced ion utilization efficiency using an electrodynamic ion funnel trap as an injection mechanism for ion mobility spectrometry. *Anal. Chem.* **2008,** *80*, (3), 612-623.

58. Bennett, J. F.; Collin, F.; Hastie, D. R., A laboratory flow reactor with gas particle separation and on-line MS/MS for product identification in atmospherically important reactions. *Atmos. Meas. Tech.* **2009,** *2*, (2), 813-823.

7 Conclusions & Future Directions

Characterizing single-particle mixing state is essential for advancing the state-of-science regarding the atmospheric impacts of aerosols, including their roles in human health effects and cloud formation. Single particle mass spectrometers, such as the aerosol time-of-flight mass spectrometer (ATOFMS) have become a primary tool for determining the size-resolved mixing state of atmospheric aerosol particles. The research in this dissertation has further improved the analytical capability of ATOFMS for the characterization of ambient aerosols by identifying new ion markers and assessing the changes in peak area due to atmospheric processing. New instrumentation is also in development to improve the characterization of organic aerosol particles, with the ultimate hope of providing molecular speciation at the single-particle level. A summary of the main conclusions from each project and suggestions for future work are discussed in the following sections.

7.1 Organosulfate analyses

7.1.1 Conclusions

Negative ion markers indicative of isoprene-organosulfate species (*m/z* -139, -153, -155, -199, and -215) were identified for the first time in ATOFMS mass spectra obtained in Atlanta, GA. Analysis of laboratory standards confirmed that ATOFMS is able to detect deprotonated molecular ions from organosulfate species. Ion peak assignments from the ambient data were further corroborated through comparison with filter samples collected during the AMIGAS measurement campaign. The off-line analyses provided unequivocal identification of the organosulfate molecules in Atlanta via chromatographic separations and high resolution mass spectrometry analysis whereas the ATOFMS data provided unique insights into the size-resolved mixing state and temporal trends of these compounds, which highlights the complementary information afforded by off-line and on-line measurements. The temporal trends were assessed for the organosulfate derived from isoprene epoxydiol (IEPOX). The organosulfate abundance was found to peak overnight due to the buildup of pollutants under a stable nocturnal boundary layer. The formation of organosulfates was postulated to occur via gas-to-particle partitioning of isoprene oxidation products, with subsequent condensed-phase reaction with sulfate. When the effects of the boundary layer were removed by normalizing by the CO concentration, production of organosulfates coincided with measured ozone, indicative of photochemical activity and possible radical formation of organosulfates. However, the nocturnal formation dominated over

the daytime production in Atlanta. Further, organosulfate markers were overwhelmingly detected in carbonaceous submicron particles, with up to ~90% of particles in the size range < 500 nm found to contain these species. While the mass contribution to individual particles could not be estimated, it is clear that organosulfates are ubiquitous organic aerosol components in the Southeastern United States. Due to the non-volatile nature of organosulfates, their formation within the particle phase can act to enhance the partitioning of SOA precursors to the particle phase, which may in turn impact human health and climate-relevant properties.

7.1.2 Future Directions

This study established that ATOFMS is well-suited to detect isoprene-derived organosulfate species and the results from Atlanta represent the first insights into the information that can be gained regarding these species. However, much more work could be done to further utilize ATOFMS to assess the contribution of organosulfate species to atmospheric SOA. In particular, the ability of ATOFMS to detect monoterpene-derived organosulfates should be assessed. Interestingly, these species have been detected via off-line methods in Atlanta,[1] but were not observed in the ATOFMS data due to either fragmentation or poor ion transmission at higher masses. Laboratory standards of the monoterpene-derived organosulfates could be analyzed on the aircraft-ATOFMS that is equipped with an improved mass spectrometer that achieves significantly better ion transmission at higher masses.[2,3] These experiments could determine the relative importance of fragmentation vs. ion transmission in hindering the detection of monoterpene-derived organosulfate compounds.

Regional comparisons would also be of great interest to determine the relative significance of the organosulfate compounds. Similar organosulfate markers have been observed in past ATOFMS studies at other US locations, including Boston, MA, Chapel Hill, NC, and Sacramento, CA. These datasets could be revisited in greater depth to determine how the temporal trends or mixing-state behavior of organosulfates vary in different locations to perhaps gain further insight into the formation mechanisms occurring in the ambient atmosphere. Significantly, different organosulfate markers have been observed in different locations. For instance, the dominant organosulfate species observed in Atlanta, the IEPOX-derived organosulfate (*m/z* -215), was not present in particles sampled in Riverside, CA and Mexico City, Mexico; however, the markers at *m/z* -155 and -153 were observed in these studies, indicating that the sources or chemistry leading to organosulfates may vary significantly from region to

region. Revisiting the ATOFMS studies that have been conducted worldwide could help identify the regional differences in the chemistry leading to particulate organosulfates.

7.2 Effects of aerosol aging on laser desorption/ionization in ATOFMS

7.2.1 Conclusions

In this work, a thermodenuder was used in-line with ATOFMS and AMS measurements to monitor the volatility of aerosol components as a function of temperature. Heating in the thermodenuder essentially removed the major secondary components, which permitted assessment of the changes in ionization as a function of particle age: particle residuals at high temperatures represented fresher particle emissions. It was observed that the degree of ionization from each particle increased as the secondary coating was removed, likely due to either increased absorption of the DI laser. The change in ionization efficiency resulted in higher apparent ion intensity for the individual components. To counteract these effects, non-volatile aerosol components were used as pseudo-internal standards. Normalizing ion peak areas by the peak area of the internal standards produced strong agreement with the AMS data, indicating that the change in ionization efficiency influenced the whole particle, rather than individual components. However, there was also evidence via covariance mapping that collision-induced matrix effects changed with heating and may have impacted select species; for instance, amines were observed to suppress other organic ions in the unheated particles, which resulted in higher fractions remaining at elevated temperatures. For the majority of the components analyzed, however, the results outlined in Chapter 4 demonstrate that peak areas from ATOFMS could be accurately related to mass when appropriately corrected.

7.2.2 Future Directions

Applying an internal standard demonstrated strong agreement with the AMS for the averaged thermodenuder temperature profile. Future work should demonstrate the applicability of this method for typical field sampling that follows the temporal trends of aerosol species. Comparisons could be made with collocated instruments such as the AMS or PILS-IC to determine how accurately peak areas can be related to mass and if this method will break down under certain atmospheric conditions. It would also be useful to check this method on data collected using a nozzle-inlet ATOFMS that has a broader size range (0.2-3 μm) than the ATOFMS used in these SOAR studies.

The peak area trends implied that particles existed in a core-shell morphology in Riverside based on previous laboratory studies. Changes in the morphology of the ambient particles with heating could be determined through comparisons to collocated microscopy studies or depth-profiling experiments could be performed with ATOFMS to ascertain the degree of heterogeneity within single particles. Laboratory experiments could further probe the effect of coating thickness on the ionization patterns. For example, elemental carbon particles could be coated with transparent species such as ammonium nitrate/sulfate, with particles selected at different sizes prior to ATOFMS analysis to select coatings of different thicknesses. A similar approach was used by Spencer *et al.*[4] Such experiments could also probe whether specific coating materials exert different effects. Coatings in the Riverside area are comprised of organics, ammonium nitrate, and ammonium sulfate; did one of these secondary components cause the majority of the ionization suppression effect?

7.3 Mixing-state dependent volatility

7.3.1 Conclusions

The thermodenuder data was subsequently analyzed via the internal standard method described above to determine the influence of chemical mixing state on the volatility of aerosol constituents, particularly nitrate. Observations suggest that the volatility of nitrate was significantly reduced in the presence of metal cations and could not be entirely attributed to non-volatile nitrate salts. Thermodynamic modeling was performed to better understand the role of metals and demonstrated that reduced availability of ammonium and increased liquid water content contributed to the suppression of nitrate volatility even when nitrate was not required to balance the charge of the metal components. Comparisons between measurements and model results imply that complex particle morphologies may exist in the Riverside region due to the extensive secondary aerosol production, resulting in different nitrate evaporation regimes. These results also highlight that the volatility of a component from certain types of particles may be very different than the average composition would suggest. Therefore, assumptions of internal mixing may misrepresent the actual behavior of particles in the atmosphere.

7.3.2 Future directions

As discussed in Chapter 5, the nitrate thermogram averaged across all ATOFMS particle types was significantly higher than the AMS despite the fact that most of the nitrate in the Riverside area is likely in the form of ammonium nitrate, which is detectable by AMS. It remains

unclear at this stage how the presence of metal ions influences the measurement of non-refractory nitrate in both the AMS and ATOFMS techniques. This discrepancy could be resolved by monitoring the same particle residuals from the thermodenuder with an ATOFMS, AMS, and a PILS-IC that can quantitatively detect both refractory and non-refractory forms of nitrate in near-real time. Intercomparison of these three instruments could determine the extent to which the AMS under-predicts or the ATOFMS over-predicts the nitrate levels from particles containing refractory material. Additional model studies should probe the influence of organics on nitrate volatility, including amines, organonitrates, and water-soluble organic compounds, to better characterize the disparity between the laboratory and ambient measurements.

7.4 Implementation of an ion funnel in PTRMS

7.4.1 Conclusions

In Chapter 6, the implementation of an ion funnel (IF) in a proton-transfer-reaction mass spectrometer was outlined. Current proton-transfer-reaction mass spectrometers applied to the analysis of organic aerosols lack high sensitivity, which may be attributable to the small orifices used to step down the pressure from the ionization region to the mass spectrometer. In contrast, ion funnels have demonstrated nearly 100% ion transmission efficiency for the detection of biomolecules from electrospray ionization sources. As this work represented the first application of an IF in a proton-transfer-reaction mass spectrometer, proof-of-concept experiments were performed using a short 40-plate IF that was designed and constructed in house. Experiments established that modulating the RF amplitude applied to the IF plates can effectively break up water clusters of both reagent and analyte ions due to RF heating. Ion simulations were also performed and demonstrated that the IF can transmit up to 90% of the analyte ions utilized in this work. IFs therefore provide high sensitivity and ion declustering capability, which collectively highlight the strong potential for ion funnels to provide substantial advances in the field of chemical ionization mass spectrometry.

7.4.2 Future directions

The sensitivity of the instrument could be substantially improved by optimizing the ion funnel geometry. In particular, the IF should be extended to provide longer interaction time between the analytes and reagent ions, thereby ensuring maximum protonation of the analyte molecules. The geometry of the vacuum chamber and ion funnel mounts should also be redesigned such that the analytes are introduced immediately in front of (or even, perhaps,

through) the ion funnel to make sure that all ions are confined and transferred. Likely the largest improvement would involve incorporating an IF trapping region, as developed by Ibrahim *et al.*[5,6] SIMION simulations will be essential for determining the best design. The IF plates should also be redesigned to reduce the capacitance between adjacent plates as much as possible in order to reduce the power needed to drive the IF, and will enable lengthening the IF. An improved aerosol inlet should also be designed and implemented. Options include collected aerosols onto an impactor with subsequent heating via thermal or laser (infrared) desorption. With these improvements, the ion funnel could provide a highly effective means of achieving sensitive molecular analysis of organic aerosols in the atmosphere, ultimately at the single-particle level.

7.5 Concluding remarks

The analysis tools developed herein can be used by others in the ATOFMS and SPMS communities. The organosulfate markers were identified in field studies around the US and spanning a decade, demonstrating that these markers will be broadly applicable to ATOFMS studies rather than unique to the Atlanta area. The additional insights into the impacts of aging on laser desorption/ionization can also be applied in future work to improve the quantification capability of ATOFMS. These methods can be used to better understand the processing of ambient aerosols, as have been demonstrated herein for organosulfate and nitrate volatility. Further, incorporating an ion funnel into proton-transfer-reaction mass spectrometers opens new doors to improving the sensitivity of these instruments and may ultimately provide improved analyses of organic aerosol constituents.

7.6 References

1. Surratt, J. D.; Gomez-Gonzalez, Y.; Chan, A. W. H.; Vermeylen, R.; Shahgholi, M.; Kleindienst, T. E.; Edney, E. O.; Offenberg, J. H.; Lewandowski, M.; Jaoui, M.; Maenhaut, W.; Claeys, M.; Flagan, R. C.; Seinfeld, J. H., Organosulfate formation in biogenic secondary organic aerosol. *J. Phys. Chem. A* **2008,** *112*, (36), 8345-8378.

2. Pratt, K. A.; Mayer, J. E.; Holecek, J. C.; Moffet, R. C.; Sanchez, R. O.; Rebotier, T. P.; Furutani, H.; Gonin, M.; Fuhrer, K.; Su, Y. X.; Guazzotti, S.; Prather, K. A., Development and Characterization of an Aircraft Aerosol Time-of-Flight Mass Spectrometer. *Anal. Chem.* **2009,** *81*, (5), 1792-1800.

3. Denkenberger, K. A.; Moffet, R. C.; Holecek, J. C.; Rebotier, T. P.; Prather, K. A., Real-time, single-particle measurements of oligomers in aged ambient aerosol particles. *Environ. Sci. Technol.* **2007,** *41*, (15), 5439-5446.

4. Spencer, M. T.; Prather, K. A., Using ATOFMS to determine OC/EC mass fractions in particles. *Aerosol Sci. Technol.* **2006,** *40*, (8), 585-594.

5. Ibrahim, Y.; Belov, M. E.; Tolmachev, A. V.; Prior, D. C.; Smith, R. D., Ion funnel trap interface for orthogonal time-of-flight mass spectrometry. *Anal. Chem.* **2007,** *79*, (20), 7845-7852.

6. Clowers, B. H.; Ibrahim, Y. M.; Prior, D. C.; Danielson, W. F.; Belov, M. E.; Smith, R. D., Enhanced ion utilization efficiency using an electrodynamic ion funnel trap as an injection mechanism for ion mobility spectrometry. *Anal. Chem.* **2008,** *80*, (3), 612-623.